Computational Photochemistry, Spectroscopy, and Potential Energy Surfaces of Complex Molecules

A Dissertation
SUBMITTED TO THE FACULTY OF
UNIVERSITY OF MINNESOTA
BY

Shaohong Li

IN PARTIAL FULFILLMENT OF THE REQUIREMENTS
FOR THE DEGREE OF
DOCTOR OF PHILOSOPHY

Adviser: Donald G. Truhlar

June 2017

Acknowledgements

I don't usually believe in luck, but in retrospect, I can't help feeling lucky, to be in such a great department, surrounded by such smart, nice, and helpful people. Without them I could not have finished this important stage of my life.

I want to first thank my advisor, Prof. Don Truhlar. He is a role model of the greatest scientists. I really learned a lot from him. I also want to thank Profs. Ilja Siepmann, Chris Cramer, Laura Gagliardi, Aaron Massari, and Yuichi Kubota for their help in research, scholarship application, job search, and graduation process, and Nancy Thao and Nick Erickson for serving as the department's point of contact and helping me with many things.

I want to say both thank you and sorry to my parents, Peize Li and Chunkui Su. It hasn't been easy for them to be away from their only child for five years, but they always support me with all their hearts and encourage me to pursue whatever career I like, without a single complaint.

It's been a pleasure to work in the Truhlar group. I want to thank all the group members, especially my collaborators Xuefei Xu, Ke Yang, Alek Marenich, Jingjing Zheng, Andy Luo, Haoyu Yu, Bo Wang, Lucas Bao, and Wei-Guang Liu for their help in research, and my officemates Zoli Varga, Wei Lin, and Yuliya Paukku for sharing the office and many happy hours with me.

During my job application I got many helping hands, especially from Paul Ching, Rajan Vatassery, Yunsong Wu, Guoliang Song, Xiangyu Zhang, Qin Jia, and Barbara Beers, to whom I'm grateful.

I want to thank my roommate Fenix Chen and my friends David Harwood, Evgenii Fetisov, Jeff Sung, and Chad Hoyer, for the happy moments we spent together.

Finally, special thanks to Yili Zhu, my significant other, who is always there for me.

Dedication

This dissertation is dedicated to Yili Zhu, who has been supporting me with love, through thick and thin, during my Ph.D.

Abstract

Computer simulation has become a useful tool for studying chemical reactions and spectroscopy. However, the reliable application of computational modeling to large and complex reactive systems involving electronically excited states is still limited. Two of the most important challenges in these applications are the accurate and efficient first-principles calculation of coupled ground- and excited-state potential energy surfaces (PESs), and the modeling of such PESs. For the former challenge, accurate electronic structure methods including static and dynamic electron correlation are often too costly for complex systems, while more affordable methods such as density functional theory (DFT) at their current stage of development are still not satisfactorily accurate for many such systems. For the latter challenge, the high dimensionality and complicated topography of the PESs of complex systems make it difficult to choose a model representation.

This thesis presents several responses to these challenges: (a) Improvements to time-dependent DFT are made to provide better accuracy for excited states and for PESs. (b) A diabatization scheme is developed for more accurate and efficient modeling of coupled PESs. (c) Simple models are presented for efficient simulation of the band shape of the electronic spectroscopy of complex molecules. (d) State-of-the-art methods are applied to simulate the electronic spectrum, and to build the PESs for the photochemistry, of a complex reactive system, thioanisole.

Table of Contents

List of Tables

List of Figures

Permission for Reusing Published Works

The following chapters are adapted from published works with permission:

Chapter 2

Adapted with permission from [Li, S. L.; Marenich, A. V.; Xu, X.; Truhlar, D. G. Configuration Interaction-Corrected Tamm–Dancoff Approximation: A Time-Dependent Density Functional Method with the Correct Dimensionality of Conical Intersections. *J. Phys. Chem. Lett.* **2013**, *5*, 322.] Copyright 2013 American Chemical Society. This is an unofficial adaptation of an article that appeared in an ACS publication. ACS has not endorsed the content of this adaptation or the context of its use.

Chapter 3

Adapted with permission from [Li, S. L.; Truhlar, D. G. Improving Rydberg Excitations within Time-Dependent Density Functional Theory with Generalized Gradient Approximations: The Exchange-Enhancement-for-Large-Gradient Scheme. *J. Chem. Theory Comput.* **2015**, *11*, 3123.] Copyright 2015 American Chemical Society. This is an unofficial adaptation of an article that appeared in an ACS publication. ACS has not endorsed the content of this adaptation or the context of its use.

Chapter 4

Adapted from [Li, S. L.; Truhlar, D. G.; Schmidt, M. W.; Gordon, M. S. Model space diabatization for quantum photochemistry. *J. Chem. Phys.* **2015**, *142*, 064106], with the permission of AIP Publishing. This is an unofficial adaptation of an article that appeared in an AIP publication. AIP has not endorsed the content of this adaptation or the context of its use.

Chapter 5

Adapted with permission from [Li, S. L.; Truhlar, D. G. Franck-Condon Models for Simulating the Band Shape of Electronic Absorption Spectra. *J. Chem. Theory Comput.* **2017**, online as Just Accepted Manuscript.] Copyright 2017 American Chemical Society.

This is an unofficial adaptation of an article that appeared in an ACS publication. ACS has not endorsed the content of this adaptation or the context of its use.

Chapter 6

Adapted from Ref. [Li, S. L.; Xu, X.; Truhlar, D. G. Computational simulation and interpretation of the low-lying excited electronic states and electronic spectrum of thioanisole. *Phys. Chem. Chem. Phys.* **2015**, *17*, 20093] with permission from the PCCP Owner Societies. This is an unofficial adaptation of an article that appeared in PCCP. The PCCP Owner Societies have not endorsed the content of this adaptation or the context of its use.

Chapter 7

Adapted with permission from [Li, S. L.; Xu, X.; Hoyer, C. E.; Truhlar, D. G. Nonintuitive Diabatic Potential Energy Surfaces for Thioanisole. *J. Phys. Chem. Lett.* **2015**, *6*, 3352.] Copyright 2015 American Chemical Society. This is an unofficial adaptation of an article that appeared in an ACS publication. ACS has not endorsed the content of this adaptation or the context of its use.

Chapter 8

Adapted from [Li, S. L.; Truhlar, D. G. Full-dimensional ground- and excited-state potential energy surfaces and state couplings for photodissociation of thioanisole. *J. Chem. Phys.* **2017**, *146*, 064301.], with the permission of AIP Publishing. This is an unofficial adaptation of an article that appeared in an AIP publication. AIP has not endorsed the content of this adaptation or the context of its use.

Chapter 1. Introduction

Photochemistry is the study of chemical processes caused by light. The understanding of the mechanism of photochemical processes will help us with many applications, including designing of functional materials such as systems that convert solar energy to electricity, using light to trigger molecular devices, and exploiting light energy to facilitate chemical reactions. In contrast to thermochemistry, which has been studied for a long time and has well established principles, photochemistry is a relatively less well understood area of research because it involves electronically excited states and ultrafast processes that are difficult to probe accurately by experiments.

Many advanced experimental techniques have been developed to study photochemistry; most of these are based on spectroscopy. Spectroscopy is the study of how a molecular system absorbs or emits electromagnetic radiation, and in my work I am especially concerned with visible and ultraviolet light. Absorption or emission spectra can be used to probe the behavior of chemical and material systems. However, the experimental spectra give only indirect information about the system, and the interpretation of the collected data is often a difficult task.

Theory and computation play a crucial role in addressing these challenges. All physical and chemical processes at the molecular level, including spectroscopy and photochemistry, are governed by quantum mechanics. In principle, we can use quantum mechanical theories to understand all types of spectroscopic and photochemical processes. Although in practice the application of quantum mechanics is limited by the computational difficulties in coping with the Schrödinger equation, many approximate quantum mechanical theories and models have proved to be very useful. We can use those theories to interpret and understand the experimental spectra, and we can carry out computer simulations to reveal details of chemical reactions at the atomic level that are unavailable from experiments.

Quantum mechanical electronic structure calculations can be used to generate some of the key quantities necessary for the understanding of photochemistry and spectroscopy. Foremost among these quantities are potential energy surfaces (PESs), whose gradient fields are sometimes called force fields. A PES is the electronic energy of a molecule in a given electronic state as a function of the positions of the atomic nuclei. The computation and modeling of PESs for complex systems, however, are difficult problems. This thesis addresses this difficulty by focusing specifically on the development and application of state-of-the-art quantum chemical theories and computational methods to compute and model the PESs for studying the spectroscopy and photochemistry of complex molecules.

This introductory chapter gives a brief overview of the various aspects of the background knowledge that underlies and motivates my research. The reader is referred to the cited references for details.

1.1. THE QUANTUM MECHANICAL DESCRIPTION OF CHEMICAL DYNAMICS

1.1.1. Fundamental equations

To apply quantum chemical theories to study photochemistry, we need to start from the quantum mechanical description of chemical dynamics. The fundamental equations are well established,[1,2,3] and I give a brief overview here.

We limit ourselves in this thesis to nonrelativistic quantum mechanics. The Hamiltonian of a quantum mechanical system determines its dynamics. An isolated molecular system consisting of nuclei and electrons has a Hamiltonian (in mass-scaled coordinates where all the components of **R** are scaled to the same reduced mass M) of

$$H(\mathbf{x},\mathbf{R}) = -\frac{1}{2M}\nabla^2_{\mathbf{R}}(\mathbf{R}) + T_{\mathrm{e}}(\mathbf{x}) + U_{\mathrm{C}}(\mathbf{x},\mathbf{R}) \tag{1.1}$$

where **x** denotes the electronic (spatial and spin) coordinates, **R** the nuclear coordinates, $\nabla^2_{\mathbf{R}}$ the Laplace operator with respect to **R**, T_{e} the electronic kinetic energy operator, and

U_C the Coulomb potential between the particles. The electronic Hamiltonian of the system is defined as

$$H_e = T_e + U_C \tag{1.2}$$

Note that, by convention, the "electronic" Hamiltonian includes the nuclear repulsion. Fixing **R**, the eigenvalues and eigenfunctions of H_e can be obtained from

$$H_e \Phi_i(\mathbf{x};\mathbf{R}) = V_i(\mathbf{R})\Phi_i(\mathbf{x};\mathbf{R}) \tag{1.3}$$

where i labels an electronic state and the notation $f(\mathbf{x};\ \mathbf{R})$ means a function f of **x** that depends parametrically on **R**. The eigenfunctions Φ_i and eigenvalues V_i are called the adiabatic electronic wave functions and adiabatic electronic energies (although the energies include also contributions from the nuclei-nuclei interactions). The Φ_i form an orthonormal and complete basis in the space of **x** given **R**.

The time-independent Schrödinger equation of the whole system is

$$H\Psi(\mathbf{x},\mathbf{R}) = E\Psi(\mathbf{x},\mathbf{R}) \tag{1.4}$$

The total wave function Ψ can be expanded in the basis of Φ_i (called the adiabatic basis),

$$\Psi(\mathbf{x},\mathbf{R}) = \sum_i \chi_i(\mathbf{R})\Phi_i(\mathbf{x};\mathbf{R}) \tag{1.5}$$

Substituting eqs. (1.5) and (1.1) into eq. (1.4), left-multiplying both sides of the resulting equation by Φ_j, and integrating over **x** yields

$$-\frac{1}{2M}\nabla_{\mathbf{R}}^2\chi_j + V_j\chi_j - \frac{1}{2M}\sum_i\left(\left\langle\Phi_j\middle|\nabla_{\mathbf{R}}^2\middle|\Phi_i\right\rangle + 2\left\langle\Phi_j\middle|\nabla_{\mathbf{R}}\middle|\Phi_i\right\rangle\cdot\nabla_{\mathbf{R}}\right)\chi_i = E\chi_j \tag{1.6}$$

where the Dirac bracket denotes integration over **x**. This can be written in matrix form

$$\left(-\frac{1}{2M}\nabla_{\mathbf{R}}^2 + \mathbf{V} - \frac{1}{2M}\left(\mathbf{G} + 2\mathbf{F}\cdot\nabla_{\mathbf{R}}\right)\right)\boldsymbol{\chi} = E\boldsymbol{\chi} \tag{1.7}$$

where $\boldsymbol{\chi}$ is a vector with components χ_j, and the elements of matrices **V**, **G**, and **F** are given by

$$V_{ji} = V_j\delta_{ji} \tag{1.8}$$

$$G_{ji} = \left\langle \Phi_j \middle| \nabla_{\mathbf{R}}^2 \middle| \Phi_i \right\rangle \tag{1.9}$$

$$\mathbf{F}_{ji} = \left\langle \Phi_j \middle| \nabla_{\mathbf{R}} \middle| \Phi_i \right\rangle \tag{1.10}$$

where δ_{ji} is the Kronecker delta function. Note that each element of the **F** matrix is a vector in the **R** space. Equations (1.6) and (1.7) are the starting point of the quantum mechanical treatment of molecular dynamics.

The **G** and **F** matrix elements in eq. (1.7) are sometimes called the nonadiabatic scalar couplings and the nonadiabatic vector couplings, respectively. In practice **G** is often neglected. If **F** is also neglected, the result is the widely-adopted Born-Oppenheimer (BO) approximation. In the BO approximation, since **V** is diagonal, eq. (1.7) decouples into one equation for each electronic state

$$-\frac{1}{2M}\nabla_{\mathbf{R}}^2 \chi_j + V_j \chi_j = E \chi_j \tag{1.11}$$

in which the electronic energy V_j, also called an adiabatic potential energy surface (PES), plays the role of an effective potential for the nuclei. The nuclear dynamics governed by a single uncoupled PES under the BO approximation is called the adiabatic dynamics.

1.1.2. Nonadiabatic processes

The neglect of **G** and **F** in eq. (1.7) can be justified under certain circumstances by the fact that the terms are multiplied by a small factor $1/(2M)$, since M, the effective mass of a nucleus, is ~2000 times larger than the mass of an electron involved in the **V** matrix. This is the mathematical equivalent of the physical statement that the nuclear and electronic motions decouple because they are in different time scales. This statement breaks down, however, when two PESs are close in energy. This can be seen mathematically by taking the nuclear derivative of both sides of eq. (1.3), left-multiplying by Φ_j, and integrating over **x**, which yields

$$\mathbf{F}_{ji} = \frac{\left\langle \Phi_j \middle| (\nabla_{\mathbf{R}} H_e) \middle| \Phi_i \right\rangle}{V_i - V_j} \tag{1.12}$$

so that when V_i is close to V_j, $\mathbf{F}_{ji}$ can be arbitrarily large and it can no longer be neglected. In this case the nuclei cannot be regarded as moving under the influence of an effective potential given by a single PES, and the couplings and transitions between electronic states have to be considered. Processes where **F** cannot be neglected are called nonadiabatic processes, and photochemistry is the most important example.

1.1.3. Conical intersections

As mentioned in Section 1.1.2, when two adiabatic PESs come close in energy, the nonadiabatic vector coupling between them can be large. In particular, at geometries where two adiabatic PESs are energetically degenerate, the vector couplings blow up. Such geometries, most generally, are called conical intersections.[2,3,4,5,6,7] (There are other types of intersections but they only occur under special conditions, such as for diatomic and linear geometries of polyatomic molecules.) They are "conical" because in a two-dimensional subspace of **R**, called the branching space, the energy degeneracy is lifted linearly and the PESs in this subspace look like a double cone. In the $(N_{\text{int}} - 2)$-dimensional subspace orthogonal to the branching space (N_{int} is the number of internal nuclear coordinates), the degeneracy is kept to the first order, so that there is a $(N_{\text{int}} - 2)$-dimensional continuum in the **R** space associated with each conical intersection where the degeneracy is preserved. Such a continuum is called a conical intersection "seam". Near such seams nonadiabatic radiationless electronic transitions can occur particularly efficiently, and thus they play a prominent role in nonadiabatic chemical dynamics including photochemistry. For this reason, the proper description of the conical intersections on the PESs is critical for nonadiabatic dynamics simulations, which turns out also to be a challenge.

1.1.4. Diabatic basis and diabatization

Recall from Section 1.1.1 that the eigenfunctions Φ_i of the electronic Hamiltonian form a complete basis of the wave function space of **x** given a fixed **R**, and if we expand the total wave function in this adiabatic basis [eq. (1.5)] we eventually get eq. (1.7). To make use of eq. (1.7) for nonadiabatic dynamics simulation, we need to compute **V** (the

adiabatic PES matrix) and **F** (the nonadiabatic vector coupling matrix) as a function of **R** (neglecting **G**). This can be done by modern electronic structure methods to satisfactory accuracy for many systems. However, we would need to fit **V** and **F** to analytic functions for quality control and quick simulation. This poses two serious problems: (a) **V** elements have cuspidal ridges (discontinuous first derivatives) along conical intersection seams; (b) **F** elements are high-dimensional vectors that blow up along conical intersection seams. This makes **V** and **F** difficult, if not impossible, to fit.

One way to get around these problems is to work in a so-called diabatic basis.[3,8,9] It turns out that if we make a unitary transformation of the adiabatic basis to a new basis,

$$\tilde{\Phi}_i = \sum_j \Phi_j B_{ji} \tag{1.13}$$

(where B_{ji} are elements of a unitary matrix **B**) and expand the total wave function in this new basis,

$$\Psi(\mathbf{x},\mathbf{R}) = \sum_i \tilde{\chi}_i(\mathbf{R})\tilde{\Phi}_i(\mathbf{x};\mathbf{R}) \tag{1.14}$$

we will have the counter part of eq. (1.7) as

$$\left(-\frac{1}{2M}\left(\nabla_{\mathbf{R}} + \tilde{\mathbf{F}}\right)^2 + \mathbf{U}\right)\tilde{\boldsymbol{\chi}} = E\tilde{\boldsymbol{\chi}} \tag{1.15}$$

where

$$\tilde{\boldsymbol{\chi}} = \mathbf{B}^{\dagger}\boldsymbol{\chi} \tag{1.16}$$

$$\mathbf{U} = \mathbf{B}^{\dagger}\mathbf{V}\mathbf{B} \tag{1.17}$$

$$\tilde{\mathbf{F}} = \mathbf{B}^{\dagger}\mathbf{F}\mathbf{B} + \mathbf{B}^{\dagger}\nabla_{\mathbf{R}}\mathbf{B} \tag{1.18}$$

(a dagger denotes Hermitian transpose.) If we could find a unitary matrix **B** such that

$$\mathbf{F}\mathbf{B} + \nabla_{\mathbf{R}}\mathbf{B} = 0 \tag{1.19}$$

then we would have $\tilde{\mathbf{F}} = 0$ and get rid of the troublesome nonadiabatic vector couplings. (Note that the transformed potential matrix **U** becomes non-diagonal and so the electronic

states are still coupled.) Such a basis $\{\tilde{\Phi}_i\}$ that makes $\tilde{\mathbf{F}}$ vanish is said to be diabatic. The $\tilde{\Phi}_i$ are called diabatic electronic wave functions. The **U** is called diabatic potential matrix, whose diagonal and off-diagonal elements are often called diabatic potential energy surfaces and diabatic couplings, respectively. Unfortunately, in general eq. (1.19) does not have a solution and a (strict) diabatic basis does not exist.[10] Fortunately, we can find "quasi-diabatic" bases such that $\tilde{\mathbf{F}}$ is small and negligible for practical applications. Clearly such diabatic bases are not unique. It also turns out that in many quasi-diabatic bases the elements of **U** are much smoother without cusps. Therefore, by working in a (quasi-)diabatic basis, we can circumvent the problem of fitting **V** and **F**. Henceforth I will follow the convention of referring to "quasi-diabatic" as "diabatic", which will not cause confusion since a strictly diabatic basis does not exist in general and I will not be talking about it.

In practice, however, the convenience of using a diabatic basis is accompanied by the technical challenge of finding the unitary transformation **B** that converts the adiabatic basis to a diabatic basis. The process of finding a diabatic basis is called diabatization, and it is a field under active development. In Chapter 4 I will give more details about diabatization methods as well as my contribution to this field.

1.2. ELECTRONIC STRUCTURE METHODS FOR POTENTIAL ENERGY SURFACES

Electronic structure methods are methods that solve (approximately) the electronic Schrödinger equation [eq. (1.3)] with a fixed **R**. They are needed for computing the adiabatic electronic wave functions and PESs for actual simulations or as a starting point for diabatization. These methods are usually classified into wave function theories (WFT)[11,12] and density functional theory (DFT).[13,14] In this section I will omit the parametric **R**-dependence of the quantities in eq. (1.3) and simply regard them as functions of **x**.

1.2.1. Wave function theories

Wave function theories and methods attempt to find an approximate solution to the wave functions, Φ_i, and the adiabatic energies, V_i, of eq. (1.3). A typical wave function method involves a hierarchy of approximate expansions of the complex many-electron wave function into smaller, more manageable units, whose expansion coefficients are optimized or computed by certain theories and algorithms.

First, the wave function Φ_i is expanded in a basis set of many-electron functions,

$$\Phi_i(\mathbf{x}) = \sum_j c_{ji}\psi_j(\mathbf{x}) \tag{1.20}$$

This is usually called a configuration-interaction (CI) expansion and the c_{ji} are called CI coefficients. The many-electron basis functions ψ_j, usually referred to as configurations, are generally chosen to be either Slater determinants (SDs), which satisfy the antisymmetry property of a wave function with respect to exchanging two electrons, or configuration state functions (CSFs), which are linear combinations of SDs that have additional desired symmetry properties.

A Slater determinant is a linear combination of products of one-electron wave functions, called molecular orbitals (MOs), arranged in the form of a determinant,

$$\psi_j(\mathbf{x}) = \begin{vmatrix} \phi_{j_1}(x_1) & \phi_{j_1}(x_2) & \cdots \\ \phi_{j_2}(x_1) & \phi_{j_2}(x_2) & \cdots \\ \vdots & \vdots & \ddots \end{vmatrix} \tag{1.21}$$

where x_i denotes the spatial and spin coordinates of the ith electron. (The overall normalization factor is omitted here.) The set $\{j_1, j_2, \ldots, j_N\}$ is a size-N subset of $\{1, 2, \ldots, M\}$ where N is the number of electrons in the system and M the number of MOs. Physically, an SD corresponds to N electrons occupying N MOs with (M-N) MOs unoccupied. (Note that here the ϕ are so-called spin orbitals, each one of which can hold one electron with a certain spin, rather than so-called spin-free orbitals, each one of which can hold two electrons, one spin-up and one spin-down.)

Each MO is expanded in a basis set of one-electron functions, sometimes called atomic orbitals (AOs),

$$\phi_i(x_k) = \sum_{j=1}^{M} d_{ji}\theta_j(x_k) \tag{1.22}$$

This is sometimes called the linear combination of atomic orbitals (LCAO) scheme, and the d_{ji} are called LCAO coefficients. Many flavors of the one-electron basis set of AOs, usually simply called the basis set when there is no confusion, are available for use. Different wave function methods differ by how the LCAO coefficients [d_{ji} in eq. (1.22)] are optimized, which configurations [ψ_j in eq. (1.20)] are chosen, and how the CI coefficients [c_{ji} in eq. (1.20)] are computed, as well as how the electronic energy V_i are computed from the electronic wave function Φ_i. A comprehensive introduction to all the popular wave function methods is beyond the scope of this section, so in the following I will only introduce the method I mainly used for computing PESs in my work, namely multi-reference perturbation theories.

Multi-reference perturbation theories (MRPTs) are flavors of many-body perturbation theory (MBPT)[11,12,15] applied to a multi-configurational zero-order wave function. A multi-reference wave function, such as the one given by MRPT, is a wave function that is built on a multi-configurational reference function. The most commonly used zero-order wave function for MRPT is a multi-configurational self-consistent field (MCSCF) wave function, especially the complete-active-space self-consistent field (CASSCF) wave function. In CASSCF, the configurations used to expand eq. (1.20) are chosen based on a scheme for choosing the MOs in eq. (1.21) that compose each configuration as follows. The MOs are classified into three categories: inactive, active, and virtual. Inactive MOs are always occupied; virtual orbitals are always unoccupied; with these two conditions satisfied, the remaining electrons are distributed in the remaining active orbitals in all possible ways, each way corresponding to one configuration. This scheme specifies all the configurations in eq. (1.20), and the complete representation of the electronic wave function is determined by eqs. (1.20), (1.21), and

(1.22). The CI and LCAO coefficients are then optimized by substituting the representation of the electronic wave function in eq. (1.3) and minimizing the electronic energy; this leads to an optimal solution for the ground state within the representation by virtue of the variational principle.

After the CASSCF wave function and energy are obtained, they are used as zero-order quantities for a many-body perturbation treatment for first-order corrections to the wave function and second-order corrections to the energy. The resulting theories are called MRPTs. CASSCF and MRPTs can be extended to multi-state cases, which compute wave functions and energies not only for the ground state but also for multiple excited states. A typical multi-state extension of CASSCF is state-averaged CASSCF (SA-CASSCF), which optimizes the CI and LCAO coefficients by minimizing a weighted average of the energies of multiple states. There are also several multi-state formulations of MRPT; an introduction to some of them can be found in Chapter 4.

These multi-reference methods are particularly useful for computing PESs for photochemistry. Photochemistry involves PESs of the excited states and at a wide range of geometries, whose wave functions need to be properly described by multi-reference representations. Multi-state MRPTs are able to treat selected ground and excited states on the same footing, which is important for balancing the accuracy for all the states and for correctly handling the conical intersections. These methods are the main workhorse for the PESs in my research of the photochemistry of thioanisole, as described in Chapters 7 and 8.

Although useful for PESs, multi-state methods have their shortcomings. They require quite some experience and expertise to use, since there are difficult technical choices to make, such as the selection of the MOs and configurations to expand the electronic wave function. Furthermore, they have steep scaling of computational complexity with respect to the size of molecule. These two shortcomings combined make them very time- and manpower-consuming to use, and they are affordable for only relatively small systems. Other methods with better scaling and that are easier to use are

under active development; density functional methods are among the most popular of such methods, and they are introduced next.

1.2.2. Density functional theory

Different from WFTs which attempt to approximately solve the electronic Schrödinger equation [eq. (1.3)] for both the wave functions and energies, DFT attempts to obtain the energies through manipulation of the electron density, without explicitly dealing with the wave functions. The electron density of an N-electron wave function $\Phi(\mathbf{x}) \equiv \Phi(x_1, x_2, \ldots, x_N)$ is defined as

$$\rho(x) = N \int dx_2 dx_3 \cdots dx_N \left|\Phi(x, x_2, x_3, \cdots, x_N)\right|^2 \tag{1.23}$$

where x here denotes collectively the three spatial coordinates of a point in space and one spin coordinate, and x_i denotes the three spatial coordinates and one spin coordinate of electron i. The quantity $\rho(x)/N$ can be regarded as the probability density of finding an electron with a particular spin at a particular spatial position.

According to the first Hohenberg-Kohn theorem,[16] the electronic ground-state energy of a system is a universal functional of its electron density. Furthermore, according to the second Hohenberg-Kohn theorem[16] and the later work of Levy,[17] in principle the energy and the density can be solved variationally. Kohn and Sham[18] turned DFT from pure theory into a practical method by developing a scheme for variationally solving for the energy and density. Now most of the practical DFT calculations in the literature are Kohn-Sham DFT (KS-DFT).

At the core of the Kohn-Sham scheme are two smart ideas. The first idea is to construct a fictitious non-interacting N-electron system with a Hamiltonian

$$H_{\mathrm{s}} = \sum_{i=1}^{N} \left(-\frac{1}{2} \nabla_i^2 + v_{\mathrm{eff}}(x_i) \right) \tag{1.24}$$

where the Laplace operator ∇_i acts on the electronic coordinate of the ith electron x_i and v_{eff} is the effective potential whose form we will find shortly. With this Hamiltonian, the ground-state energy functional of the density is

$$E_S[\rho] = T_S[\rho] + \int v_{\text{eff}}(x)\rho(x)dx \tag{1.25}$$

where T_S is the kinetic energy of the fictitious system. On the other hand, the Schrödinger equation of this Hamiltonian can be written as N coupled one-electron equations

$$\left(-\frac{1}{2}\nabla_x^2 + v_{\text{eff}}(x)\right)\varphi_j(x) = \varepsilon_j\varphi_j(x) \tag{1.26}$$

The solution is a set of one-electron orbitals $\{\varphi_j\}$ called the KS orbitals. For the ground state, N electrons occupy the lowest N orbitals, and the electron density is

$$\rho(x) = \sum_{j=1}^{N} |\varphi_j(x)|^2 \tag{1.27}$$

If we know v_{eff}, we can solve these equations and obtain the electron density. In fact, requiring the electron density of this fictitious system to be the same as the real interacting system and using the idea in the next paragraph, it is indeed possible to find v_{eff}.

The second smart idea is to express the ground-state energy functional of the density for the real system in the following form

$$E_0[\rho(x)] = T_S[\rho(x)] + \int v_{\text{ext}}(x)\rho(x)dx + \frac{1}{2}\int \frac{\rho(x)\rho(x')}{|x-x'|}dxdx' + E_{\text{xc}}[\rho(x)] \tag{1.28}$$

where T_S is the kinetic energy of the fictitious system having the same density as the real system, v_{ext} is the external potential (in molecular systems it is usually the Coulomb potential due to nucleus-electron interactions), the third term on the right-hand side of the equation is the classic electron-electron Coulomb interaction, and E_{xc} is everything left. This is essentially a definition of E_{xc}, which is called the exchange-correlation functional, although it includes also the kinetic energy difference of the fictitious system and the real system.

Using the variational principle, the electron density of the fictitious system and of the real system can be found by taking the derivative and finding the stationary point of

eqs. (1.25) and (1.28) respectively, under the constraint that $\int \rho(x)dx = N$. Now if we require the two densities to be equal, we will find

$$v_{\text{eff}}(x) = v(x) + \int \frac{\rho(x')}{|x - x'|}dx' + \frac{\delta E_{\text{xc}}[\rho]}{\delta\rho} \equiv v(x) + \int \frac{\rho(x')}{|x - x'|}dx' + v_{\text{xc}}(x) \qquad (1.29)$$

where δ denotes functional derivative and v_{xc} is called the exchange-correlation potential. Now with the expression for v_{eff}, we can find the KS orbitals by solving eq. (1.26) self-consistently, obtain the density using eq. (1.27), and obtain the ground-state energy using eq. (1.28).

However, there is still one part missing for this scheme: E_{xc} is unknown. Without an expression for E_{xc}, the KS scheme is merely a reformulation of the equations. Fortunately there are already many good exchange-correlation functionals available and even better ones are under active development. The state of the art of this field can be found in many review papers, for instance ref. 19.

DFT as formulated above is a ground-state theory. Additional formulation is needed to extend it to excited states. The most popular one is linear-response time-dependent DFT (LR-TDDFT or simply TDDFT),[20,21] which can be further simplified by the Tamm-Dancoff approximation (TDA).[22,23,24] LR-TDDFT and TDA-TDDFT have been successfully applied to many applications,[25] but there are still well-known problems.[19,26] Two of the problems that affect their usefulness for PESs and spectroscopy are the incorrect dimensionality of conical intersections and underestimation of Rydberg excitation energies. In Chapters 2 and 3 I will discuss these problems in more detail and describe my contributions to address these two problems.

1.3. NONADIABATIC DYNAMICS SIMULATIONS

Having the Schrödinger equation in the adiabatic [eq. (1.7)] or diabatic [eq. (1.15)] representation with the PESs and couplings either computed or neglected, we now move on to the nonadiabatic molecular dynamics (MD) simulations. Ordinary trajectory-based Born-Oppenheimer (BO) MD treats the nuclei as classical particles moving on a single PES. To embody the nonadiabatic effect into the propagation of nuclear degrees of

freedom, one may adopt a fully-quantum treatment of the system, treating both the electrons and nuclei by quantum mechanics. A typical example of such quantum dynamics methods is the multi-configuration time-dependent Hartree (MCTDH)[51] method. However, the high computational cost of quantum dynamics simulations limits their feasibility to very small molecules with only a few degrees of freedom. To incorporate quantum effects while retaining the high efficiency of trajectory-based MD, semi-classical trajectory methods are developed to treat such nonadiabatic problems.

The basic idea of the semi-classical trajectory methods considered here is to treat the propagation of nuclear degrees of freedom classically and that of electronic degrees of freedom quantum mechanically. (In comparison, ordinary trajectory-based MD does not treat electronic degrees of freedom explicitly; they are implicitly included in the PESs). The main focus is the treatment of the interaction between the two sets of degrees of freedom, i.e. how the electronic degrees of freedom affect the evolution of the nuclear degrees of freedom and *vice versa*. Differing in such treatment, many popular semi-classical trajectory methods can be categorized into two types: surface-hopping and mean-field potential. Both types of methods propagate the electronic degrees of freedom according to the electronic time-dependent Schrödinger equation in which the nuclei provide a time-dependent external potential. However, they differ in how the nuclear degrees of freedom are propagated.

In surface-hopping methods, the nuclei move on one PES at a time, but at some point the nuclei has a probability to "hop" from one PES to another. Different surface-hopping methods differ in how the probability is calculated and where the nuclei can "hop", but one of their common goals is to mimic the propagation of the nuclear quantum wave packet by an ensemble of independent classical trajectories. For instance, in a popular "fewest switches" method developed by Tully,[27] surface hopping can occur at any geometry and the probability is specifically designed to be consistent with the change of occupation numbers of the electronic states. When the electronic transition occurs, the potential energy changes discontinuously and the nuclear velocities are adjusted so as to

conserve total energy. Apart from the surface hopping, the nuclei move on a single surface at any particular time just as in BO MD.

In mean-field potential methods, the effective potential in which the nuclei move is taken as a weighted average of the involved PESs. Simple mean-field methods such as the semi-classical Ehrenfest (SE) method[28] can correctly describe the coherent behavior of the electronic wave function being a superposition of the electronic eigenfunctions in strong-interaction regions where PESs are close in energy, but they cannot describe the decoherence of the electronic wave function in weak-interaction regions. A scheme to introduce decoherence into the mean-field method leads to the coherent switching with decay of mixing (CSDM) method.[29]

1.4. ELECTRONIC ABSOPRTION SPECTROSCOPY AND THE SHAPE OF SPECTRAL BANDS

Electronic absorption spectroscopy is the study of the absorption of radiation, usually in the UV and visible range, due to electronic transitions, and the resulting absorbance-versus-photon energy graph is called an electronic absorption spectrum. In practical experiments on polyatomic systems, the spectral lines due to individual nuclear motion states are often not resolved, and the absorption spectrum appears as continuous spectral bands, each band corresponding to an electronic transition from one electronic state to another. Three ingredients are needed to simulate a spectral band: the position, the strength, and the shape of the band. The position is determined by the electronic excitation energy and the strength by the transition dipole moment, both of which can be computed by electronic structure methods. With the recent improvements in electronic structure methods, especially equation-of-motion and linear-response methods and quasi-degenerate and multi-state perturbation methods, it is now feasible to calculate excitation energies and transition dipole moments for many types of electronic transitions of fairly large and complex molecules, with an error of only a few tenths of an electron volt. The shape of a band is affected by many broadening factors, such as the finite lifetime of excited states, collisions (pressure broadening), thermal Doppler effects, and resolution of

the spectrometer. A more prominent effect in determining the band shape, which is the focus here, is the vibronic effect. Each electronic transition is always accompanied by vibrational transitions; as a result each electronic transition gives rise to a vibronic band. For unresolved spectra where the individual vibrational lines are not discernable, the spectrum simply appears as a broadened band.

Various theories and models have been proposed to simulate the vibronic effect. The simplest is to employ the classical Franck-Condon principle and calculate only the vertical electronic transitions and convolute each transition with a broadening function, whose width is chosen empirically.[30,31,32,33,34] This approach is convenient but has several flaws, especially the ambiguity in the choice of the width parameter, but also that this model does not recognize the asymmetry of the vibronic band shape, in particular that the band maximum is not located at the vertical excitation energy.

At the other extreme are sophisticated time-independent[35,36,37,38,39] and time-dependent[40,41,42,43,44] approaches to explicitly simulate the vibronic excitations. These methods can generate highly accurate vibronic spectra, but they require special expertise to use, and they may be unsuitable for complex molecules. For example, transition metal complexes often have tens of low-lying electronic states contributing to the electronic spectra. The vibronic bands often overlap, obscuring fine vibrational details and leading to structureless spectra. In this case it would be a substantial amount of work, and it may not be necessary, to simulate the vibrational structures of all the relevant bands.

A method with sophistication intermediate between the two types of methods above is the ensemble method.[45,46,47] It simulates vibronic excitations by single-point excitations at an ensemble of geometries representing the initial nuclear wave functions of the molecule, usually sampled from a molecular dynamics simulation. This method is relatively inexpensive, and it can simulate the unresolved vibronic band shape, as well as going beyond the Franck-Condon approximation by taking into account the dependence of transition dipole moment on the geometry. However, it can be difficult to generate the ensemble of geometries, for instance, if no convenient force field is available for the molecular dynamics simulation.

To overcome the difficulties of the aforementioned methods, I proposed two models that are simple enough to be applicable to complex systems without adding a major load to the cost and effort, yet are able to capture the overall profile of unresolved bands. The models are described in detail in Chapter 5.

1.5. ORGANIZATION OF THIS THESIS

The remainder of this thesis presents the research I have conducted during my doctoral training, including development and application of computational methods for studying the photochemistry and spectroscopy of complex molecules. Chapters 2 to 5 are about method development, and Chapters 6 to 8 are a computational study of the photochemistry and spectroscopy of a complex system, thioanisole.

Chapter 2 develops a method called the configuration interaction-corrected Tamm-Dancoff approximation (CIC-TDA). As mentioned in Section 1.2.2, one problem of the LR-TDDFT and TDA-TDDFT methods is that conical intersections of the reference state and a response state occur in $F - 1$ instead of the correct $F - 2$ dimensions, where F is the number of internal degrees of freedom. CIC-TDA is designed to fix this problem. It calculates the coupling between the reference state and an intersecting response state by interpreting the KS reference-state Slater determinant and linear response as if they were wave functions. Both formal analysis and test results show that CIC-TDA gives similar results to TDA-TDDFT far from a conical intersection, but the intersection occurs with the correct dimensionality.

Chapter 3 develops a scheme called exchange-enhancement-for-large-gradient (XELG) to improve the accuracy of TDDFT on Rydberg excitations. TDDFT with conventional local and hybrid functionals such as the local and hybrid generalized gradient approximations (GGA) seriously underestimates the excitation energies of Rydberg states, which limits its usefulness for applications like spectroscopy and photochemistry. The XELG scheme modifies the exchange enhancement factor to improve GGA functionals for Rydberg excitations within the TDDFT framework while retaining their accuracy for valence excitations and for the thermochemical energetics

calculated by ground-state density functional theory (DFT). The scheme is applied to a popular hybrid GGA functional and tested on datasets of valence and Rydberg excitations and atomization energies, and the results are encouraging.

Chapter 4 introduces a method called model space diabatization (MSD) for diabatizing MS-MRPT wave functions. An advantage over previous diabatization schemes is that dynamical correlation calculations are based on standard post-MCSCF multi-state methods even though the diabatization is based on state-averaged MCSCF results. The strategy is illustrated by applications to LiH, LiF, and thioanisole, with the fourfold-way diabatization and XMC-QDPT, and the results illustrate its validity.

Chapter 5 presents two Franck-Condon models for the band shape of electronic absorption spectroscopy. These models are suitable for simulating the unresolved vibronic band shapes of electronic spectra that involve many vibrational modes. The models are straightforward and can be easily applied to simulate absorption spectra that are composed of many electronic transitions. As compared to carrying out molecular dynamics simulations, they require relatively few electronic structure calculations, and the additional cost for constructing the spectra is negligible.

Chapter 6 simulates and interprets the low-lying excited states and the electronic absorption spectrum of thioanisole. The nature of the four lowest singlet states are investigated using electronic structure calculations by MRPT, by completely-renormalized equation-of-motion coupled cluster theory with single and double excitations and noniterative inclusion of connected triples (CR-EOM-CCSD(T)), and by TDDFT. The assignment of the electronic spectrum is clarified by simulating it using a normal-mode sampling approach combined with TDA-TDDFT.

Chapter 7 investigates the diabatization of two singlet states of thioanisole in the S-CH_3 bond stretching and C-C-S-C torsion two-dimensional nuclear coordinate space containing a conical intersection, which is important for its photochemistry. Two systematic methods are used: the (orbital-dependent) fourfold way and the (orbital-free) Boys localization diabatization method. These very different methods yield strikingly similar diabatic potential energy surfaces that cross at geometries where the adiabatic

surfaces are well separated and do not exhibit avoided crossings, and the contours of the diabatic gap and diabatic coupling are similar for the two methods. The validity of the diabatization is supported by comparing the nonadiabatic couplings calculated from the diabatic matrix elements to those calculated by direct differentiation of the adiabatic states.

Chapter 8 constructs the analytic potential energy surfaces (PESs) and state couplings of the ground and two lowest singlet excited states of thioanisole in a diabatic representation based on electronic structure calculations including dynamic correlation. They cover all 42 internal degrees of freedom and a wide range of geometries including the Franck-Condon region and the reaction valley along the breaking S-CH_3 bond with the full ranges of the torsion angles. The parameters in the PESs and couplings are fitted to the results of smooth diabatic electronic structure calculations including dynamic electron correlation by the XMC-QDPT method for the adiabatic state energies followed by diabatization by the fourfold way. The fit is accomplished by the Anchor Points Reactive Potential method with two reactive coordinates and 40 nonreactive degrees of freedom, where the anchor-point force fields are obtained with a locally modified version of the *QuickFF* package.

REFERENCES FOR CHAPTER 1

[1] Jasper, A. W.; Kendrick, B. K.; Mead, C. A.; Truhlar, D. G. In *Modern Trends in Chemical Reaction Dynamics: Experiment and Theory (Part 1)*; Yang, X., Liu, K., Eds.; World Scientific: Singapore, 2004, p 329.

[2] Jasper, A. W.; Truhlar, D. G. In *Conical Intersections: Theory, Computation, and Experiment*; Domcke, W., Yarkony, D. R., Koppel, H., Eds.; World Scientific, Singapore: 2011.

[3] Cederbaum, L. S. In *Conical Intersections: Electronic Structure, Dynamics and Spectroscopy*; Domcke, W., Yarkony, D. R., Köppel, H., Eds.; World Scientific Publishing Co. Pte. Ltd.: 2004.

[4] Yarkony, D. R. *Rev. Mod. Phys.* **1996**, *68*, 985.

[5] Worth, G. A.; Cederbaum, L. S. *Annu. Rev. Phys. Chem.* **2004**, *55*, 127.

[6] Matsika, S.; Krause, P. In *Annual Review of Physical Chemistry, Vol 62*; Leone, S. R., Cremer, P. S., Groves, J. T., Johnson, M. A., Eds. 2011; Vol. 62, p 621.

[7] Domcke, W.; Yarkony, D. R. In *Annual Review of Physical Chemistry, Vol 63*; Johnson, M. A., Martinez, T. J., Eds. 2012; Vol. 63, p 325.

[8] Pacher, T.; Cederbaum, L. S.; Köppel, H. *Adv. Chem. Phys.* **1993**, *84*, 293.

[9] Köppel, H. In *Conical Intersections: Electronic Structure, Dynamics and Spectroscopy*; Domcke, W., Yarkony, D. R., Köppel, H., Eds.; World Scientific Publishing Co. Pte. Ltd.: 2004.

[10] Mead, C. A.; Truhlar, D. G. *J. Chem. Phys.* **1982**, *77*, 6090.

[11] Szabo, A.; Ostlund, N. S. *Modern Quantum Chemistry: Introduction to Advanced Electronic Structure Theory*; McGraw-Hill, Inc., 1989.

[12] Helgaker, T.; Jorgensen, P.; Olsen, J. *Molecular Electronic-Structure Theory*; John Wiley & Sons Ltd West Sussex, 2000.

[13] Parr, R. G.; Yang, W. *Density-Functional Theory of Atoms and Molecules*; Oxford University Press: New York, 1989.

[14] Engel, E.; Dreizler, R. M. *Density Functional Theory: An Advanced Course*; Springer-Verlag Berlin Heidelberg, 2011.

[15] Shavitt, I.; Bartlett, R. J. *Many-Body Methods in Chemistry and Physics*; Cambridge University Press, 2009.

[16] Hohenberg, P.; Kohn, W. *Phys. Rev.* **1964**, *136*, B864.

[17] Levy, M. *Proc. Natl. Acad. Sci. U.S.A.* **1979**, *76*, 6062.

[18] Kohn, W.; Sham, L. J. *Phys. Rev.* **1965**, *140*, 1133.

[19] Yu, H. S.; Li, S. L.; Truhlar, D. G. *J. Chem. Phys.* **2016**, *145*, 130901.

[20] Marques, M. A. L.; Gross, E. K. U. *Annu. Rev. Phys. Chem.* **2004**, *55*, 427.

[21] Casida, M. E. In *Recent Advances in Density Functional Methods, Part I*; Chong, D. P., Ed.; World Scientific: Singapore: 1995, p 155.

[22] Tamm, I. *J. Phys. (Moscow)* **1945**, *9*, 449.

[23] Dancoff, S. M. *Phys. Rev.* **1950**, *78*, 382.

[24] Hirata, S.; Head-Gordon, M. *Chem. Phys. Lett.* **1999**, *314*, 291.

[25] Laurent, A. D.; Jacquemin, D. *Int. J. Quantum Chem.* **2013**, *113*, 2019.

[26] Casida, M. E.; Huix-Rotllant, M. *Annu. Rev. Phys. Chem.* **2012**, *63*, 287.

[27] Tully, J. C. *J. Chem. Phys.* **1990**, *93*, 1061.

[28] Meyer, H. D.; Miller, W. H. *J. Chem. Phys.* **1979**, *70*, 3214.

[29] Zhu, C. Y.; Nangia, S.; Jasper, A. W.; Truhlar, D. G. *J. Chem. Phys.* **2004**, *121*, 7658.

[30] Jiang, X.; Karlsson, K. M.; Gabrielsson, E.; Johansson, E. M.; Quintana, M.; Karlsson, M.; Sun, L.; Boschloo, G.; Hagfeldt, A. *Adv. Funct. Mater.* **2011**, *21*, 2944.

[31] Yang, C.-H.; Beltran, J.; Lemaur, V.; Cornil, J.; Hartmann, D.; Sarfert, W.; Fröhlich, R.; Bizzarri, C.; De Cola, L. *Inorg. Chem.* **2010**, *49*, 9891.

[32] Farrer, N. J.; Woods, J. A.; Salassa, L.; Zhao, Y.; Robinson, K. S.; Clarkson, G.; Mackay, F. S.; Sadler, P. J. *Angew. Chem. Int. Ed.* **2010**, *49*, 8905.

[33] Fernández-Hernández, J. M.; Yang, C.-H.; Beltrán, J. I.; Lemaur, V.; Polo, F.; Fröhlich, R.; Cornil, J.; De Cola, L. *J. Am. Chem. Soc.* **2011**, *133*, 10543.

[34] Salassa, L.; Garino, C.; Salassa, G.; Gobetto, R.; Nervi, C. *J. Am. Chem. Soc.* **2008**, *130*, 9590.

[35] Santoro, F.; Improta, R.; Lami, A.; Bloino, J.; Barone, V. *J. Chem. Phys.* **2007**, *126*, 084509.

[36] Santoro, F.; Lami, A.; Improta, R.; Barone, V. *J. Chem. Phys.* **2007**, *126*, 184102.

[37] Santoro, F.; Lami, A.; Improta, R.; Bloino, J.; Barone, V. *J. Chem. Phys.* **2008**, *128*, 224311.

[38] Hazra, A.; Nooijen, M. *Int. J. Quantum Chem.* **2003**, *95*, 643.

[39] Charaf-Eddin, A.; Cauchy, T.; Felpin, F.-X.; Jacquemin, D. *RSC Advances* **2014**, *4*, 55466.

[40] Petrenko, T.; Neese, F. *J. Chem. Phys.* **2007**, *127*, 164319.

[41] Tang, J.; Lee, M. T.; Lin, S. H. *J. Chem. Phys.* **2003**, *119*, 7188.

[42] Ianconescu, R.; Pollak, E. *J. Phys. Chem. A* **2004**, *108*, 7778.

[43] Peng, Q.; Niu, Y.; Deng, C.; Shuai, Z. *Chem. Phys.* **2010**, *370*, 215.

[44] Santoro, F.; Jacquemin, D. *WIREs Comput. Mol. Sci.* **2016**, *6*, 460.

[45] Aidas, K.; Kongsted, J.; Osted, A.; Mikkelsen, K. V.; Christiansen, O. *J. Phys. Chem. A* **2005**, *109*, 8001.

[46] Crespo-Otero, R.; Barbatti, M. *Theor. Chem. Acc.* **2012**, *131*, 1.

[47] Marenich, A. V.; Cramer, C. J.; Truhlar, D. G. *J. Phys. Chem. B* **2014**, *119*, 958.

Chapter 2. Configuration Interaction-Corrected Tamm-Dancoff Approximation: A Time-Dependent Density Functional Method with the Correct Dimensionality of Conical Intersections.

2.1. INTRODUCTION

The Kohn-Sham density functional theory (KS-DFT) of electronic structure is intrinsically a ground-state theory, but excited states show up as poles in the response of the ground state to an external perturbation, and based on this a time-dependent formulation (TDDFT) has been used to obtain excited-state energies.[1] One typically makes the adiabatic linear response (LR) approximation to KS theory (LR-TDDFT), and this leads to a set of equations (often called the Casida equations[2]) that are very convenient for computation and that are analogous in form to the linear-response time-dependent Hartree-Fock approximation in wave function theory[3,4] (WFT); these equations can be called respectively the Kohn-Sham and Hartree-Fock linear response approximations (LR-TDDFT and HF-LR). The LR-TDDFT equations can be further simplified by the Tamm-Dancoff approximation[5,6] (TDA) to obtain a set of equations[7] (we will call them the TDA-TDDFT equations) with an analogous form to the WFT configuration interaction method in which only single excitations are considered[8,9,10] (usually called "configuration interaction singles" or CIS, but sometimes called the TDA); to avoid confusion with TDA-TDDFT, we will call this WFT method HF-TDA. TDA-TDDFT typically gives similar results to the full LR-TDDFT equations, but is more stable near state intersections.[11] Whereas HF-TDA is usually too inaccurate for practical work, due to missing dynamical correlation energy, TDA-TDDFT is now known to provide reasonable accuracy for electronic excitation energies of singly excited valence states,[12,13] and with some functionals good results can be obtained for Rydberg states or long-range charge transfer states, although no single exchange-correlation functional has

been shown to be very good for all three kinds of excitation, and doubly excited states are still problematic.[11,14]

Despite the above difficulties for some types of excitations, LR-TDDFT and TDA-TDDFT are becoming the workhorses of electronic spectroscopy for all but the smallest molecules. However, their application to photochemistry is impeded by a problem of another type that occurs in both LR-TDDFT and TDA-TDDFT, even for singly excited valence states. This problem is well understood, and precisely the same problem occurs in HF-TDA. It is well known that for a molecule with F internal degrees of freedom, conical intersections occur in a subspace of $F - 2$ dimensions.[15,16,17] However, in TDA-TDDFT and HF-TDA conical intersections between the reference state and a response state occur in $F - 1$ dimensions.[18] In the present chapter we show how to eliminate this problem, by combining ideas from HF-TDA and TDA-TDDFT. The resulting method, which we call configuration interaction-corrected TDA (or CIC-TDA), gives results very similar to TDA-TDDFT far from a conical intersection, but it has the correct dimensionality for conical intersections.

Further discussion of TDDFT relevant to photochemical problems is provided elsewhere.[19,20,21,22]

2.2. THEORY

For simplicity, we give equations only for closed-shell reference states; the generalization to open-shell reference states is straightforward. The procedure starts with the solution of the usual Kohn-Sham self-consistent-field problem for the reference state; this yields a set of doubly occupied molecular orbitals $i, j, \ldots$ and a set of virtual molecular orbitals $a, b, \ldots$ (We call this reference state the KS-SCF state. It is usually the ground state at the equilibrium geometry, but it may correspond to an excited state elsewhere, for example on the "other side" of an intersection. Nevertheless it is often convenient to call it the ground state more generically and to call the response states the excited states.) The TDA-TDDFT equations for excited singlet states constitute a Hermitian eigenvalue problem given by

$$\mathbf{AZ} = \omega\mathbf{Z} \tag{2.1}$$

where ω is the excitation energy, **Z** is the amplitude vector describing the excited state, and, assuming real orbitals, the matrix elements of **A** are (all equations are in hartree atomic units):

$$A_{ia,jb}^{\text{KS-TDA}} = \delta_{ij}\delta_{ab}(\varepsilon_a - \varepsilon_i) + \left(ai \mid jb\right) - \frac{X}{100}\left(ab \mid ji\right) + (1 - \frac{X}{100})\left(ai \mid f_{\text{xc}} \mid jb\right) \tag{2.2}$$

where X is the percentage of Hartree-Fock exchange if a hybrid exchange-correlation (xc) functional is used; the spin-free two-electron integrals are defined, following Szabo and Ostlund,[23] by

$$\left(ai \mid jb\right) = \iint d^3\mathbf{r}_1 d^3\mathbf{r}_2 \frac{\phi_a(\mathbf{r}_1)\phi_i(\mathbf{r}_1)\phi_j(\mathbf{r}_2)\phi_b(\mathbf{r}_2)}{\left|\mathbf{r}_1 - \mathbf{r}_2\right|} \tag{2.3}$$

and f_{xc} is the "xc kernel" with matrix elements

$$\left(ai \mid f_{\text{xc}} \mid jb\right) = \iint d^3\mathbf{r}_1 d^3\mathbf{r}_2 \phi_a(\mathbf{r}_1)\phi_i(\mathbf{r}_1) \frac{\delta^2 E_{\text{xc}}}{\delta\rho(\mathbf{r}_1)\delta\rho(\mathbf{r}_2)} \phi_j(\mathbf{r}_2)\phi_b(\mathbf{r}_2) \tag{2.4}$$

where ϕ is a molecular orbital, ρ is the electron density, E_{xc} is the xc functional, and δ denotes functional variation. The dimension of the square **A** matrix is $(N^{\text{occ}} \cdot N^{\text{virt}})^2$, where N^{occ} and N^{virt} are respectively the number of doubly occupied and virtual orbitals in the reference state.

HF-TDA theory has the same structure as eq. (2.1), but **A** is replaced by,[24]

$$H_{i'a',j'b'} = \left\langle \Phi_{i'}^{a'} \middle| H \middle| \Phi_{j'}^{b'} \right\rangle = \delta_{i'j'}\delta_{a'b'}(\varepsilon_{a'} - \varepsilon_{i'}) + \left(a'i' \mid j'b'\right) - \left(a'b' \mid j'i'\right) \tag{2.5}$$

where $\Phi_{i'}^{a'}$ denotes the singly excited determinant with occupied orbital i' replaced by virtual orbital a' (the primes denote HF orbitals instead of KS orbitals). This matrix involve only singly excited determinants and no ground-state (closed-shell) determinant

Φ_0^{HF}, because the coupling between the ground-state determinant and any singly excited determinant,

$$H_{0,i'a'} \equiv \left\langle \Phi_0^{\mathrm{HF}} \middle| H \middle| \Phi_{i'}^{a'} \right\rangle = (a' \mid f^{\mathrm{HF}}(1', 2', ..., N^{\mathrm{OCC}}) \mid i'), \tag{2.6}$$

vanishes by virtue of Brillouin's theorem, where the Fock operator is defined as

$$f^{\mathrm{HF}}(1', 2', ..., N^{\mathrm{OCC}}) = h + \sum_{j'}^{N^{\mathrm{occ}}} 2J_{j'} - \sum_{j'}^{N^{\mathrm{occ}}} K_{j'} \tag{2.7}$$

which is composed of the "core" operator *h* (kinetic energy plus external potential), the Coulomb operator $J_{j'}$, and the exchange operator $K_{j'}$, the latter two summed over all doubly occupied Hartree-Fock orbitals. The same argument applies to TDA-TDDFT: the KS reference ground state Φ_0^{KS} and linear-response excited determinants do not couple. However, such de-coupling is an artifact. For instance, if doubly excited determinants are included in the configuration-interaction basis set, the singly excited determinants will couple to the reference determinant indirectly via doubly excited determinants. This artificial de-coupling is the cause of the incorrect $F-1$ dimensionality of conical intersections between the ground (reference) state and the excited (response) state in HF-TDA and TDA-TDDFT where F is the number of internal degrees of freedom. This point has been discussed by Levine *et al.,*[18] and it can be also seen from the fact that HF-TDA and TDA-TDDFT, because of the absence of coupling of the reference ground state and the response excited states, automatically satisfy one of the constraints proposed by Longuet-Higgins16 for the energetic two-fold degeneracy of the ground state and an excited state to occur.

By introducing coupling between the reference state and the intersecting response state into TDA-TDDFT, the dimensionality of the conical intersection is corrected. Here we propose a method, to be called CIC-TDA, for including such coupling in TDA-TDDFT. Coupling between the closed-shell determinant and any singly excited determinant vanishes in HF-TDA because the primed HF orbitals are eigenvectors of the

self-consistent Fock operator $f^{\mathrm{HF}}(1',2',...,N^{\mathrm{OCC}})$. The analogue in TDA-TDDFT, $A_{0,ia} = (a \mid f^{\mathrm{KS}} \mid i)$, vanishes for the same reason, where the KS operator is defined as

$$f^{\mathrm{KS}} = h + \sum_{j}^{N^{\mathrm{occ}}} 2J_j + v_{\mathrm{xc}} \tag{2.8}$$

where v_{xc} is the exchange-correlation potential defined as the functional variation of the exchange-correlation functional E_{xc} with respect to electron density. It is well known that the Kohn-Sham determinant and the TDA response written as a linear combination of singly excited Slater determinants are not actually wave functions for the physical system under consideration; for example, the Kohn-Sham determinant of the ground state is an antisymmetrized product of orbitals that yields the same density as the real system, but it is the wave function of a reference system in which the electrons do not interact. Our solution to the conical intersection problem is to calculate $A_{0,ia}$ by wave function theory as if the Kohn-Sham determinant and the TDA response written as a linear combination of singly excited Slater determinants were approximate wave functions of the real system. This yields:

$$A_{0,ia}^{\mathrm{CIC}} = H_{0,ia} \equiv \left\langle \Phi_0^{\mathrm{KS}} \middle| H \middle| \Phi_i^a \right\rangle = (a \mid h + \sum_{j}^{N^{\mathrm{occ}}} 2J_j - \sum_{j}^{N^{\mathrm{occ}}} K_j \mid i) \tag{2.9}$$

which does not vanish. By including this coupling, the conical intersection will appear with the correct dimensionality. An important point is that $A_{0,ia}^{\mathrm{CIC}}$ should usually be small since its finiteness is due to the difference between the KS orbitals and the HF orbitals, which are generally similar. More detailed analysis of the coupling is given later in this chapter, but first we explain in more detail how we implement eq. (2.9).

CIC-TDA proceeds in four steps. Firstly, the dominant determinant Φ_i^a (corresponding to an $i \rightarrow a$ single excitation) of the intersecting excited state is identified.

Secondly, the coupling between this determinant and the reference determinant is calculated using eq. (2.9). Thirdly, the TDA-TDDFT **A** matrix is expanded to a new square matrix **A´** of dimension $(N^{\text{occ}} \cdot N^{\text{virt}} + 1)^2$ that includes the reference determinant in the basis,

$$\mathbf{A}' = \begin{pmatrix} E^{\text{KS}} & \mathbf{c}^{\mathsf{T}} \\ \mathbf{c} & \mathbf{A} \end{pmatrix} \tag{2.10a}$$

$$\mathbf{c}^{\mathsf{T}} = \begin{pmatrix} 0 & \cdots & 0 & A_{0,ia}^{\text{CIC}} & 0 & \cdots & 0 \end{pmatrix} \tag{2.10b}$$

It includes additionally a $(N^{\text{occ}} \cdot N^{\text{virt}})$-dimensional column vector **c**, a row vector $\mathbf{c}^{\mathsf{T}}$ (which is the transpose of **c)**, and the energy of the reference state E^{KS}. Note that in TDA-TDDFT the absolute energy of the reference state is usually subtracted from the diagonal elements of **A** so that the eigenvalues are excitation energies, and in this case E^{KS} in **A´** is set to zero. The **c** vector has the new coupling matrix element of eq. (2.9) in the row of the dominant determinant of the intersecting excited state and zeros as all other components. In this way the coupling between the states of interest is included without changing the TDA-TDDFT energies significantly (as demonstrated in the results given later in this chapter). Finally, the expanded matrix is diagonalized to obtain the energies of the ground state and the intersecting excited state as the smallest eigenvalues.

Since the KS orbitals are not eigenvectors of the Fock operator, the coupling given in eq. (2.9) does not vanish identically; instead, it can be expressed as

$$\begin{aligned} A_{0,ia}^{\text{CIC}} &= (a \mid h \mid i) + (a \mid \sum_{j}^{N^{\text{occ}}} 2J_j \mid i) + (a \mid v_{\text{xc}} \mid i) + (a \mid \sum_{j}^{N^{\text{occ}}} -K_j \mid i) - (a \mid v_{\text{xc}} \mid i) \\ &= (a \mid f^{\text{KS}} \mid i) + (a \mid \sum_{j}^{N^{\text{occ}}} -K_j \mid i) - (a \mid v_{\text{xc}} \mid i) \\ &= (a \mid \sum_{j}^{N^{\text{occ}}} -K_j \mid i) - (a \mid v_{\text{xc}} \mid i) \end{aligned} \tag{2.11}$$

This shows that the coupling is equal to the difference between the matrix elements of HF exchange and KS exchange-correlation. Basic matrix algebra shows that CIC-TDA lowers the ground-state energy $E_0^{\text{KS-TDA}}$ and raises the excited-state energy $E_1^{\text{KS-TDA}}$ by a similar amount Δ. Near an intersection, where $E_1^{\text{KS-TDA}} - E_0^{\text{KS-TDA}} \to 0$, it is easily shown that $\Delta \to \left| A_{0,ia}^{\text{CIC}} \right|$; and far from an intersection, $\Delta \to \left| A_{0,ia}^{\text{CIC}} \right|^2 / \left(E_1^{\text{KS-TDA}} - E_0^{\text{KS-TDA}} \right)$. According to our tests (see below), $A_{0,ia}^{\text{CIC}}$ is typically of the order of magnitude of 0.1 eV, while $\Delta E^{\text{KS-TDA}}$ is generally several eV in regions where $E_0^{\text{KS-TDA}}$ and $E_1^{\text{KS-TDA}}$ are well separated. Therefore, it is anticipated that CIC-TDA is able to lift the incorrect degeneracy of TDA-TDDFT states around a true intersection whereas it does not change the TDA-TDDFT energies significantly where the potential energy surfaces (PESs) are well-separated. At a symmetry-allowed conical intersection, $A_{0,ia}^{\text{CIC}}$ is zero by symmetry and CIC-TDA gives the same position of intersection as TDA-TDDFT; however, CIC-TDA surfaces, unlike TDA-TDDFT surfaces, also have the correct topology for same-symmetry conical intersections.

If desired, oscillator strengths may be calculated using the same methods as are used without the configuration-interaction correction.

We note that conical intersections between two excited states already have the correct dimensionality and do not require this correction. We also note that another way to correct the treatment of conical intersections is to use spin-flip TDDFT, where the reference state is a triplet[18,25,26,27,28] but the present chapter is concerned with a correct treatment based on conventional TDDFT with a singlet reference state.

2.3. COMPUTATIONAL DETAILS

The CIC-TDA method has been implemented in a locally modified version of the GAMESS[29,30] package for both closed-shell singlet ground states and doublet ground

states, and all calculations were performed using this software. For practical convenience, the CIC-TDA matrix in this implementation of the CIC-TDA method is built from the TDA-TDDFT **A** matrix of dimension $(N^{\text{occ}} \cdot N^{\text{virt}})^2$ by replacing the row and column corresponding to the excitation from the *lowest* occupied molecular orbital (LOMO) to the *highest* unoccupied molecular orbital (HUMO) with $\mathbf{c}^{\mathsf{T}}$ and $\mathbf{c}$ as defined in eq. (2.10b) and by setting the element at the intersection of that row and column to zero. In other words, we employ a CIC-TDA matrix **A'** of dimension $(N^{\text{occ}} \cdot N^{\text{virt}})^2$ rather than $(N^{\text{occ}} \cdot N^{\text{virt}}+1)^2$ by excluding the Slater determinant corresponding to the LOMO→HUMO excitation from the basis set of Slater determinants used in eq. (2.5). This approximation has a negligible effect on the energy of the low-lying excited states because we know from chemical intuition (and it has also been tested) that such LOMO →HUMO configuration has negligible contribution to those states.

Diagonalization of the CIC-TDA matrix is carried out by the Davidson algorithm, which is much less expensive than a direct diagonalization. The spatial symmetry restriction is turned off in all calculations.

We found, for both TDA-TDDFT and CIC-TDA, that in order to get electronic excitation energies that are smooth functions of geometry, one must use fine grids and very tight convergence criteria in the SCF iterations that produce the KS reference state.

2.4. TESTS AND DISCUSSION

Calculations were performed on two test systems. These two systems are good test cases because their conical intersections have been studied previously, and the conical intersections are well understood. In the examples, it happens that the first excited electronic state is dominated by the HOMO→LUMO singly excited determinant, where the HOMO is the highest occupied molecular orbital (orbital *i* in eq 2.9) and LUMO is the lowest unoccupied (or virtual) molecular orbital (orbital *a* in eq 2.9). In this case, $A^{\text{CIC}}_{0,ia}$, where *ia* corresponds to the HOMO→LUMO excitation, is the first element of **c**.

Therefore this single coupling matrix element and its transpose are added to the TDA-TDDFT matrix **A** to produce the CIC-TDA matrix **A′**. One- and two-dimensional cuts through the PESs of the ground state and an intersecting excited state in the vicinity of the conical intersections were calculated using both TDA-TDDFT and CIC-TDA. A practical point that is worth noting is that the KS-SCF solution tends to be relatively unstable near state crossings and in regions where the KS closed-shell reference state is not the ground state, making it harder, both for TDA-TDDFT and for CIC-TDA, to converge to smooth orbitals and smooth potential energy curves. Therefore we used a tight grid and strict convergence criteria.

Test case 1. The first system is ammonia (NH_3). The coordinates are the same as used previously[32]; in particular, r_1, r_2, and r_3 are the N–H bond lengths, θ_1, θ_2, and θ_3 are H–N–H bond angles, **T** is a vector that trisects the three N–H bonds, β is the angle between **T** and any of the bonds, and θ'_1, θ'_2, and θ'_3 are are the angles between the projections of the bonds on a plane perpendicular to **T**. Multi-reference perturbation theory predicts a symmetry-allowed conical intersection between the ground state (of symmetry A_1) and a singlet excited (B_1) states at a C_{2v} geometry with a stretched N-H bond r_1, with the other two N-H bond lengths at $r_2 = r_3 = 1.039$ Å and the three H-N-H bond angles at $\theta_1 = \theta_2 = \theta_3 = 120°$.[31,32] To investigate the behavior of TDA-TDDFT and CIC-TDA in the vicinity of this conical intersection, the M06[33,34] exchange-correlation functional with the 6-31+G(d)[35,36,37] basis set was used to calculate the PESs of the two lowest-energy states (A_1 and B_1) along N-H bond stretching r_1 and inversion angle β, with r_1 and r_2 fixed at 1.039 Å and the three projected bond angles θ'_1, θ'_2, and θ'_3 fixed at 120°. The B_1 state mainly corresponds to an excitation from the HOMO to the LUMO of the closed-shell A_1 reference state.[31] At the conical intersection, the HOMO has b_1 symmetry and n_p character, and the LUMO has a_1 symmetry and σ* character; thus the HOMO→LUMO singly excited determinant is denoted as nσ*.

A two-dimensional cross section of the PESs of the two lowest-energy singlet states (S_0 and S_1) in the r_1-β subspace is shown in Figure 2.1. Moving away from the planar intersection by decreasing β from 90°, the degeneracy of the two states is lifted and a

cone results.[31,32] However, TDA-TDDFT method shows a spurious seam of degeneracy for $\beta < 90°$. By contrast, CIC-TDA gives a correct double-cone topology.

Several one-dimensional cross-sections of the 2-dimensional PESs with different β are shown in Figures 2.2 and 2.3. For $\beta = 90°$, the CIC-TDA and TDA-TDDFT potential energy curves overlap because the coupling vanishes by symmetry; thus this result is not shown in the figures. For $\beta = 89°$, TDA-TDDFT gives an artificial intersection at $r_1 =$ 2.24 Å, and CIC-TDA lifts the degeneracy by 0.058 eV. For $\beta = 88.5°$, the degeneracy is lifted by 0.093 eV, which is larger than for $\beta = 89°$ as it should for a double-cone topology. We also note that TDA-TDDFT gives an unphysical "double crossing" for $\beta =$ 88.5° which is fixed by CIC-TDA. Moving away from the crossing, CIC-TDA converges to TDA-TDDFT, as can be seen for $\beta = 88.5°$.

Test case 2. The second system is penta-2,4-dieniminium cation, which will be denoted as PSB3 because it is a model molecule of the retinal protonated Schiff base (PSB) with three conjugated double bonds. Previous studies[28,38] found a conical intersection between the ground and the first singlet excited states of PSB3 near a bond length alternation (BLA) path connecting the saddle points of two reaction paths of the *cis-trans* isomerization. For the present study, we used the 14 structures along BLA path from the original literature,[38] then added more structures by quadratic interpolation between the 9th and 12th structures to increase the density of points in the region closest to the conical intersection. Then TDA-TDDFT and CIC-TDA calculations were performed with the M05-2X[34,39] xc functional and the 6-31G(d)[35,36] basis set (the same as used in previous work[28]) to calculate potential energy curves of the two states along this path. The reference state is a closed-shell π^2 state; the response state is a $\pi\pi^*$ state which corresponds to the HOMO→LUMO excitation. To obtain smooth convergence, a tighter grid and convergence than the previous study[28] are used in the present calculations.

The TDA-TDDFT and CIC-TDA potential energy curves for PSB3 along the BLA path are shown in Figure 2.4. In this case CIC-TDA again corrects an unphysical "double crossing" obtained by TDA-TDDFT. The degeneracy at the first crossing of TDA-TDDFT at a BLA coordinate of ~0.0224 Å is lifted by 0.04 eV by CIC-TDA. The

deviation of CIC-TDA from TDA-TDDFT increases from ~0.025 Å onward because $|A^{\mathrm{CIC}}_{0,ia}|$ increases and, according to the formal analysis above, the deviation is approximately equal to $|A^{\mathrm{CIC}}_{0,ia}|$ when two PESs are close.

Further discusssion. We note that the present treatment does not remove the adiabatic approximation, and so it is not an attempt to make TDDFT more accurate (closer to formally exact TDDDFT) in general, but rather to improve the description of excited stated in the vicinity of S_0–S_1 conical interaction schemes.

A procedure called Brillouin-corrected dressed TDDFT (b-D-TDDFT), described in a thesis,[40] was proposed as an extension of conventional dressed TDDFT. In dressed TDDFT one uses a modified correlation functional to take account of two-particle–two-hole states.[41,42] In order to implement dressed D-TDDFT with a nonlocal exchange-correlation functional in a computer program that did not have SCF capability for nonlocal functionals, the SCF ground state determined with a local functional was modified by adding all possible single excitations with perturbation theory; this gives a nonvanishing contribution since the perturbation theory is applied with a nonlocal functional on a zero-order state obtained with a local functional.[40] That method has some similarity to the present method, but differs in fundamental ways, including: (1) the motivation and justification for the method is entirely different, in particular the present method is explicitly designed to correct the conical intersection problem that occurs with either local or nonlocal exchange-correlation functionals; (2) we include the coupling of the ground state to a single excitation in the TDA calculation, not as a prior step; (3) we include only one single excitation, not all of them (although one could add additional single excitations if the character of S_1 at S_0-S_1 conical intersections changes qualitatively as a function of geometry). Difference (3) is very important; including all single excitations would lead to a much larger change from conventional TDDFT, but the present method is designed to make a significant change only in the vicinity of the S_0–S_1 conical intersection.

2.5. SUMMARY

We propose a new approximation called configuration-interaction-corrected TDA (CIC-TDA) that corrects the dimensionality problem of TDA-TDDFT for conical intersections. The new scheme includes a coupling between the reference state and the intersecting response excited state and thus removes the unphysical state crossings of TDA-TDDFT, but not the physical crossings of dimensionality $F - 2$. In regions of nuclear configuration space where the reference state is well separated from the excited states, CIC-TDA energies converge to TDA-TDDFT and therefore it gives the same accuracy as TDA-TDDFT in those regions. The new method was tested on two molecules, ammonia and PSB3, and the results are consistent with the expectations based on formal analysis in all respects: the coupling $A_{0,ia}^{\mathrm{CIC}}$ is a small quantity, CIC-TDA lifts artificial state crossings of TDA-TDDFT, and it converges to TDA-TDDFT far from an intersection.

We emphasize that CIC-TDA is aimed at remedying the incorrect dimensionality of conical intersections in TDA-TDDFT, but it does not improve the TDA-TDDFT energy more generally, as can be seen from the formal analysis given in this chapter. Improving TDA-TDDFT more generally requires improved xc functionals, which is a separate issue. The new method is general and can be applied with any approximate xc functional and hence can be applied with better functionals when they become available. However, as mentioned in the introduction, there are many problems where the currently available functionals already provide useful accuracy.[12,13] The CIC-TDA approximation is well defined, easy to implement, and simple to use. The results presented here show that this scheme will allow realistic application of density functional methods to photochemical problems involving conical intersections.

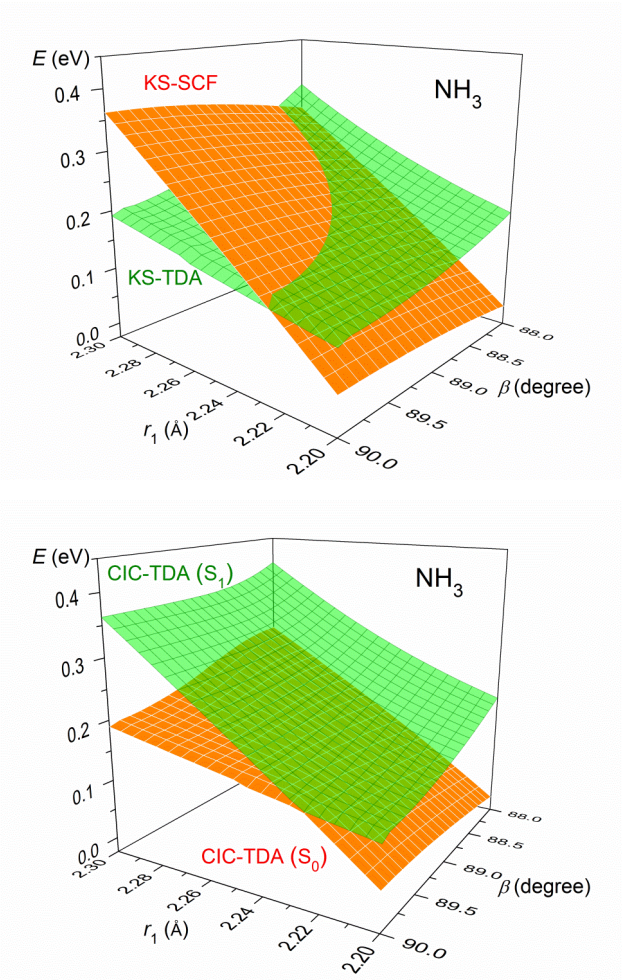

Figure 2.1. PESs of the two lowest-energy states of NH_3 in r_1-β nuclear configuration space as calculated by (top) TDA-TDDFT and (bottom) CIC-TDA.

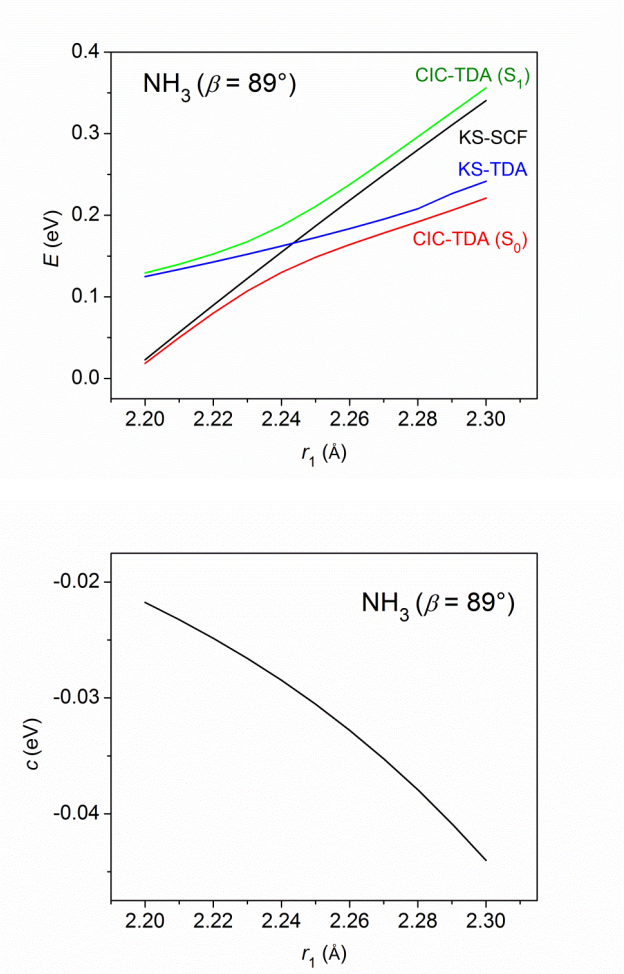

Figure 2.2. Potential energy curves of the two lowest-energy states and the coupling c of NH_3 (c is shorthand for $A_{0,ia}^{\mathrm{CIC}}$) as a function of the N-H bond length r_1 with the inversion angle β fixed at 89°. (top) Potential energy curves as calculated by TDA-TDDFT and the new CIC-TDA. (bottom) Coupling c used in CIC-TDA calculation.

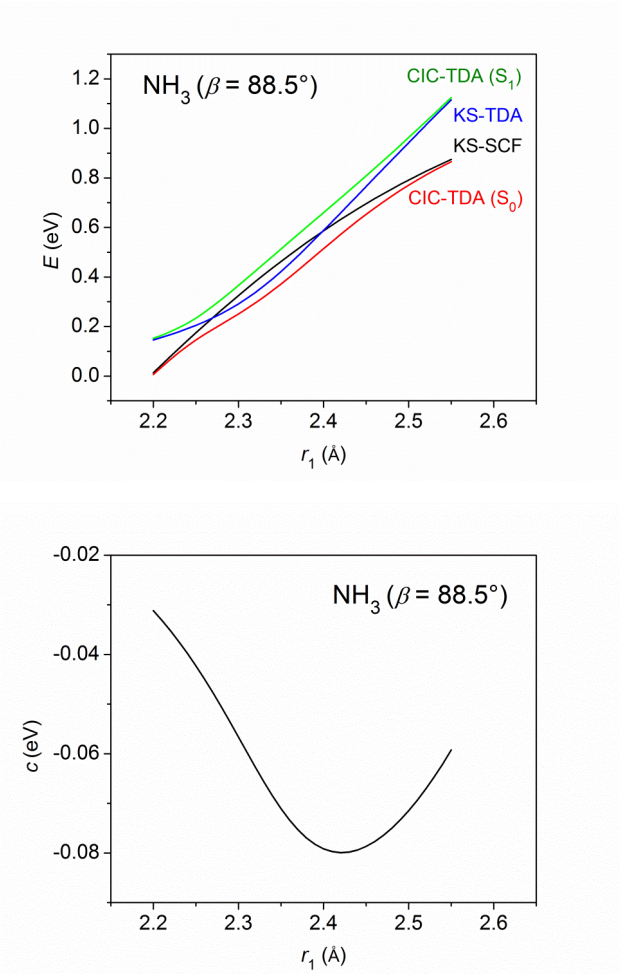

Figure 2.3. Potential energy curves of the two lowest-energy states and the coupling c (c is shorthand for $A^{\mathrm{CIC}}_{0,ia}$) of NH_3 as a function of the N-H bond length r_1 with the inversion angle β fixed at 88.5°. (top) Potential energy curves as calculated by TDA-TDDFT and the new CIC-TDA. (bottom) Coupling c used in CIC-TDA calculation.

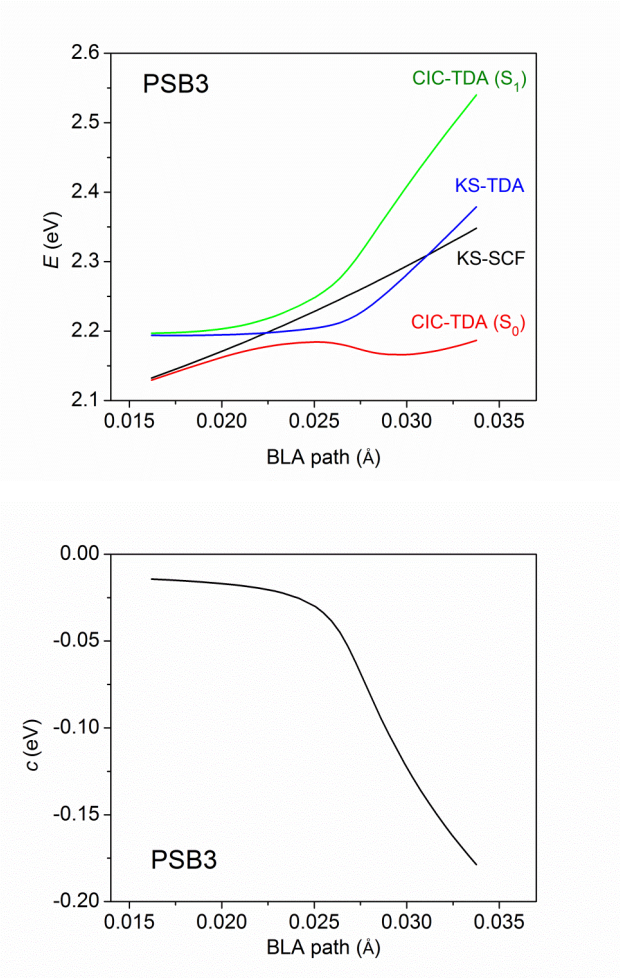

Figure 2.4. Potential energy curves of the two lowest-energy states and the coupling c of PSB3 (c is shorthand for $A_{0,ia}^{\mathrm{CIC}}$) along the BLA path. (top) Potential energy curves as calculated by TDA-TDDFT and the new CIC-TDA. (bottom) Coupling c used in CIC-TDA calculation.

REFERENCES FOR CHAPTER 2

[1] Marques, M. A. L.; Gross, E. K. U. Time-dependent density functional theory. *Annu. Rev. Phys. Chem.* **2004**, *55*, 427-455.

[2] Casida, M. E. Time-dependent density-functional response theory for molecules. In Recent Advances in Density Functional Methods, Part I; Chong, D. P., Ed.; World Scientific: Singapore: 1995, pp. 155-193.

[3] Karplus, M.; Kolker, H. J. Time-Dependent Variation-Perturbation Method for Many-Electron Systems. *J. Chem. Phys.* **1963,** *39*, 2997-3000.

[4] McLachlan, A. D.; Ball, M. A. Time-Dependent Hartree—Fock Theory for Molecules. *Rev. Mod. Phys.* **1964,** *36***,** 844-855.

[5] Tamm, I. Relativistic interaction of elementary particles. *J. Phys.* (Moscow) **1945**, *9*, 449-460.

[6] Dancoff, S.M. Non-adiabatic meson theory of nuclear forces. *Phys. Rev.* **1950**, *78*, 382-385.

[7] Hirata, S.; Head-Gordon, M. Time-dependent density functional theory within the Tamm–Dancoff approximation. *Chem. Phys. Lett.* **1999**, *314*, 291-299.

[8] A. Herzenberg, D. Sherrington, and M. Suveges, Correlations of electrons in small molecules. *Proc. Phys. Soc.* (London) **1964**, *84*, 465-476.

[9] T. H. Dunning and V. McKoy, Nonempirical Calculations on Excited States: The Ethylene Molecule. *J. Chem. Phys.* **1967**, *47*, 1735-1747.

[10] Truhlar, D. G. Application of the Configuration-Interaction Method and the Random Phase Approximation to the *Ab Initio* Calculation of Electronic Excitation Energies of H_2O. *Int. J. Quantum Chem.* **1973**, *7*, 807-817.

[11] Casida, M. E.; Huix-Rotllant, M. Progress in Time-Dependent Density-Functional Theory. *Annu. Rev. Phys. Chem.* **2012**, *63*, 287-323.

[12] Isegawa, M.; Peverati, R.; Truhlar, D. G. Performance of recent and high-performance approximate density functionals for time-dependent density functional theory calculations of valence and Rydberg electronic transition energies. *J. Chem. Phys.* **2012**, *137*, 244104.

[13] Laurent, A. D.; Jacquemin, D. TD-DFT Benchmarks: A Review. *Int. J. Quantum Chem.* **2013**, *113*, 2019-2039.

[14] González, L.; Escudero, D.; Serrano-Andrés, L. Progress and Challenges in the Calculation of Electronic Excited States. *ChemPhysChem* **2012**, *13*, 28-51.

[15] Longuet-Higgins, H. C. The Intersection of Potential Energy Surfaces in Polyatomic Molecules. *Proc. Roy. Soc., Ser. A* (London). **1975**, *344*, 147-156.

[16] Mead, C. A. The "noncrossing" rule for electronic potential energy surfaces: The role of time-reversal invariance. *J. Chem. Phys.* **1979**, *70*, 2276-2283.

[17] Jasper, A. W.; Kendrick, B. K.; Mead, C. A.; Truhlar, D. G. Non-Born-Oppenheimer Chemistry: Potential Surfaces, Couplings, and Dynamics. In *Modern Trends in Chemical Reaction Dynamics: Experiment and Theory (Part 1)*; Yang, X. Liu, K., Eds.; World Scientific: Singapore, 2004; pp. 329-391.

[18] Levine, B. G.; Ko, C.; Quenneville, J.; MartÍnez, T. J. Conical intersections and double excitations in time-dependent density functional theory. *Mol. Phys.* **2006**, *104*, 1039-1051.

[19] Cordova, F.; Doriol, L. J.; Ipatov, A.; Casida, M. E.; Filippi, C.; Vela, A. Troubleshooting Time-Dependent Density-Functional Theory for Photochemical Applications: Oxirane. *J. Chem. Phys.* **2007**, *127*, 164111.

[20] Tapavicza, E.; Tavernelli, I.; Rothlisberger, U.; Filippi, C.; Casida, M. E. Mixed time-dependent density-functional theory/classical surface hopping study of oxirane photochemistry. *J. Chem. Phys.* **2008**, *129*, 124108.

[21] Miquel Huix-Rotllant, M.; Natarajan, B.; Ipatov, A.; Wawire, C. M.; Deutsch, T.; Casida, M. E. Assessment of Noncollinear Spin-Flip Tamm-Dancoff Approximation. Time-Dependent Density-Functional Theory for the Photochemical Ring-Opening of Oxirane. *Phys. Chem. Chem. Phys.*, **2010**, *12*, 12811-12825.

[22] Kadik, B.; Van Voorhis, T. Conical intersections using constrained density functional theory–configuration interaction. *J. Chem. Phys.,* **2010**, *133*, 061102.

[23] Szabo, A.; Ostlund, N. S. *Modern Quantum Chemistry: Introduction to Advanced Electronic Structure Theory*; McGraw-Hill, Inc., 1989.

[24] Dreuw, A.; Head-Gordon, M. Single-Reference ab Initio Methods for the Calculation of Excited States of Large Molecules. *Chem. Rev.* **2005**, *105*, 4009-4037.

[25] Shao, Y.; Head-Gordon, M.; Krylov, A. I. The spin–flip approach within time-dependent density functional theory: Theory and applications to diradicals. *J. Chem. Phys.* **2003**, *118*, 4807-4818.

[26] Minezawa, N.; Gordon, M. S. Optimizing conical intersections by spin-flip density functional theory: Application to ethylene. *J. Phys. Chem. A* **2009**, *113*, 12749-12753.

[27] Isegawa, M.; Truhlar, D. G. Valence Excitation Energies of Alkenes, Carbonyl Compounds, and Azabenzenes by Time-Dependent Density Functional Theory: Linear Response of the Ground State Compared to Collinear and Noncollinear Spin-Flip TDDFT with the Tamm-Dancoff Approximation. *J. Chem. Phys.* **2013***, 138,* 134111.

[28] X. Xu, S. Gozem, M. Olivucci, and D. G. Truhlar, Combined Self-Consistent-Field and Spin-Flip Tamm-Dancoff Density Functional Approach to Potential Energy Surfaces for Photochemistry. *J. Phys. Chem. Lett.* **2012**, *4*, 253-258.

[29] Schmidt, M. W.; Baldridge, K. K.; Boatz, J. A.; Elbert, S. T.; Gordon, M. S.; Jensen, J. H.; Koseki, S.; Matsunaga, N.; Nguyen, K. A.; Su, S. J.; Windus, T. L.; Dupuis, M.; Montgomery, J. A. General Atomic and Molecular Electronic-Structure System. *J. Comp. Chem.* **1993**, *14*, 1347.

[30] Gordon, M. S.; Schmidt, M. W. Advances in electronic structure theory: GAMESS a decade later. In *Theory and Applications of Computational Chemistry: The First Forty Year*s, Dykstra, C. E.; Frenking, G.; Kim, K. S.; Scuseria G. E., Eds.; Elsevier: Amsterdam, 2005; p. 1167.

[31] Nangia, S.; Truhlar, D. G. Direct calculation of coupled diabatic potential-energy surfaces for ammonia and mapping of a four-dimensional conical intersection seam. *J. Chem. Phys.* **2006**, *124*, 124309.

[32] Li, Z.; Valero, R.; Truhlar, D. Improved direct diabatization and coupled potential energy surfaces for the photodissociation of ammonia. *Theor. Chem. Acc.* **2007**, *118*, 9-24.

[33] Zhao, Y.; Truhlar, D. G. The M06 suite of density functionals for main group thermochemistry, thermochemical kinetics, noncovalent interactions, excited states, and transition elements: two new functionals and systematic testing of four M06-class functionals and 12 other functionals. *Theor. Chem. Acc.* **2008**, *120*, 215-241.

[34] Zhao, Y.; Truhlar, D. G. Density Functionals with Broad Applicability in Chemistry. *Acc. Chem. Res.* **2008**, *41*, 157-167.

[35] Hehre, W. J.; Ditchfield, R.; Pople, J. A. Self---Consistent Molecular Orbital Methods. XII. Further Extensions of Gaussian---Type Basis Sets for Use in Molecular Orbital Studies of Organic Molecules. *J. Chem. Phys.* **1972**, *56*, 2257-2261.

[36] Hariharan, P. C.; Pople, J. A. The influence of polarization functions on molecular orbital hydrogenation energies. *Theoret. Chim. Acta* **1973**, *28*, 213-222.

[37] Clark, T.; Chandrasekhar, J.; Spitznagel, G. W.; Schleyer, P. V. R. Efficient diffuse function-augmented basis sets for anion calculations. III. The 3-21+G basis set for first-row elements, Li–F. *J. Comp. Chem.* **1983**, *4*, 294-301.

[38] Gozem, S.; Huntress, M.; Schapiro, I.; Lindh, R.; Granovsky, A. A.; Angeli, C.; Olivucci, M. Dynamic Electron Correlation Effects on the Ground State Potential Energy Surface of a Retinal Chromophore Model. *J. Chem. Theory Comput.* **2012**, *8*, 4069-4080.

[39] Zhao, Y.; Schultz, N. E.; Truhlar, D. G. Design of Density Functionals by Combining the Method of Constraint Satisfaction with Parametrization for Thermochemistry, Thermochemical Kinetics, and Noncovalent Interactions. *J. Chem. Theory Comput.* **2006**, *2*, 364-382.

[40] Huix-Rotlland, M. Improved correlation kernels for linear-response time-dependent density-functional theory. Ph.D. thesis, Joseph Fourier University (Grenoble I), Mar. 17, 2012, http://tel.archives-ouvertes.fr/tel-00680039 (accessed Dec. 19, 2013)

[41] Maitra, N. T.; Zhang, F.; Cave, R. J.; Burke. K. Double excitations within time-dependent density functional theory linear response. *J. Chem. Phys.* **2004**, *120*, 5932-5937.

[42] Huix-Rotllant, M.; Ipatov, A.; Rubio, A.; Casida, M. E. Assessment of Dressed Time-Dependent Density-Functional Theory for the Low-Lying Valence States of 28 Organic Chromophores. *Chem. Phys.* **2011**, *391*, 120-129.

Chapter 3. Improving Rydberg Excitations within Time-Dependent Density Functional Theory with Generalized Gradient Approximations: The Exchange-Enhancement-for-Large-Gradient Scheme

3.1. INTRODUCTION

Linear-response time-dependent density functional theory (TDDFT) with conventional local functionals such as the local spin-density approximation (LSDA) and generalized-gradient approximation (GGA) is well known to suffer from severe underestimation of the energies of Rydberg excitations.[1,2,3] This can be ascribed to the self-interaction error (SIE) due to the failure of local exchange approximations to exactly cancel the spurious Coulomb interaction of an electron with itself. Global hybrid functionals alleviate the SIE by mixing a fraction of self-interaction-free nonlocal Hartree-Fock exchange, but this does not solve the problem. The exchange-correlation (xc) potential (v_{xc}) derived from these functionals is everywhere too shallow (not negative enough) and does not exhibit the $-1/r$ limit as $r\rightarrow\infty$, where r is the distance from an electron to the nearest nucleus of a finite system. This leads to overall large upshifts of the core and valence Kohn-Sham (KS) orbital energies and small upshifts of the Rydberg orbital energies, resulting in still reasonable valence-valence orbital energy gaps but much too narrow valence-Rydberg energy gaps.[4] These too narrow gaps are the cause of the underestimation of the Rydberg excitation energies with TDDFT. It greatly limits the applicability of TDDFT for spectroscopy and photochemistry of molecules. It is worth emphasizing that this can be a problem even for cases where the excitation energies of interest are lower than the energies of any Rydberg states because the underestimated energies of the Rydberg states by TDDFT brings them down to where they mix with valence states and muddy the whole spectrum.

There have been attempts in the literature to correct the SIE within the framework of KS DFT; examples include methods that directly model the xc potential,[5,6,7,8,9] the range-separated hybrid scheme,[10] and the HOMO (highest occupied molecular orbital) depopulation method.[11,12] They are able to significantly improve the Rydberg excitations but also have their own problems. Directly correcting the xc potential does not generate an xc energy functional and therefore cannot be used to predict total energies.[13] The schemes for correcting xc potentials also often involve system-dependent parameters like the ionization potential, making them inconvenient to use. Range-separated hybrid functionals have adjustable parameters that control the mixing of short- and long-range exchange, and it is not always clear how they should be determined to balance the performance for energetics and different types of electronic excitations.[14] HOMO depopulation is not size-extensive and is thus unsuitable for photochemistry.[15] In this chapter, with the aim of developing better functionals suitable for both spectroscopy and potential energy surfaces for photochemistry, we propose a new scheme to improve the description of Rydberg excitations of local and hybrid GGA functionals without sacrificing their good performance for valence excitations, ground-state energetics, and bond energies. The new scheme is fundamental in the sense that it modifies the exchange-correlation functional rather than a derived property or methodological step. Apart from providing a correction to existing GGAs, it can also serve as a component of a new strategy for the development of new xc functionals.

3.2. THEORY

The theoretical foundation of our method is based on the arguments of Tozer and Handy.[16] It is well known that the exact KS xc potential is discontinuous with respect to the fractional number of electrons when the number changes through integers,[17] but the model xc potentials derived from LSDA and GGA lack such derivative discontinuity due to the self-interaction error.[18] One consequence is that the model potentials produce HOMO energies ($\varepsilon_{\mathrm{HOMO}}$) higher than the negative of the ionization potential ($-I$) of the system, as opposed to $\varepsilon_{\mathrm{HOMO}} = -I$ given by the exact potential. Tozer and Handy

argued,[16] however, that the potential and the HOMO energies given by LSDA and GGA can be regarded as reasonable if one views the potential as modeling an average over the derivative discontinuity, but with this viewpoint the xc potential should asymptotically go like $-1/r + I + \varepsilon_{\mathrm{HOMO}}$, which approaches a positive value $I + \varepsilon_{\mathrm{HOMO}}$ as $r \to \infty$, instead of $-1/r$, which vanishes as $r \to \infty$. Therefore, to improve the LSDA and GGA potential one may push the potential up in the large-r region as Tozer and Handy did in their AC scheme,[6,19] as an alternative to pulling it down in the small-r region to make it closer to the exact potential as van Leeuwen and Baerends did in their LB94 potential.[5] In this chapter, we follow the philosophy of Tozer and Handy but pursue it in a different manner. Instead of correcting the xc potential, we correct the GGA xc functional so that it generates the kind of potential that we desire. In particular, we utilize the fact that the value of the reduced density gradient is small in the core and valence regions of a finite system but blows up exponentially in the Rydberg and asymptotic regions. We show that, by augmenting the enhancement factor of an existing GGA exchange functional for large values of the reduced density gradient, we can shift the exchange potential upward in the Rydberg region (as discussed below, the exchange energy functional is more negative, but the exchange potential is shifted upward) with only a minor effect on the potential in the core and valence regions. The scheme is therefore called exchange-enhancement-for-large-gradient (XELG). It gives a more reasonable low-lying Rydberg orbital energy spectrum and in turn better Rydberg excitation energies, while keeping the performance for valence excitations and ground-state energetics of the original GGA.

Analysis of the exchange potential derived from GGA functionals in the asymptotic region. To see how the form of the exchange functional can affect the behavior of the exchange potential, we start with a formal asymptotic analysis. A GGA exchange functional can be written in the following form,[20]

$$E_{\mathrm{x}}^{\mathrm{GGA}} = \sum_{\sigma=\alpha,\beta} E_{\mathrm{x},\sigma}^{\mathrm{GGA}} = \sum_{\sigma=\alpha,\beta} \int d^3\mathbf{r} \rho_\sigma \varepsilon_{\mathrm{x}}^{\mathrm{LSDA}}(\rho_\sigma) F_{\mathrm{x}}(s_\sigma) \tag{3.1}$$

where ρ_σ is the spin density, $\varepsilon_{\mathrm{x}}^{\mathrm{LSDA}}$ is the exchange energy density per electron of the LSDA functional,[21]

$$\varepsilon_{\mathrm{x}}^{\mathrm{LSDA}}(\rho_\sigma) = C_1 \rho_\sigma^{1/3}, \quad C_1 = -\frac{3}{4}\left(\frac{6}{\pi}\right)^{1/3}, \tag{3.2}$$

s_σ is the reduced spin density gradient consistent with the definition in ref. 22,

$$s_\sigma = C_2 \frac{|\nabla \rho_\sigma|}{\rho_\sigma^{4/3}}, \quad C_2 = \frac{1}{2(6\pi^2)^{1/3}}, \tag{3.3}$$

and $F_{\mathrm{x}}(s_\sigma)$ is the exchange enhancement factor that defines a particular approximate exchange functional. In this chapter we will always work with functionals of spin densities rather than of total density.

Next we will see how the behavior of $F_{\mathrm{x}}(s_\sigma)$ affects the exchange potential in the asymptotic region where ρ_σ decays exponentially. To obtain an expression for the exchange potential, we first rewrite eq. (3.1) as

$$E_{\mathrm{x}} = \sum_{\sigma=\alpha,\beta} \int d^3\mathbf{r}\, f(\rho_\sigma, s_\sigma), \tag{3.4}$$

which defines *f*. The exchange potential for orbitals of spin σ is then given by[23]

$$v_{\mathrm{x},\sigma} = \frac{\delta E_{\mathrm{x}}}{\delta \rho_\sigma} = \frac{\partial f}{\partial \rho_\sigma} - \nabla \cdot \frac{\partial f}{\partial \nabla \rho_\sigma} \tag{3.5}$$

where the vector $\dfrac{\partial f}{\partial \nabla \rho_\sigma}$ is defined as

$$\frac{\partial f}{\partial \nabla \rho_\sigma} \equiv \mathbf{i}\frac{\partial f}{\partial(\partial \rho_\sigma / \partial x)} + \mathbf{j}\frac{\partial f}{\partial(\partial \rho_\sigma / \partial y)} + \mathbf{k}\frac{\partial f}{\partial(\partial \rho_\sigma / \partial z)} \tag{3.6}$$

where **i**, **j**, **k** are the unit vectors associated with the Cartesian coordinates *x*, *y*, and *z*, and *f* depends on $\nabla \rho_\sigma$ via s_σ.

In the asymptotic region far away from the nuclei of a finite system, the spin density decays exponentially[19] and can be written as

$$\rho_\sigma(r) \sim Ae^{-\gamma r} \tag{3.7}$$

where r is the distance from the nuclei, A is a positive constant, and γ is related to the ionization potential I of the system by $\gamma = 2(-2I)^{1/2}$. Accordingly s_σ is given by

$$s_\sigma \sim C_2 \gamma A^{-1/3} e^{(1/3)\gamma r}. \tag{3.8}$$

In this region s_σ grows exponentially and acquires large values, while in the valence and core regions of a finite system the value of s_σ is much smaller (typically less than 3).

Substituting eqs. (3.7) and (3.8) in eq. (3.5), we can derive the expression of the exchange potential in the asymptotic region,

$$v_{\mathrm{x},\sigma} \sim \frac{1}{3} C_1 C_2 \gamma \left(4\frac{F_\mathrm{x}}{s_\sigma} - 4\frac{dF_\mathrm{x}}{ds_\sigma} + s_\sigma \frac{d^2 F_\mathrm{x}}{ds_\sigma^2} \right) + 2C_1 C_2 \frac{1}{r}\frac{dF_\mathrm{x}}{ds_\sigma}. \tag{3.9}$$

As already discussed by Engel *et al.*,[24] it is possible to recover the $-1/r$ asymptotic form of $v_{\mathrm{x},\sigma}$ by setting $F_\mathrm{x} \sim (-2C_1C_2)^{-1} s_\sigma$ asymptotically. However, Engel *et al.* showed that the correct asymptotic form is irrelevant for recovering the atomic exchange energies,[24] and it is also irrelevant for our purpose of raising the potential to positive values in large-r regions.

For our purpose, we require that $v_{\mathrm{x},\sigma}$ goes asymptotically to a positive constant. This can be achieved by requiring

$$\lim_{s\to\infty} F_\mathrm{x} \sim s \ln s \tag{3.10}$$

asymptotically. It is straightforward to show that with this form of F_x eq. (3.9) becomes

$$v_{\mathrm{x},\sigma} \sim -\frac{1}{3} C_1 C_2 \gamma + 2C_1 C_2 \frac{\ln(C_2 \gamma A^{-1/3}) + 1}{r}; \quad \lim_{r\to\infty} v_{\mathrm{x},\sigma} = -\frac{1}{3} C_1 C_2 \gamma > 0 \tag{3.11}$$

(note that $C_1 < 0$). With the XELG scheme introduced next, we will modify $F_{\rm x}$ of a standard GGA to obtain an asymptotic form like eq. (3.10) as $s_\sigma \to \infty$ while keeping the form of $F_{\rm x}$ of the standard GGA in the valence and core regions where s_σ is small.

Exchange-enhanced GGA. The exchange-enhanced GGA (xe-GGA) is defined by multiplying $E_{{\rm x},\sigma}^{\rm GGA}$ in eq. (3.1) by a XELG factor $g(s_\sigma)$, namely,

$$E_{{\rm x},\sigma}^{\text{xe-GGA}} = \int d^3\mathbf{r}\rho_\sigma \varepsilon_{\rm x}^{\rm LSDA}(\rho_\sigma) F_{\rm x}(s_\sigma) g(s_\sigma). \tag{3.12}$$

Essentially it defines a new enhancement factor $\tilde{F}_{\rm x}(s_\sigma) = F_{\rm x}(s_\sigma) g(s_\sigma)$, but we write it as a product because we will take $F_{\rm x}(s_\sigma)$ from a standard GGA functional (or the local part of a global hybrid GGA functional) that performs well for valence excitations and apply the correction $g(s_\sigma)$ to improve the Rydberg excitations. The resulting exchange-enhanced functional will be called xe-*GGA*, where *GGA* is the name of a standard local or global hybrid GGA functional to be corrected. Since xe-GGA is itself a GGA, it has the desirable formal properties that a GGA has, e.g., DFT and TDDFT with xe-GGA are size-extensive.

As a test of the formalism, we choose the PBE exchange functional[22] as the standard GGA exchange functional to be corrected (combined with the standard PBE correlation functional). The reason for this choice is that PBE0,[25] a reasonably simple global hybrid GGA that mixes 25% Hartree-Fock nonlocal exchange with 75% PBE local exchange, is widely available in popular computer programs, it has good performance for valence excitations (see, for example, refs. 26, 27, and 28), and the corrected xe-PBE exchange functional can be readily combined with 25% Hartree-Fock exchange to construct an xe-PBE0 functional. The exchange enhancement factor of PBE is given by

$$F_{\rm x}^{\rm PBE}(s_\sigma) = 1 + \kappa - \frac{\kappa}{1 + \mu s_\sigma^2 / \kappa}, \quad \kappa = 0.804, \quad \mu \sim 0.21951 \tag{3.13}$$

and it goes asymptotically to a constant (1+κ) as $s_\sigma \to \infty$. To satisfy the asymptotic form of eq. (3.10) and also to maintain the form of eq. (3.13) for small s_σ, we choose the following form of $g(s_\sigma)$,

$$g(s_\sigma) = 1 + bs_\sigma \ln(1 + as_\sigma) \tag{3.14}$$

where a and b are (positive) parameters. This function is smooth and simple and has the following properties:

(1) $g(0) = 1$, which preserves the LSDA limit of PBE.

(2) $g(s_\sigma) \to 1 + abs_\sigma^2$ as $s_\sigma \to 0$, which is smooth at $s_\sigma = 0$.

(3) $g(s_\sigma) \to bs_\sigma \ln(as_\sigma)$ as $s_\sigma \to \infty$, which satisfies the asymptotic requirement of eq. (3.10). In particular, the asymptotic form of $v_{\mathrm{x},\sigma}$ in the region where $\rho_\sigma(r) \sim Ae^{-\gamma r}$ is

$$v_{\mathrm{x},\sigma} \sim -\frac{1}{3}C_1C_2\gamma b + 2C_1C_2 b\frac{\ln(C_2\gamma a A^{-1/3}) + 1}{r}; \quad \lim_{r\to\infty} v_{\mathrm{x},\sigma} = -\frac{1}{3}C_1C_2\gamma b > 0. \tag{3.15}$$

where the parameters C_1 and C_2 are defined above.

(4) With appropriate parameters a and b, $g(s_\sigma)$ is close to one for small s_σ, which is necessary to preserve the behavior of PBE in the valence and core regions of finite systems.

Having chosen the functional form, we next need to determine the parameters a and b. One may determine them by analyzing the asymptotic form, eq. (3.15), but we will show later that it is the shape of the potential in the intermediate-r region rather than in the asymptotic region that determines its performance for Rydberg excitations. Therefore, to properly model the potential in regions that are important for electronic excitations, we optimize the parameters against the 11 experimental gas-phase vertical excitation energies (two valence and nine Rydberg) of formaldehyde collected by Caricato *et al.*[29] The calculations were performed with the Tamm-Dancoff approximation[30] to TDDFT[31]

(denoted as TDA-TDDFT) with the xe-PBE0 functional, which combines 75% xe-PBE exchange given by eqs. (3.12)–(3.14) and 25% Hartree-Fock exchange, and the 6-31(2+,2+)G(d,p) basis set.[32] (TDA-TDDFT is used throughout this chapter in favor of full linear-response TDDFT. It has been shown that the performance of TDA-TDDFT is on average very similar to that of full TDDFT, but it is more stable near state intersections, which is a significant advantage when applied to potential energy surfaces for photochemistry.[2]) The optimized parameters (which are unitless) are $a = 0.0035$, $b = 2.0$. The exchange enhancement factor F_x of PBE and xe-PBE is plotted in Figure 3.1. The two curves are very close up to $s_\sigma = 2$ where they start to diverge, with F_x^{PBE} going to a constant $(1+\kappa)$ and $F_x^{\text{xe-PBE}}$ increasing as $(1+\kappa)[1+bs_\sigma \ln(1+as_\sigma)]$. (The enhancement factor of the B88 exchange functional[33] also increases to infinity as $s_\sigma \to \infty$; however, it increases as $\sim(s_\sigma/\ln s_\sigma)$, which is much slower than xe-PBE and, unlike xe-PBE, it still leads to an exchange potential that vanishes at $r \to \infty$. Furthermore it is not designed to increase in the region important for Rydberg orbitals while having a negligible effect on the region important for valence orbitals.)

Next we will analyze the behavior and test the performance of xe-PBE0 with the optimized parameters. Although we optimized the functional against the excitation energies of formaldehyde, we will test it on datasets of various molecular and atomic excitation energies. In this way we can examine the generality of the functional form and the transferability of the parameters. We will also test xe-PBE0 on a dataset of atomization energies to show that the XELG scheme applied to PBE0 does not compromise its performance on ground-state energetics. This is critical for the modeling of potential energy surfaces.

3.3. COMPUTATIONAL DETAILS

All ground- and excited-state calculations were performed with standard KS-DFT and TDA-TDDFT, using a locally modified version of the GAMESS[34] electronic structure package.

For the first test on the Be atom, the aug-cc-pVQZ[35,36] basis set was used. To produce the plots of the reduced spin density gradient s_σ and of the local exchange potential $v_{x,\sigma}$ of PBE and xe-PBE, the quantities were computed by substituting the spin density and its gradient, given by PBE0 for s_σ and $v_{x,\sigma}^{PBE}$ and by xe-PBE0 for $v_{x,\sigma}^{xe\text{-}PBE}$, into the analytic expressions of s_σ and $v_{x,\sigma}$. (The difference of the self-consistent-field densities given by PBE0 and xe-PBE0 is very small.)

For the second test on molecular and atomic excitation energies, two large databases were used: (1) the MEE69 database containing 69 molecular excitation energies (30 valence, 39 Rydberg) of 11 organic molecules (acetaldehyde, acetone, ethylene, formaldehyde, isobutene, pyrazine, pyridazine, pyridine, pyrimidine, s-tetrazine, t-butadiene) as used in refs. 15, 26, and 29; (2) the AEE24 database containing 24 atomic excitation energies (eight valence, 16 Rydberg) of six atoms and atomic cations (Be, B^+, Ne, Na^+, Mg, Al^+) as used in refs. 15 and 47. All molecular excitation energies were computed by TDA-TDDFT on geometries taken from ref. 26. The basis set used for the organic molecules is 6-31(2+,2+)G(d,p).[32] The basis sets used for the atoms and atomic cations are: aug-cc-pVQZ[35,36] for Be and B^+, d-aug-cc-pVQZ[35,36] for Ne, aug-cc-pCVQZ[37] for Na^+, and aug-cc-pV(Q+d)Z[35,36,38] for Mg and Al^+. These diffuse basis sets are suitable for describing the low-lying Rydberg excitations as well as the valence ones. The tested functionals are PBE0 and xe-PBE0 as well as two local GGAs (PBE, BLYP[33,39]), one global hybrid GGA (B3LYP[40]), four range-separated hybrid GGAs [CAM-B3LYP,[41] LC-BLYP ($\mu = 0.33$),[10,33,39] LC-BOP ($\mu = 0.33$),[10,33,42] LC-BOP ($\mu = 0.47$),[10,33,42,43] where μ is the parameter in the LC scheme that controls range separation], and two hybrid meta-GGAs (M06, M06-2X[44,45]).

For the third test on atomization energies, a database called AE6/11 was used, which is a representative subset of the MGAE109/11 database[46] and which contains the atomization energies of six small molecules [SiH_4, S_2, SiO (multiplicity = 1), C_3H_4 (propyne), HCOCOH, C_4H_8 (cyclobutane)]. The KS-DFT calculations were carried out with the aug-cc-pV(T+d)Z basis set.[35,36,38]

3.4. RESULTS AND DISCUSSION

Test case 1: Be atom. As the first test, we apply DFT and TDA-TDDFT with xe-PBE0 to a simple but very interesting system, namely the Be atom, and compare to standard PBE0 to investigate the effect of XELG. The orbital energies given by DFT and excitation energies given by TDA-TDDFT are collected in Tables 3.1 and 3.2 respectively. Table 3.1 shows that from PBE0 to xe-PBE0 the energies of the core (2s) and valence orbitals (2s and 2p) change by a few hundredths of an eV while the energy of the 3s Rydberg orbital increases by 0.72 eV. As a result, Table 3.2 shows that the valence excitation energies given by PBE0 and xe-PBE0 differ by less than 0.05 eV while xe-PBE0 improves the Rydberg excitations by 0.2–0.3 eV. Although the performance of xe-PBE0 here on Be is not very satisfactory, it is not surprising because the xe functional is optimized against an organic molecule, and previous tests have shown that atomic excitations are more difficult for TDDFT than excitations of organic molecules.[26,47] Nevertheless, molecular excitations are more important in practical applications, and we will show later that xe-PBE0 performs very well on molecular excitations. The important message here is that we have achieved our goal: improving Rydberg excitations without sacrificing the accuracy of valence excitations.

To gain more insight into how the scheme works, we plot in Figure 3.2 the reduced spin density gradient s_σ and the exchange potential $v_{\mathrm{x},\sigma}$ generated by PBE and xe-PBE for the Be atom as a function of the distance from the nucleus. Note that s_σ is small in the core and valence regions and starts to grow rapidly after $r \cong 5$ bohr. Accordingly, the shape of $v_{\mathrm{x},\sigma}^{\text{xe-PBE}}$ matches that of $v_{\mathrm{x},\sigma}^{\text{PBE}}$ in the core and valence regions whereas in the Rydberg region $v_{\mathrm{x},\sigma}^{\text{xe-PBE}}$ keeps increasing to positive values, as expected. Such rise of the exchange potential causes the rise of the Rydberg orbital energies and improves the calculated Rydberg excitation energies.

Figure 3.2 plots s_σ and $v_{\mathrm{x},\sigma}$ only up to $r = 20$ bohr. As $r \to \infty$, however, the current calculation does not generate an exchange potential that has the correct asymptotic

behavior due to the use of Gaussian basis set for molecular orbitals. A finite number of Gaussian basis functions, which behave as e^{-r^2}, cannot describe the e^{-r} tail of the density all the way out to infinite separation. The $r\to\infty$ tail of the calculated density is dominated by the most diffuse basis function and behaves as e^{-r^2}. In fact, the limitation of the basis set is already obvious in Figure 3.2. Figure 3.2(a) is a plot of $v_{\mathrm{x},\sigma}$ versus s_σ in logarithmic scale; if s_σ has the correct exponentially increasing asymptotic behavior as eq. (3.8) shows, the plot should be a straight line in the asymptotic region. This is indeed (approximately) the case in the range of $r \sim 4$–10 bohr, in which the $v_{\mathrm{x},\sigma}^{\text{xe-PBE}}$ plotted in Figure 3.2(b) is also well behaved. However, beyond this region, ln s_σ has an unphysical deviation from linearity with r, and correspondingly the $v_{\mathrm{x},\sigma}^{\text{xe-PBE}}$ plotted in Figure 3.2(b) also has an unphysical fluctuation. To properly describe the large-r region one needs to use a better and more diffuse Gaussian basis set or a Slater-type basis set. Nonetheless, we do not regard this as a serious drawback of the XELG scheme because such large-r regions are irrelevant for most electronic states of chemical interest, and in the case that it is relevant one can improve the behavior by improving the basis set.

Test case 2: molecular and atomic excitation energies. In this subsection we test the performance of our xe-PBE0 functional on the MEE69 and AEE24 databases of excitation energies. Table 3.3 summarizes the mean signed error (MSE) and mean unsigned error (MUE) of the MEE69 molecular excitation energies, as compared to reference values. There are several interesting messages in this table. PBE0, B3LYP, and M06, which are global hybrid functionals with low Hartree-Fock exchange (25%, 20%, and 27%, respectively), are quite good for valence excitations but underestimate Rydberg excitations. M06-2X, a global hybrid meta-GGA with high percentage of Hartree-Fock exchange (54%), and LC-BOP (μ = 0.33), LC-BLYP (μ=0.33), and CAM-B3LYP, which are three range-separated GGAs, are good for Rydberg excitations but not as good for valence excitations. LC-BOP (μ = 0.47), whose parameter μ was re-optimized[43] against atomization energies and which was shown to give better geometries, barrier heights, and

reaction enthalpies,[43] is inaccurate for both valence and Rydberg excitations. Comparing the results for the two LC-BOP functionals demonstrates the difficulty of simultaneously predicting accurate values for ground-state properties, valence excitations, and Rydberg excitations with DFT and TDDFT and a single functional. In terms of orbitals, the ground-state properties involve only occupied orbitals, while valence and Rydberg excitations involve also valence and Rydberg virtual orbitals. In a sense the problem is the difficulty of properly describing all of those orbitals.[6]

Turning back to Table 3.3, we see that xe-PBE0 has a balanced performance for valence and Rydberg excitations. Compared to PBE0, the error for the valence excitations slightly increases by only 0.03 eV, but the error for the Rydberg excitations is reduced by 0.23 eV. We have achieved this by improving the Rydberg virtual orbitals while maintaining the reasonably good description of occupied and valence virtual orbitals provided by PBE0.

The errors in the atomic excitation energies of the AEE24 database are summarized in Table 3.4, which shows that the situation for atoms is rather different. All the tested functionals, including the range-separated functionals, have satisfactory accuracy for the valence excitations but they all severely underestimate the Rydberg excitations. Nonetheless xe-PBE0 still improves the Rydberg excitations over PBE0 by 0.74 eV. Also, if we compare LC-BLYP ($\mu = 0.33$) to BLYP and CAM-B3LYP to B3LYP, we see that the inclusion of more Hartree-Fock exchange for long electron-electron distances by the range separation scheme improves the Rydberg excitations but by only a relatively small amount. The reason why neither the range separation nor our XELG scheme improves the Rydberg excitations to a satisfactory extent seems to be that the atomic Rydberg excitations are less diffuse than the molecular ones, i.e. the Rydberg orbitals are closer to the valence region in space. Therefore, with the range separation scheme the electron-electron distance is not large enough to include enough Hartree-Fock exchange; with the XELG scheme the reduced spin density gradient is not large enough for the XELG factor to take effect. On the other hand, to obtain good atomic excitations, if the Hartree-Fock exchange rises too rapidly with r in the range separation scheme or if the XELG factor

rises too rapidly with s_σ in the XELG scheme, the valence properties may be compromised. We did re-optimize our xe-PBE0 against some atomic excitation energies, but as expected the functional is worse for molecular excitations, so we retain the optimization against formaldehyde as our standard set of parameters.

The difficulty of calculating accurate Rydberg energies for atoms with a scheme that also yields accurate results for molecules poses a great challenge for conventional TDDFT. Xu *et al.*[47] showed that spin-flip TDDFT,[48,49] when carried out noncollinearly, is able to obtain good atomic excitation energies, but the proper way to carry out the calculation can be complicated and it has not been systematically tested on molecular excitations. Nevertheless, molecular excitations are of more interest in practical applications than atomic excitations (because essentially all atomic excitation energies of interest are already known from old experiments), and we will not pursue atomic excitations further in this chapter.

Test case 3: atomization energies. Next we confirm that xe-PBE0 does not spoil the ground-state properties by testing it on the AE6/11 database of atomization energies and comparing the results to PBE0. Table 3.5 compares the unsigned error per bond for each molecule given by PBE0 and xe-PBE0. The mean unsigned error of xe-PBE0 is 0.46 kcal/mol larger than that of PBE0, which is acceptable. The XELG method increases the exchange energy density in all regions of a system. The increase is small in the core and valence regions where there is substantial amount of electron density, and it is not small in the Rydberg and asymptotic regions where the electron density is exponentially small; accordingly the increase of exchange energy at a point (which equals electron density times the increase of exchange energy density) in any region of space is expected to be small. However, the integration of exchange energy per point over the whole space does contribute a non-negligible amount of additional exchange energy to the system, and therefore the total exchange energy of each atom and molecule is more negative. When atomization energy is computed, however, such additional exchange energy of the molecule and of the atoms cancels to a large extent, bringing on an additional mean unsigned error of less than 0.5 kcal/mol. If one were to re-optimize the GGA in the

presence of the XELG exchange enhancement factor, the small averaged increase in the magnitude of the error in atomization energies could be mitigated.

3.5. FURTHER DISCUSSION AND CONCLUDING REMARKS

We have demonstrated that xe-PBE0 improves the Rydberg excitations by upshifting the Rydberg orbital energies. Although the design of the XELG factor $g(s_\sigma)$ in eq. (3.12) makes use of the asymptotic analysis with the aim to raise the $s_\sigma \to \infty$ asymptote of $g(s_\sigma)$ to a positive constant, we observe that the good performance for Rydberg states is attributed to the better modeling of the potential in the middle-r region (e.g. ~5–10 bohr for Be in Figure 3.2(b)) rather than of the asymptote. This was confirmed by optimizing another form of $g(s_\sigma)$ that has different asymptotic behavior but has equally good performance for Rydberg states. This observation provides more flexibility in choosing the functional form of $g(s_\sigma)$ for optimizing future density functionals. We also remind the readers that, despite the rather good overall performance of xe-PBE0 given in this work, the parameters in $g(s_\sigma)$ are optimized against the excitation energies of only one molecule. Optimization against more molecular excitation data may lead to more balanced modeling of the region of the potential relevant to more diverse excitations.

As an alternative to doing TDA-xe-PBE0 with xe-PBE0 orbitals as we did in this work, one could carry out TDA-PBE0 calculations with xe-PBE0 orbitals. This can yield similar results to the xe-PBE0 method presented here, but the optimal parameters are different. However, we do not advocate this because the advantage of the xe-PBE0 method presented here is that everything is done in a standard way; we have simply improved the xc functional. Nevertheless this is one more way of showing that the essence of the present approach is that we have improved the Rydberg orbitals.

An important point worth emphasizing is that the XELG scheme accomplishes its objective by changing the exchange-correlation functional in such a way as to improve the asymptotic potential. We accomplished this by improving the xc functional instead of directly manipulating the xc potential. The strategy employed here should be distinguished from methods that attempt to minimize the self-interaction error by means

of Hartree-Fock exchange, for example, by using global or range-separated hybrid functionals. The distinction can be readily understood by the fact that, with XELG, the energies of the core and valence orbitals barely change compared to the standard gradient-approximation functional that is being improved. Nevertheless, the Rydberg orbitals are improved in the sense that they are more compatible with the valence orbitals and the orbital energy *gaps* are more reasonable, although all orbital energies are less negative or more positive than those generated by the exact xc potential. The excitation energies are improved because it is the orbital energy gaps instead of the individual orbital energies that are relevant in the TDDFT calculations.

Another class of problematic cases for TDDFT that are of broad interest is charge-transfer excitations. We have not discussed this class in the present work because this problem has other sources.[2,50] It is not to be remedied by better modeling of only the xc potential and is thus beyond the scope of the present work.

To summarize, we propose a scheme, called exchange-enhancement-for-large-gradient (XELG), that improves the description of TDDFT with GGA functionals for Rydberg excitations, with only minor influence on the accuracy for valence excitations and ground-state energetics. The improved performance for Rydberg states is achieved by enhancing the exchange energy for large reduced spin density gradient, giving rise to an upshift of the exchange potential in the Rydberg region, which in turn raises the Rydberg orbital energies. The first application of the scheme to the PBE0 functional shows encouraging results. The scheme also has the merits that it is simple, it can be easily implemented in any DFT and TDDFT code, it provides size-extensive energetics (since it generates nothing more than a GGA), it is flexible as regards the choice of the functional to be corrected, and there is flexibility in choosing the form of the XELG factor $g(s_\sigma)$. A possible drawback is the difficulty to precisely control the potential by controlling the functional since the relation between them is complicated; more exploration would be required to fully achieve the potential of the scheme. Nevertheless the scheme offers a new and general strategy to develop better density functionals for Rydberg excitations,

which is very important for the application of TDDFT to the modeling of spectroscopy and photochemistry.

Table 3.1. Orbital energies of Be (in eV) calculated by DFT with the PBE0 and xe-PBE0 functionals.

	1s (core)	2s (HOMO)	2p (LUMO)	3s (Rydberg)
PBE0	-111.92	-6.49	-1.22	0.32
xe-PBE0	-111.99	-6.50	-1.19	1.04

Table 3.2. Excitation energies of Be (in eV) from experiment and calculated by TDA-TDDFT with the PBE0 and xe-PBE0 functionals.

	T_1 (2s2p) (valence)	S_1 (2s2p) (valence)	T_2 (2s3s) (Rydberg)	S_2 (2s3s) (Rydberg)
exp.[a]	2.73	5.28	6.46	6.78
PBE0	2.29	5.20	5.72	6.09
xe-PBE0	2.28	5.24	5.95	6.39

[a] ref. 47.

Table 3.3. Mean signed errors (MSE) and mean unsigned errors (MUE) over the MEE69 database as calculated by TDA-TDDFT. [a]

	MSE (eV)			MUE (eV)		
xc functional	valence	Rydberg	all	valence	Rydberg	all
LC-BOP (μ = 0.33)	0.32	-0.13	0.07	0.40	0.21	0.29
LC-BLYP (μ = 0.33)	0.15	-0.17	-0.03	0.43	0.24	0.32
xe-PBE0	0.25	0.14	0.19	0.33	0.36	0.35
CAM-B3LYP	0.35	-0.23	0.02	0.41	0.31	0.35
M06-2X	0.36	-0.17	0.06	0.45	0.29	0.36
PBE0	0.21	-0.57	-0.23	0.30	0.59	0.46
LC-BOP (μ = 0.47)	0.61	0.51	0.55	0.64	0.51	0.56
B3LYP	0.09	-0.85	-0.44	0.25	0.86	0.59
M06	-0.10	-1.28	-0.77	0.27	1.28	0.84
PBE	-0.38	-1.36	-0.93	0.47	1.36	0.97
BLYP	-0.41	-1.54	-1.05	0.48	1.54	1.08

[a] The functionals are listed in order of increasing overall MUE.

Table 3.4. Mean signed errors (MSE) and mean unsigned errors (MUE) over the AEE24 database as calculated by TDA-TDDFT.[a]

	MSE (eV)			MUE (eV)		
xc functional	valence	Rydberg	all	valence	Rydberg	all
xe-PBE0	-0.20	-0.86	-0.64	0.25	0.86	0.66
M06-2X	0.09	-1.21	-0.78	0.27	1.21	0.90
LC-BOP (μ = 0.47)	-0.16	-1.59	-1.11	0.23	1.59	1.13
PBE0	-0.21	-1.60	-1.14	0.25	1.60	1.15
CAM-B3LYP	-0.12	-1.76	-1.21	0.22	1.76	1.25
B3LYP	-0.13	-1.89	-1.30	0.22	1.89	1.33
LC-BOP (μ = 0.33)	-0.09	-2.24	-1.52	0.18	2.24	1.55
LC-BLYP (μ = 0.33)	-0.09	-2.33	-1.58	0.22	2.33	1.62
M06	-0.20	-2.50	-1.73	0.23	2.50	1.75
PBE	-0.16	-2.53	-1.74	0.24	2.53	1.77
BLYP	-0.11	-2.70	-1.84	0.23	2.70	1.88

[a] The functionals are listed in order of increasing overall MUE.

Table 3.5. Unsigned error per bond (in kcal/mol) for the molecules in the AE6/11 database as calculated by DFT with two functionals.

	SiH_4	S_2	SiO	C_3H_4	HCOCOH	C_4H_8	MUE
PBE0	2.44	1.28	5.17	0.25	0.03	0.50	1.61
xe-PBE0	2.89	0.08	6.62	0.79	1.39	0.65	2.07

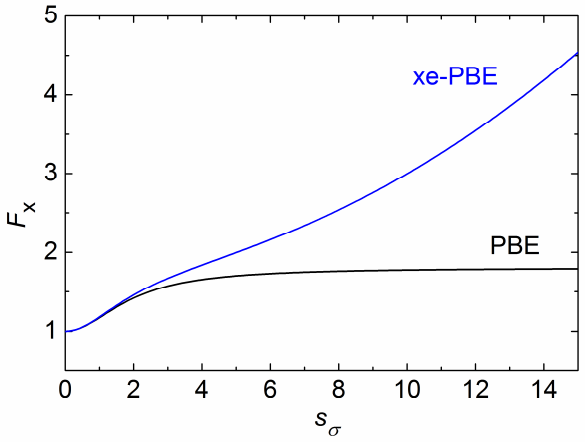

Figure 3.1. Plot of the GGA enhancement factor of PBE and xe-PBE as a function of the reduced spin density gradient.

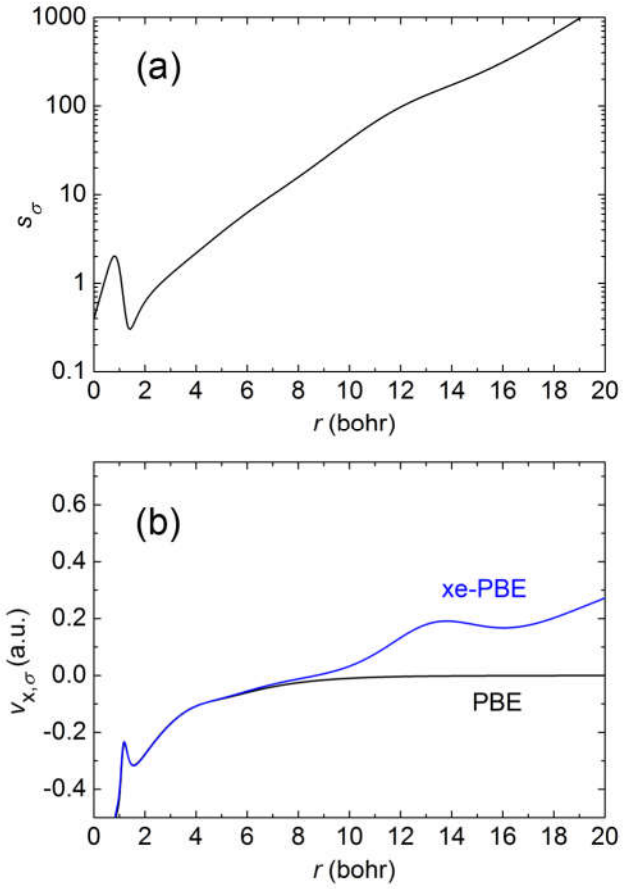

Figure 3.2. Plots of the reduced spin density gradient (a) and the exchange potential (b) of a Be atom as a function of the distance from the nucleus.

REFERENCES FOR CHAPTER 3

[1] Casida, M. E.; Jamorski, C.; Casida, K. C.; Salahub, D. R. Molecular excitation energies to high-lying bound states from time-dependent density-functional response theory: Characterization and correction of the time-dependent local density approximation ionization threshold. *J. Chem. Phys.* **1998,** *108*, 4439-4449.

[2] Casida, M. E.; Huix-Rotllant, M. Progress in Time-Dependent Density-Functional Theory. *Annu. Rev. Phys. Chem.* **2012,** *63*, 287-323.

[3] González, L.; Escudero, D.; Serrano-Andrés, L. Progress and Challenges in the Calculation of Electronic Excited States. *ChemPhysChem* **2012,** *13*, 28-51.

[4] van Meer, R.; Gritsenko, O. V.; Baerends, E. J. Physical Meaning of Virtual Kohn–Sham Orbitals and Orbital Energies: An Ideal Basis for the Description of Molecular Excitations. *J. Chem. Theory Comput.* **2014,** *10*, 4432-4441.

[5] van Leeuwen, R.; Baerends, E. J. Exchange-correlation potential with correct asymptotic behavior. *Phys. Rev. A* **1994,** *49*, 2421-2431.

[6] Tozer, D. J.; Handy, N. C. Improving virtual Kohn–Sham orbitals and eigenvalues: Application to excitation energies and static polarizabilities. *J. Chem. Phys.* **1998,** *109*, 10180-10189.

[7] Kümmel, S.; Kronik, L. Orbital-dependent density functionals: Theory and applications. *Rev. Mod. Phys.* **2008,** *80*, 3-60.

[8] Hirata, S.; Zhan, C.-G.; Aprà, E.; Windus, T. L.; Dixon, D. A. A New, Self-Contained Asymptotic Correction Scheme To Exchange-Correlation Potentials for Time-Dependent Density Functional Theory. *J. Phys. Chem. A* **2003,** *107*, 10154-10158.

[9] Schipper, P. R. T.; Gritsenko, O. V.; van Gisbergen, S. J. A.; Baerends, E. J. Molecular calculations of excitation energies and (hyper)polarizabilities with a statistical average of orbital model exchange-correlation potentials. *J. Chem. Phys.* **2000,** *112*, 1344-1352.

[10] Iikura, H.; Tsuneda, T.; Yanai, T.; Hirao, K. A long-range correction scheme for generalized-gradient-approximation exchange functionals. *J. Chem. Phys.* **2001,** *115*, 3540-3544.

[11] Gaiduk, A. P.; Firaha, D. S.; Staroverov, V. N. Improved Electronic Excitation Energies from Shape-Corrected Semilocal Kohn-Sham Potentials. *Phys. Rev. Lett.* **2012,** *108*, 253005.

[12] Gaiduk, A. P.; Mizzi, D.; Staroverov, V. N. Self-interaction correction scheme for approximate Kohn-Sham potentials. *Phys. Rev. A* **2012,** *86*, 052518.

[13] Gaiduk, A. P.; Staroverov, V. N. How to tell when a model Kohn–Sham potential is not a functional derivative. *J. Chem. Phys.* **2009,** *131*, 044107.

[14] Nguyen K. A.; Day P. N.; Pachter R. The performance and relationship among range-separated schemes for density functional theory. *J. Chem. Phys.* **2011***, 135*, 074109.

[15] Li, S. L.; Truhlar, D. G. Testing time-dependent density functional theory with depopulated molecular orbitals for predicting electronic excitation energies of valence, Rydberg, and charge-transfer states and potential energies near a conical intersection. *J. Chem. Phys.* **2014,** *141*, 104106.

[16] Tozer, D. J.; Handy, N. C. The development of new exchange-correlation functionals. *J. Chem. Phys.* **1998,** *108*, 2545-2555.

[17] Perdew, J. P.; Parr, R. G.; Levy, M.; Balduz, J. L. Density-Functional Theory for Fractional Particle Number: Derivative Discontinuities of the Energy. *Phys. Rev. Lett.* **1982,** *49*, 1691-1694.

[18] Cohen, A. J.; Mori-Sánchez, P.; Yang, W. Insights into Current Limitations of Density Functional Theory. *Science* **2008,** *321*, 792-794.

[19] Tozer, D. J.; Handy, N. C. On the determination of excitation energies using density functional theory. *Phys. Chem. Chem. Phys.* **2000,** *2*, 2117-2121.

[20] Perdew, J. P.; Yue, W. Accurate and simple density functional for the electronic exchange energy: Generalized gradient approximation. *Phys. Rev. B* **1986***, 33*, 8800-8802.

[21] (a) Dirac, P. A. M. Note on exchange phenomena in the Thomas atom. *Proc. Cambridge Philos. Soc.* **1930,** *26*, 376. (b) Gáspár, R. Über eine Approximation des Hartree-Fockschen Potentials Durch eine Universelle Potentialfunktion. *Acta Phys. Acad. Scientiarum Hungaricae* **1954,** *3*, 263. (c) Gáspár, R. Statistical Exchange for Electron in Shell and the Xα Method. *Acta Phys. Acad. Scientiarum Hungaricae* **1974,** *35*, 213.

[22] Perdew, J. P.; Burke, K.; Ernzerhof, M. Generalized Gradient Approximation Made Simple. *Phys. Rev. Lett.* **1996,** *77*, 3865-3868.

[23] Parr, R. G.; Yang, W. *Density-Functional Theory of Atoms and Molecules*. Oxford University Press: New York, 1989.

[24] Engel, E.; Chevary, J. A.; Macdonald, L. D.; Vosko, S. H. Asymptotic properties of the exchange energy density and the exchange potential of finite systems: relevance for generalized gradient approximations. *Z Phys D - Atoms, Molecules and Clusters* **1992,** *23*, 7-14.

[25] Adamo, C.; Barone, V. Toward reliable density functional methods without adjustable parameters: The PBE0 model. *J. Chem. Phys.* **1999,** *110*, 6158-6170.

[26] Isegawa, M.; Peverati, R.; Truhlar, D. G. Performance of recent and high-performance approximate density functionals for time-dependent density functional theory calculations of valence and Rydberg electronic transition energies. *J. Chem. Phys.* **2012,** *137*, 244104.

[27] Jacquemin, D.; Planchat, A.; Adamo, C.; Mennucci, B. TD-DFT assessment of functionals for optical 0-0 transitions in solvated dyes. *J. Chem. Theory Comput*. **2012**, *8*, 2359-2372.

[28] Charaf-Eddin, A.; Planchat, A.; Mennucci, B.; Adamo, C.; Jacquemin, D. Choosing a functional for computing absorption and fluorescence band shapes with TD-DFT. *J. Chem. Theory Comput*. **2013**, *9*, 2749-2760.

[29] Caricato, M.; Trucks, G. W.; Frisch, M. J.; Wiberg, K. B. Electronic Transition Energies: A Study of the Performance of a Large Range of Single Reference Density Functional and Wave Function Methods on Valence and Rydberg States Compared to Experiment. *J. Chem. Theory Comput.* **2010,** *6*, 370-383.

[30] (a) Tamm, I. Relativistic interaction of elementary particles. *J. Phys. (Moscow)* **1945,** *9*, 449-460. (b) Dancoff, S. M. Non-adiabatic meson theory of nuclear forces. *Phys. Rev.* **1950,** *78*, 382-385.

[31] Hirata, S.; Head-Gordon, M. Time-dependent density functional theory within the Tamm–Dancoff approximation. *Chem. Phys. Lett.* **1999,** *314*, 291-299.

[32] (a) Hehre, W. J.; Ditchfield, R.; Pople, J. A. Self---Consistent Molecular Orbital Methods. XII. Further Extensions of Gaussian---Type Basis Sets for Use in Molecular Orbital Studies of Organic Molecules. *J. Chem. Phys.* **1972,** *56*, 2257-2261. (b) Hariharan, P. C.; Pople, J. A. The influence of polarization functions on molecular orbital hydrogenation energies. *Theoret. Chim. Acta* **1973,** *28*, 213-222. (c) Clark, T.; Chandrasekhar, J.; Spitznagel, G. W.; Schleyer, P. V. R. Efficient diffuse function-augmented basis sets for anion calculations. III. The 3-21+G basis set for first-row elements, Li–F. *J. Comput. Chem.* **1983,** *4*, 294-301. (d) Wiberg, K. B.; de Oliveira, A. E.; Trucks, G. A comparison of the electronic transition energies for ethene, isobutene, formaldehyde, and acetone calculated using RPA, TDDFT, and EOM-CCSD. Effect of basis sets. *J. Phys. Chem. A* **2002,** *106*, 4192-4199.

[33] Becke, A. D. Density-functional exchange-energy approximation with correct asymptotic behavior. *Phys. Rev. A* **1988,** *38*, 3098-3100.

[34] (a) Schmidt, M. W.; Baldridge, K. K.; Boatz, J. A.; Elbert, S. T.; Gordon, M. S.; Jensen, J. H.; Koseki, S.; Matsunaga, N.; Nguyen, K. A.; Su, S. J.; Windus, T. L.; Dupuis, M.; Montgomery, J. A. General Atomic and Molecular Electronic-Structure System. *J. Comput. Chem.* **1993,** *14*, 1347-1363. (b) Gordon, M. S.; Schmidt, M. W. Advances in electronic structure theory: GAMESS a decade later. In *Theory and Applications of Computational Chemistry: The First Forty Years*, Dykstra, C. E.; Frenking, G.; Kim, K. S.; Scuseria, G. E., Eds. 2005; pp 1167-1189.

[35] Dunning, T. H. Gaussian basis sets for use in correlated molecular calculations. I. The atoms boron through neon and hydrogen. *J. Chem. Phys.* **1989,** *90*, 1007-1023.

[36] Woon, D. E.; Dunning, T. H. Gaussian basis sets for use in correlated molecular calculations. III. The atoms aluminum through argon. *J. Chem. Phys.* **1993,** *98*, 1358-1371.

[37] https://bse.pnl.gov/bse/portal (accessed Mar. 24, 2014).

[38] Dunning, T. H.; Peterson, K. A.; Wilson, A. K. Gaussian basis sets for use in correlated molecular calculations. X. The atoms aluminum through argon revisited. *J. Chem. Phys.* **2001,** *114*, 9244-9253.

[39] Lee, C. T.; Yang, W. T.; Parr, R. G. Development of the Colle-Salvetti correlation-energy formula into a functional of the electron-density. *Phys. Rev. B* **1988,** *37*, 785-789.

[40] Stephens, P. J.; Devlin, F. J.; Chabalowski, C. F.; Frisch, M. J. Ab Initio Calculation of Vibrational Absorption and Circular Dichroism Spectra Using Density Functional Force Fields. *J. Phys. Chem.* **1994,** *98*, 11623-11627.

[41] Yanai, T.; Tew, D. P.; Handy, N. C. A new hybrid exchange–correlation functional using the Coulomb-attenuating method (CAM-B3LYP). *Chem. Phys. Lett.* **2004,** *393*, 51-57.

[42] Tsuneda, T.; Suzumura, T.; Hirao, K. A new one-parameter progressive Colle–Salvetti-type correlation functional. *J. Chem. Phys.* **1999,** *110*, 10664-10678.

[43] Song, J.-W.; Hirosawa, T.; Tsuneda, T.; Hirao, K. Long-range corrected density functional calculations of chemical reactions: Redetermination of parameter. *J. Chem. Phys.* **2007,** *126*, 154105.

[44] Zhao, Y.; Truhlar, D. G. The M06 suite of density functionals for main group thermochemistry, thermochemical kinetics, noncovalent interactions, excited states, and transition elements: two new functionals and systematic testing of four M06-class functionals and 12 other functionals. *Theor. Chem. Acc.* **2008,** *120*, 215-241.

[45] Zhao, Y.; Truhlar, D. G. Density Functionals with Broad Applicability in Chemistry. *Acc. Chem. Res.* **2008,** *41*, 157-167.

[46] (a) Peverati, R.; Truhlar, D. G. Communication: A global hybrid generalized gradient approximation to the exchange-correlation functional that satisfies the second-order density-gradient constraint and has broad applicability in chemistry. *J. Chem. Phys.* **2011,** *135*, 191102. (b) http://comp.chem.umn.edu/db/dbs/mgae109.html (accessed April 12, 2015.)

[47] Xu, X.; Yang, K. R.; Truhlar, D. G. Testing Noncollinear Spin-Flip, Collinear Spin-Flip, and Conventional Time-Dependent Density Functional Theory for Predicting Electronic Excitation Energies of Closed-Shell Atoms. *J. Chem. Theory Comput.* **2014,** *10*, 2070-2084.

[48] Shao, Y.; Head-Gordon, M.; Krylov, A. I. The spin–flip approach within time-dependent density functional theory: Theory and applications to diradicals. *J. Chem. Phys.* **2003,** *118*, 4807-4818.

[49] (a) Wang, F.; Ziegler, T. Time-dependent density functional theory based on a noncollinear formulation of the exchange-correlation potential. *J. Chem. Phys.* **2004,** *121*, 12191-12196. (b) Wang, F.; Ziegler, T. The performance of time-dependent density functional theory based on a noncollinear exchange-correlation potential in the calculations of excitation energies. *J. Chem. Phys.* **2005,** *122*, 074109. (c) Wang, F.; Ziegler, T. Use of noncollinear exchange-correlation potentials in multiplet resolutions by time-dependent density functional theory. *Int. J. Quantum Chem.* **2006,** *106*, 2545-2550.

[50] Dreuw, A.; Weisman, J. L.; Head-Gordon, M. Long-range charge-transfer excited states in time-dependent density functional theory require non-local exchange. *J. Chem. Phys.* **2003,** *119*, 2943-2946.

Chapter 4. Model Space Diabatization for Quantum Photochemistry

4.1. INTRODUCTION

The Born-Oppenheimer approximation decouples the motion of electrons from that of nuclei in molecular systems, and this leads to the concepts of adiabatic electronic states and potential energy surfaces (PESs). The adiabatic electronic states and their energies are calculated with fixed nuclear positions, and the nuclei move in the potential created by the electrons in a single electronically adiabatic state. This approximation is valid when the electronic states are separated by a large energy gap but breaks down near intersections or avoided crossings where two or more electronic states become close in energy and are consequently closely coupled.[1,2,3] In this case the coupling of electronic states by the nuclear momentum vector operators cannot be neglected, and more than one adiabatic electronic state has to be taken into account in the equations of motion for the nuclei. For N atoms the nuclear momentum couplings, often called nonadiabatic couplings, are $3N$-dimensional vectors that are unsmooth near, and singular at, conical intersections, making them cumbersome to use in dynamics simulations. Nevertheless, by changing the electronic basis from the adiabatic states to so-called diabatic states,[4] it is possible to reduce the magnitude of those vector couplings to be negligible for most purposes.

Sometimes the diabatic states are called "quasi-diabatic" while "diabatic" is reserved for the basis in which the vector couplings strictly vanish, but since strict diabatic states do not exist in general,[5] we – as do many others – simply use the term "diabatic" to refer to bases in which the vector couplings are negligible (or neglected) but do not necessarily vanish. In a diabatic basis the electronic states are still coupled by the electronic Hamiltonian operator, and the couplings appear as off-diagonal elements of the electronic Hamiltonian matrix, but these couplings, usually called diabatic couplings, are

smooth scalars that are relatively easy to use in dynamics calculations and are suitable for analytic representations. Therefore diabatic bases are preferable to adiabatic basis for many aspects of dynamics calculations.

Diabatic states are not unique, and many methods have been proposed for obtaining them for specific problems;[4,6,7,8,9,10,11,12,13,14,15,16,17,18,19,20,21,22,23,24,25,26,27,28,29,30,31] for example in some methods this is done by enforcing the smoothness of some molecular properties. Of special interest are methods applicable to electronic structure calculations that add dynamical correlation to multi-configurational self-consistent field (MCSCF)-type wave functions[32,33,34,35,36] since currently these are the most reliable wave function approximations for describing potential energy surfaces of closely coupled electronic states. The present chapter is concerned with quasidegenerate perturbation theory (QDPT) methods in which the final step is the diagonalization of a low-dimensional effective Hamiltonian in a model space where the dimension is the number of adiabatic states of interest. The most popular of such methods[37,38,39.40,41,42] are in principle able to treat several states in a balanced manner and recover a large part of the dynamical correlation with a relatively modest computational cost compared to the more expensive multireference configuration interaction (MRCI) or multireference coupled cluster (MRCC) theories. Examples of such methods are the state-averaged complete active space self-consistent field method (SA-CASSCF) followed by second-order multi-configurational quasi-degenerate perturbation theory (MC-QDPT),[37] extended MC-QDPT (XMC-QDPT),[38] multi-state complete active space second-order perturbation theory (MS-CASPT2),[39] extended MS-CASPT2 (XMS-CASPT2),[42] and quasi-degenerate second-order *n*-electron valence state perturbation theory (QD-NEVPT2).[40]

The fourfold way[18,19,21,29] is a diabatization method that enforces the smoothness of wave functions by first constructing diabatic molecular orbitals (DMOs) by a threefold density criterion and a sometimes employed fourth criterion based on reference orbitals and then applying a configurational uniformity step originally proposed by Atchity and Ruedenberg.[13,15] The fourfold way was developed to have general applicability to diverse types of electronic states and electronic excitation problems. It was formulated in the

context of SA-CASSCF and MC-QDPT, but it is straightforwardly extended to the other QDPT methods mentioned in the previous paragraph. However, as currently formulated, the fourfold way with any of these QDPT theories evaluates second-order perturbation energies in the DMO basis. Although it is possible to formulate QDPT in a way that is invariant to certain transformations of orbitals (see, for example, ref. 38 for the case of XMC-QDPT), such a reformulation is computationally inefficient and is not implemented in electronic structure packages. In the original paper on applying the fourfold way with MC-QDPT[19] we pointed out the dependence of MC-QDPT energies on orbital rotations, and we resolved the ambiguity by defining the adiabatic energies as those calculated using the DMOs rather than the canonical molecular orbitals (CMOs). In the original work and subsequent work[43,44,45,46,47,48,49] we found, when we checked, only small differences between the two sets of adiabatic energies; however, for a current application to thioanisole we found differences of up to 0.8 eV when using DMOs obtained by the fourfold way and up to 0.05 eV when using DMOs obtained by the threefold way. Therefore, we developed the scheme presented here to give a diabatic potential energy matrix that, when diagonalized, gives precisely the adiabatic energies of standard QDPT with CMOs.

The diabatization strategy for MC-QDPT and XMC-QDPT (denoted collectively as (X)MC-QDPT) developed here is called model space diabatization (MSD). It utilizes information from an initial CASSCF-level diabatization and a standard QDPT calculation to perform a final diabatization at the QDPT level. In this chapter we will use the fourfold-way diabatization at the CASSCF level and the XMC-QDPT method to demonstrate the strategy, but by construction MSD can also be applied with other diabatization schemes[50] or other MCSCF-type wave functions[41] for the initial diabatization step. As will be shown later, the MSD scheme requires that the MCSCF-level diabatization generates diabatic states that span the same space as do the MCSCF adiabatic states for the subset of states being considered, but its formulation does not involve the details of the MCSCF-level diabatization. All information needed for MSD is already generated by the MCSCF-level diabatization and by standard QDPT calculations,

and the additional calculations only involve elementary matrix algebra like multiplication and transpose, whose computational cost and complexity are negligible compared to the MCSCF and QDPT steps.

To test the new strategy, we choose three challenging test cases, namely the potential energy curves of the ground and excited states of LiH, LiF, and thioanisole. These systems all have state crossings, and are challenging because the positions of the crossings are sensitive to dynamical correlation; thus the crossings occur at quite different places for MCSCF and QDPT. To give the reader an example, Figure 4.1 shows the potential energy curves of the three lowest $^1\Sigma^+$ states of LiF as calculated by SA-CASSCF and XMC-QDPT. (The details of the calculations will be given later.) The difference of the positions of the avoided crossings is clear, and this poses the question of whether the new strategy can account for such a shift of state crossings while keeping the potential curves smooth, especially in the intermediate region between the two state crossing locations.

The present chapter is about using model space quantities in certain steps of the generation of diabatic states. As such, it is not about the fourfold way per se. Nevertheless, our examples use the fourfold way, and hence some discussion of the fourfold way is useful as background. Some steps of the fourfold way are automatic, but others are not. The fourfold way produces diabatic molecular orbitals (DMOs, which are smoothly varying), and then the transformation of the usual configuration state functions (CSFs) written in terms of canonical (adiabatic) MOs into orthogonal diabatic CSFs (CSFs written in terms of DMOs) is unique. Next one must specify the diabatic prototype CSFs that produce smooth diabatic states. The choice of diabatic prototypes near the equilibrium geometry usually corresponds to what one would expect on the basis of a valence bond analysis (for example, distinguishing a valence excitation from a charge transfer one) or other conventional way of classifying the character of the states (for example, distinguishing an $n \rightarrow \pi^*$ excitation from a $\pi \rightarrow \pi^*$ one), but every molecule is different and has its own nuances so no general prescription can be given. Ideally one would need only one diabatic prototype per diabatic state, but in

practice, one obtains smoother results if one adds some dominating correlating configurations to the diabatic prototype lists. Once the diabatic prototypes are specified, the method becomes automatic, and it generates orthogonal diabatic state functions. The resulting diabatic states will depend, to some extent on the choice of reference orbitals (if needed) in the fourth term of the DMO generation and on the choice of diabatic prototypes in the CSF transformation step, but if the choices made are physically correct, the various results should be qualitatively similar; the lack of uniqueness was already mentioned in an earlier paragraph and is a well known issue in generating diabatic states, i.e., unique diabatic states do not exist because strictly diabatic states do not exist. An instructive analogy is with multiconfiguration self-consistent-field calculations, such as CASSCF and RASSCF. CASSCF results depend quantitatively on the choice of active space, and RASSCF results also depend quantitatively on the restrictions, but in either case — if one makes physical choices — the various results should be qualitatively similar. For a dissociation process, the diabatic states might (but need not) correspond to the lowest energy states at an asymptote. For example, in an alkali hydride or alkali halide, one clearly has a mixture of ionic and covalent states at equilibrium, but the ionic diabatic state might cross several covalent states between equilibrium and dissociation. In some experiments, the actual production of ionic dissociated states might be energetic forbidden, but a diabatic treatment of the photodissociation to produce various neutral excited states will nevertheless require one to have an ionic state included in the diabatic state list.

The present chapter uses example of conical intersections where two adiabatic states intersect. In general, one expects that there are also points of confluence of three or more potential energy surfaces.[1] Although the method presented here would be expected to be valid also for such cases, we limit explicit discussion to the intersection of just two states.

The rest of the chapter is organized as follows. In Sections 4.2.1 and 4.2.2 we will review the fourfold-way diabatization and the relevant theoretical aspects of (X)MC-QDPT (the differences between MC-QDPT and XMC-QDPT have no effect on the

procedures, so we can discuss them both at the same time). Section 4.2.3 then introduces the MSD strategy and the detailed algorithm for calculations. Section 4.3 presents the computational details of three test cases, namely LiH, LiF, and thioanisole, and Section 4.4 presents the results and discussion. Section 4.5 gives a summary.

4.2. THEORY

4.2.1. Review of the fourfold way

The fourfold way[18,19,21,29] is a general diabatization scheme based on configurational uniformity that generates diabatic states spanning the same model space as the selected adiabatic states; the diabatic states and the adiabatic states are related by an orthogonal transformation. The fourfold way was first formulated at the CASSCF level[18] and then extended to the MC-QDPT level[19] and to include spin-orbit coupling.[45] At the MC-QDPT level, it can be used with diabatic molecular orbitals obtained at either the MC-QDPT level[19] or the CASSCF level.[29] It has been successfully applied to a variety of systems at both the CASSCF and MC-QDPT levels.[43,44,45,46,47,48,49] However, as mentioned in the Introduction, for some cases the original fourfold way at the MC-QDPT level may give results that are quite different from the standard MC-QDPT method. These problematic cases are the motivation for developing the present MSD strategy.

The fourfold way generates diabatic states that are smooth and retain their valence character for all molecular geometries of interest; it accomplishes this by means of configurational uniformity. In particular, the "valence character" of a diabatic state is determined by a group of configuration state functions (CSFs) called diabatic prototypes of which at least one is dominant at each molecular geometry of interest, with the requirement that the diabatic prototype groups corresponding to different diabatic states cannot have any CSFs in common. For the many-electron CSFs to be smooth functions of geometry, they must be expressed in terms of smooth one-electron molecular orbitals (MOs), but the canonical MOs (CMOs) generated by SA-CASSCF or indeed by any variational procedure often change character due to avoided crossings and so are not suitable for this purpose. The first step of the fourfold-way diabatization is therefore to

generate smooth MOs, which are called diabatic MOs (DMOs). We next review the procedure for obtaining DMOs from SA-CASSCF wave functions.

In the inactive and external orbital spaces, the DMOs are identical to CMOs since these orbitals are doubly occupied or unoccupied in all the "internal" CSFs (CSFs generated by distributing all active electrons in all active orbitals in all possible ways, from which the CASSCF wave functions are constituted) and thus inconsequential in characterizing the internal CSFs. In the active orbital space the DMOs are obtained by an orthogonal transformation of the CMOs that satisfies the "threefold density criterion" and, if needed, the "maximum overlap of reference MOs" (MORMO) criterion.

The threefold density criterion is to maximize the following functional of the orbitals,

$$D_3 = \alpha_{\mathrm{N}} D^{\mathrm{NO}} + \alpha_{\mathrm{R}} D^{\mathrm{ON}} + \alpha_{\mathrm{T}} D^{\mathrm{TD}} \tag{4.1}$$

where D^{NO}, called the natural orbital term, measures how close the MOs are to state-averaged natural orbitals; D^{ON}, called the occupation number term, is the sum of the diagonal elements of the one-particle density matrix of all the states; and D^{TD}, called the transition density term, is related to the transition density matrix. The D_3 functional is the weighted average of these three functionals of the orbitals with the weights usually taken as $\alpha_{\mathrm{N}} = 2$, $\alpha_{\mathrm{R}} = 1$, and $\alpha_{\mathrm{T}} = 0$ to 0.5. The threefold density criterion with these particular weights is shown[18] to generate satisfactory DMOs in many situations, but there are difficult cases that require an additional criterion, the MORMO criterion. The reference orbitals for the MORMO criterion can be obtained in two ways. One way is to choose a reference geometry at which the adiabatic states are already approximately equal to the desired diabatic states and use the threefold density criterion to obtain preliminary DMOs, from which a subset of λ DMOs are chosen as reference orbitals. Another way is to use appropriately modified CMOs at a reference geometry, where the modification would typically be to drop some components on all but one center. At any geometry other than the reference geometry, λ DMOs are constructed by maximizing a

functional related to a generalized "overlap" with the reference DMOs. The rest of DMOs are constructed by the threefold density criterion.

After the DMOs are generated, complete active space configuration interaction (CAS-CI) calculations are carried out in the DMO basis. These calculations give the same wave functions and energies as CASSCF calculations in the CMO basis. Dominant CSFs for each state are identified at one or several key geometries and are grouped into diabatic prototype groups. Finally, diabatic states at the CASSCF level are constructed by maximizing the preponderance of one of the CSFs in each of the diabatic prototype groups in one or another of the diabatic CSFs. For diabatization at the MC-QDPT level, one performs MC-QDPT calculations in the DMO basis (either the CASSCF DMO basis or a new DMO basis determined at the MC-QDPT level) and diabatizes the MC-QDPT wave functions in the same manner.

In this chapter, the calculations of fourfold way diabatization at the XMC-QDPT level use only the CASSCF DMO basis since this basis gives smoother diabatic potentials.[29]

4.2.2. Analysis of the (X)MC-QDPT wave functions

In this chapter we use Granovsky's XMC-QDPT,[38] which is an extension of Nakano's original MC-QDPT.[37] The XMC-QDPT and MC-QDPT differ in the choice of the zero-order Hamiltonian. Granovsky showed that XMC-QDPT gives smoother potential energy surfaces than MC-QDPT. However, the choice of zero-order Hamiltonian is irrelevant to the construction and analysis of our MSD strategy, and hence we outline here only the relevant theoretical framework shared by XMC-QDPT and MC-QDPT (denoted together as (X)MC-QDPT) and give an analysis of the wave functions. For more details, we refer the readers to the original papers.[37,38,51]

In (X)MC-QDPT, the zero-order wave function space is partitioned into three parts: the *P* space including all CASSCF states of immediate interest (also called the model space in this chapter), the *O* space consisting of the other CASSCF states, and the *S* space consisting of CSFs that have excitations out of the active space (known as external CSFs).

The *P* and *O* spaces together form the CAS-CI space (*R* space) spanned by the CSFs with active electrons distributed among the active orbitals (known as internal CSFs). (The *P*, *O*, *S*, and *R* spaces were denoted P_0, P_1, *Q*, and *P*, respectively, in ref. 19.) The *O* and *S* spaces together form the *Q* space complementary to the *P* space. The zero-order wave functions are chosen to be the CASSCF states in the *R* space and the individual external CSFs in the *S* space. The corresponding partitioning of the electronic Hamiltonian matrix in the basis of zero-order wave functions is illustrated in Figure 4.2, following ref. 38.

The (X)MC-QDPT method uses a unitary transformation **G** to block-diagonalize the electronic Hamiltonian **H** in the basis of zero-order wave functions,

$$\mathbf{G}^{-1}\mathbf{H}\mathbf{G} = \tilde{\mathbf{H}} \tag{4.2}$$

Here $\tilde{\mathbf{H}}$ is a block-diagonal matrix whose *PQ* and *QP* blocks are zero; the *QQ* block is not of interest, and the *PP* block is defined as the effective Hamiltonian matrix, $\mathbf{H}^{\text{eff}}$. Upon left-multiplication of both sides of eq. (4.2) by **G**, it can be written as

$$\begin{pmatrix} \mathbf{H}_{PP} & \mathbf{H}_{PQ} \\ \mathbf{H}_{QP} & \mathbf{H}_{QQ} \end{pmatrix}\begin{pmatrix} \mathbf{G}_{PP} & \mathbf{G}_{PQ} \\ \mathbf{G}_{QP} & \mathbf{G}_{QQ} \end{pmatrix} = \begin{pmatrix} \mathbf{G}_{PP} & \mathbf{G}_{PQ} \\ \mathbf{G}_{QP} & \mathbf{G}_{QQ} \end{pmatrix}\begin{pmatrix} \mathbf{H}^{\text{eff}} & \mathbf{0} \\ \mathbf{0} & \tilde{\mathbf{H}}_{QQ} \end{pmatrix} \tag{4.3}$$

where each block is a rectangular matrix. Diagonalization of $\mathbf{H}^{\text{eff}}$ gives eigenvectors and eigenvalues of $\mathbf{H}^{\text{eff}}$ as well as of $\tilde{\mathbf{H}}$. For the *i*-th eigenvector, we have

$$\begin{pmatrix} \mathbf{H}^{\text{eff}} & \mathbf{0} \\ \mathbf{0} & \tilde{\mathbf{H}}_{QQ} \end{pmatrix}\begin{pmatrix} \mathbf{m}_{P,i} \\ \mathbf{0} \end{pmatrix} = \begin{pmatrix} \mathbf{H}^{\text{eff}}\mathbf{m}_{P,i} \\ \mathbf{0} \end{pmatrix} = E_i\begin{pmatrix} \mathbf{m}_{P,i} \\ \mathbf{0} \end{pmatrix} \tag{4.4}$$

where $\mathbf{m}_{P,i}$ is a column vector of the same dimension as the *P* space; $\mathbf{m}_{P,i}$ is an eigenvector of $\mathbf{H}^{\text{eff}}$, and we will call it a "model state"; E_i is the corresponding eigenvalue. By right-multiplying eq. (4.3) by the model state we have

$$\begin{aligned}
&\begin{pmatrix} \mathbf{H}_{PP} & \mathbf{H}_{PQ} \\ \mathbf{H}_{QP} & \mathbf{H}_{QQ} \end{pmatrix}\begin{pmatrix} \mathbf{G}_{PP} & \mathbf{G}_{PQ} \\ \mathbf{G}_{QP} & \mathbf{G}_{QQ} \end{pmatrix}\begin{pmatrix} \mathbf{m}_{P,i} \\ \mathbf{0} \end{pmatrix} \\
&= \begin{pmatrix} \mathbf{G}_{PP} & \mathbf{G}_{PQ} \\ \mathbf{G}_{QP} & \mathbf{G}_{QQ} \end{pmatrix}\begin{pmatrix} \mathbf{H}^{\text{eff}} & \mathbf{0} \\ \mathbf{0} & \tilde{\mathbf{H}}_{QQ} \end{pmatrix}\begin{pmatrix} \mathbf{m}_{P,i} \\ \mathbf{0} \end{pmatrix} \\
&= E_i \begin{pmatrix} \mathbf{G}_{PP} & \mathbf{G}_{PQ} \\ \mathbf{G}_{QP} & \mathbf{G}_{QQ} \end{pmatrix}\begin{pmatrix} \mathbf{m}_{P,i} \\ \mathbf{0} \end{pmatrix}
\end{aligned} \tag{4.5}$$

which yields

$$\begin{pmatrix} \mathbf{H}_{PP} & \mathbf{H}_{PQ} \\ \mathbf{H}_{QP} & \mathbf{H}_{QQ} \end{pmatrix}\begin{pmatrix} \mathbf{G}_{PP}\mathbf{m}_{P,i} \\ \mathbf{G}_{QP}\mathbf{m}_{P,i} \end{pmatrix} = E_i \begin{pmatrix} \mathbf{G}_{PP}\mathbf{m}_{P,i} \\ \mathbf{G}_{QP}\mathbf{m}_{P,i} \end{pmatrix} \tag{4.6}$$

Thus we see that E_i is also an eigenvalue of the Hamiltonian matrix **H** in the chosen (finite) basis of zero-order wave functions. According to eq. (4.6), the eigenvector of the effective Hamiltonian, $\mathbf{m}_{P,i}$, and the (X)MC-QDPT wave function (eigenvector of **H**), ψ_i, are related by

$$\psi_i = \begin{pmatrix} \mathbf{G}_{PP}\mathbf{m}_{P,i} \\ \mathbf{G}_{QP}\mathbf{m}_{P,i} \end{pmatrix} \tag{4.7}$$

Recalling that the *Q* space is composed of *O* and *S* spaces, we can rewrite eq. (4.7) as

$$\psi_i = \begin{pmatrix} \mathbf{G}_{PP}\mathbf{m}_{P,i} \\ \mathbf{G}_{OP}\mathbf{m}_{P,i} \\ \mathbf{G}_{SP}\mathbf{m}_{P,i} \end{pmatrix} \tag{4.8}$$

In (X)MC-QDPT at the second order, as implemented in the GAMESS[52] electronic structure software package and as we use it here, $\mathbf{G}_{PP}$ is unity and the $\mathbf{G}_{OP}$ part of $\mathbf{G}_{QP}$ is zero,[37] so eq. (4.8) becomes

$$\psi_i = \begin{pmatrix} \mathbf{m}_{P,i} \\ \mathbf{0} \\ \mathbf{G}_{SP}\mathbf{m}_{P,i} \end{pmatrix} \tag{4.9}$$

Note that all components of $\mathbf{G}_{SP}\mathbf{m}_{P,i}$ are in the *S* space, and therefore all components of ψ_i in the CAS-CI space are from $\mathbf{m}_{P,i}$. This means the model states are the projection of the (X)MC-QDPT wave functions on the CAS-CI space at the second order of perturbation. This is the key relationship to be exploited by our proposed model space diabatization strategy.

4.2.3. The model space diabatization (MSD) strategy

Notation. In a given basis, e.g., the zero-order wave functions described above or the individual CSFs, an adiabatic or diabatic wave function can be expressed as a column vector. For example, in the CSF basis, a wave function can be written as

$$|v\rangle = \sum_{\mu=1}^{N^{\mathrm{CSF}}} v_\mu \left|\mathrm{CSF}_\mu\right\rangle \tag{4.10}$$

where N^{CSF} is the number of CSFs. A vector **v** with components v_μ can be used to represent this wave function. Hereafter in this section we use collections of such vectors $\{\mathbf{v}_i\}$ (*i* runs from 1 to the number of states) to represent the adiabatic and diabatic states without explicit reference to the basis.

The CASSCF diabatic states $\{\mathbf{d}_i\}$ are given by an orthogonal transformation of the CASSCF adiabatic states of interest $\{\mathbf{c}_i\}$. This transformation is denoted $\mathbf{B}^{\mathrm{CD}}$, and we have

$$\mathbf{d}_i = \sum_{j=1}^{N} \mathbf{c}_j B_{ji}^{\mathrm{CD}} \tag{4.11}$$

where *N* is the dimension of the model space. The (X)MC-QDPT model states $\{\mathbf{m}_i\}$ (representing the same wave functions as the $\mathbf{m}_{P,i}$ in the previous section) are also

obtained by orthogonally transforming the CASSCF states, and the transformation is denoted $\mathbf{B}^{\mathrm{CM}}$,

$$\mathbf{m}_i = \sum_{j=1}^{N} \mathbf{c}_j B_{ji}^{\mathrm{CM}} \tag{4.12}$$

Its inverse transformation, $\mathbf{B}^{\mathrm{MC}}$, that converts the model states to CASSCF states, is the transpose of $\mathbf{B}^{\mathrm{CM}}$,

$$\mathbf{B}^{\mathrm{MC}} = \left(\mathbf{B}^{\mathrm{CM}}\right)^{\mathrm{T}} \tag{4.13}$$

All of the transformations are represented by $N \times N$ orthogonal matrices.

The MSD strategy applied with fourfold-way diabatization and (X)MC-QDPT. We seek a transformation of the wave functions given by eq. (4.9) such that each diabatic state thus generated has the largest projection on the configuration space of a specific diabatic prototype group, i.e., that it is dominated by the configurations of this group; the equations for such a transformation are given by Atchity and Ruedenberg.[15] The prototype groups for (X)MC-QDPT diabatic states are taken to be the same as for CASSCF diabatic states. Therefore, only the components of the wave functions in the CAS-CI space are relevant for the diabatization. Diabatizing the QDPT wave functions (eq. (4.9)) is equivalent to diabatizing the model states, resulting in the same transformation. Since the model states span the same N-dimensional model space as the selected CASSCF adiabatic states, diabatization of the CASSCF states and of the model states will result in exactly the same diabatic states. From these discussions we conclude that diabatic states obtained by configurational uniformity from the (X)MC-QDPT wave functions are equivalent *within the CAS-CI space* to the diabatic states obtained from the CASSCF wave functions.

By virtue of this conclusion, the transformation from the (X)MC-QDPT wave functions to the QDPT diabatic states, $\mathbf{B}^{\mathrm{MD}}$, is exactly the same as the transformation from the model states to the CASSCF diabatic states. Such transformation is equivalent to

first transforming the model states back to CASSCF states and then transforming the CASSCF states to the diabatic states:

$$\mathbf{B}^{\mathrm{MD}} = \mathbf{B}^{\mathrm{MC}}\mathbf{B}^{\mathrm{CD}} \tag{4.14}$$

The diabatic electronic Hamiltonian **U** (which is the potential energy matrix governing nuclear motions) is given by similarity-transforming the diagonal adiabatic potential energy matrix **V** whose diagonal elements are the (X)MC-QDPT energies:

$$\mathbf{U} = \left(\mathbf{B}^{\mathrm{MD}}\right)^{\mathrm{T}} \mathbf{V}\mathbf{B}^{\mathrm{MD}} \tag{4.15}$$

where $\mathbf{B}^{\mathrm{MD}}$ is an orthogonal matrix (unitary matrix if we were using a complex treatment). All the necessary ingredients (the matrices $\mathbf{B}^{\mathrm{MC}}$, $\mathbf{B}^{\mathrm{CD}}$, and **V**) are standard outputs of the CASSCF-level fourfold way and the (X)MC-QDPT calculations. Additional calculations are simply matrix multiplication and transposes.

Although in this chapter we discuss and apply the MSD method with the fourfold way and (X)MC-QDPT, by construction it can also be used with other MCSCF-level diabatization and other QDPT methods if they produce the corresponding $\mathbf{B}^{\mathrm{MC}}$ and $\mathbf{B}^{\mathrm{CD}}$ matrices. This is equivalent to the requirement that the MCSCF-level diabatization and the QDPT generate diabatic states and model states that span the same space as do the MCSCF adiabatic states.

Consistency of the phases of wave functions. The consistency of the phases of wave functions is an important technical issue that has to be handled carefully when the strategy is applied to potential energy surfaces. Any procedure that generates consistent phases would be acceptable, and the best scheme probably depends on the particular problem (for example, whether the system has an even or odd number of electrons) and on the software used. In the rest of this section we discuss the general problem and present one scheme (the one we used for the applications in this chapter) for ensuring consistent phases.

The wave functions are defined up to a phase factor $e^{i\theta}$, which is ±1 if the wave functions are taken to be real, which is the case for almost all practical calculations. Accordingly, the sign of the rows and columns of the transformation matrices depends on the phases of both the wave functions being transformed and the transformed wave functions. Although the absolute phases are arbitrary, it is essential for calculating dynamics that the phases be defined consistently from point to point. In general, one can determine the phase along a path through coordinate space (for example, along a trajectory) by enforcing continuity of the signed matrix elements as a function of coordinate change. This strategy is general and applies to the case of either an even or an odd number of electrons. However, for an even number of electrons, we have devised a way to do this very efficiently by using intermediate quantities in the calculation, and the rest of this section is devoted to explaining this algorithm.

In particular, the MSD strategy concatenates two transformations obtained from two separate calculations, namely $\mathbf{B}^{\mathrm{MC}}$ from a CASSCF diabatization and $\mathbf{B}^{\mathrm{CD}}$ from a (X)MC-QDPT, to calculate $\mathbf{B}^{\mathrm{MD}}$ and uses eq. (4.15) to calculate the diabatic potential energy matrix **U**. The signs of the matrix elements of $\mathbf{B}^{\mathrm{MC}}$ and $\mathbf{B}^{\mathrm{CD}}$ are affected by the phases of the many-electron wave functions, the signs of whose CAS-CI coefficients are further affected by the phases of the orbitals, which will be discussed below.

Whereas the phases of the diabatic states (affecting the signs of the columns of $\mathbf{B}^{\mathrm{CD}}$) and of the (X)MC-QDPT model states (affecting the signs of the rows of $\mathbf{B}^{\mathrm{MC}}$) are not important since they influence eventually only the signs of the off-diagonal elements of **U** (diabatic couplings), the phases of the CASSCF adiabatic states are critical and must be consistent in $\mathbf{B}^{\mathrm{MC}}$ and $\mathbf{B}^{\mathrm{CD}}$; otherwise we would get an incorrect $\mathbf{B}^{\mathrm{MD}}$ (the mathematical details behind this statement are given in Appendix A1). Unfortunately standard implementations of the methods do not automatically generate phases that are consistent between the (X)MC-QDPT part of the calculation (giving $\mathbf{B}^{\mathrm{MC}}$) and the fourfold way part of the calculation (giving $\mathbf{B}^{\mathrm{CD}}$); nor do they generate phases consistent

from point to point in coordinate space. Nevertheless, we do not need uniquely defined phases; we only need the phases to be consistent, and we are able to ensure this by examining their CAS-CI coefficients.

We note that the signs of the CSFs and thus of the CAS-CI coefficients can also be arbitrary because of the undetermined phases of the orbitals, with the important exception that closed-shell singlet CSFs with all occupied orbitals being doubly occupied are unaffected by the signs of orbitals, and the signs of their CAS-CI coefficients are determined by the overall phase of the wave function only. We used this exception in the scheme we used in this chapter, taking advantage of the fact that all systems considered in this chapter have an even number of electrons. For such systems we can determine the phases of the CASSCF states in the (X)MC-QDPT and fourfold way calculations by the sign of the CAS-CI coefficient of a closed-shell CSF, and we can then adjust the signs of the rows of $\mathbf{B}^{\mathrm{CD}}$ so that it is consistent with $\mathbf{B}^{\mathrm{MC}}$. After attaining consistency between $\mathbf{B}^{\mathrm{MC}}$ and $\mathbf{B}^{\mathrm{CD}}$ at one geometry, we can enforce the smoothness of the two matrices at all geometries as a convenient way to ensure that $\mathbf{B}^{\mathrm{MC}}$ and $\mathbf{B}^{\mathrm{CD}}$ are also consistent in phase for those geometries. Based on this analysis, the scheme we used to adjust the signs of the elements of $\mathbf{B}^{\mathrm{MC}}$ and $\mathbf{B}^{\mathrm{CD}}$ so that they are consistent in the phases of the CASSCF states and across the molecular geometry space of interest is as follows:

(1) Choose a molecular geometry where DMOs are close to CMOs, and find the CASSCF wave functions and their CAS-CI coefficients.

(2) Choose a certain CSF with all occupied orbitals doubly occupied, for example, the ground-state closed-shell CSF. Examine its CAS-CI coefficient for each state, whose sign is used as the "indicator" of the phase of that state. Note that in the diabatization output the CSFs are in the DMO basis and their coefficients are different from those in the CMO basis in the (X)MC-QDPT output. However they will be close when DMOs are close to CMOs.

(3) If for the *i*-th CASSCF state the sign of the "indicator" coefficient is different in the fourfold way and (X)MC-QDPT, then change the signs of all elements of

the i-th row of $\mathbf{B}^{\mathrm{CD}}$. This adjustment will account for the different phase of the i-th CASSCF state in the two calculations. Do this for all the CASSCF states.

(4) A geometry is used as a reference after $\mathbf{B}^{\mathrm{CD}}$ at this geometry has been adjusted using the above steps. At a geometry adjacent to the reference geometry (the "current" geometry), the signs of the matrix elements of $\mathbf{B}^{\mathrm{MC}}$ and $\mathbf{B}^{\mathrm{CD}}$ are determined as follows. By changing the signs of any rows and columns of the matrices at the current geometry in all possible ways, we maximize an overlap-like function M for $\mathbf{B}^{\mathrm{MC}}$ and $\mathbf{B}^{\mathrm{CD}}$ respectively,

$$M = \sum_{i,j} B_{ij}^{(\mathrm{ref})} B_{ij}^{(\mathrm{curr})} \tag{4.16}$$

where B_{ij} are elements of matrix $\mathbf{B}$, which is either $\mathbf{B}^{\mathrm{MC}}$ or $\mathbf{B}^{\mathrm{CD}}$; the sum is over all matrix elements; superscripts "ref" or "curr" means the matrix is for the reference or current geometry. The current geometry is then used as the new reference and the matrices for the next adjacent geometry are adjusted in the same manner. We can follow a path of geometries and repeat this step for all geometries of interest. This is equivalent to enforcing the smoothness of the transformation matrices across the geometries, which is more efficient than applying steps (1)-(4) at each geometry individually. Of course one can use steps (1)-(4) to check the results if needed. The path to follow can be general; for example, it can encircle a conical intersection, in which case the adiabatic wave functions change sign due to the geometric phase effect[53] while the diabatic wave functions do not.

The procedure of ensuring the consistency in the phases of matrices across different geometries is applicable to any system. However, the procedure used here for making the phases of CASSCF wave functions consistent in $\mathbf{B}^{\mathrm{MC}}$ and $\mathbf{B}^{\mathrm{CD}}$ at a given geometry is limited to systems with an even number of electrons since it utilizes the CI coefficients of a singlet CSF with all occupied orbitals being doubly occupied but there is no such CSF

for systems with an odd number of electrons. For such systems, one practically convenient alternative is to try all possible combinations of the phases of CASSCF wave functions in $\mathbf{B}^{\mathrm{MC}}$ and $\mathbf{B}^{\mathrm{CD}}$ and generate a set of diabatic potential energy curves for each combination of phases following a path while ensuring the consistency across the path. By looking at the sets of potential energy curves one should be able to select the correct one, because the curves generated with consistent phases should be smooth and reflect the difference of positions of state crossings in the CASSCF-level and (X)MC-QDPT-level diabatizations. This procedure is convenient due to the fact that there are only a limited number of combinations of phases (2^{N-1} combinations for a model space of dimension N where N is usually a small number in practical calculations of coupled potential energy surfaces) and that the procedure of generating diabatic potential energy curves using MSD is very efficient without the need of additional electronic structure calculations. More efficient schemes can probably be devised, but they will probably be software dependent.

4.3. COMPUTATIONAL DETAILS

All SA-CASSCF, fourfold-way diabatizations, and XMC-QDPT calculations were carried out with the GAMESS[52] software package. Intruder state avoidance[54] for XMC-QDPT was used throughout with the energy denominator shift parameter[52] set equal to 0.02. The model space diabatization strategy was performed, using in-house developed codes, to extract the needed information from the outputs of the CASSCF diabatization and XMC-QDPT calculations, to adjust the phases of the matrices, and to calculate the diabatic potential energy matrices. The strategy was applied to the potential energy surfaces of three molecules: LiH, LiF, and thioanisole. The fourfold way at the XMC-QDPT level was also performed, with CASSCF DMOs in all cases, on these molecules for comparison.

The potential energy curves of the three lowest $^1\Sigma^+$ states of LiH were calculated with SA-CASSCF averaging over the three states with equal weights, and with XMC-QDPT with a three-dimensional model space, for internuclear distances from 1.5 to 6.0 Å.

The coordinate system is defined by putting Li at the origin and H on the positive *z* axis. The active space consists of two electrons in five orbitals, which have the character of 2*s* and $2p_z$ of Li and 1*s*, $2p_x$, and $2p_y$ of H. Further increase of the active space results in no qualitative difference in the potential energy curves. The basis set used was aug-cc-pVDZ.[55] The SA-CASSCF calculations were constrained to A_1 states in C_{4v} spatial symmetry. The XMC-QDPT calculations were carried out with C_1 spatial symmetry.

The potential energy curves of LiH were diabatized using the fourfold way. The threefold density criterion with parameters $\alpha_N = 2$, $\alpha_R = 1$, and $\alpha_T = 0.5$ is sufficient to generate satisfactory DMOs. The diabatic prototypes include one CSF for each state, corresponding nominally to configurations $(1s_H)^2$, $(1s_H)(1s_{Li})$, and $(1s_H)(1p_{z,Li})$.

The potential energy curves of the three lowest $^1\Sigma^+$ states of LiF were calculated with SA-CASSCF by averaging over the three states with equal weights, and with XMC-QDPT with a three-dimensional model space, for internuclear distances from 3.0 to 8.0 Å. The coordinate system is defined by putting Li at the origin and F on the positive *z* axis. In C_{2v} spatial symmetry, the active space consists of eight electrons in eight orbitals, which have the character of one *s* and one p_y on Li and one *s*, one p_y, two p_x, and two p_z on F. (Here the labeling of *x* and *y* is arbitrary and interchangeable; notice, however, that the C_{2v} symmetry does not treat the degenerate *x* and *y* components of the π space equivalently.) Further increase of the active space results in no qualitative difference in the potential energy curves. The basis set used was aug-cc-pVTZ.[55,56] The SA-CASSCF and XMC-QDPT calculations were constrained to A_1 states in C_{2v} spatial symmetry.

The potential energy curves of LiF were diabatized using the fourfold way. The threefold density criterion with parameters $\alpha_N = 2$, $\alpha_R = 1$, and $\alpha_T = 0.5$ is sufficient to generate satisfactory DMOs. The diabatic prototypes include one CSF for each state,

corresponding nominally to three configurations: closed-shell Li^+F^-, excitation ($p_{z,F}$) $\rightarrow$ (s_{Li}) from the closed shell, and excitation ($p_{y,F}$) $\rightarrow$ ($p_{y,Li}$) from the closed shell.

The geometry of thioanisole was first optimized by density functional theory with the M06-2X exchange-correlation functional[57,58] and the MG3S basis set[59] using the *Gaussian 09*[60] software package. The optimized geometry has C_s symmetry, and the coordinate system is defined by taking the symmetry plane as the *xy* plane with the Ph-S bond on the *x* axis. The potential energy curves of the three lowest singlet states of thioanisole, which are two A' and one A" states, were calculated along the $S\text{-}CH_3$ bond distance coordinate from 1.8 to 4.0 Å while other coordinates were fixed at their values at the equilibrium geometry, with SA-CASSCF averaging over the three states with equal weights and XMC-QDPT having a three-dimensional model space. The active space consists of 14 electrons in 13 orbitals, which have the character of three π and three π* orbitals on the phenyl ring, one σ and one σ* orbital on the Ph-S bond, one σ and one σ* orbital on the $S\text{-}CH_3$ bond, and one *s*, one p_z, and one *d* orbital on the sulfur. (The *d* orbital is a combination of d_{xz} and d_{yz}, and its orientation changes with $S\text{-}CH_3$ distance.) The σ and σ* canonical orbitals on the $S\text{-}CH_3$ bond become more localized when the diabatic orbitals are formed, as discussed below. The basis set used is a mixed one with 6-311+G(d)[61,62] for C and H and MG3S[59] for S. The SA-CASSCF and XMC-QDPT calculations were carried out in C_1 spatial symmetry.

The potential energy curves of thioanisole were diabatized using the fourfold way. The threefold density criterion with parameters $\alpha_N = 2$, $\alpha_R = 1$, and $\alpha_T = 0.5$ together with the MORMO criterion was used to generate DMOs. Two MORMO reference orbitals were used. One of them was prepared by taking a π CMO at $r_{S\text{-}CH_3} = 4.0$ Å and keeping its components in the atomic orbitals (AOs) of Ph-S and dropping the components in the AOs of CH_3. The other one was prepared by taking a sulfur p_y-like CMO and keeping its components in the AOs of sulfur only. With this choice of

MORMO reference orbitals, the DMOs are close to CMOs except that at short $S\text{-}CH_3$ distances the σ and σ* CMOs on the $S\text{-}CH_3$ bond become a p_y-like DMO on sulfur and a sp^3-like DMO on CH_3.

The selection of MORMO reference orbitals and diabatic prototypes is complicated because we chose them to be appropriate for calculating global potential energy surfaces, not just for the local cuts presented here. The diabatic prototypes are chosen as follows. For conciseness of description, we define a reference CSF corresponding to the closed-shell $[Ph\text{-}S]^-$ anion, with the bonding- and non-bonding-like DMOs on Ph-S doubly occupied (one *s*, one p_y, and one p_z orbital on sulfur, three π orbitals on Ph, and one bonding orbital on the Ph-S bond) and the other anti-bonding-like orbitals on Ph-S and the sp^3-like orbital on CH_3 unoccupied. The prototype for the first state is one CSF corresponding to a single excitation from the p_y-like orbital on sulfur to the sp^3-like orbital on CH_3. Prototypes for the second state are three CSFs, two corresponding to single excitations from π to π*, and the other one corresponding to a double excitation from the p_z-like orbital on sulfur to a π* orbital on Ph-S and the sp^3-like orbital on CH_3. Prototypes for the third state are two CSFs, one corresponding to a single excitation from the p_z-like orbital on sulfur to the sp^3-like orbital on CH_3, the other corresponding to a single excitation from a π orbital to the sp^3-like orbital on CH_3.

4.4. RESULTS AND DISCUSSION

4.4.1. LiH

The ionic-covalent crossing of LiH is a classic problem whose study dates back to the early days of quantum chemistry.[63,64] The lowest three $^1\Sigma^+$ states of LiH, denoted here as V_1, V_2, and V_3, are one ionic $[(1s_H)^2]$ and two covalent $[(1s_H)(2s_{Li})$,

$(1s_{\mathrm{H}})(2p_{z,\mathrm{Li}})]$ states. The adiabatic and diabatic potential energy curves given by SA-CASSCF and the fourfold way are shown in Figure 4.3(a). The curve of V_3 is unsmooth at internuclear distance ~2.6 Å because it has an avoided crossing with a higher state, and it also affects V_1 and V_2 via state averaging. However the higher state is not calculated since it has no significant influence on the diabatization. The ionic diabatic state U_1 transforms smoothly from adiabatic state V_1 near the equilibrium bond length of 1.595 Å (ref. 65) to V_3 in the dissociation limit as the internuclear distance increases. The two covalent diabatic states U_2 and U_3 change from V_2 and V_3 at short bond lengths to V_1 and V_2 respectively at the dissociation limit. There are two diabatic crossings, one at 2.8-2.9 Å between U_1 and U_2 and the other at ~3.7 Å between U_1 and U_3. The squared diabatic couplings shown in Figure 4.3(b) are overall smooth except a small "kink" at $r_{\text{Li-H}} \sim 2.5$ Å caused by the sudden change of character of V_3. The couplings peak in the region where the diabatization mixes different adiabatic states and they decrease toward zero in the asymptotic region, as expected.

The adiabatic potential energy curves given by XMC-QDPT are shown in Figure 4.4 together with the ones given by SA-CASSCF for comparison. The zero of energy for each theory is chosen to be the S_0 energy at $r_{\text{Li-H}} = 6.0$ Å given by that theory. The figure shows that XMC-QDPT deviates from SA-CASSCF significantly for S_0 at short bond lengths, for S_1 in the intermediate region, and for S_2 at the dissociation limit. This is because in those regions the particular adiabatic state has ionic character. The dynamical correlation introduced by XMC-QDPT for the covalent states is similar for different internuclear distances, leading to an overall downshift of the absolute energies without significant effect on the relative energies, while the dynamical correlation for the ionic state is more pronounced, resulting in further lowering of the energies. Because of this, the diabatic crossing between the ionic and a covalent state should occur at different internuclear distances in SA-CASSCF and in XMC-QDPT. Such a difference has to be

incorporated by the transformation $\mathbf{B}^{\mathrm{MC}}$ that converts XMC-QDPT model states to CASSCF states since $\mathbf{B}^{\mathrm{CD}}$, the transformation of CASSCF adiabatic states to diabatic states, has no information about this difference.

The XMC-QDPT-level diabatic potential energy curves given by the MSD strategy are shown in Figure 4.5(a). The sign of $\mathbf{B}^{\mathrm{CD}}$ has been adjusted for $r_{\mathrm{Li\text{-}H}}$ = 1.5 following steps (2)-(4) discussed in Section 4.2.3 as well as for all other $r_{\mathrm{Li\text{-}H}}$ following step (5) to ensure the consistency of phases in $\mathbf{B}^{\mathrm{MC}}$ and $\mathbf{B}^{\mathrm{CD}}$ for each geometry and consistency over all geometries. The diabatic crossings occur at 3.0-3.1 Å between U_1 and U_2 and at 4.2-4.3 Å between U_1 and U_3, both at longer $r_{\mathrm{Li\text{-}H}}$ compared to CASSCF. To emphasize the significance of phase consistency, diabatic potential energy curves obtained with inconsistent phases in $\mathbf{B}^{\mathrm{MC}}$ and $\mathbf{B}^{\mathrm{CD}}$ (but the individual matrices are smooth over different geometries) are also given in Figure 4.5(b)–(d) for comparison. (There are four possible combinations of the signs of rows in a 3×3 matrix $\mathbf{B}^{\mathrm{CD}}$, with $\mathbf{B}^{\mathrm{CD}}$ and $-\mathbf{B}^{\mathrm{CD}}$ considered as the same, only one of which is consistent with a given $\mathbf{B}^{\mathrm{MC}}$.) The diabatic curves in Figure 4.5(b)–(d) are still smooth, but the shapes are incorrect. For instance, in Figure 4.5(b) and Figure 4.5(c) the crossing between U_1 and U_3 occurs at similar position as for CASSCF diabatization, and the same happens for the crossing between U_1 and U_2 in Figure 4.5(d). The squared diabatic couplings shown in Figure 4.6 are qualitatively similar to those at the CASSCF level in Figure 4.3(b).

For this system the DMOs generated by the threefold density criterion are close to CMOs and as a result the XMC-QDPT energies in the DMO basis differ only slightly from those in the CMO basis (mean unsigned deviation = 0.01 eV, maximum deviation = -0.03 eV); therefore we have an additional check for the diabatic curves generated by the MSD strategy, namely to compare them to those generated by the fourfold way at the

MC-QDPT level. Figure 4.7 shows they match well, further verifying the validity of the MSD strategy.

4.4.2. LiF

The potential energy curves of the ground $X^1\Sigma^+$ and the excited $1^1\Sigma^+$ states of LiF also provide a challenging case for electronic structure methods because of their intrinsically multi-configurational character (usually called multireference character) when the bond stretches and because of the ionic-covalent avoided crossing[66,67] at internuclear distance $r_{\text{Li-F}} \sim 7.2$ Å.[67] On the left side of the avoided crossing where $r_{\text{Li-F}}$ is less than 7.2 Å, the $X^1\Sigma^+$ state has ionic character and the $1^1\Sigma^+$ state has covalent character, while the character of the two states switches on the other side of the crossing. Obtaining the correct distance for the avoided crossing depends on calculating the asymptotic energies of the ionic and covalent states accurately, and this requires a very high level calculation, especially for F^-. However, the present work is focused on diabatization methodology, not on obtaining a converged calculation of the crossing point. As for LiH, the ionic state of LiF is more sensitive than the covalent states to dynamical correlation, and SA-CASSCF and XMC-QDPT give significantly different locations of the ionic-covalent avoided crossings as discussed below. It therefore constitutes another difficult test case for MSD which utilizes information from diabatization at the CASSCF level to perform diabatization at the XMC-QDPT level..

The adiabatic and diabatic potential energy curves calculated by SA-CASSCF and the fourfold-way diabatization are shown in Figure 4.8(a). The ionic diabatic state U_1 corresponds to adiabatic state V_1 at short Li-F distances, to V_2 at intermediate distances, and to V_3 at long distances, similar to LiH. The diabatic crossings occur at 4.1-4.2 Å between the ionic U_1 and covalent U_2 and at ~7.0 Å between U_1 and the covalent U_3. The squared diabatic couplings shown in Figure 4.8(b) are again smooth and decrease toward zero in the asymptotic region.

The XMC-QDPT adiabatic and diabatic potential energy curves are shown in Figure 4.9(a). The adiabatic curves are considerably different from the CASSCF ones due to the significantly different amount of dynamical correlation for different states and at different geometries. As a consequence, the avoided crossing between S_0 and S_1 occurs at much longer $r_{\text{Li-F}}$, and the avoided crossing between S_1 and S_2 vanishes in the calculated region of geometry. These differences are fully captured by the MSD strategy. The resulting diabatic potential energy curves have only one crossing at ~6.1 Å between U_1 and U_2. Like what we have done for LiH, the diabatic curves of LiF generated from inconsistent $\mathbf{B}^{\text{MC}}$ and $\mathbf{B}^{\text{CD}}$ are shown in Figure 4.9(b)–(d). It is even more obvious here that the consistency of phase is essential for the correct diabatization, otherwise the diabatic curves will exhibit erratic shapes. (There are exceptions for which the phase is practically unimportant, to be discussed in the next subsection.) The squared diabatic couplings, shown in Figure 4.10(a), have small bumps at ~4.5 Å and ~7.1 Å but the curves are still overall smooth. We note that the bumps originate from the fourfold way rather than the MSD strategy, as explained in the following.

As for LiH, the DMOs are also similar to CMOs for LiF and so the XMC-QDPT energies in the DMO basis are essentially the same as the standard XMC-QDPT energies in the CMO basis. Consequently the fourfold way at the XMC-QDPT level is in principle equivalent to MSD. Indeed they give essentially the same diabatic potential curves, differing by less than 0.01 eV (not shown here). The squared diabatic couplings (Figure 4.10) given by the two schemes are also essentially the same despite some numerical differences. Obviously the bumps at ~4.5 Å and ~7.1 Å are also present in the curves given by the fourfold way at the XMC-QDPT level (Figure 4.10(b)), showing that it is not an inaccuracy introduced by MSD. Nonetheless this "unsmoothness" is minor without noticeable influence on the potential energy curves and should not be a problem.

To test the sensitivity of the MSD strategy to suing a model space of a different dimension, calculations were also carried out by SA-CASSCF averaging over only two

states (again with equal weights) and with a two-dimensional model space for XMC-QDPT. The conclusions about the success of the MSD strategy are unchanged.

4.4.3. Thioanisole

Thioanisole has 66 electrons, which is rather larger than is typical for a system used for testing new methods. We chose it because the use of MORMO reference orbitals in fourfold-way diabatization results in DMOs that are significantly different from CMOs, such that XMC-QDPT in the CASSCF DMO basis gives inaccurate energies, making the original MC-QDPT diabatization scheme[19,29] unsuitable.

At equilibrium geometry of thioanisole, the ground state S_0 and the first excited singlet state S_1 belong to the A' irreducible representation (irrep) in the C_s group, while the second excited singlet state S_2 belongs to A". S_0 is a closed-shell state, S_1 is a ππ* state, and S_2 is an nπ* state. Within C_s symmetry, as the distance, $r_{S\text{-}CH_3}$, between sulfur and CH_3 increases, a symmetry-allowed conical intersection occurs first between S_1 and S_2. After this intersection, S_1 becomes an A" state, and the second intersection occurs between S_1 and S_0 at longer $r_{S\text{-}CH_3}$. The intersections can be seen in the CASSCF adiabatic and diabatic potential energy curves in Figure 4.11(a), located at $r_{S\text{-}CH_3}$ = 2.0–2.1 Å and ~3.3 Å. The crossing states should not mix in diabatization since they belong to different irreps, and the diabatic energies essentially overlap with the adiabatic ones. The diabatic states simply connect different adiabatic states as they pass the intersections so that U_1 and U_2 remain A' states and U_3 remains a A" state. The squared diabatic couplings, shown in Figure 4.11(b), are overall small. U_{23} undergoes an abrupt increase at $r_{S\text{-}CH_3}$ = 2.5 Å because V_3 passes another crossing (with the uncalculated V_4) and acquires a major configuration shared by V_1 so that the fourfold way distinguishes the two states less well. The coupling is nevertheless unimportant since

its magnitude is still far smaller than the energy gap between the two states. At the XMC-QDPT level, the intersections occur at different locations, $r_{S\text{-}CH_3}$ = 1.9-2.0 Å and ~3.5 Å, due to the inclusion of dynamical correlation (Figure 4.12(a)). The diabatic potential energies again match the adiabatic ones, and the difference of location of the intersections is properly reflected. The fact that the CASSCF diabatic wave functions are essentially the same as the adiabatic wave functions means that $\mathbf{B}^{CD}$ serves only to map the adiabatic states to diabatic states one-to-one with virtually no mixing, and as a consequence the phase inconsistency is not a problem since it affects only the mixing of states. (All four possible phase choices of $\mathbf{B}^{CD}$ give essentially the same diabatic curves, which are not shown individually.) Diabatization at the XMC-QDPT level again introduces a minor unsmoothness to the squared diabatic couplings in Figure 4.12(b) compared to Figure 4.11(b), but the couplings are so small that the lack of smoothness is insignificant.

4.5. SUMMARY

We have proposed a diabatization strategy called model space diabatization that, when used with an MCSCF-level diabatization and a QDPT post-SCF method, generates diabatic states and diabatic potential energy matrix at the standard QDPT level. Diagonalizing the diabatic potential energy matrix produced by model space diabatization gives states and energies that agree exactly with usual adiabatic states and energies.

The new diabatization method has been applied with the fourfold-way SA-CASSCF-level diabatization and XMC-QDPT adiabatic energies to obtain diabatic potential energy curves for LiH and LiF and cuts through the diabatic potential energy surfaces for thioanisole. These cases provide a critical challenge to the new method because shape of potential energy curves at the XMC-QDPT level are qualitatively different from those at the SA-CASSCF level for these molecules as a result of the inclusion of dynamical correlation; in particular the avoided crossings or conical intersections occur at different geometries according to the two levels of theory. We find

that these differences are properly accounted for by the MSD method, and the resulting diabatic potential energy curves are smooth with the correct shape.

The original fourfold way for QDPT calculations used diabatic molecular orbitals (DMOs) determined at the QDPT level.[19] We have now made two changes. First, in a previous paper,[29] we showed that the method could be used, even for QDPT calculations, with DMOs determined at the CASSCF level. Second, in the present chapter, we show that it can be used, even for QDPT calculations, with an adiabatic-to-diabatic transformation determined at the CASSCF level; this preserves the accuracy of the QDPT adiabatic energies even when the DMOs differ largely from the canonical molecular orbitals. With these two changes, the method becomes more convenient and more general. Although we have mainly discussed MSD as an extension of the fourfold way, it is also a general scheme that can in principle be used with any other MCSCF-level diabatization scheme that produces diabatic states spanning the same space as do the MCSCF adiabatic states. Furthermore it can be used with any QDPT method that produces model states spanning the same space.

The MSD strategy is simple in that it can be applied as an independent step after the MCSCF diabatization calculations and QDPT calculations are finished, and its use does not require one to modify the electronic structure codes; furthermore the additional computational cost is negligible. With these advantages the strategy is recommended for QDPT-level diabatization of potential energy surfaces involving avoided crossings or conical intersections.

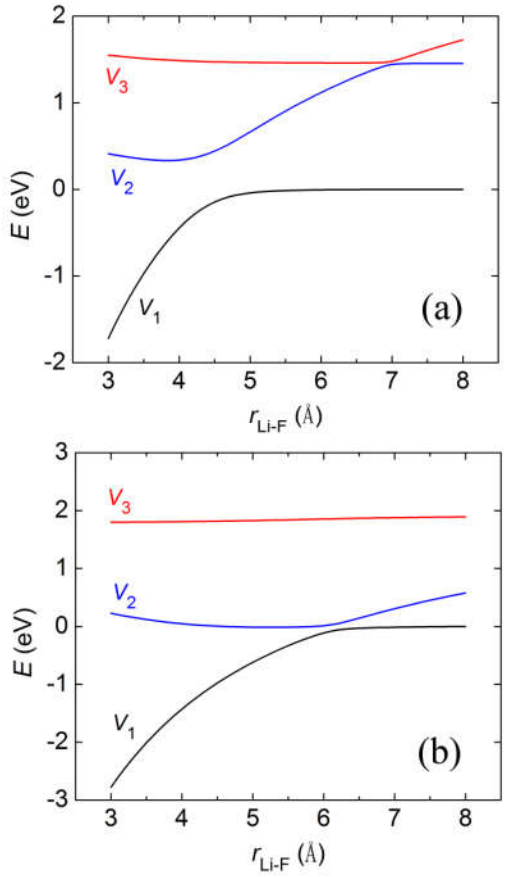

Figure 4.1. Adiabatic (V_1 - V_3) potential energy curves of LiF as functions of the internuclear separation as calculated by (a) SA-CASSCF and (b) XMC-QDPT.

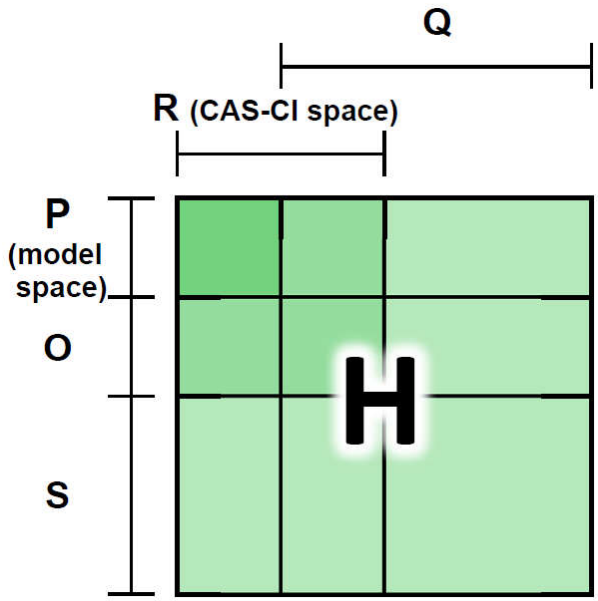

Figure 4.2. Schematic of the partitioning of the electronic Hamiltonian matrix into blocks corresponding to subspaces of the wave function space (see the text for an explanation of the notation).

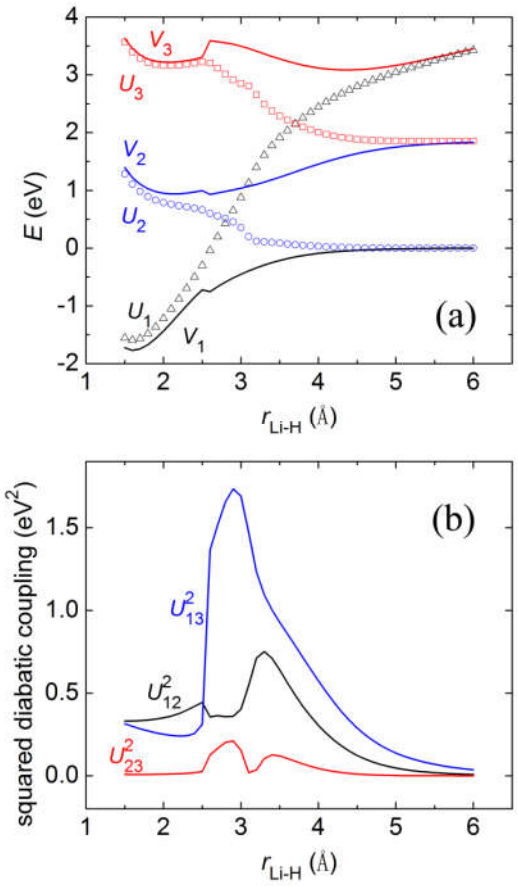

Figure 4.3. Potentials and couplings for LiH as functions of the internuclear separation as calculated by SA-CASSCF and the fourfold way at the CASSCF level. (a) Adiabatic (V_1 - V_3; solid lines) and diabatic (U_1 - U_3; open symbols) potential energy curves and (b) the squared diabatic couplings $(U_{ij})^2$ between diabatic states i and j (i, j = 1-3).

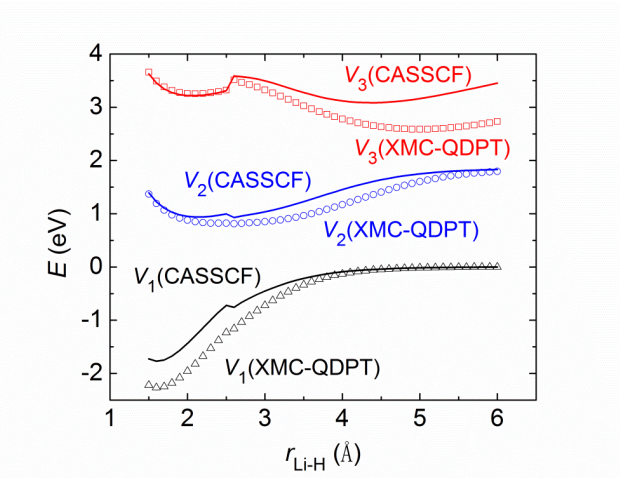

Figure 4.4. Adiabatic (V_1 - V_3) potential energy curves of LiH as functions of the internuclear separation as calculated by SA-CASSCF (solid lines) and XMC-QDPT (open symbols). The zero of energy is set to be the ground-state energy at dissociation limit ($r_{\text{Li-H}}$ = 6.0 Å) given by the respective theories.

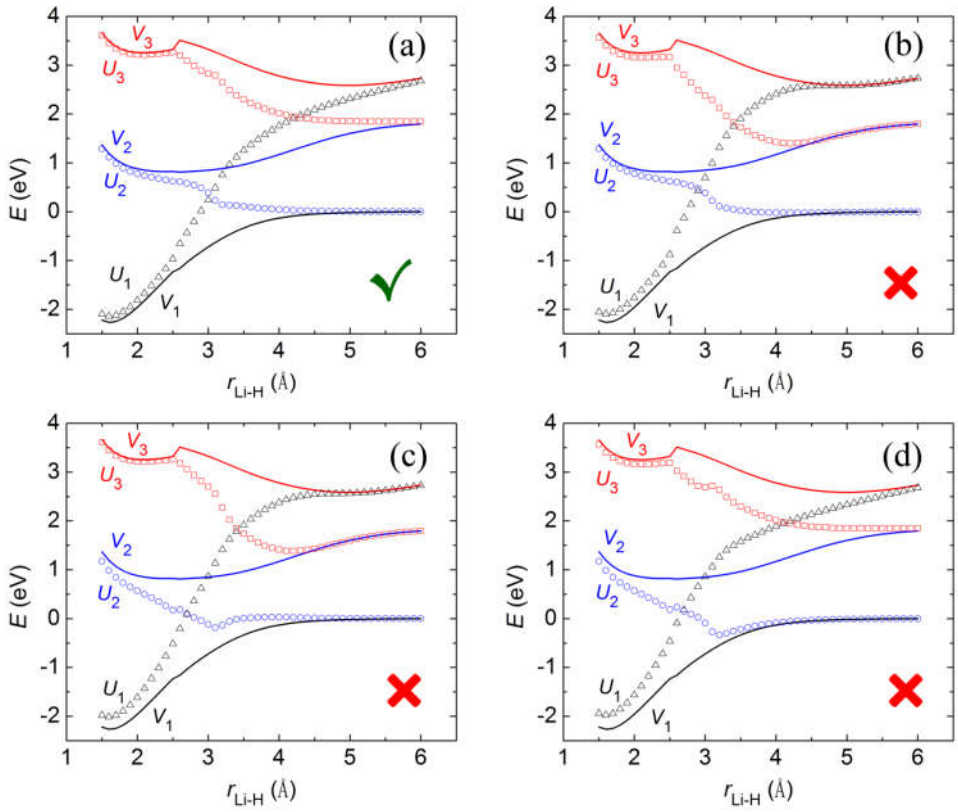

Figure 4.5. Adiabatic (V_1 - V_3 ; solid lines) and diabatic (U_1 - U_3 ; open symbols) potential energy curves of LiH as functions of the internuclear separation as calculated by XMC-QDPT and the MSD strategy with transformation matrices corresponding to (a) consistent phases and (b–d) inconsistent phases of the wave functions. Only (a) is the proper result from the correct application of the MSD strategy (indicated by the check mark, as opposed to a red **x** for the other cases).

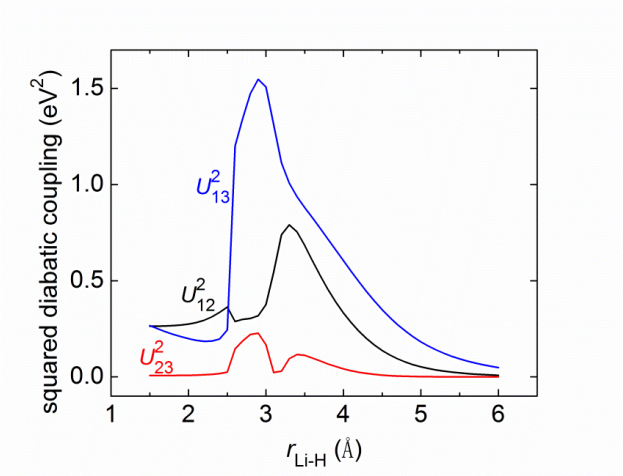

Figure 4.6. Squared diabatic couplings $(U_{ij})^2$ between diabatic states i and j (i, j = 1-3) of LiH as functions of the internuclear separation as calculated by the MSD strategy.

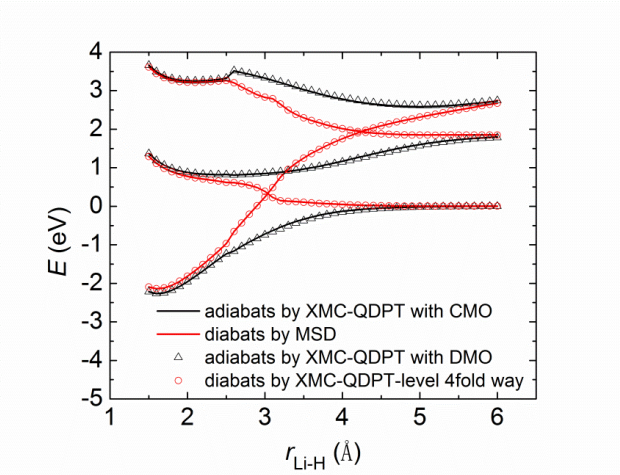

Figure 4.7. Adiabatic and diabatic potential energy curves of LiH as functions of the internuclear separation. Black lines: adiabatic curves calculated by XMC-QDPT with CMOs. Red lines: diabatic curves calculated by MSD. Black triangles: adiabatic curves calculated by XMC-QDPT with CASSCF DMOs. Red circles: diabatic curves calculated by the fourfold way at the XMC-QDPT level with CASSCF DMOs.

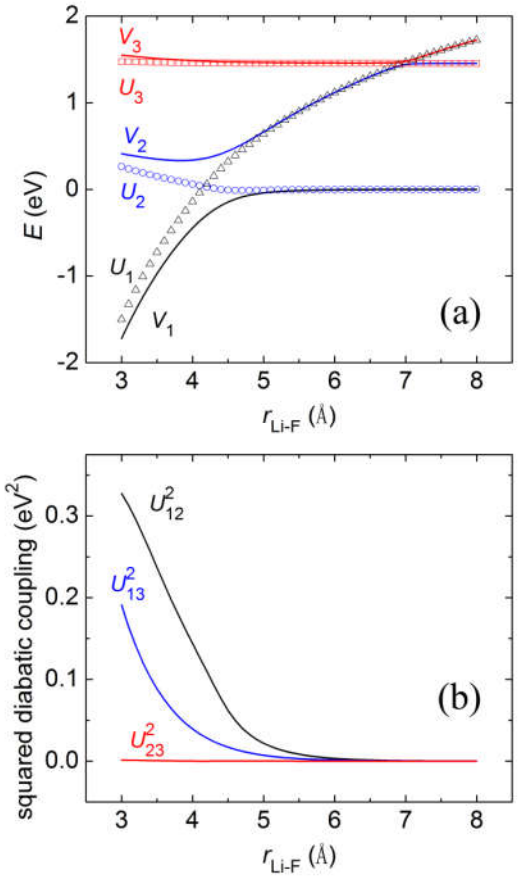

Figure 4.8. Potentials and couplings for LiF as functions of the internuclear separation as calculated by SA-CASSCF and the fourfold way at the CASSCF level. (a) Adiabatic (V_1 - V_3 ; solid lines) and diabatic (U_1 - U_3 ; open symbols) potential energy curves; (b) the squared diabatic couplings $(U_{ij})^2$ between diabatic states *i* and *j* (i, j = 1-3) .

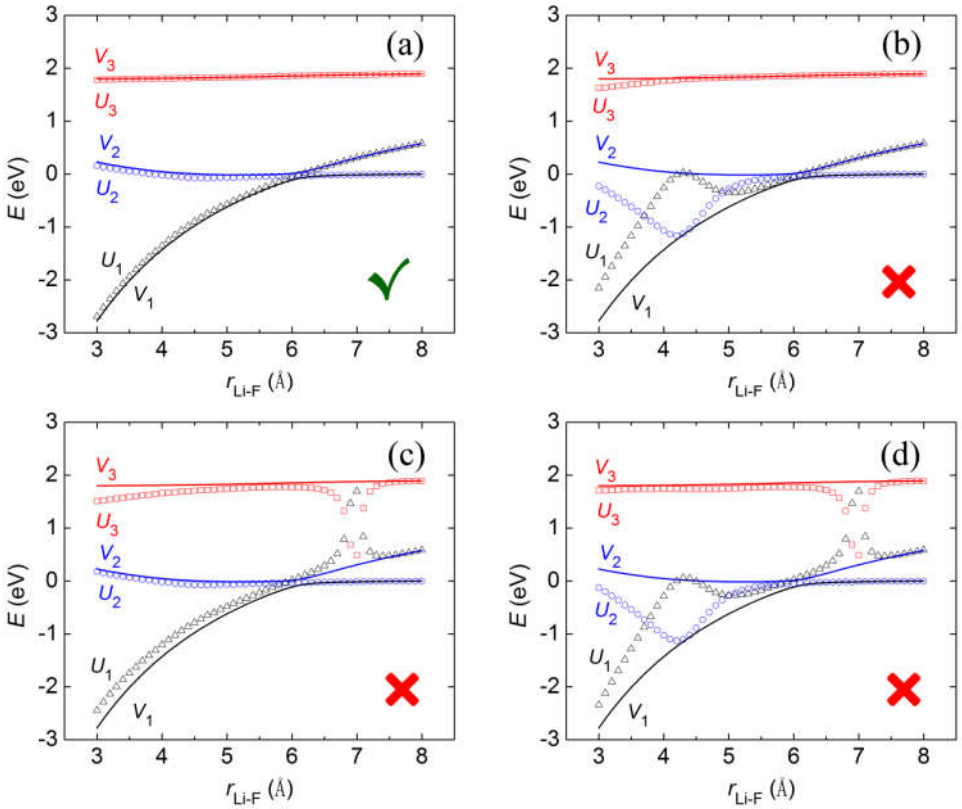

Figure 4.9. Adiabatic (V_1 - V_3 ; solid lines) and diabatic (U_1 - U_3 ; open symbols) potential energy curves of LiF as functions of the internuclear separation as calculated by XMC-QDPT and the MSD strategy with transformation matrices corresponding to (a) consistent phases (indicated by a check mark) and (b–d) inconsistent phases (indicated by a red **x**) of the wave functions. Only the one with the check mark is the proper result from the correct application of the MSD strategy.

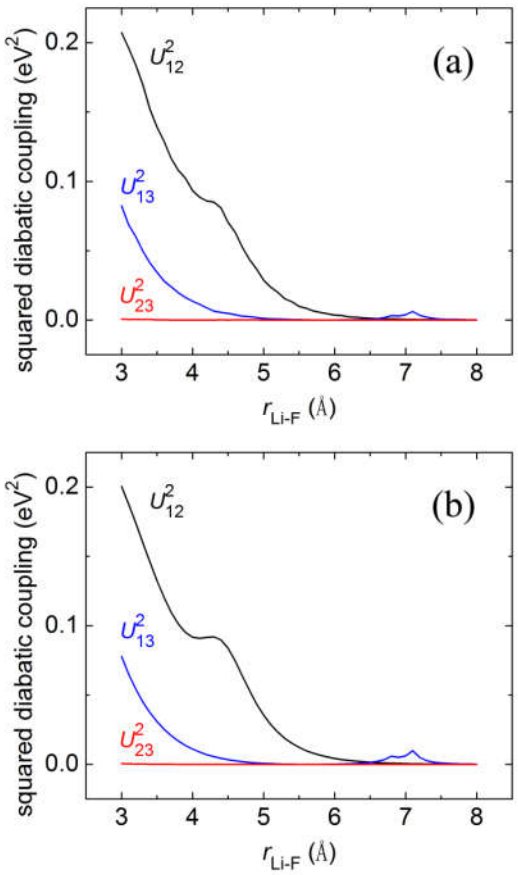

Figure 4.10. Potentials and couplings of LiF as functions of the internuclear separation as calculated by MSD. (a) Squared diabatic couplings $(U_{ij})^2$ between diabatic states *i* and *j* (*i*, *j* = 1-3) and (b) the fourfold way at the XMC-QDPT level with CASSCF DMOs.

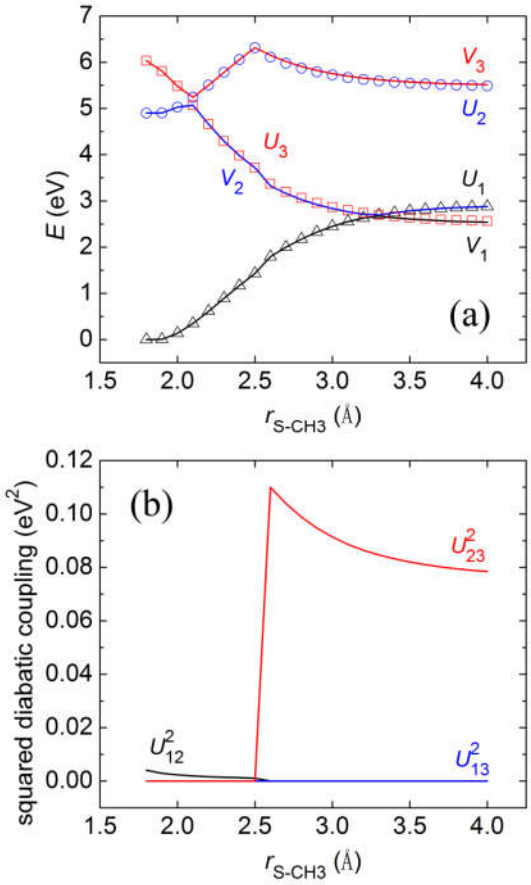

Figure 4.11. Potentials and couplings for thioanisole along the $S\text{-}CH_3$ distance with the other coordinates fixed at the S_0 equilibrium geometry, as calculated by SA-CASSCF and the fourfold way at the CASSCF level. (a) Adiabatic (V_1 - V_3; solid lines) and diabatic (U_1 - U_3; open symbols) potential energy curves. (b) Squared diabatic couplings $(U_{ij})^2$ between diabatic states *i* and *j* (*i*, *j* = 1-3).

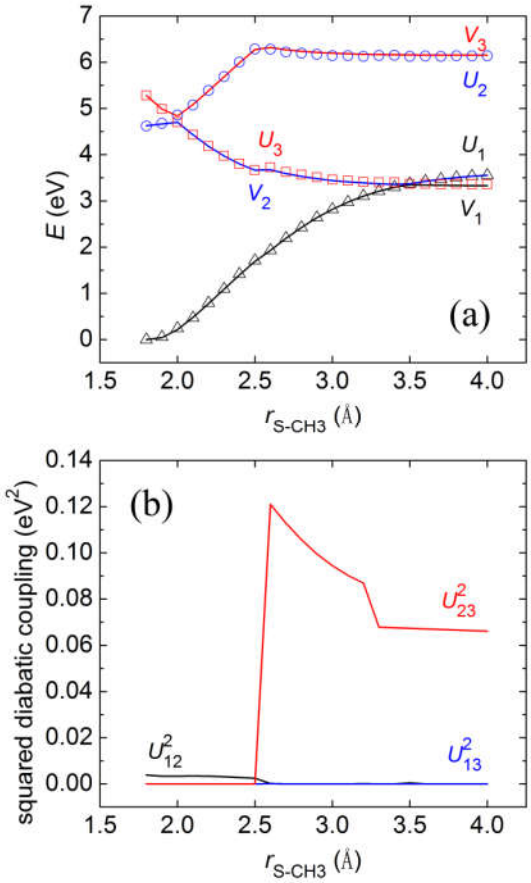

Figure 4.12. Potentials and couplings for thioanisole along the $S\text{-}CH_3$ distance with the other coordinates fixed at the S_0 equilibrium geometry, as calculated by XMC-QDPT and the MSD strategy. (a) Adiabatic (V_1-V_3; solid lines) and diabatic (U_1-U_3; open symbols) potential energy curves. (b)Squared diabatic couplings $(U_{ij})^2$ between diabatic states *i* and *j* (*i*, *j* = 1-3).

REFERENCES FOR CHAPTER 4

[1] A. W. Jasper, C. A. Kendrick, C. A. Mead, and D. G. Truhlar, in *Modern Trends in Chemical Reaction Dynamics: Experiment and Theory (Part 1)*, edited by X. Yang, and K. Liu (World Scientific, Singapore, 2004), p. 329.

[2] L. S. Cederbaum, in *Conical Intersections: Electronic Structure, Dynamics and Spectroscopy*, edited by W. Domcke, D. R. Yarkony, and H. Köppel (World Scientific, Singapore, 2004), p. 3.

[3] W. Domcke, and D. R. Yarkony, Annu. Rev. Phys. Chem. **63**, 325 (2012).

[4] B. C. Garrett and D. G. Truhlar, in *Theoretical Chemistry: Theory of Scattering: Papers in Honor of Henry Eyring*, edited by D. Henderson (Academic, New York, 1981), p. 215.

[5] C. A. Mead and D. G. Truhlar, J. Chem. Phys. **77**, 6090 (1982).

[6] W. Lichten, Phys. Rev. **131**, 229 (1963).

[7] A. Macias and A. Riera, J. Phys. B **11**, L489 (1978).

[8] J. B. Delos, Rev. Mod. Phys. **53**, 287 (1981).

[9] F. Spiegelmann and J. P. Malrieu, J. Phys. B **17**, 1259 (1984).

[10] V. Sidis, Adv. Chem. Phys. **82**, 73 (1992).

[11] R. Cimiraglia, in *Time-Dependent Quantum Molecular Dynamics*, edited by J. Broeckhoeve and L. Lathouwers (Plenum, New York, 1992), pp. 11–26.

[12] W. Domcke and C. Woywod, Chem. Phys. Lett. **216**, 362 (1993).

[13] K. Ruedenberg and G. J. Atchity, J. Chem. Phys. **99**, 3799 (1993).

[14] R. Thürwachter and P. Halvick, Chem. Phys. **221**, 33 (1997).

[15] G. J. Atchity and K. Ruedenberg, Theor. Chem. Acc. **97**, 47 (1997).

[16] D. Simah, B. Hartke, and H.-J. Werner, J. Chem. Phys. **111**, 4523 (1999).

[17] E. S. Kryachko and D. R. Yarkony, Int. J. Quantum Chem. **76**, 235 (2000).

[18] H. Nakamura and D. G. Truhlar, J. Chem. Phys. **115**, 10353 (2001).

[19] H. Nakamura and D. G. Truhlar, J. Chem. Phys. **117**, 5576 (2002).

[20] M. P. Fülscher and L. Serrano-Andrés, Mol. Phys. **100**, 903 (2002).

[21] H. Nakamura and D. G. Truhlar, J. Chem. Phys. **118**, 6816 (2003).

[22] H. Köppel, in *Conical Intersections: Electronic Structure, Dynamics and Spectroscopy*, edited by W. Domcke, D. R. Yarkony, and H. Köppel (World Scientific Publishing Co., Singapore, 2004), p. 175.

[23] O. Godsi, C. R. Evenhuis, and M. A. Collins, J. Chem. Phys. **125**, 104105 (2006).

[24] C. Mota and A. J. C. Varandas, J. Phys. Chem. A **112**, 3768 (2008).

[25] A. Cembran, L. Song, Y. Mo, and J. Gao, J. Chem. Theory Comput. **5**, 2702 (2009).

[26] R. Valero, L. Song, J. Gao, and D. G. Truhlar, J. Chem. Theory Comput. **5**, 1 (2009).

[27] T. Van Voorhis, T. Kowalczyk, B. Kaduk, L.-P. Wang, C.-L. Cheng, Q. Wu, Annu. Rev. Phys. Chem. **61**, 149 (2010).

[28] A. J. Zhang, P.-Y. Zhang, T.-S. Chu, K.-L. Han, and G.-Z. He J. Chem. Phys. **137**, 194305 (2012).

[29] K. R. Yang, X. Xu, and D. G. Truhlar, Chem. Phys. Lett. **573**, 84 (2013).

[30] C. E. Hoyer, X. Xu, D. Ma, L. Gagliardi, and D. G. Truhlar, J. Chem. Phys. **141**, 114104 (2014).

[31] W. Eisfeld, O. Vieuxmaire, and A. Viel, J. Chem. Phys. **140**, 224109 (2014).

[32] P. Siegbahn, A. Heiberg, B. Roos, and B. Levy, Phys. Scr. **21**, 323 (1980).

[33] J. Olsen, B. O. Roos, P. Jørgensen, and H. J. A. Jensen, J. Chem. Phys. **89**, 2185 (1988).

[34] H. Nakano and K. Hirao, Chem. Phys. Lett. **317**, 90 (2000).

[35] J. Ivanic, J. Chem. Phys. **119**, 9364 (2003).

[36] D. Ma, G. Li Manni, L. Gagliardi, J. Chem. Phys. **135**, 044128 (2011).

[37] H. Nakano, J. Chem. Phys. **99**, 7983 (1993); H. Nakano, Chem. Phys. Lett. **207**, 372 (1993).

[38] A. A. Granovsky, J. Chem. Phys. **134**, 214113 (2011).

[39] J. Finley, P.-Å. Malmqvist, B. O. Roos, and L. Serrano-Andrés, Chem. Phys. Lett. **288**, 299 (1998).

[40] C. Angeli, S. Borini, M. Cestari, and R. Cimiraglia, J. Chem. Phys. **121**, 4043 (2004).

[41] H. Nakano, R. Uchiyama, and K. Hirao, J. Comput. Chem. **23**, 1166 (2002); M. Miyajima, Y. Watanabe, and H. Nakano, J. Chem. Phys **124**, 044101 (2006); R. Ebisuzaki, Y. Watanabe, and H. Nakano, Chem. Phys. Lett. **442**, 164 (2007); R. Ebisuzaki, Y. Watanabe, Y. Kawashima, and H. Nakano, J. Chem. Theory Comput. **7**, 998 (2011).

[42] T. Shiozaki, W. Győrffy, P. Celani, and H.-J. Werner, J. Chem. Phys. **135**, 081106 (2011).

[43] R. Valero and D. G. Truhlar, J. Chem. Phys. **125**, 194305 (2006).

[44] Z. H. Li, R. Valero, and D. G. Truhlar, Theor. Chem. Acc. **118**, 9 (2007).

[45] R. Valero and D. G. Truhlar, J. Phys. Chem. A **111**, 8536 (2007).

[46] R. Valero, D. G. Truhlar, and A. W. Jasper, J. Phys. Chem. A **112**, 5756 (2008).

[47] R. Valero, L. Song, J. Gao, and D. G. Truhlar, J. Chem. Theory Comput. **5**, 1 (2009).

[48] R. Valero and D. G. Truhlar, J. Chem. Phys. **137**, 22A539 (2012).

[49] X. Xu, K. R. Yang, and D. G. Truhlar, J. Chem. Theory Comput. **9**, 3612 (2013).

[50] See, for example, (a) C. Woywod, M. Stengle, W. Domcke, H. Flöthmann, and R. Schinke, J. Chem. Phys. **107**, 7282 (1997); (b) D. Simah, B. Hartke, and H.-J. Werner, J. Chem. Phys. **111**, 4523 (1999); (c) C. Hoyer, X. Xu, D. Ma, L. Gagliardi, and D. G. Truhlar, J. Chem. Phys. **141**, 114104 (2014).

[51] K. Hirao, Chem. Phys. Lett. **190**, 374 (1992); K. Hirao, Chem. Phys. Lett. **196**, 397 (1992); K. Hirao, Int. J. Quantum Chem. **S26**, 517 (1992).

[52] M. W. Schmidt, K. K. Baldridge, J. A. Boatz, S. T. Elbert, M. S. Gordon, J. H. Jensen, S. Koseki, N. Matsunaga, K. A. Nguyen, S. J. Su, T. L. Windus, M. Dupuis, and J. A. Montgomery, J. Comput. Chem. **14**, 1347 (1993); M. S. Gordon and M. W. Schmidt, in *Theory and Applications of Computational Chemistry: The First Forty Years*, edited by C. E. Dykstra, G. Frenking, K. S. Kim, and G. E. Scuseria (Elsevier, Amsterdam, 2005), pp. 1167–1189.

[53] C. A. Mead and D. G. Truhlar, J. Chem. Phys. **70**, 2284-2296 (1979). Erratum: **78**, 6344 (1983).

[54] H. A. Witek, Y.-K. Choe, J. P. Finley, and K. Hirao, J. Comput. Chem. **23**, 957 (2002).

[55] J. T. H. Dunning, J. Chem. Phys. **90**, 1007 (1989).

[56] R. A. Kendall, J. T. H. Dunning, and R. J. Harrison, J. Chem. Phys. **96**, 6796 (1992).

[57] Y. Zhao and D. G. Truhlar, Theor. Chem. Acc. **120**, 215 (2008).

[58] Y. Zhao, and D. G. Truhlar, Acc. Chem. Res. **41**, 157 (2008).

[59] B. J. Lynch, Y. Zhao, and D. G. Truhlar, J. Phys. Chem. A **107**, 1384 (2003).

[60] G. W. T. M. J. Frisch, H. B. Schlegel, G. E. Scuseria, J. R. C. M. A. Robb, G. Scalmani, V. Barone, B. Mennucci, H. N. G. A. Petersson, M. Caricato, X. Li, H. P. Hratchian, J. B. A. F. Izmaylov, G. Zheng, J. L. Sonnenberg, M. Hada, K. T. M. Ehara, R. Fukuda, J. Hasegawa, M. Ishida, T. Nakajima, O. K. Y. Honda, H. Nakai, T. Vreven, J. A. Montgomery, Jr., F. O. J. E. Peralta, M. Bearpark, J. J. Heyd, E. Brothers, V. N. S. K. N. Kudin, T. Keith, R. Kobayashi, J. Normand, A. R. K. Raghavachari, J. C. Burant, S. S. Iyengar, J. Tomasi, N. R. M. Cossi, J. M. Millam, M. Klene, J. E. Knox, J. B. Cross, C. A. V. Bakken, J. Jaramillo, R. Gomperts, R. E. Stratmann, A. J. A. O. Yazyev, R. Cammi, C. Pomelli, J. W. Ochterski, K. M. R. L. Martin, V. G. Zakrzewski, G. A. Voth, J. J. D. P. Salvador, S. Dapprich, A. D. Daniels, J. B. F. O. Farkas, J. V. Ortiz, J. Cioslowski, and D. J. Fox, *Gaussian 09*, Revision C.01 (Gaussian, Inc., Wallingford CT, 2010).

[61] R. Krishnan, J. S. Binkley, R. Seeger, and J. A. Pople, J. Chem. Phys. **72**, 650 (1980).

[62] T. Clark, J. Chandrasekhar, G. W. Spitznagel, and P. V. R. Schleyer, J. Comput. Chem. **4**, 294 (1983).

[63] R. S. Mulliken, Phys. Rev. **50**, 1028 (1936).

[64] W. C. Stwalley and W. T. Zemke, J. Phys. Chem. Ref. Data **22**, 87 (1993).

[65] http://cccbdb.nist.gov/expbondlengths2.asp?descript=rLiH&all=0; accessed 3 October 2014.

[66] M. Hanrath, Mol. Phys. **106**, 1949 (2008).

[67] A. J. C. Varandas, J. Chem. Phys. **131**, 124128 (2009), **135**, 119902(E) (2011).

Chapter 5. Franck-Condon Models for Simulating the Band Shape of Electronic Absorption Spectra

5.1. INTRODUCTION

As described in Section 1.4, simulation of line shapes is an important ingredient needed for understanding and interpreting experimental UV/Vis spectra, and vibronic broadening makes an especially important contribution to the line shapes. The present chapter attempts to account for vibronic broadening without calculating all the individual vibronic-state-to-vibronic-state transition probabilities, which is usually impractical.

I am especially interested in an approach that is suitable for the electronic spectroscopy of complex systems, such as transition metal complexes, that are composed of a fairly large number of electronic excitations. Some approaches to simulate vibronic effects are already available, [1,2,3,4,5,6,7,8,9,10,11,12,13,14,15,16,17,18] as described in Section 1.4; however, most of the existing methods are not suitable for this kind of system. First, many of the methods are too complicated to be applied to many electronic excitations of complex systems. Second, most experimental spectra of complex systems are not resolved, which makes the effort of accurately simulating the fine vibrational structure unnecessarily ambitious. In many situations, what we care about is just an unresolved spectrum, such as the ones usually obtained experimentally. In this chapter I present two models suitable for this purpose, and their usefulness is demonstrated by testing on two multi-mode, multiple-electronic-transition molecules, namely naphthalene and permanganate.

The models are a symmetric Gaussian model and an asymmetric bell-shaped model derived from the time-dependent formulation of absorption spectroscopy developed by Heller and co-workers[19,20,21,22] and that is implemented in the *ORCA* [11,23] computer program. The Gaussian model was derived in ref. 17 but was not tested. Here I correct some mistakes in the derivation, extend it to the asymmetric model, and show that the

simple models are satisfactory for simulating unresolved vibronic spectra. One particular scenario in which these models will be useful is the evaluation of electronic structure methods for simulating an unresolved experimental spectrum. In many of such applications, by using the methods presented here for the width and shape of the bands, combined with the electronic structure method for the location and strength of the bands, we can ensure that the factor that limits the quality of comparison of the simulation to experiment is the electronic structure method itself rather than the treatment of the band shape.

5.2. THEORY

5.2.1. Assumptions about the potential energy surfaces and the transition dipole moments

We will work under the Franck-Condon (FC) approximation, which assumes that the transition dipole moment does not vary with the geometry in the Franck-Condon region relevant to spectroscopy. We also assume that the potential energy surfaces (PESs) are harmonic and that the PESs of the excited states have the same frequencies and normal modes (without Duschinsky rotation[24,25]) as the ground state and that only the equilibrium geometry is shifted. These approximations to the PESs have been evaluated in previous studies, in which they are called the IMDHO (independent mode, displaced harmonic oscillator),[26] LCM (linear coupling model),[27] or VG (vertical gradient)[28] model. Those studies showed that these approximations can often yield satisfactory results when combined with either time-independent or time-dependent methods. In this work we will call these approximations collectively the Franck-Condon displaced-harmonic-oscillator (FC-DHO) approximations. Theses approximations are desirable in practice, especially for complex systems like transition metal complexes, since under these approximations the only quantities needed for simulating a spectrum using the models presented in this work are the vertical excitation energies, oscillator strengths, ground-state vibrational frequencies, and the gradients of excited state PESs with respect to nuclear coordinates at

the ground state equilibrium geometry. We also assume zero temperature so that all the excitations start from the vibrational ground state of the electronic ground state.

5.2.2. The Gaussian FC-DHO model for the vibronic band shape

We present here a straightforward derivation of the model; readers are referred to the literature for more details of this kind of method.[11,16,19,20,21,22] We start from the time-domain expression of the absorption cross section of the *n*th excited state under the Born-Oppenheimer (BO) and FC approximation, incorporating homogeneous and inhomogeneous broadening[11,16]

$$\sigma_n(E) \propto f_n \,\mathrm{Re} \int_0^\infty \left\langle \chi_{00} \middle| \chi_n(t) \right\rangle e^{i(E+E_{00})t/\hbar - \Gamma_n t/\hbar - (1/2)\Theta_n^2 t^2/\hbar^2}\, dt \tag{5.1}$$

where n labels an electronic excited state, E is the energy of the incident photon, f_n is the oscillator strength of the electronic transition, Re is the operator that takes the real part, χ_{00} is the nuclear wave function of the vibrational ground state on the electronic ground state PES, χ_n is the time-dependent nuclear wave function on the excited electronic state PES defined by $\left|\chi_n(t)\right\rangle = e^{-iH_n t/\hbar}\left|\chi_{00}\right\rangle$ where H_n is the nuclear-motion Hamiltonian of the excited state, E_{00} is the energy of the ground vibrational state of the ground electronic state, Γ_n is the homogeneous broadening factor, and Θ_n is the inhomogeneous broadening factor. The Dirac bracket denotes integration over the nuclear coordinates. This is the expression for a single excited electronic state; if multiple excited electronic states are involved, one must sum their contributions. Figure 5.1 illustrates E_{00} and other energetic quantities to be used in following equations.

Next we employ an approximation to the overlap integral of the nuclear wave functions, under the FC-DHO assumption,[22]

$$\left\langle \chi_{00} \middle| \chi_n(t) \right\rangle = \exp\left[\sum_j \left(-\frac{\Delta_{nj}^2}{2}(1 - e^{-i\omega_j t}) - \frac{i\omega_j t}{2} \right) - \frac{i}{\hbar}\Delta E_{0n}^{\mathrm{a}} t \right] \tag{5.2}$$

where the sum runs over all normal modes j, Δ_{nj} is the displacement of dimensionless

normal coordinate j from the ground-state equilibrium geometry to the excited-state equilibrium geometry, ω_j is the frequency of mode j, and $\Delta E_{0n}^{\mathrm{a}}$ is the electronic energy difference between the excited electronic state and the ground electronic state at their respective equilibrium geometries (sometimes called the classical adiabatic excitation energy).

Equations (5.1) and (5.2) can already be used for numerical simulation, and they are implemented in *ORCA*. For simplicity we will call this model the "full FC-DHO model". However, our goal is a simpler model, and next we derive a simple Gaussian model. This model was reported in ref. 17 but here we present a more straightforward derivation, by keeping only the low-order terms in the Taylor expansion of the exponential term in eq (5.2). Such low-order terms will give a useful approximation to the vibronic band.

Expanding the exponential term in eq (5.2) to second order,

$$e^{-i\omega_j t} \approx 1 - i\omega_j t - \frac{1}{2}\omega_j^2 t^2 \tag{5.3}$$

it gives

$$\left\langle \chi_{00} \middle| \chi_n(t) \right\rangle = \exp\left[\sum_j \left(-\frac{i\omega_j t}{2}(\Delta_{nj}^2 + 1) \right) - \frac{i}{\hbar}\Delta E_{0n}^{\mathrm{a}} t + \sum_j \left(-\frac{\Delta_{nj}^2}{4}\omega_j^2 t^2 \right) \right] \tag{5.4}$$

By using eq (5.4) and neglecting the broadening factors, eq (5.1) can be rewritten as

$$\sigma_n(E) \propto f_n \,\mathrm{Re} \int_0^\infty dt e^{-\alpha t^2 + i\beta_n(E)t} \approx f_n e^{-[\beta_n(E)]^2/4\alpha} \tag{5.5}$$

where

$$\beta_n(E) = \frac{E}{\hbar} - \left[\frac{\Delta E_{0n}^{\mathrm{a}} - E_{00}}{\hbar} + \sum_j \frac{\omega_j}{2}(\Delta_j^2 + 1) \right] \tag{5.6}$$

and

$$\alpha = \sum_j \frac{\Delta_j^2 \omega_j^2}{4} \tag{5.7}$$

With the harmonic approximation, we have

$$\sum_j \frac{\omega_j}{2} = \frac{E_{00}}{\hbar} \tag{5.8}$$

and

$$\Delta E_{0n}^{\mathrm{a}} + \sum_j \frac{\hbar\omega_j}{2}\Delta_j^2 = \Delta E_{0a}^{\mathrm{v}} \tag{5.9}$$

so that eq (5.6) simplifies to

$$\beta_n(E) = \frac{1}{\hbar}\left(E - \Delta E_{0n}^{\mathrm{v}}\right) \tag{5.10}$$

where $\Delta E_{0n}^{\mathrm{v}}$ is the vertical excitation energy. Combining eqs (5.5), (5.7), and (5.10) yields the Gaussian FC-DHO approximation:

$$\sigma_n(E) \propto f_n \exp\left(-\frac{\left(E - \Delta E_{0n}^{\mathrm{v}}\right)^2}{\hbar^2 \sum_j \Delta_j^2 \omega_j^2}\right) \tag{5.11}$$

This is a Gaussian function centered at the vertical excitation energy, with a half width at half maximum (HWHM) of $\hbar\sqrt{(\ln 2)\sum_j \Delta_j^2\omega_j^2}$, and with height proportional to the oscillator strength.

To apply the above model, we need f_n (oscillator strength), $\Delta E_{0n}^{\mathrm{v}}$ (vertical excitation energy), ω_j (ground-state vibrational frequencies), and Δ_j (displacements of the excited-state equilibrium geometry relative to the ground state equilibrium geometry in dimensionless normal coordinates) from electronic structure calculations. The first three can be readily obtained from electronic structure calculations. Under the FC-DHO approximations, the displacements can be calculated from the normal modes and frequencies of the ground-state PES and the gradient of the excited-state PES with

respect to nuclear coordinates at the ground-state equilibrium geometry, as discussed in the next subsection.

5.2.3. Deriving the displacement of excited-state equilibrium geometry relative to the ground state equilibrium geometry in the FC-DHO approximation

In this section we are concerned with electronic states only, and by "ground state" and "excited state" we mean electronic ground and excited state, respectively. Let **q** be the vector of the mass-weighted Cartesian displacements from the ground-state equilibrium geometry to an arbitrary geometry, defined by

$$q_i = \sqrt{m_i}\left(x_i - x_i^0\right) \tag{5.12}$$

where i labels one of the $3N$ Cartesian coordinates (N is the number of atoms), x_i is the ith Cartesian coordinate of an arbitrary geometry, m_i is the mass of the atom corresponding to x_i, and x_i^0 is a Cartesian coordinate of the ground-state equilibrium geometry. The excited-state potential energy is expanded to second order about the ground-state equilibrium geometry as

$$E_n(\mathbf{q}) = E_n^0 + \mathbf{g}^T\mathbf{q} + \frac{1}{2}\mathbf{q}^T\mathbf{F}\mathbf{q} \tag{5.13}$$

where E_n^0 is the energy, **g** is the gradient, and **F** is the Hessian of the excited-state PES at the ground-state equilibrium geometry. Notice that because of the mass weighting in eq (5.12), **F** has units of frequency squared. Because we made the FC-DHO approximations, **F** is the same as for the ground state. Therefore, the unitless matrix **A** whose rows are ground-state normal mode eigenvectors diagonalizes the Hessian:

$$\mathbf{A}\mathbf{F}\mathbf{A}^T = \mathbf{\Lambda} \tag{5.14}$$

where **Λ** is a diagonal matrix whose diagonal elements are squares of the ground-state harmonic frequencies.

The equilibrium geometry of the excited state, $\mathbf{q}_0$, is found by setting $\partial E_n/\partial \mathbf{q} = 0$,

$$\left.\frac{\partial E_n}{\partial \mathbf{q}}\right|_{\mathbf{q}=\mathbf{q}_0} = 0 = \mathbf{g} + \mathbf{F}\mathbf{q}_0 \tag{5.15}$$

Therefore

$$\mathbf{q}_0 = -\mathbf{F}^{-1}\mathbf{g} = -\mathbf{A}^T\mathbf{\Lambda}^{-1}\mathbf{A}\mathbf{g} \tag{5.16}$$

Then the displacement in terms of dimensionless normal coordinates is

$$\mathbf{\Delta} = \frac{1}{\sqrt{\hbar}}\mathbf{\Lambda}^{1/4}\mathbf{A}\mathbf{q}_0 \tag{5.17}$$

(Notice that both sides of eq (5.17) are unitless.) The components Δ_j of the vector $\mathbf{\Delta}$ can be used for eq (5.11).

5.2.4. The third-order FC-DHO model

The Gaussian FC-DHO model of eq (5.11) is obtained by expanding the exponential term in eq (5.2) to the second order. A natural extension is to expand it to a higher order. If we expand it to the third order, we have

$$\sigma_n(E) \propto f_n \,\mathrm{Re}\int_0^\infty dt e^{-\alpha t^2 + i[\beta_n(E)t + \gamma t^3]} = f_n \int_0^\infty dt e^{-\alpha t^2} \cos\left(\beta_n(E)t + \gamma t^3\right) \tag{5.18}$$

where α and $\beta_n(E)$ are given by eqs (5.7) and (5.10), and

$$\gamma = \frac{1}{12}\sum_j \Delta_j^2 \omega_j^3 \tag{5.19}$$

The integrand on the right-hand side of eq (5.18) involves a Gaussian centered at $t = 0$, whose amplitude is modulated by a cosine function. The integral will have large values if the cosine function oscillates slowly near $t = 0$ and have small values otherwise. The integral will have its maximum when $\beta_n(E)t + \gamma t^3$ is close to zero near $t = 0$, which occurs if $\beta_n(E)$ is a small negative value since $\gamma > 0$. Therefore, this model gives the maximum of the band being slightly red-shifted compared to the vertical excitation energies. This

red shift of the band maximum is consistent with the observation that the band maximum is normally to the red of the vertical excitation energy.[17] Moreover, if we numerically integrate eq (5.18), we will see, as shown in the Results and Discussion section, that it gives a bell-shaped band with a heavier tail on the high-energy side along with the red-shifted maximum.

In the remainder of the text we will call this model the third-order FC-DHO model.

5.3. COMPUTATIONAL DETAILS

Following the choice of electronic structure method in ref. 42, the ground-state equilibrium geometry of naphthalene was optimized and the vibrational modes and harmonic frequencies computed, by BHandHLYP/TZVP[29,30] as implemented in *Gaussian 09*.[31] TDDFT calculations for the vertical excitation energies, oscillator strengths, and analytic energy gradients were done with the same exchange-correlation functional and basis set.

Following the choice of electronic structure method in ref. 43, the ground-state equilibrium geometry of permanganate anion was optimized, and the vibrational modes and harmonic frequencies computed, by BPW91[32] and the Slater-type TZ2P basis set.[33] Vertical excitation energies and oscillator strengths were computed by the statistical average of orbital potential (SAOP) method[34,35] and the TZ2P basis set. The gradients of the excited states were computed numerically for this molecule.

Gaussian 09[31] was used for the DFT and TDDFT calculations for naphthalene. *ADF*[36,37,38] was used for the DFT and SAOP calculations for permanganate. The ORCA_ASA module of *ORCA*[23] was used for the simulation of spectra based on the full FC-DHO model (eqs (5.1) and (5.2)). A Python package, FCBand,[39] was used for the simulation of spectra based on the Gaussian (eq (5.11)) and third-order (eq (5.18)) FC-DHO models.

5.4. RESULTS AND DISCUSSION

In this section we validate the Gaussian FC-DHO model against the full FC-DHO model and against the experimental spectra of two molecules, naphthalene and

permanganate. These two molecules were chosen because their experimental vibronic spectra are available in the literature,[40,41] and also because there have been previous attempts to simulate these spectra.[42,43] Because we used the electronic structure methods that were previously shown to have good performance for the systems in those studies, we can reduce the error caused by the electronic structure calculations when simulating the spectra so as to better examine the error caused by the band shape assumptions in the models.

We remind the readers that accurately reproducing the vibrational structures of the experimental spectra would require more sophisticated models beyond the full FC-DHO model with the FC-DHO approximations, which is not the purpose of this work. The purpose of the present work is to show that the simple models requiring only a small amount of electronic structure calculation can simulate an unresolved spectrum. Because of the simplicity of the model, it can be applied with a low cost to spectra that are composed of a fairly large number of excited states, even for a fairly complex system like a transition metal complex. We will show that the models give a reasonable shape for the vibronic bands and thus strike a balance between accuracy and computational cost.

5.4.1. Naphthalene

The $S_0 \rightarrow S_2$ transition is the first dipole-allowed transition of naphthalene that has $\pi \rightarrow \pi^*$ (HOMO→LUMO) character. It is considered a prototypical system of the bright excitations of aromatic systems and has been extensively studied.[40,42,44,45] Figure 5.2 compares two models to experiment. The full FC-DHO model, despite the simple FC-DHO approximations, reproduces the vibrational features of the experimental spectrum quite well, especially in the low-energy region. The Gaussian FC-DHO model, which is an approximation to the full FC-DHO model, gives a satisfactory overall shape of the band, although, as expected from the symmetry of the Gaussian function, the Gaussian FC-DHO model gives a symmetric band, while the experimental band is heavier on the right tail than on the left tail.

The third-order FC-DHO model does a better job of simulating the asymmetry of the band. Figure 5.3 shows three simulations for the same excitation of naphthalene. The third-order FC-DHO model has a maximum shifted to lower energy by ~650 cm^{-1} (0.08 eV) compared to the Gaussian FC-DHO model, whose maximum is located at the vertical excitation energy. The third-order FC-DHO model also has an asymmetric shape with a heavier right tail; although it has a non-physical negative left tail, one can simply replace the negative values with zeros for the purpose of simulation. Another interesting comparison can be made between the third-order FC-DHO model and the full FC-DHO model convoluted with a large empirical inhomogeneous broadening of Θ_n = 800 cm^{-1}; such a large broadening is adopted to simulate an unresolved spectrum. The third-order FC-DHO model and the full FC-DHO model have an excellent match (except for the negative left tail of the third-order FC-DHO model). Although the match would not be as good if a different broadening factor were used, the important point here is that the third-order FC-DHO model (like the very close Gaussian FC-DHO model) is capable of simulating the overall shape of an unresolved spectrum.

5.4.2. Permanganate

The permanganate ion, MnO_4^-, has a closed-shell ground state belonging to the A_1 irreducible representation (irrep) of the T_d point group,[46] and only $A_1 \rightarrow T_2$ singlet-singlet transitions are dipole and spin allowed. The absorption spectrum of the four lowest $A_1 \rightarrow T_2$ transitions has been studied experimentally[40] and theoretically.[43] We followed ref. 43 for the electronic structure calculations and the empirical adjustment of vertical excitations, and combined them with our models to simulate the spectrum and to compare with the experimental one in ref. 40. Tables 5 and 5 list the computed vibrational frequencies of the ground state and the vertical excitation energies respectively.

Figure 5.4 shows that for such a complex system as permanganate the full FC-DHO model with the FC-DHO approximation reproduces less well the vibrational features of the experiment than the model does for naphthalene; as ref. 43 shows it needs more sophisticated methods to simulate the vibrational features of permanganate. The

simulated 2 T_2 and 3 T_2 bands are stronger than experiment; such stronger bands may be partly due to the electronic structure as well as to the band shape model. Nonetheless, the Gaussian FC-DHO model is able to produce an overall unresolved profile of the full FC-DHO model. For this case consisting of many bands across a wide energy range, the difference between the Gaussian FC-DHO model and the third-order FC-DHO model (not shown here) is inconsequential.

5.5. SUMMARY

In this work we presented the derivation of a simple Gaussian model and an asymmetric bell-shaped model (the third-order model) for the calculating the vibronic band shape of the electronic spectroscopy of molecules under the FC-DHO (Franck-Condon, displaced harmonic oscillator) approximations. These models are approximations to a more sophisticated time-dependent model (the full FC-DHO model). By testing the new models on the low-lying excitations of two molecules, naphthalene and permanganate, we showed that the models are capable of capturing the unresolved band shape of the full FC-DHO model. The resulting band shapes compare well to the experimental spectra when the FC-DHO approximations are reasonable and when the underlying electronic structure is good for the problem.

Among the two models, the Gaussian model is simpler but does not describe the asymmetry of the bands, whereas the third-order model introduces an asymmetry shape and a red-shifted maximum but needs numerical integration. The third-order model also gives a region of small negative values in the low-energy tail of the spectrum, but in practice these negative values can simply be set to zero.

These models are suitable for simulating the unresolved electronic spectra of complex molecules for the following reasons. First, most experimental spectra of complex systems do not have resolved vibrational fine structure. Second, the models are relatively black-box and do not require decision making or human intervention; therefore they can be easily streamlined to simulate spectra of complex systems such as transition-metal complexes that involve tens or even hundreds of electronic excitations. Third, the

required electronic structure calculations such as ground-state vibrational frequencies and excited-state gradients are relatively inexpensive, and no complicated or error-prone calculations like excited-state geometry optimization are needed. The models are independent of the electronic structure and can be used along with any electronic structure method that is good for the problem at hand. Given the quantities provided by the electronic structure calculations, the added cost for simulating the spectrum is negligible.

Table 5.1. Vibrational frequencies of the ground state of permanganate. [a]

mode	irrep	frequency (cm-1)
1–2	e	349
3–5	t_2	399
6	a_1	875
7–9	t_2	940

[a] Computed by BPW91/TZ2P.

Table 5.2. Oscillator strengths and vertical excitation energies of permanganate.

	f [a]	E_{vert} (eV) [a]	ΔE_{adj} (eV) [b]	$E_{adj\text{-}vert}$ (eV) [c]
1 T_2	6.89E-03	3.00	-0.54	2.46
2 T_2	2.10E-03	4.03	-0.44	3.59
3 T_2	9.58E-03	4.92	-0.79	4.13
4 T_2	2.30E-03	5.95	-0.52	5.43

[a] Oscillator strengths (f) and vertical excitation energies (E_{vert}) computed by SAOP/TZVP.

[b] Empirical adjustment of vertical excitation energies following ref. 43.

[c] Adjusted vertical excitation energies, $E_{adj\text{-}vert} = E_{vert} + \Delta E_{adj}$

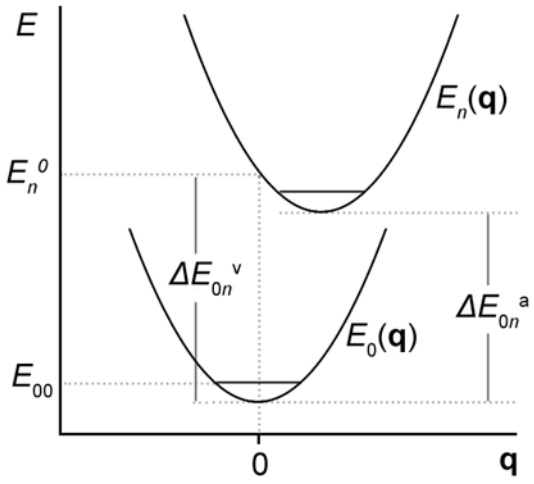

Figure 5.1. Illustration of the PESs of the electronic ground ($E_0(\mathbf{q})$) and excited ($E_n(\mathbf{q})$) states and of some important energies (E_{00} and E_n^0) and energy differences (ΔE_{0n}^{a} and ΔE_{0n}^{v}).

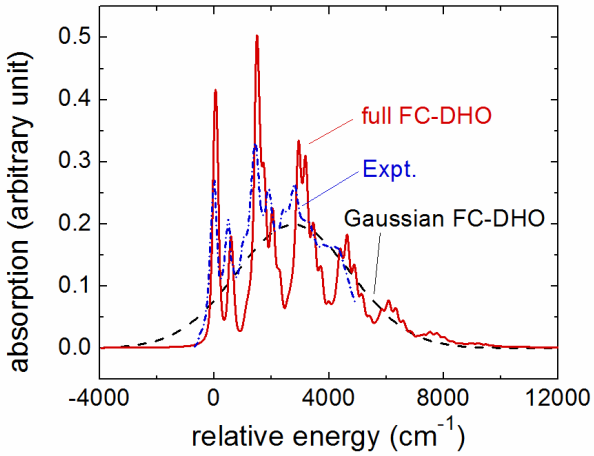

Figure 5.2. Absorption spectrum of the $S_0 \rightarrow S_2$ transition of naphthalene as given by the full FC-DHO model (red solid line), the Gaussian FC-DHO model (black dash line), and the experiment [40] (blue dotted-dash line). (The spectra are horizontally translated to align the 0-0 excitation peak at the zero of energy so as to reduce the error in the position of the bands caused by the electronic structure method. The absorption strengths are scaled for good visual comparison.)

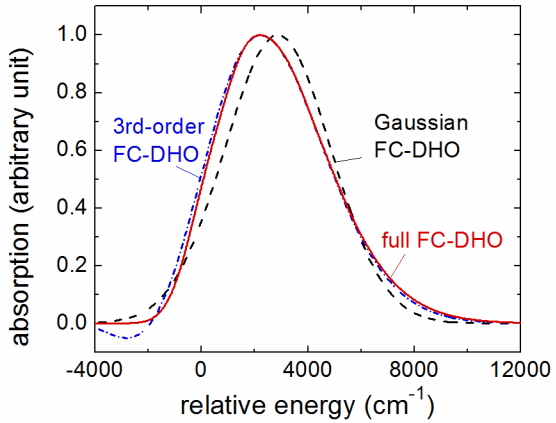

Figure 5.3. Absorption spectrum of the $S_0 \rightarrow S_2$ transition of naphthalene given by the Gaussian FC-DHO model (black dash line), the third-order FC-DHO model (red solid line), and the full FC-DHO model with a large empirical broadening (blue dotted-dash line). (Although it is not necessary in this case, for consistency with the treatment in Figure 5.2, the spectra are horizontally translated to align the 0-0 excitation at zero of energy. The absorption strengths are scaled to have a maximum of unity.)

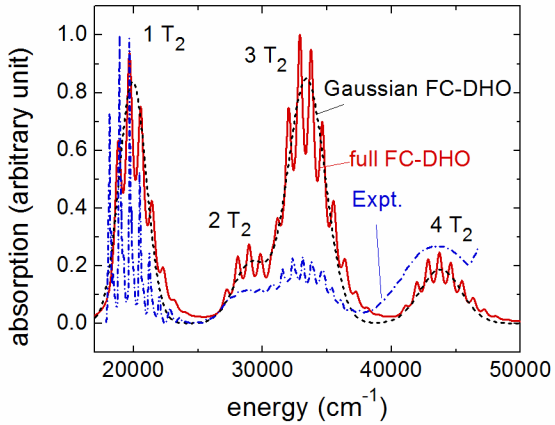

Figure 5.4. Absorption spectrum of the lowest four $A_1 \rightarrow T_2$ singlet-singlet transitions of permanganate given by the full FC-DHO model, the Gaussian FC-DHO model, and the experiment.[40] (The absorption strengths are scaled for proper comparison.)

REFERENCES FOR CHAPTER 5

[1] Jiang, X.; Karlsson, K. M.; Gabrielsson, E.; Johansson, E. M.; Quintana, M.; Karlsson, M.; Sun, L.; Boschloo, G.; Hagfeldt, A. Highly efficient solid-state dye-sensitized solar cells based on triphenylamine dyes. *Adv. Funct. Mater.* **2011**, *21*, 2944.

[2] Yang, C.-H.; Beltran, J.; Lemaur, V.; Cornil, J.; Hartmann, D.; Sarfert, W.; Fröhlich, R.; Bizzarri, C.; De Cola, L. Iridium metal complexes containing N-heterocyclic carbene ligands for blue-light-emitting electrochemical cells. *Inorg. Chem.* **2010**, *49*, 9891.

[3] Farrer, N. J.; Woods, J. A.; Salassa, L.; Zhao, Y.; Robinson, K. S.; Clarkson, G.; Mackay, F. S.; Sadler, P. J. A potent trans-diimine platinum anticancer complex photoactivated by visible light. *Angew. Chem. Int. Ed.* **2010**, *49*, 8905.

[4] Fernández-Hernández, J. M.; Yang, C.-H.; Beltrán, J. I.; Lemaur, V.; Polo, F.; Fröhlich, R.; Cornil, J.; De Cola, L. Control of the mutual arrangement of cyclometalated ligands in cationic iridium (III) complexes. Synthesis, spectroscopy, and electroluminescence of the different isomers. *J. Am. Chem. Soc.* **2011**, *133*, 10543.

[5] Salassa, L.; Garino, C.; Salassa, G.; Gobetto, R.; Nervi, C. Mechanism of ligand photodissociation in photoactivable [Ru (bpy) 2L2] 2+ complexes: a density functional theory study. *J. Am. Chem. Soc.* **2008**, *130*, 9590.

[6] Santoro, F.; Improta, R.; Lami, A.; Bloino, J.; Barone, V. Effective method to compute Franck-Condon integrals for optical spectra of large molecules in solution. *J. Chem. Phys.* **2007**, *126*, 084509.

[7] Santoro, F.; Lami, A.; Improta, R.; Barone, V. Effective method to compute vibrationally resolved optical spectra of large molecules at finite temperature in the gas phase and in solution. *J. Chem. Phys.* **2007**, *126*, 184102.

[8] Santoro, F.; Lami, A.; Improta, R.; Bloino, J.; Barone, V. Effective method for the computation of optical spectra of large molecules at finite temperature including the Duschinsky and Herzberg–Teller effect: the Q x band of porphyrin as a case study. *J. Chem. Phys.* **2008**, *128*, 224311.

[9] Hazra, A.; Nooijen, M. Derivation and efficient implementation of a recursion formula to calculate harmonic Franck–Condon factors for polyatomic molecules. *Int. J. Quantum Chem.* **2003**, *95*, 643.

[10] Charaf-Eddin, A.; Cauchy, T.; Felpin, F. X.; Jacquemin, D. Vibronic Spectra of Organic Electronic Chromophores, *RSC Adv.* **2014***, 4*, 55466.

[11] Petrenko, T.; Neese, F. Analysis and prediction of absorption band shapes, fluorescence band shapes, resonance Raman intensities, and excitation profiles using the time-dependent theory of electronic spectroscopy. *J. Chem. Phys.* **2007**, *127*, 164319.

[12] Tang, J.; Lee, M. T.; Lin, S. H. Effects of the Duschinsky mode-mixing mechanism on temperature dependence of electron transfer processes. *J. Chem. Phys.* **2003**, *119*, 7188.

[13] Ianconescu, R.; Pollak, E. Photoinduced cooling of polyatomic molecules in an electronically excited state in the presence of Dushinskii rotations. *J. Phys. Chem. A* **2004**, *108*, 7778.

[14] Peng, Q.; Niu, Y.; Deng, C.; Shuai, Z. Vibration correlation function formalism of radiative and non-radiative rates for complex molecules. *Chem. Phys.* **2010**, *370*, 215.

[15] Santoro, F.; Jacquemin, D. Going beyond the vertical approximation with time-dependent density functional theory, *WIREs Comput. Mol. Sci.* **2016**, *6*, 460.

[16] Aidas, K.; Jacob Kongsted, J.; Osted, A.; Mikkelsen, K. V. Coupled cluster calculation of the *n* $\rightarrow \pi^*$ electronic transition of acetone in aqueous solution. *J. Phys. Chem. A* **2005***, 109*, 8001-8010.

[17] Crespo-Otero, R.; Barbatti, M. Spectrum simulation and decomposition with nuclear ensemble: formal derivation and application to benzene, furan and 2-phenylfuran. *Theor. Chem. Acc.* **2012**, *131*, 1.

[18] Marenich, A. V.; Cramer, C. J.; Truhlar, D. G. Electronic absorption spectra and solvatochromic shifts by the vertical excitation model: solvated clusters and molecular dynamics sampling. *J. Phys. Chem. B* **2014**, *119*, 958.

[19] Heller, E. J. Quantum corrections to classical photodissociation models. *J. Chem. Phys.* **1978**, *68*, 2066.

[20] Lee, S. Y.; Heller, E. J. Time-dependent theory of Raman scattering. *J. Chem. Phys.* **1979**, *71*, 4777.

[21] Kulander, K. C.; Heller, E. J. Time dependent formulation of polyatomic photofragmentation: Application to H3+. *J. Chem. Phys.* **1978**, *69*, 2439.

[22] Tannor, D. J.; Heller, E. J. Polyatomic Raman scattering for general harmonic potentials. *J. Chem. Phys.* **1982**, *77*, 202.

[23] Neese, F. The ORCA program system. *WIREs Comput. Mol. Sci.* **2012**, *2*, 73.

[24] Duschinsky, F. On the interpretation of electronic spectra of polyatomic molecules. I: The Franck-Condon principle. *Acta Physicochim. URSS* **1937***, 7*, 551.

[25] Kupka, H. J. *Transitions in molecular systems*; WILEY-VCH Verlag GmbH & Co. KGaA: Weinheim, 2010.

[26] Karasulu, B.; Götze, J. P.; Thiel, W. Assessment of Franck–Condon methods for computing vibrationally broadened UV–Vis absorption spectra of flavin derivatives: riboflavin, roseoflavin, and 5-thioflavin. *J. Chem. Theory Comput.* **2014**, *10*, 5549.

[27] Macak, P.; Luo, Y.; Ågren, H. Simulations of vibronic profiles in two-photon absorption. *Chem. Phys. Lett.* **2000**, *330*, 447.

[28] Ferrer, F. J. A.; Santoro, F. Comparison of vertical and adiabatic harmonic approaches for the calculation of the vibrational structure of electronic spectra. *Phys. Chem. Chem. Phys.* **2012**, *14*, 13549.

[29] Schäfer, A.; Horn, H.; Ahlrichs, R. Fully optimized contracted Gaussian basis sets for atoms Li to Kr. *J. Chem. Phys.* **1992**, *97*, 2571.

[30] Schäfer, A.; Huber, C.; Ahlrichs, R. Fully optimized contracted Gaussian basis sets of triple zeta valence quality for atoms Li to Kr. *J. Chem. Phys.* **1994**, *100*, 5829.

[31] Frisch, M. J.; Trucks, G. W.; Schlegel, H. B.; Scuseria, G. E.; Robb, M. A.; Cheeseman, J. R.; Scalmani, G.; Barone, V.; Mennucci, B.; Petersson, G. A.; Nakatsuji, H.; Caricato, M.; X. Li; Hratchian, H. P.; Izmaylov, A. F.; Bloino, J.; Zheng, G.; Sonnenberg, J. L.; Hada, M.; Ehara, M.; Toyota, K.; Fukuda, R.; Hasegawa, J.; Ishida, M.; Nakajima, T.; Honda, Y.; Kitao, O.; Nakai, H.; Vreven, T.; Montgomery, J. A., Jr.; Peralta, J. E.; Ogliaro, F.; Bearpark, M.; Heyd, J. J.; Brothers, E.; Kudin, K. N.; Staroverov, V. N.; Keith, T.; Kobayashi, R.; Normand, J.; Raghavachari, K.; Rendell, A.; Burant, J. C.; Iyengar, S. S.; Tomasi, J.; Cossi, M.; Rega, N.; Millam, J. M.; Klene, M.; Knox, J. E.; Cross, J. B.; Bakken, V.; Adamo, C.; Jaramillo, J.; Gomperts, R.; Stratmann, R. E.; Yazyev, O.; Austin, A. J.; Cammi, R.; Pomelli, C.; Ochterski, J. W.; Martin, R. L.; Morokuma, K.; Zakrzewski, V. G.; Voth, G. A.; Salvador, P.; Dannenberg, J. J.; Dapprich, S.; Daniels, A. D.; Farkas, O.; Foresman, J. B.; Ortiz, J. V.; Cioslowski, J.; Fox, D. J.; *Gaussian 09* D.01 ed.; Gaussian, Inc., Wallingford CT: 2010.

[32] Becke, A. D. Density-functional exchange-energy approximation with correct asymptotic behavior. *Phys. Rev. A* **1988**, *38*, 3098.

[33] Van Lenthe, E.; Baerends, E. J. Optimized Slater-type basis sets for the elements 1–118. *J. Comput. Chem.* **2003**, *24*, 1142.

[34] Schipper, P.; Gritsenko, O.; Van Gisbergen, S.; Baerends, E. Molecular calculations of excitation energies and (hyper) polarizabilities with a statistical average of orbital model exchange-correlation potentials. *J. Chem. Phys.* **2000**, *112*, 1344.

[35] Gritsenko, O.; Schipper, P.; Baerends, E. Approximation of the exchange-correlation Kohn–Sham potential with a statistical average of different orbital model potentials. *Chem. Phys. Lett.* **1999**, *302*, 199.

[36] Te Velde, G. t.; Bickelhaupt, F. M.; Baerends, E. J.; Fonseca Guerra, C.; van Gisbergen, S. J.; Snijders, J. G.; Ziegler, T. Chemistry with ADF. *J. Comput. Chem.* **2001**, *22*, 931.

[37] Guerra, C. F.; Snijders, J.; Te Velde, G.; Baerends, E. Towards an order-*N* DFT method. *Theor. Chem. Acc.* **1998**, *99*, 391.

[38] ADF2014, SCM, Theoretical Chemistry, Vrije Universiteit, Amsterdam, The Netherlands, http://www.scm.com (accessed March 14, 2017).

[39] S. L. Li and D. G. Truhlar, FCBand 2017; available for free download at http://comp.chem.umn.edu/fcband/ (accessed March 26, 2017).

[40] Ferguson, J.; Reeves, L.; Schneider, W. Vapor absorption spectra and oscillator strengths of naphthalene, anthracene, and pyrene. *Can. J. Chem.* **1957**, *35*, 1117.

[41] Holt, S. L.; Ballhausen, C. J. Low temperature absorption spectra of $KMnO_4$ in $KClO_4$. *Theor. Chim. Acta* **1967**, *7*, 313.

[42] Dierksen, M.; Grimme, S. The vibronic structure of electronic absorption spectra of large molecules: a time-dependent density functional study on the influence of "Exact" Hartree− Fock exchange. *J. Phys. Chem. A* **2004**, *108*, 10225.

[43] Neugebauer, J.; Baerends, E. J.; Nooijen, M. Vibronic structure of the permanganate absorption spectrum from time-dependent density functional calculations. *J. Phys. Chem. A* **2005**, *109*, 1168.

[44] Hashimoto, T.; Nakano, H.; Hirao, K. Theoretical study of the valence π→π* excited states of polyacenes: Benzene and naphthalene. *J. Chem. Phys.* **1996**, *104*, 6244.

[45] Schreiber, M.; Silva-Junior, M. R.; Sauer, S. P. A.; Thiel, W. Benchmarks for electronically excited states: CASPT2, CC2, CCSD, and CC3. *J. Chem. Phys.* **2008**, *128*, 134110.

[46] Ziegler, T. A chronicle about the development of electronic structure theories for transition metal complexes. In *Molecular Electronic Structures of Transition Metal Complexes II*; Mingos, D. M. P., Day, P., Dahl, J. P., Eds.; Springer-Verlag: Berlin Heidelberg, 2012.

Chapter 6. Photochemistry and Spectroscopy of Thioanisole. I. Computational Simulation and Interpretation of the Low-Lying Excited Electronic States and Electronic Spectrum

6.1. INTRODUCTION

As discussed by Sobolewski, Domcke, and coworkers,[1,2,3,4] many organic molecules with aromatic rings and heteroatoms have photoinduced hydrogen detachment channels in the gas phase and proton transfer channels in protic solvents that are mediated by a repulsive $^1\pi\sigma^*$ or $^1n\sigma^*$ state. Among these, phenol and thiophenol, as well as their derivatives anisole and thioanisole, exhibit qualitatively similar potential energy profiles that may be considered prototypes of this behavior.[5,6,7,8,9,10,11,12,13] For thioanisole, the existence and nature of the $^1n\sigma^*$ state has been identified and discussed in previous work.[13,14] It was conjectured, based on complete active space self-consistent field (CASSCF) calculations and spectroscopic studies, that the ultrafast dynamics of the photodissociation of thioanisole into thiophenoxyl and methyl radicals is facilitated by the coupling of the optically accessible $^1\pi\pi^*$ state to the dark $^1n\sigma^*$ state. The detailed mechanism of the reaction is, however, still open to question.

Our ultimate goal is to use theory and computation to gain more insight into the mechanism, by constructing the potential energy surfaces of the relevant ground and excited states and performing dynamical simulation on the coupled surfaces. As the first step, in this chapter we study the ultraviolet absorption spectrum of thioanisole to obtain more information about the character of the electronic excited states in the Franck-Condon region and to validate electronic structure methods for calculating these states. A vapor-phase experimental spectrum was reported in a recent article[14] but has yet to be fully interpreted and understood. Instead of assigning states to the spectral bands simply according to their vertical excitation energies and transition probabilities, we attempt to

simulate the spectrum using a normal-mode sampling strategy as detailed below so as to directly compare the simulated profile to the experimental spectrum.

The rest of this chapter will proceed as follows. After describing the computational details in Section 6.2, we discuss in Section 6.3 the optimized geometries of S_0 and S_1, the character of the excited states, and the interpretation of the electronic spectrum based on our simulation. Finally we conclude our discussion in Section 6.4.

6.2. COMPUTATIONAL DETAILS

6.2.1. Basis sets, electronic structure methods, and software

We used five basis sets. In order of decreasing completeness, they are:

• augmented correlation-consistent polarized valence triple zeta with an additional tight d function for sulfur: aug-cc-pV(T+d)Z;[15,16,17]

• minimally augmented, multiply polarized valence triple zeta: MG3S;[18]

• minimally augmented, polarized valence triple zeta (multiply polarized for sulfur), denoted as MB hereafter: 6-311+G(d)[19,20] for carbon and hydrogen and MG3S for sulfur;

• partially augmented, correlation-consistent polarized valence double zeta with an additional tight d function for sulfur: jun-cc-pV(D+d)Z;[15,16,17, 21]

• minimally augmented, polarized valence double zeta: 6-31+G(d);[20,22,23,24]

We used both Kohn-Sham density functional theory (KS-DFT) and wave function theory (WFT) for electronic structure calculations. The levels of theory and their abbreviations are listed in Table 6.1 along with references[25,26,27,28,29,30,31,32,33,34,35,36,37,38,39,40,41,42] that explain each level of theory.

We used the following software to perform various types of calculations: *Gaussian 09*,[43] *GAMESS*,[44,45] *NWChem*,[46] *ANT* (incorporating the MOPAC 5.021mn code),[47,48] and *Multiwfn*.[49] The calculations done with each software package are listed in Table 6.2.

6.2.2. Coordinates and geometry optimization

The equilibrium geometry of both S_0 and S_1 has C_S symmetry with the symmetry plane in the phenyl ring. The equilibrium geometry of S_0 is shown in Figure 6.1, which also illustrates our convention for numbering the carbon atoms. The molecular orientation is defined by putting the C2, C1, and S atoms in the *xy* plane with the C1-S bond pointing to the positive *x* direction.

The ground-state equilibrium geometry was optimized by M06-2X/MG3S and by CASSCF(12,11)/MB.[50] The equilibrium geometry of S_1 was also optimized by CASSCF(12,11)/MB. The 11 active orbitals used in the CASSCF(12,11) calculations nominally correspond to three π and three π^* on the phenyl ring, two $\sigma_{C\text{-}S}$ and two $\sigma_{C\text{-}S}^*$ on the C1-S and S-C7 bonds, and $n(p_z)$ on the sulfur. (See Figure 6.2.) All the active orbitals delocalize to some extent; for example, the two $\sigma_{C\text{-}S}$ have components on both the C1-S and S-C7 bonds, and the orbital we label as $n(p_z)$ has both a component on S and a π component on the ring.

6.2.3. Excitation energies and simulation of the electronic absorption spectrum in the vapor phase

The vertical excitation energies (VEEs) to the two or three lowest singlet excited states in the Franck-Condon region were calculated by MC-QDPT, XMC-QDPT, EOM-CCSD, CR-EOM-CCSD(T), TDDFT, and TDA-TDDFT. (X)MC-QDPT calculations were carried out with a three-dimensional model space based on an SA(3)-CASSCF(12,11) reference. The 11-orbital active space has the same character as described in Section 6.2.2.

Our strategy to simulate the spectrum of the vapor-phase thioanisole at low pressure is to sample a certain number of representative geometries according to the ground-state vibrational distribution, calculate their contributions to the spectrum, and add the contributions. In particular, we first optimized the ground-state geometry of thioanisole and performed normal mode analysis by the semiempirical PM3 method. We then

sampled 200 geometries with a ground-state harmonic oscillator distribution along each Cartesian normal coordinate. For each sampled geometry, we calculated the VEEs and oscillator strengths of the four lowest excited states using TDA–τ-HCTHhyb/6-31+G(d). These VEEs and oscillator strengths from the sampled geometries were collected to generate a stick spectrum. This stick spectrum accounts for the broadening and peak shift of the spectrum due to the statistical distribution of geometries generated by ground-state molecular vibrations, taking into account also the dependence of transition probabilities on geometry. Finally, we broadened the sticks with Gaussian functions with half width at half maximum (HWHM) equal to 0.15 eV to produce a smooth profile of electronic spectrum. The Gaussian broadening mimics the missing effects such as broadening due to lifetime broadening, thermally excited vibrations, rotational broadening, anharmonic broadening, and instrumental resolution. At the longest wavelengths, the resolution is presumably limited by spectral congestion (the jet-cooled excitation spectrum in ref. [51] shows resolved rovibrational structure). At shorter wavelengths, lifetime broadening probably dominates.

6.3. RESULTS AND DISCUSSION

6.3.1. Optimized geometries of S_0 and S_1

The optimized geometry of S_0 has C_S symmetry with phenyl, S, C7, and one H of the methyl group in a plane and the other two hydrogens of the methyl group above and below the plane. The length of the C1–S and S–C7 bonds given by M06-2X (by CASSCF) are 1.76 Å (1.80 Å) and 1.80 Å (1.83 Å) respectively. The C1-S-C7 bond angle given by M06-2X (by CASSCF) is 102.88° (103.84°). The length of the C–C bonds in the phenyl ring is in the range of 1.38–1.40 Å by either method. Originally there was debate on whether the C2-C1-S-C7 torsion at the ground-state equilibrium of thioanisole is zero or not, but recent experiments and electronic structure calculations support the former,[51,52] with which our results are consistent. Since M06-2X is more reliable for geometries than CASSCF (because the latter lacks dynamic correlation), we use the M06-2X geometry as

the equilibrium geometry for S_0 in the following calculations, except for the calculation of adiabatic excitation energy as will be discussed below.

The optimized geometry of S_1 by CASSCF(12,11)/MB is similar to the S_0 equilibrium geometry optimized at the same level, with the C–C bonds in the phenyl ring lengthened by ~0.03 Å, the C1–S bond shortened by 0.03 Å, the S-C7 bond lengthened by 0.02 Å, and the C1-S-C7 bond angle increased by 1°, which is also consistent with previous work.[51]

6.3.2. Nature of the four lowest singlet states and electronic spectroscopy

For the photochemistry of thioanisole with the low excitation energies (~4.2–4.5 eV) used in the experiments,[13,14] only the two lowest singlet electronically excited states (S_1 and S_2) are deemed to be important. However, the third excited singlet state (S_3) makes an important contribution to the spectrum, so in this section we consider the four lowest singlet states. At the equilibrium geometry of the ground state with C_S symmetry, S_0 is a closed-shell state belonging to the A′ irreducible representation (irrep), S_1 and S_3 are $^1\pi\pi^*$ states (simply to be called $\pi\pi^*$) belonging to the A′ irrep, and S_2 is a $^1n\sigma^*$ state (simply to be called $n\sigma^*$) belonging to the A″ irrep. The dominant configurations of the four states given by SA-CASSCF are listed in Table 6.3. Table 6.3 actually shows that one of the dominant configurations of both S_1 and S_3 has $n\pi^*$ character, but considering the facts that the other dominant configuration is $\pi\pi^*$ and that the n orbital also has π character, we simply follow other authors[13,14] and label S_1 and S_3 as $\pi\pi^*$.

The vertical excitation energies (VEEs) calculated by a variety of electronic structure methods are listed in Table 6.4. There are several messages we can take from this table. Firstly, MC-QDPT and XMC-QDPT based on the same SA-CASSCF reference give essentially the same VEEs at the S_0 equilibrium geometry. Secondly, SA(3)-MC-QDPT(12,11) and CR-EOM-CCSD(T), which are very different kinds of high-level methods, give very similar VEEs when used with the extensive aug-cc-

pV(T+d)Z basis set, which suggests that both should be quite accurate. Thirdly, TDA–τ-HCTHhyb with a small 6-31+G* basis set gives VEEs close to our best estimate values from CR-EOM-CCSD(T)/aug-cc-pV(T+d)Z. Because of the accuracy and low computational cost of TDA–τ-HCTHhyb/6-31+G*, we use it for the simulation of electronic spectrum discussed later.

To further validate the methods we use, we calculate the $S_1 \leftarrow S_0$ adiabatic excitation energy by using the following formula:

$$\Delta E^{(0-0)}(S_1 \leftarrow S_0) = V_e(S_1) + ZPE(S_1) - V_e(S_0) - ZPE(S_0) \qquad (6.1)$$

where V_e (S_i) (i = 0, 1) is the electronic energy of S_i calculated by SA(3)-MC-QDPT(12,11)/MB at the S_i geometry optimized by CASSCF(12,11)/MB, and ZPE(S_i) is the zero-point energy of S_i calculated by CASSCF(12,11)/MB. The calculated adiabatic excitation energy is 4.22 eV, in excellent agreement with the experimental value of 4.28 eV.[13,14,51]

The S_1 state is often called a "bright" state;[14] even though this description makes sense as compared to the dark $n\sigma^*$ state, some readers may think it corresponds to the bright band of the experimental vapor-phase UV absorption spectrum which peaks at 4.96 eV [see Figure 6.3(a)]. This view may be strengthened by our EOM-CCSD/aug-cc-pV(T+d)Z calculation, which gives the $S_1 \leftarrow S_0$ VEE equal to 4.84 eV (see Table 6.4). However, if we compare our best estimate of $S_1 \leftarrow S_0$ VEE by CR-EOM-CCSD(T) (4.53 eV) to the maximum of the experimental spectrum (4.96 eV), the discrepancy is as large as 0.4 eV. On the other hand, the experimental adiabatic excitation energy of 4.28 eV[13,14] also differs significantly from the maximum of the spectral band. These facts imply that the experimentally bright band may not correspond to the $S_1 \leftarrow S_0$ excitation.

There have been disagreements in the literature about the nature of states and the interpretation of the electronic spectrum. For instance, Lim *et al.*[13] and Roberts *et al.*[14] reported S_1 as a bright $\pi\pi^*$ state and S_2 a dark $n\sigma^*$ state, and Roberts *et al.* assigned the strong absorption band peaked at ~4.9 eV to $S_3 \leftarrow S_0$ transition based on their single-

point TD-CAM-B3LYP, LR-CCSD, and CCSDR(3) calculations, although their calculated $S_3 \leftarrow S_0$ VEE is higher than 5.3 eV. Liu *et al.*,[53] on the other hand, reported S_1 as a dark $\pi\pi^*$ state, S_2 a bright $\pi\pi^*$ state, and S_3 a dark $n\sigma^*$ state based on their TD-B3LYP/6-31G(d) calculation, assigning the experimental band to $S_2 \leftarrow S_0$ transition. Our calculations of VEEs (Table 6.4) and oscillator strengths (Table 6.5) suggest the same assignment as refs. 13 and 14. Interestingly, our TD-B3LYP/MB calculation disagrees with the TD-B3LYP/6-31G(d) calculation in ref. 53 on the nature of the states while our calculation agrees with ref. 14. The reason why the TD-B3LYP/6-31G(d) calculation in ref. 53 gave incorrect results is that the lack of diffuse functions in the 6-31G(d) basis set fails to properly describe the $n\sigma^*$ state because it has a significant amount of Rydberg character, which makes their calculated excitation energy for the first $n\sigma^*$ state (which should be S_2) higher than the second $\pi\pi^*$ state (which should be S_3). We confirmed this explanation of the source of error in their calculation by performing a TD-B3LYP/6-31+G(d) calculation, which gives the first $n\sigma^*$ state lower than the second $\pi\pi^*$ state.

To further clarify the nature of states and the interpretation of the electronic spectrum, we simulated the spectrum in the vapor phase using a normal-mode sampling approach as described in Section 6.2.3. The experimental spectrum shown in Figure 6.3(a), as a reproduction of Figure S6 in the Electronic Supplementary Information of ref. 14, has two closely located peaks at 239 nm (5.19 eV) and 250 nm (4.96 eV) respectively. We aim to simulate the lower-energy peak at 250 nm only, in order to verify our understanding of the lowest excited states (but we will discuss the other peak later in this section). We are interested in the three lowest excitations because we expect that, according to our calculated vertical excitations, the second $\pi\pi^*$ state (S_3 at the equilibrium geometry) may be responsible for the strong band at 250 nm. In practice we calculated the four lowest excitations because at some sampled geometries the second $\pi\pi^*$ state is S_4.

The simulated spectrum shown in Figure 6.3(b) has a strong band peaked at 243 nm (5.10 eV) and a tail extending to longer wavelengths. Compared to Figure 6.3(a), Figure

6.3(b) has an overall shift to higher energy, but the profile reasonably resembles the experiment. Although the peak of the experimental spectrum is at 250 nm (4.96 eV), 0.14 eV is an acceptable error for this type of simulation. The other peak of Figure 6.3(a) at higher energy does not appear in the simulation, which will be discussed further later. Despite the small quantitative differences, this simulation further supports our characterization of the excited states and our interpretation of the electronic spectrum.

Another important datum here is that the peak of the simulated spectrum (5.10 eV) shifts to longer wavelength compared to the VEE calculated at the same TDA–τ-HCTChyb/6-31+G* level (5.18 eV) by a non-negligible amount (0.08 eV). This result is computed with harmonic vibrations, and if anharmonicity were taken into account the shift could be even larger.[54] This indicates that one should not take the wavelength of the peak of an unresolved electronic spectrum as a "benchmark" of VEE, a conclusion that has long been recognized but is still often ignored.

A noteworthy point is that our TDDFT (with B3LYP and τ-HCTHhyb) and SA-CASSCF calculations do not reveal another electronic state energetically near the bright $\pi\pi^*$ state that has comparable transition probability to that state, at either the equilibrium geometry or nearby geometries in the Franck-Condon region. Accordingly the two peaks of the experimental spectrum at 239 and 250 nm may correspond to the same electronic state but be split vibronically, although the splitting is rather large (0.23 eV). More study will be needed to clarify why there are two peaks. We emphasize that the aim of the present simulation is to clarify the nature of the excited states and the spectrum—not to quantitatively reproduce the experimental band shape. Achieving a quantitative simulation of the band shape, including reproducing the fine features at ~280–290 nm, may require more realistic sampling of the ground-state potential energy surface, explicitly taking into account the anharmonicity of the surfaces and hot bands, and accounting for the quantization of vibrations.

The transitions between the states can be further understood by examining their oscillator strengths and transition dipole moments. All of these transitions are allowed since in the C_S symmetry the x and y components of the dipole operator transform as the

A′ irrep and the *z* component as the A" irrep, and accordingly the *x* and *y* components of the dipole operator couple S_1 and S_3 (A′) to S_0 (A′) and the *z* component couples S_2 (A") to S_0. As displayed in Table 6.5, SA-CASSCF, EOM-CCSD, and TDDFT qualitatively agree on the large oscillator strength of the $S_3 \leftarrow S_0$ transition. EOM-CCSD and TDDFT agree as well on the oscillator strengths of $S_1 \leftarrow S_0$ being one order of magnitude smaller than that of $S_3 \leftarrow S_0$ and on the oscillator strength of $S_2 \leftarrow S_0$ being negligible. The small oscillator strength of the $S_2 \leftarrow S_0$ transition may be attributed to the relatively small spatial overlap of the $n(p_z)$ and σ* orbitals involved in the transition. SA-CASSCF predicts the oscillator strength of $S_1 \leftarrow S_0$ to be smaller than of $S_2 \leftarrow S_0$, both two orders of magnitudes smaller than that of $S_3 \leftarrow S_0$, which is inaccurate due to lack of dynamical correlation.

6.4. CONCLUDING REMARKS

In this chapter, we clarified the nature of the four lowest singlet states of thioanisole at the equilibrium geometry using various wave function and density functional methods. We simulated the electronic absorption spectrum using a normal mode sampling approach, and its good agreement with experiment confirms our understanding of the spectrum, which is as follows. The transitions from S_0 (closed-shell) to S_1 (ππ*) and to S_2 (nσ*) both have relatively small probability and contribute to the low-energy tail of the spectrum, whereas $S_3 \leftarrow S_0$ is mainly responsible for the bright band at 250 nm. We also confirmed that TDDFT, CR-EOMCCSD(T), MC-QDPT, and XMC-QDPT are all reasonably accurate for computing the excitation energies. For potential energy surfaces, however, MC-QDPT and XMC-QDPT are more desirable at the current stage of development. Since XMC-QDPT generates smoother potential energy surfaces near state intersections,[36] it appears suitable for future work of constructing the potential energy surfaces of thioanisole.

Table 6.1. Electronic structure methods [a]

Abbreviation	Name of method	Ref.
M06-2X	M06-2X exchange-correlation functional	25
TD–M06-2X	linear-response time-dependent density functional theory (TDDFT) with the M06-2X exchange-correlation functional	25,26
TD–B3LYP	TDDFT with the B3LYP exchange-correlation functional	27
TDA–τ-HCTHhyb	TDA-TDDFT (TDDFT with the Tamm-Dancoff approximation) with the τ-HCTHhyb exchange-correlation functional	28,29,30, 31
CASSCF(n,m)	single-state complete active space self-consistent-field theory with n active electrons in m active orbitals	32
SA-CASSCF(n,m)[b]	state-averaged complete-active-space self-consistent-field theory with n active electrons in m active orbitals	33
MC-QDPT[c]	multi-configurational quasi-degenerate perturbation theory	34,35
XMC-QDPT[c]	extended multi-configurational quasi-degenerate perturbation theory	36
EOM-CCSD[d]	equation-of-motion coupled cluster theory with singles and doubles	37,38
CR-EOM-CCSD(T)[d,e]	completely-renormalized equation-of-motion coupled cluster theory with singles, doubles, and noniterative connected triples	39,40
PM3	parametrized model 3	41,42

[a] All KS-DFT calculations in this chapter used an ultrafine (99,590) grid with 99 radial shells and 590 grid points per shell for numerical integration except the TDA-TDDFT calculations for simulating the electronic spectrum, which used a fine (75,302) grid.

[b] SA(N)-CASSCF denotes that the average is over N states. In this chapter, state averages are always carried out with equal weights for all states averaged.

[c] All MC-QDPT and XMC-QDPT calculations were carried out with intruder state avoidance[55] with an energy denominator shift of 0.02 E_h.

[d] In these calculations, the 1s orbitals on H and C and the 1s, 2s, and 2p orbitals on S were not correlated.

[e] All CR-EOM-CCSD(T) calculations were carried out with variant IA of the method for the so-called δ-corrected excitation energies which incorporates a noniterative connected triples correction to EOM-CCSD excitation energies rather than to state energies.

Table 6.2. Software and calculations

Software	Ref. for software	Calculations done with the software
Gaussian 09	43	KS-DFT, TDDFT, TDA-TDDFT
GAMESS	44,45	CASSCF, SA-CASSCF, MC-QDPT, XMC-QDPT
NWChem	46	EOM-CCSD, CR-EOM-CCSD(T)
ANT	47,48	Geometry sampling for the simulation of electronic spectrum
Multiwfn	49	Gaussian broadening for the simulation of electronic spectrum

Table 6.3. The CI coefficients of the dominant configurations of the four lowest singlet states of thioanisole at the equilibrium geometry[a] as calculated by SA(4)-CASSCF(12,11)/MB.

state	dominant configuration(s)[b]	CI coefficient
S_0	222222 00000	0.93
S_1	222221 10000	0.62
	222212 00100	0.58
S_2	222221 01000	0.84
	222122 01000	0.33
S_3	222221 00100	0.86
	222122 00100	0.26

[a] Geometry optimized by M06-2X/MG3S.

[b] The occupation numbers of the dominant configurations correspond to orbitals in Figure 6.2 in the same order.

Table 6.4. Vertical excitation energies (in eV) as calculated by different methods and basis sets. [a]

method	basis	$S_1\,(2\,A')$	$S_2\,(1\,A'')$	$S_3\,(3\,A')$
EOM-CCSD	aug-cc-pV(T+d)Z	4.84	5.21	5.52
CR-EOM-CCSD(T)	aug-cc-pV(T+d)Z	4.53	5.03	5.25
TD–M06-2X	MG3S	4.94	5.05	5.30
TD–B3LYP	MB	4.60	4.82	5.00
TDA–τ-HCTHhyb	6-31+G*	4.65	4.97	5.18
TD-CAM-B3LYP [b]	aug-cc-pVTZ	4.95	5.14	5.31
SA(3)-MC-QDPT(12,11)	MB	4.64	5.13	-
SA(3)-XMC-QDPT(12,11)	MB	4.64	5.13	-
SA(3)-MC-QDPT(12,11)	aug-cc-pV(T+d)Z	4.52	5.02	-

[a] All data are from this work, calculated at the equilibrium geometry optimized by M06-2X/MG3S, unless specified otherwise.

[b] Ref. 14.

Table 6.5. Oscillator strengths as calculated by different methods and basis sets . [a]

method	basis	$S_1\,(2\,A')$	$S_2\,(1\,A'')$	$S_3\,(3\,A')$
EOM-CCSD	jun-cc-pV(D+d)Z	0.0086	0.0000	0.2745
TD–M06-2X	MG3S	0.0177	0.0001	0.2628
TD–B3LYP	MB	0.0158	0.0001	0.2433
TDA–τ-HCTHhyb	6-31+G*	0.0177	0.0001	0.2938
TD-CAM-B3LYP [b]	aug-cc-pVTZ	0.0154	0.0005	0.2311
SA(4)-CASSCF(12,11)	MB	0.0005	0.0014	0.3832

[a] All data are from this work, calculated at the equilibrium geometry optimized by M06-2X/MG3S, unless specified otherwise.

[b] Ref. 14.

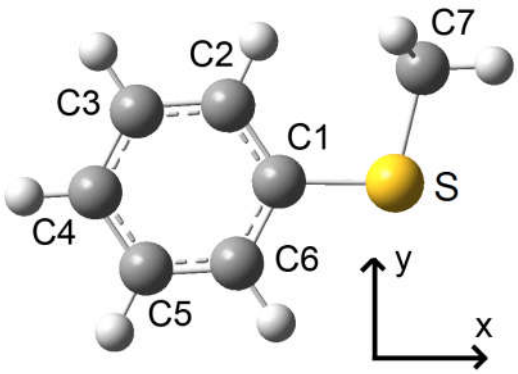

Figure 6.1. Equilibrium geometry of thioanisole with C_S symmetry as optimized by M06-2X/MG3S. Orientation of the x and y axes and numbering of the carbon atoms for convenience of description are also shown.

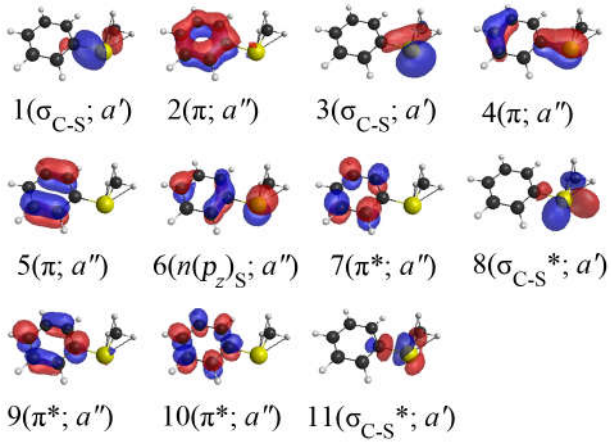

Figure 6.2. Schematic of three-state-averaged active orbitals at the equilibrium geometry with C_S symmetry from SA-CASSCF calculations. The character and the irrep of the orbitals are given in parantheses.

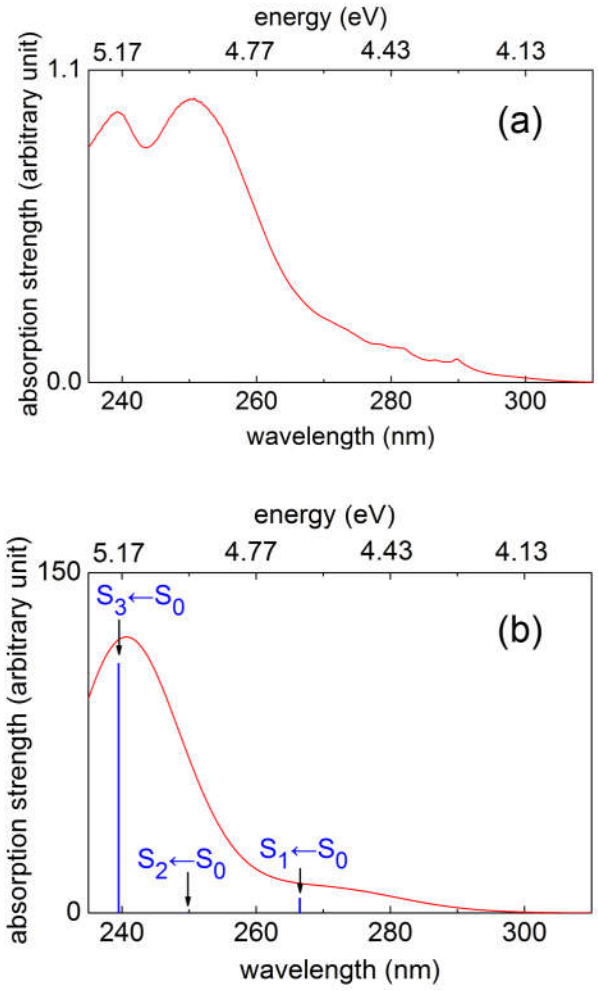

Figure 6.3. (a) Experimental vapor-phase UV spectrum of thioanisole. (Adapted from Figure S6 in the Electronic Supplementary Information of ref. 14 with the permission of the authors.) (b) Simulated electronic spectrum of thioanisole (red curve) and the position of vertical excitation energies (blue sticks) as calculated by TDA-τ-HCTHhyb/6-31+G*.

REFERENCES FOR CHAPTER 6

[1] A. L. Sobolewski and W. Domcke, *Chem. Phys. Lett.*, 1999, **315**, 293-298.

[2] A. L. Sobolewski and W. Domcke, *Chem. Phys.*, 2000, **259**, 181-191.

[3] A. L. Sobolewski and W. Domcke, *J. Phys. Chem. A*, 2001, **105**, 9275-9283.

[4] A. L. Sobolewski, W. Domcke, C. Dedonder-Lardeux and C. Jouvet, *Phys. Chem. Chem. Phys.*, 2002, **4**, 1093-1100.

[5] Z. Lan, W. Domcke, V. Vallet, A. L. Sobolewski and S. Mahapatra, *J. Chem. Phys.*, 2005, **122**, 224315.

[6] M. G. D. Nix, A. L. Devine, B. Cronin, R. N. Dixon and M. N. R. Ashfold, *J. Chem. Phys.*, 2006, **125**, 133318.

[7] O. P. J. Vieuxmaire, Z. Lan, A. L. Sobolewski and W. Domcke, *J. Chem. Phys.*, 2008, **129**, 224307.

[8] X. Xu, K. R. Yang and D. G. Truhlar, *J. Chem. Theory Comput.*, 2013, **9**, 3612-3625.

[9] X. Xu, J. Zheng, K. R. Yang and D. G. Truhlar, *J. Am. Chem. Soc.*, 2014, **136**, 16378-16386.

[10] K. R. Yang, X. Xu, J. Zheng and D. G. Truhlar, *Chem. Sci.*, 2014, **5**, 4661-4680.

[11] I. S. Lim, J. S. Lim, Y. S. Lee and S. K. Kim, *J. Chem. Phys.*, 2007, **126**, 034306.

[12] R. Omidyan and H. Rezaei, *Phys. Chem. Chem. Phys.*, 2014, **16**, 11679-11689.

[13] J. S. Lim and S. K. Kim, *Nat. Chem.*, 2010, **2**, 627-632.

[14] G. M. Roberts, D. J. Hadden, L. T. Bergendahl, A. M. Wenge, S. J. Harris, T. N. V. Karsili, M. N. R. Ashfold, M. J. Paterson and V. G. Stavros, *Chem. Sci.*, 2013, **4**, 993-1001.

[15] T. H. Dunning, *J. Chem. Phys.*, 1989, **90**, 1007-1023.

[16] D. E. Woon and T. H. Dunning, *J. Chem. Phys.*, 1993, **98**, 1358-1371.

[17] T. H. Dunning, K. A. Peterson and A. K. Wilson, *J. Chem. Phys.*, 2001, **114**, 9244-9253.

[18] B. J. Lynch, Y. Zhao and D. G. Truhlar, *J. Phys. Chem. A*, 2003, **107**, 1384-1388.

[19] R. Krishnan, J. S. Binkley, R. Seeger and J. A. Pople, *J. Chem. Phys.*, 1980, **72**, 650-654.

[20] T. Clark, J. Chandrasekhar, G. W. Spitznagel and P. V. R. Schleyer, *J. Comput. Chem.*, 1983, **4**, 294-301.

[21] E. Papajak, J. Zheng, X. Xu, H. R. Leverentz and D. G. Truhlar, *J. Chem. Theory Comput.*, 2011, **7**, 3027-3034.

[22] W. J. Hehre, R. Ditchfield and J. A. Pople, *J. Chem. Phys.*, 1972, **56**, 2257-2261.

[23] P. C. Hariharan and J. A. Pople, *Theoret. Chim. Acta*, 1973, **28**, 213-222.

[24] M. M. Francl, W. J. Pietro, W. J. Hehre, J. S. Binkley, M. S. Gordon, D. J. DeFrees and J. A. Pople, *J. Chem. Phys.*, 1982, **77**, 3654-3665.

[25] Y. Zhao and D. G. Truhlar, *Theor. Chem. Acc.*, 2008, **120**, 215-241.

[26] M.E. Casida, in *Recent Advances in Density Functional Methods Part I*, D.P. Chong (Ed.), World Scientific, Singapore, 1995, pp. 155-192.

[27] A. D. Becke, *Phys. Rev. A*, 1988, **38**, 3098-3100; C. T. Lee, W. T. Yang and R. G. Parr, *Phys. Rev. B*, 1988, **37**, 785-789; B. Miehlich, A. Savin, H. Stoll and H. Preuss, *Chem. Phys. Lett.*, 1989, **157**, 200-206; A. D. Becke, *J. Chem. Phys.*, 1993, **98**, 5648-5652.

[28] I. Tamm, *J. Phys. (Moscow)*, 1945, **9**, 449-460.

[29] S. M. Dancoff, *Phys. Rev.*, 1950, **78**, 382-385.

[30] S. Hirata and M. Head-Gordon, *Chem. Phys. Lett.*, 1999, **314**, 291-299.

[31] A. D. Boese and N. C. Handy, *J. Chem. Phys.*, 2002, **116**, 9559-9569.

[32] M. W. Schmidt and M. S. Gordon, *Annu. Rev. Phys. Chem.*, 1998, **49**, 233-266.

[33] H.-J. Werner and W. Meyer, *J. Chem. Phys.,* 1981, **74**, 5794-5801.

[34] H. Nakano, *J. Chem. Phys.*, 1993, **99**, 7983.

[35] H. Nakano, *Chem. Phys. Lett.*, 1993, **207**, 372-378.

[36] A. A. Granovsky, *J. Chem. Phys.*, 2011, **134**, 214113.

[37] H. Koch and P. Jørgensen, *J. Chem. Phys.*, 1990, **93**, 3333-3344.

[38] J. F. Stanton and R. J. Bartlett, *J. Chem. Phys.*, 1993, **98**, 7029-7039.

[39] K. Kowalski and P. Piecuch, *J. Chem. Phys.*, 2004, **120**, 1715-1738.

[40] K. Kowalski, *J. Chem. Phys.*, 2009, **130**, 194110.

[41] J. J. P. Stewart, *J. Comput. Chem.*, 1989, **10**, 209-220.

[42] J. J. P. Stewart, *J. Comput. Chem.*, 1989, **10**, 221-264.

[43] Gaussian 09, Revision D.01, M. J. Frisch, G. W. Trucks, H. B. Schlegel, G. E. Scuseria, M. A. Robb, J. R. Cheeseman, G. Scalmani, V. Barone, B. Mennucci, G. A. Petersson, H. Nakatsuji, M. Caricato, X. Li, H. P. Hratchian, A. F. Izmaylov, J. Bloino, G. Zheng, J. L. Sonnenberg, M. Hada, M. Ehara, K. Toyota, R. Fukuda, J. Hasegawa, M. Ishida, T. Nakajima, Y. Honda, O. Kitao, H. Nakai, T. Vreven, J. A. Montgomery, Jr., J. E. Peralta, F. Ogliaro, M. Bearpark, J. J. Heyd, E. Brothers, K. N. Kudin, V. N. Staroverov, R. Kobayashi, J. Normand, K. Raghavachari, A. Rendell, J. C. Burant, S. S. Iyengar, J. Tomasi, M. Cossi, N. Rega, J. M. Millam, M. Klene, J. E. Knox, J. B. Cross, V. Bakken, C. Adamo, J. Jaramillo, R. Gomperts, R. E. Stratmann, O. Yazyev, A. J. Austin, R. Cammi, C. Pomelli, J. W. Ochterski, R. L. Martin, K. Morokuma, V.

G. Zakrzewski, G. A. Voth, P. Salvador, J. J. Dannenberg, S. Dapprich, A. D. Daniels, Ö. Farkas, J. B. Foresman, J. V. Ortiz, J. Cioslowski, and D. J. Fox, Gaussian, Inc., Wallingford CT, 2009.

[44] M. W. Schmidt, K. K. Baldridge, J. A. Boatz, S. T. Elbert, M. S. Gordon, J. H. Jensen, S. Koseki, N. Matsunaga, K. A. Nguyen, S. J. Su, T. L. Windus, M. Dupuis and J. A. Montgomery, *J. Comput. Chem.*, 1993, **14**, 1347-1363.

[45] M. S. Gordon and M. W. Schmidt, in *Theory and Applications of Computational Chemistry: The First Forty Years*, eds. C. E. Dykstra, G. Frenking, K. S. Kim and G. E. Scuseria 2005, pp. 1167-1189.

[46] M. Valiev, E. J. Bylaska, N. Govind, K. Kowalski, T. P. Straatsma, H. J. J. Van Dam, D. Wang, J. Nieplocha, E. Apra, T. L. Windus and W. de Jong, *Comput. Phys. Commun.*, 2010, **181**, 1477-1489.

[47] J. Zheng, Z.-H. Li, A. W. Jasper, D. A. Bonhommeau, R. Valero, R. Meana-Pañeda, and D. G. Truhlar, ANT, version 2014-2, University of Minnesota, Minneapolis, 2015. http://comp.chem.umn.edu/ant

[48] J. J. P. Stewart, L. Fiedler, P. Zhang, J. Zheng, I. Rossi, W.-P. Hu, G. C. Lynch, Y.-P. Liu, Y.-Y. Chuang, J. Pu, J. Li, C. J. Cramer, P. L. Fast, J. Gao, and D. G. Truhlar, MOPAC–version 5.021mn (2013), University of Minnesota, Minneapolis, MN 55455.

[49] T. Lu and F. Chen, *J. Comput. Chem.*, 2012, **33**, 580-592.

[50] MG3S is a well-established basis set for ground-state geometry optimization with DFT. We have also performed the optimization with another well-established basis set, namely def2-TZVP, and the optimized coordinates differ from the ones with MG3S by ~0.001 Å.

[51] M. Hoshino-Nagasaka, T. Suzuki, T. Ichimura, S. Kasahara, M. Baba and S. Kawauchi, *Phys. Chem. Chem. Phys.*, 2010, **12**, 13243-13247.

[52] M. Nagasaka-Hoshino, T. Isozaki, T. Suzuki, T. Ichimura and S. Kawauchi, *Chem. Phys. Lett.*, 2008, **457**, 58-61.

[53] M.-X. Liu, B.-B. Xie, M.-J. Li, Y.-Y. Zhao, K.-M. Pei, H.-G. Wang and X. Zheng, *J. Raman Spectrosc.*, 2013, **44**, 440-446.

[54] B. Lasorne, J. Jornet-Somoza, H. D. Meyer, D. Lauvergnat, M. A. Robb and F. Gatti, *Spectroc. Acta Pt. A-Molec. Biomolec. Spectr.*, 2014, **119**, 52-58.

[55] H. A. Witek, Y.-K. Choe, J. P. Finley and K. Hirao, *J. Comput. Chem.*, 2002, **23**, 957-965.

Chapter 7. Photochemistry and Spectroscopy of Thioanisole. II. Nonintuitive Diabatic Potential Energy Surfaces

7.1. INTRODUCTION

Diabatization is a transformation of the basis of electronic wave functions from the adiabatic basis, in which the electronic wave functions are eigenfunctions of the electronic Hamiltonian and are coupled by the nuclear momentum operator, to a diabatic basis in which the diabatic wave functions are smooth and are coupled by the electronic Hamiltonian operator.[1] The coupling matrix elements in the adiabatic representation are vectors and are usually called nonadiabatic couplings, and the coupling matrix elements in the diabatic representation are scalars and are usually called diabatic couplings. A diabatic basis has the advantages over the adiabatic basis that the potential energy surfaces and couplings are smooth even at and near adiabatic state crossing seams, where the adiabatic surfaces have cuspidal ridges and the nonadiabatic couplings are singular; therefore the diabatic basis is more suitable for dynamical simulations, which is its *raison d'être*. A recent brief overview of diabatization methods may be found in an article by Eisfeld et al.[2]

It has been proven that a strictly diabatic basis in which the nonadiabatic couplings vanish does not exist in general,[3] and we seek instead a diabatic basis in which the nonadiabatic couplings, though not vanishing, can be neglected for realistic dynamical simulations. Diabatic states are usually defined chemically so as to have a definite valence character (for example, $n \rightarrow \pi^*$, $\pi \rightarrow \pi^*$, charge transfer, etc.) and to retain that character over the whole important range of coordinate space. Two diabatic potential energy surfaces cross when the adiabatic states switch their character, which is in many cases associated with the presence of a locally avoided crossing or a conical intersection. We present here, however, a case where the diabatic potential energy surfaces cross at geometries where the adiabatic surfaces are widely apart in energy, and no avoided

crossing is present. This is a difficult case for diabatization since there is no obvious hint from the adiabatic surfaces about what the diabatic surfaces may be like. A similar situation can occur for mixed-valence charge-transfer systems when the electronic coupling between the electron donor and acceptor is strong,[4] although in such systems the diabatic surfaces may be inferred from a double-well model.

The molecule under consideration here is thioanisole. Its photochemistry is very intriguing because experimentally an unusual dynamical "resonance" of the branching ratio of photoproducts was observed but is yet to be fully interpreted.[5,6,7,8] Furthermore, thioanisole is an example of a σ*-mediated photodissociation, which is "a centerpiece for understanding exceptionally efficient radiationless relaxation mechanisms in many heteroatom-containing aromatic species."[6] The construction and diabatization of the potential energy surfaces for this kind of system will enable the performance of dynamical simulations to study the mechanisms of the photochemical processes. A cut of the three lowest singlet adiabatic potential energy surfaces (labeled S_0, S_1, and S_2) of thioanisole relevant to the photodissociation of the S-CH_3 bond is shown in Figure 7.1, where the bond distance is labeled *R*. There are two conical intersections, one between S_1 and S_2 at shorter *R* (labeled CI1) and another between S_0 and S_1 at longer *R* (labeled CI2). In this chapter, we focus on the region (indicated by the blue rectangle in Figure 7.1) containing two lowest states for *R* = 2.2–3.6 Å; this region contains CI2. The diabatization of all three surfaces in the whole region relevant to the photochemistry is a larger problem and is not considered in this chapter.

The diabatization is performed in this chapter by using wave functions and adiabatic surfaces calculated by the state-averaged complete-active-space self-consistent-field (SA-CASSCF) method in a two-dimensional nuclear coordinate subspace spanned by *R* and the C2-C1-S-C7 torsion (denoted by ϕ) with all other internal coordinates fixed at their values in the equilibrium geometry of S_0. We note that additional coordinates, for example, the sulfur atom moving out of the plane of the phenyl ring, may be important be important in the actual dynamics,[7,8] but these two coordinates are sufficient for the present discussion of diabatization. The definitions of the coordinates are illustrated in

Figure 7.2, which also shows our numbering of the carbon atoms and the orientation of the coordinate axes we will use. Two diabatization methods are used, namely the fourfold way,[9,10,11,12] which enforces the smoothness of diabatic wave functions, and Boys localization,[13] which maximizes the difference of the dipole moments of the two diabatic states.

7.2. COMPUTATIONAL DETAILS

The equilibrium geometry of thioanisole was optimized by Kohn-Sham density functional theory with the M06-2X functional[14,15] and the MG3S[16] basis set. (Details of the optimized geometry can be found in ref. 17.) All the nuclear coordinates except R and ϕ were fixed at their ground-state equilibrium values in the calculation of potential energy surfaces.

The fourfold way and Boys localization diabatizations were applied to the two lowest singlet states by the method of three-state state-averaged complete active space self-consistent field with 12 active electrons in 11 active orbitals [SA(3)-CASSCF(12,11)] by using the algorithm of ref. 18. The details of the active space can be found in ref. 17. The fourfold way calculations used two reference orbitals, namely $n(p_y)$ and $n(p_z)$ on the sulfur. The basis set used was 6-311+G(d)[19,20] for carbon and hydrogen and MG3S for sulfur; this combined basis is labeled MB.

The direct calculation of nonadiabatic couplings was performed by finite difference using the *DDR* program in the *MOLPRO* package.[21,22] The transformation from diabatic matrix elements to nonadiabatic couplings between adiabatic states was carried out using the formula[23]

$$\left\langle \mathrm{S}_0 \left| \frac{\partial}{\partial \phi} \right| \mathrm{S}_1 \right\rangle = \frac{1}{V_2 - V_1} \sum_{k=1}^{2} \sum_{l=1}^{2} d_{1k} d_{2l} \frac{\partial}{\partial \phi} U_{kl} \tag{7.1}$$

where V_1 and V_2 are the adiabatic energies of S_0 and S_1, U_{kl} are matrix elements of the diabatic potential energy matrix, and d_{ij} are matrix elements of the (real) adiabatic-to-diabatic transformation matrix defined by

$$\phi_j = \sum_{i=1}^{2} \psi_i d_{ij} \tag{7.2}$$

where ϕ_i and ψ_i are respectively the i-th diabatic and adiabatic state. (In terms of the notations S_0, S_1, DS1, and DS2 used to denote the states in earlier discussions, the ϕ_i correspond to S_0 and S_1 and the ψ_i correspond to DS1 and DS2.)

Other software packages used for the calculations are: *Gaussian 09*[24] for DFT, *GAMESS*[25,26] for the fourfold way and the related CASSCF, and a development version of *Molcas*[27,28,29] (incorporating a DQ diabatization[30] code) for Boys localization and the related CASSCF.

7.3. RESULTS AND DISCUSSION

We will first consider two limiting situations, namely the potential energy curves along R with $\phi = 0°$ and with $\phi = 90°$, and discuss the diabatization with the fourfold way in some detail in light of the electronic structure. Then we will perform the two-dimensional diabatization with both the fourfold way and Boys localization in the whole two-dimensional R and ϕ space for the range of R in the blue rectangle of Figure 7.1. Finally we will discuss the nonintuitiveness of the diabatization.

To discuss the characters of the wave functions as a function of R with ϕ fixed at 0°, we label the important canonical molecular orbitals (CMOs) as follows: orbital a is $\sigma_{S\text{-}C7}$ at small R and $n(p_y)$ on the sulfur at large R, b is $n(p_z)$ on the sulfur at all R, and c is $\sigma_{S\text{-}C7}^*$ at small R and n on the methyl at large R. Figure 7.3(a) illustrates the adiabatic potential energy curves (adiabats) along R, and it shows the dominant configurations of the adiabatic wave functions at R = 2.2 and 3.6 Å, as represented by the occupation numbers of a, b, and c. The shapes of the orbitals at four values of R are shown in Figure 7.3(b): At R = 2.2 Å, although the S-C7 bond is already stretched, the adiabatic ground state S_0 is still dominated by the closed-shell configuration a^2b^2, while the excited state

S_1 is dominated by a configuration a^2bc with $n\sigma^*$ character. At R = 3.6 Å where the S-C7 bond is more than half broken, S_0 is dominated by a^2bc while S_1 is dominated by ab^2c. Thus the electronic configurations at R = 3.6 Å are already consistent with those at $R = \infty$ where experiments and calculations agree that the ground state of the thiophenoxyl radical has a singly-occupied non-bonding p_z orbital on the sulfur, and the excited state has a singly occupied p_y orbital.[31,32]

Diabatization with the fourfold way requires specification of dominant configurations (called diabatic prototypes) in each diabatic state, but the CMOs a and c change character with R and ϕ and are therefore unsuitable for characterizing the important configurations of the diabatic states. Therefore we use the fourfold way to transform the CMOs in the CASSCF active space to diabatic molecular orbitals (DMOs) that preserve their character at different geometries, and then we apply the configurational uniformity criterion of Achity and Ruedenberg[33] to transform the many-electron wave functions to a diabatic representation. Computational details of this transformation are given in Computational Details section below. The three resulting DMOs, α, β, and γ, that correspond to the CMOs a, b, and c are shown in Figure 7.4(b). They have respectively the character of $n(p_y)$ on the sulfur, $n(p_z)$ on the sulfur, and n on the methyl, regardless of geometry. In terms of these DMOs the two diabatic states can be characterized by the $\alpha\beta^2\gamma$ and the $\alpha^2\beta\gamma$ configuration respectively. (We leave the $\alpha^2\beta^2$ configuration out of the prototypes even though it is dominant in the ground state at short R; we will discuss this point below.) The resulting diabatic states have smooth diabatic potential energy curves (shown in Figure 7.4(a)) that energetically match the adiabatic curves for ϕ fixed at 0°. We label the diabatic state characterized by $\alpha\beta^2\gamma$ as DS1 and that characterized by $\alpha^2\beta\gamma$ as DS2, and we label the corresponding diabatic potential curves as U_1 and U_2. The diabatic couplings U_{12} between DS1 and DS2 are essentially zero for the geometries in Figure 7.4.

The corresponding situation for ϕ fixed at 90° is shown in Figure 7.5; the canonical orbital a' is $n(p_y)$ on the sulfur at all R, b' is $\sigma_{S\text{-}C7}$ at small R and $n(p_z)$ on the sulfur at

large R, and c' is $\sigma_{S\text{-}C7}$* at small R and n on the methyl at large R. At R = 2.2 Å, S_0 is closed-shell, and S_1 is dominated by the $(a')(b')^2(c')$ configuration. At R = 3.6 Å, the situation is similar to the case with $\phi = 0°$. This similarity can be understood from the fact that R = 3.6 Å is close to the bond-breaking limit where the electronic structure of the thiophenoxyl moiety is only mildly affected by the position of the separated methyl. The DMOs for ϕ fixed at 90° are shown in Figure 7.6(b); we can again characterize the two diabatic states by the $\alpha\beta^2\gamma$ and $\alpha^2\beta\gamma$ configurations respectively, as indicated in Figure 7.6(a). The diabatic potential energy curves are also similar to the adiabatic ones in energy, and the diabatic couplings are close to zero.

The two diabatic states can also be distinguished by their dipole moments, and Boys localization gives qualitatively the same results for both $\phi = 0°$ and $\phi = 90°$ as those by the above fourfold way calculations. The two-dimensional diabatic potential surfaces given by Boys localization are shown in Figure 7.7, which will be discussed below.

Next we apply both the fourfold way (with the same strategy as employed above) and Boys localization to diabatize the potential energy surfaces in the whole two-dimensional R-ϕ space for the R range of the blue box of Figure 7.1. Figure 7.7 compares the adiabatic and diabatic potential surfaces. In Figure 7.7(a) the degeneracy of the S_0 and S_1 conical intersection that occurs in C_s geometries ($\phi = 0$) is lifted in the space shown for nonsymmetrical geometries. Figure 7.7(b) shows that the diabatic surfaces generated by the fourfold way are indeed smooth. Boys localization gives qualitatively the same result [Figure 7.7(c)]. Figures 7.8 and 7.9 plot the difference of the two diabatic energies (the "diabatic gap") for a given diabatization scheme and also show the squared diabatic couplings given by the fourfold way and Boys localization. For both methods of diabatization, the diabatic crossing seam (the zero contour in Figures 7.8(a) and 7.9(a)) can be clearly seen to start from CI2 at $\phi = 0°$ and $R \sim 3.3$ Å and end at a nonsymmetrical geometry (i.e., ϕ neither 0° or 90°) with R = 2.2 Å. Figures 7.8 and 7.9 show striking agreement between the two very different diabatization methods for the shapes of the contours of both the diabatic gap and the magnitude of the diabatic coupling, and this is very encouraging.

Figure 7.10 demonstrates the nonintuitive nature of the diabatization by showing the one-dimensional cut of the adiabats and diabats along ϕ with R = 2.2 Å. In the kind of cases that one usually sees in discussions of diabatic potential curves, the diabats cross where the adiabats come close in energy and there is a conical intersection or a locally avoided crossing, which is a local minimum of the magnitude of the difference of the adiabatic energies within the considered coordinate subspace. In the case of Figure 7.10, however, the two adiabatic potential energy curves along ϕ with R = 2.2 Å are widely separated energetically and no avoided crossing is present. This is an example where diabatization methods based on electronic structure have advantages over those by ansatz. The latter method[2,34,35] requires an educated guess of the form of diabatic states or potentials, which may not be obvious. In the case of Figure 7.10 it is difficult to conjecture a physically motivated form of the diabatic potentials by inspecting the adiabatic potentials.

One may wonder if such nonintuitive result is reasonable or if it is an artifact of the specific diabatization methods. One criterion for the quality of the diabatization is how well the outcome of dynamical simulations on the diabatic surfaces compares to experiment; but we can also test the diabatization in the absence of a full dynamical simulation. We do this by calculating the nonadiabatic couplings between adiabatic states by a transformation from the diabatic matrix elements and compare them to the ones calculated by directly differentiating the adiabatic wave functions. Figure 7.11 shows the ϕ component of the nonadiabatic coupling between S_0 and S_1, defined as

$$F_{12,\phi} = \langle S_0 | \frac{\partial}{\partial \phi} | S_1 \rangle , \tag{7.3}$$

as a function of ϕ at R = 2.2 Å, the same path as in Figure 7.10. The three sets of nonadiabatic couplings will not be the same in general due to the existence of the non-removable part[3] of nonadiabatic couplings and due to the approximation[36,37] of neglecting even the removable part of the coupling in the diabatic representation, but Figure 7.11 shows that they are similar in magnitude, within about a factor of two or better. All three sets of couplings are small, which means there is no unphysical overestimation of the

nonadiabatic coupling arising from the diabatic crossing. Since the diabatizations are able to reproduce the adiabatic energies exactly (by construction) and since they give $F_{12,\phi}$ close to that calculated by direct differentiation, we conclude that they are reasonable.

We have mentioned that in our definition of the diabatic prototypes for the fourfold way we have left out the closed-shell $\alpha^2\beta^2$ configuration. The reason is that it is ambiguous whether $\alpha^2\beta^2$ should be in the same prototype list as $\alpha\beta^2\gamma$ or $\alpha^2\beta\gamma$. The configuration $\alpha^2\beta^2$ is dominant in the wave function characterized by $\alpha\beta^2\gamma$ at $\phi = 0°$ and short R (see Figure 7.4) but it is also important in the wave function characterized by $\alpha^2\beta\gamma$ at $\phi = 90°$ and short R (see Figure 7.6), yet $\alpha\beta^2\gamma$ and $\alpha^2\beta\gamma$ should be in distinct prototype lists that do not share any configuration. In two alternative schemes to diabatization of thioanisole, we have tried putting $\alpha^2\beta^2$ in the same prototype list as $\alpha\beta^2\gamma$ and putting $\alpha^2\beta\gamma$ in the other list. They also give reasonable diabats, but the diabats are less smooth around the diabatic crossings at short R and large ϕ. In the fourfold way diabatization of a similar system, phenol,[38] a scheme similar to one of the alternative schemes for thioanisole mentioned above was used, and the results are similar to those for thioanisole with the same scheme. The different outcomes of the schemes are due to quantitative differences in the application of the fourfold way algorithm and are not due to qualitative chemical differences.

It is worth emphasizing here that diabatic potential energy surfaces are not unique, and different diabatization patterns can be equally good. We advocate the following criteria for the quality of a diabatization: (1) the diabatic potential energy matrix elements (diabatic surfaces and couplings) should be smooth functions of nuclear coordinates; (2) the diabatic potential energy matrix, when diagonalized, should reproduce, approximately or exactly, a selected set of adiabatic energies (for example, the difference between the calculated adiabatic potentials and those obtained by diagonalization of the diabatic potential matrix should be smaller than the uncertainty (reliability) of the calculated adiabatic potentials); and (3) the nonadiabatic couplings between adiabatic states calculated by transforming the diabatic potential energy matrix elements should be

similar in magnitude to the ones calculated by differentiating the adiabatic states, or else the nonadiabatic coupling between the diabatic states[39] should be small. It is not always necessary to check criterion 3, but it is certainly comforting when one checks it and it is satisfied, as in the present work. The ultimate test is that the outcome of dynamical simulations with the diabatic potential energy matrix should agree with experimental observables, but if disagreement is found it could be due to errors in the calculated adiabatic states and potentials, not in the diabatization. The diabatizations of thioanisole presented in this work have met criteria (1), (2), and (3). The diabatization of phenol presented in previous work was justified by criteria (1) and (2) and the reasonable agreement of simulations with experiment.[40]

7.4. SUMMARY

In this chapter we presented the diabatization of two electronic states of thioanisole along the S-CH_3 bond-stretching and C-C-S-C torsional coordinates in the vicinity of a conical intersection using two diabatization methods, the orbital-dependent fourfold way and orbital-free Boys localization. Diabatization by either method produces reasonable and similar, yet counterintuitive, results: the diabatic surfaces cross at nuclear coordinates where the adiabatic surfaces exhibit no avoided crossings. Nevertheless the diabatic potential energy matrix elements are smooth, are able to reproduce the adiabatic energies, and can be transformed to reasonable nonadiabatic couplings between adiabatic states. There is striking agreement between the two very different diabatization methods for the contours of both the diabatic gap and the magnitude of the diabatic coupling, even in this nonintuitive case where the diabatic potential energy surfaces cross at nonsymmetrical geometries where the adiabatic potential curves show no avoidance. This demonstrates that systematic diabatization schemes can generate useful diabatic states for dynamics calculations even when there is no obvious valence bond argument to provide guidance. In future work we hope to use one of the diabatization schemes to generate global potential energy surfaces of the three lowest singlet states of thioanisole over a broader

range of nuclear coordinates important for its photochemistry, which will open the way for dynamical simulation of the photochemical process.

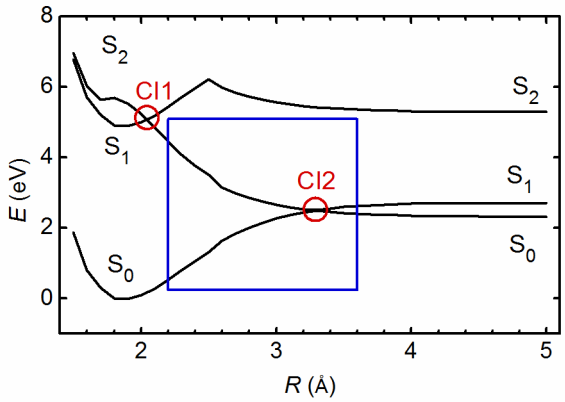

Figure 7.1. The potential energy curves of the three lowest adiabatic singlet states of thioanisole along the S-CH_3 bond-stretching coordinate R with other coordinates fixed at their ground-state equilibrium values, as calculated by SA(3)-CASSCF(12,11)/MB. (See Computational Details for the explanation of this abbreviation.) The blue rectangle indicates that in this chapter we are interested in S_0 and S_1 in the range of R = 2.2–3.6 Å. The cut shown here is for $\phi = 0$, which yields a geometry with C_S symmetry; see Figure 7.2 for the definition of ϕ.

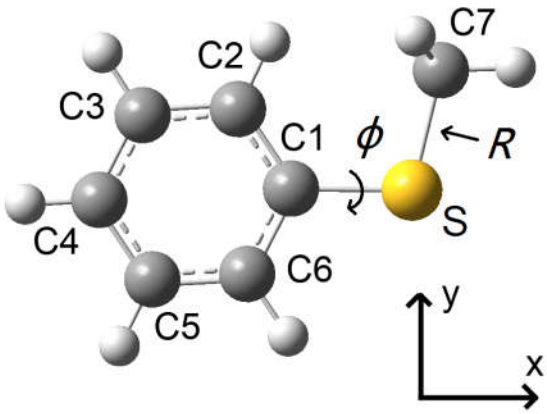

Figure 7.2. Labeling of the carbon atoms and the two coordinates of interest (S-C7 distance R and C2-C1-S-C7 torsion ϕ) and the definition of molecular orientation. We assume that the phenyl group and S are in the xy plane, with the C1–S axis along x.

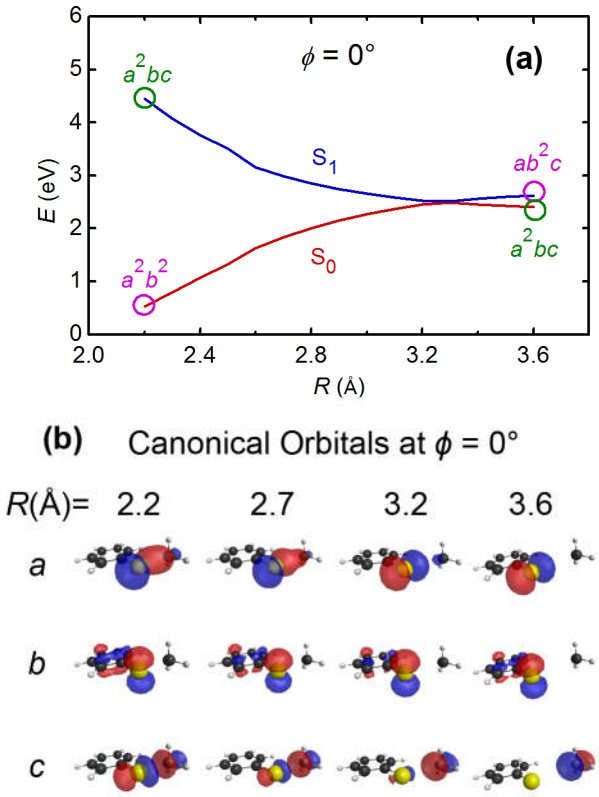

Figure 7.3. (a) Adiabatic potential energy curves as functions of R with $\phi = 0°$ as calculated by SA(3)-CASSCF(12,11)/MB. (See Computational Details for an explanation of this abbreviation.) The dominant configurations of the adiabatic wave functions at $R = 2.2$ or 3.6 Å in terms of the occupation numbers of the canonical orbitals a, b, and c are also shown. (b) The shapes of canonical molecular orbitals a, b, and c at several R.

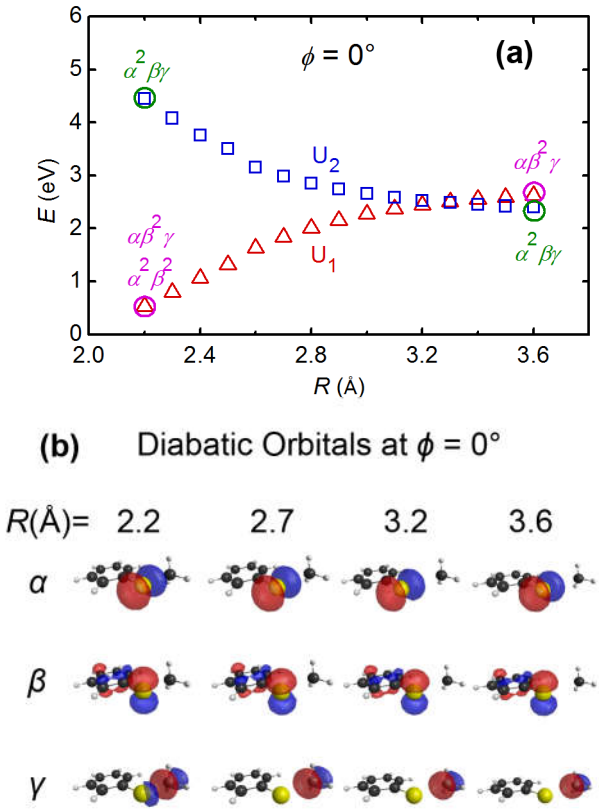

Figure 7.4. (a) Diabatic potential energy curves as functions of R with $\phi = 0°$ as calculated by the fourfold way. The dominant configurations of the diabatic wave functions at $R = 2.2$ or 3.6 Å in terms of the occupation numbers of the diabatic orbitals α, β, and γ are also shown. (b) The shape of diabatic molecular orbitals α, β, and γ at several R.

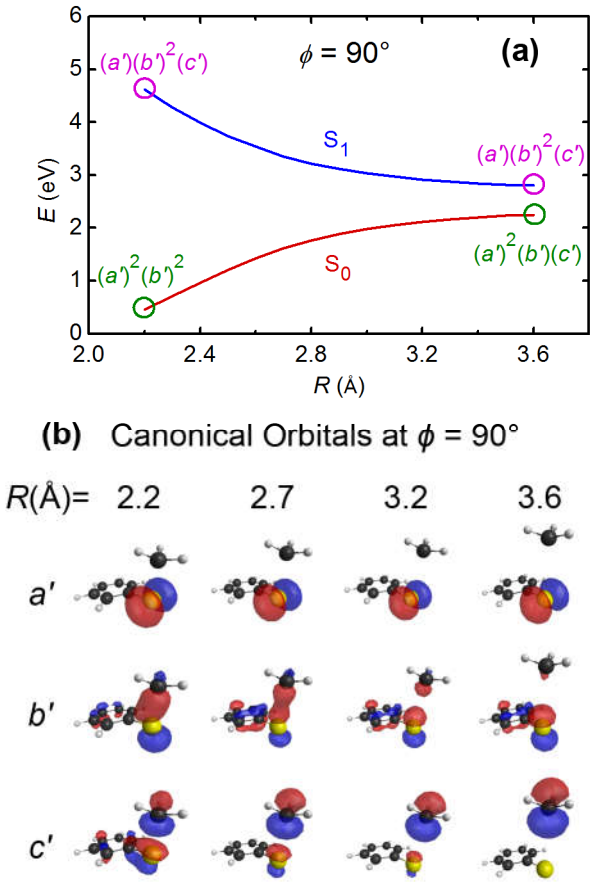

Figure 7.5. (a) Adiabatic potential energy curves as functions of R with $\phi = 90°$ as calculated by SA(3)-CASSCF(12,11)/MB. (See Computational Details for an explanation of this abbreviation.) The dominant configurations of the wave functions at $R = 2.2$ or 3.6 Å in terms of the occupation numbers of the canonical orbitals a', b', and c' are also shown. (b) The shapes of the canonical molecular orbitals a', b', and c' at several R.

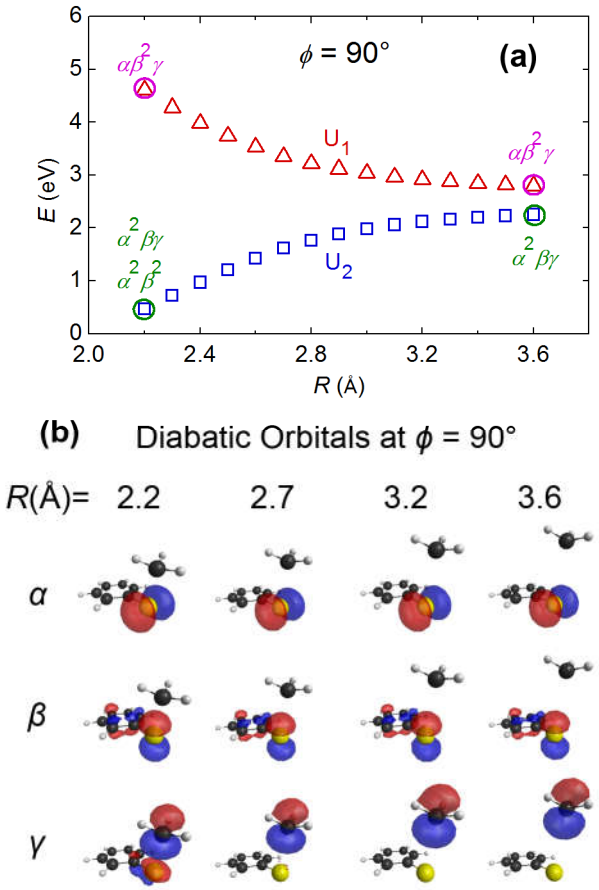

Figure 7.6. (a) Diabatic potential energy curves as functions of R with $\phi = 90°$ as calculated by the fourfold way. The dominant configurations of the diabatic wave functions at $R = 2.2$ or 3.6 Å in terms of the occupation numbers of the diabatic orbitals α, β, and γ are also shown. (b) The shapes of diabatic molecular orbitals α, β, and γ at several R.

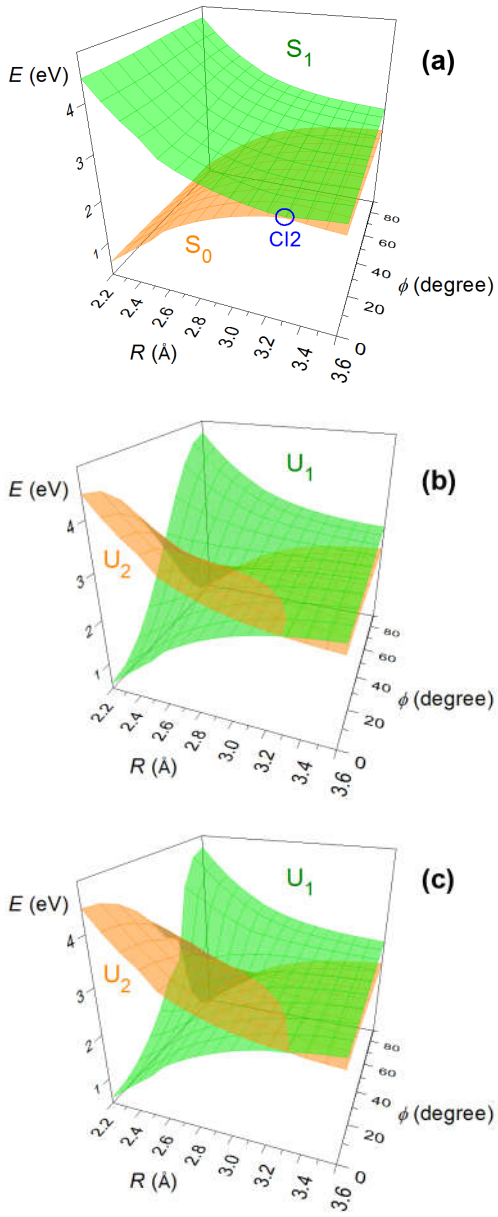

Figure 7.7. (a) Two-dimensional adiabatic potential surfaces as calculated by SA(3)-CASSCF(12,11)/MB. (See Computational Details for an explanation of this abbreviation.) (b) Corresponding diabatic potential surfaces given by the fourfold way. (c) Corresponding diabatic potential energy surfaces given by Boys localization.

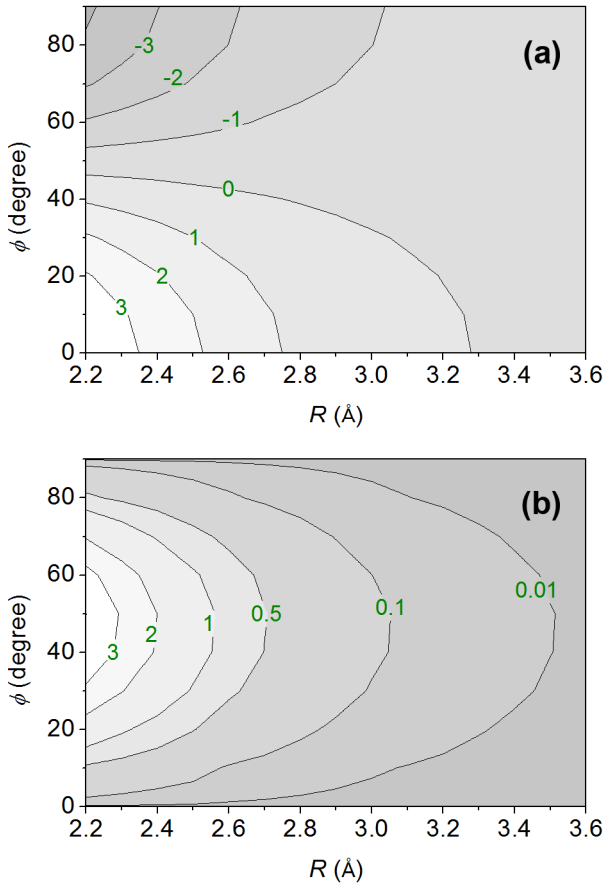

Figure 7.8. Contour plot of (a) the diabatic gap (U_2–U_1) in eV and (b) the squared diabatic coupling (U_{12}^2) in $(eV)^2$ as functions of nuclear coordinates R and ϕ, as given by the fourfold way.

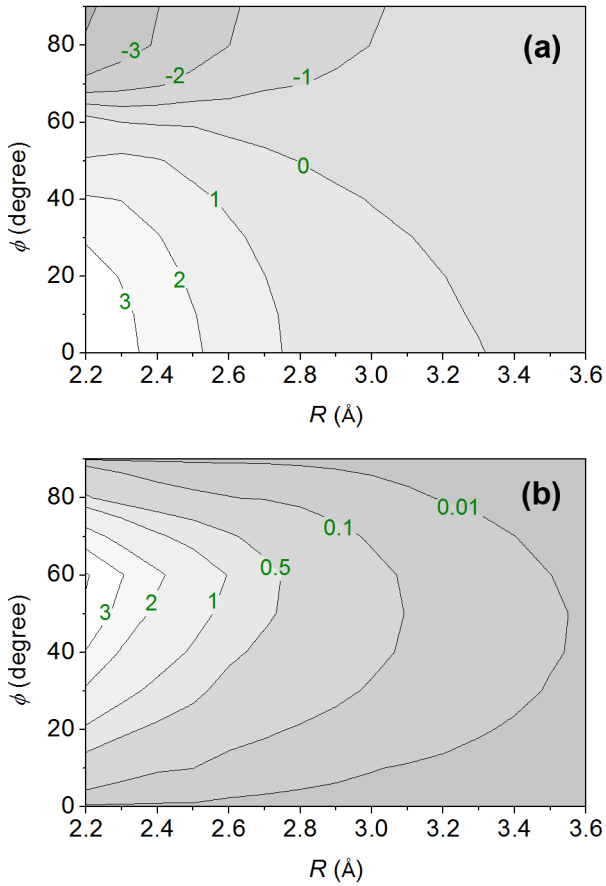

Figure 7.9. Contour plot of (a) the diabatic gap (U_2–U_1) in eV and (b) the squared diabatic coupling (U_{12}^2) in $(eV)^2$ as functions of nuclear coordinates R and ϕ, as given by Boys localization.

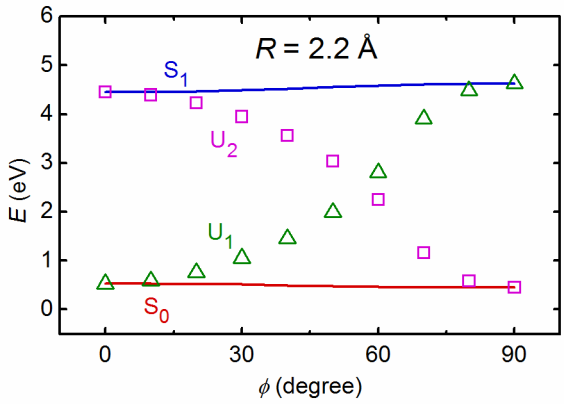

Figure 7.10. Adiabats given by SA(3)-CASSCF(12,11)/MB and diabats given by Boys localization as a function of ϕ with R fixed at 2.2 Å.

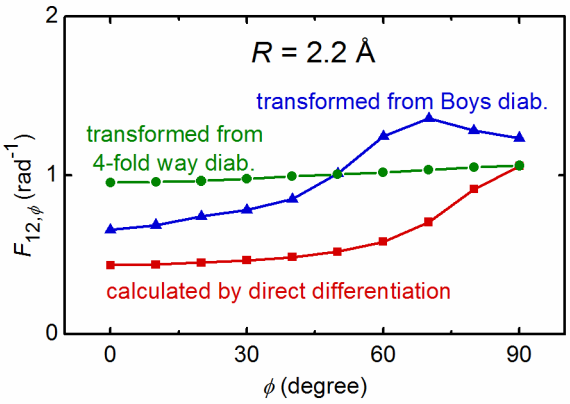

Figure 7.11. The ϕ component of nonadiabatic coupling between S_0 and S_1 along ϕ at R = 2.2 Å, as calculated by three approaches.

REFERENCES FOR CHAPTER 7

[1] Garrett, B. C.; Truhlar, D. G. The Coupling of Electronically Adiabatic States in Atomic and Molecular Collisions. In *Theoretical Chemistry: Theory of Scattering: Papers in Honor of Henry Eyring*; Henderson, D., Ed.; Theoretical Chemistry: Advances and Perspectives Series, Vol. 6A; Academic: New York, 1981; pp. 215-299.

[2] Eisfeld, W.; Vieuxmaire, O.; Viel, A. Full-Dimensional Diabatic Potential Energy Surfaces Including Dissociation: The ^{2}E" State of NO_3. *J. Chem. Phys.* **2014**, *140*, 224109.

[3] Mead, C. A.; Truhlar, D. G. Conditions for the Definition of a Strictly Diabatic Electronic Basis for Molecular Systems. *J. Chem. Phys.* **1982,** *77*, 6090-6098.

[4] Brunschwig, B. S.; Creutz, C.; Sutin, N. Optical Transitions of Symmetrical Mixed-Valence Systems in the Class II-III Transition Regime. *Chem. Soc. Rev.* **2002,** *31*, 168-184.

[5] Lim, J. S.; Kim, S. K. Experimental Probing of Conical Intersection Dynamics in the Photodissociation of Thioanisole. *Nat. Chem.* **2010,** *2*, 627-632.

[6] Roberts, G. M.; Hadden, D. J.; Bergendahl, L. T.; Wenge, A. M.; Harris, S. J.; Karsili, T. N. V.; Ashfold, M. N. R.; Paterson, M. J.; Stavros, V. G. Exploring Quantum Phenomena and Vibrational Control in σ* Mediated Photochemistry. *Chem. Sci.* **2013,** *4*, 993-1001.

[7] Han, S.; Lim, J. S.; Yoon, J.-H.; Lee, J.; Kim, S.-Y.; Kim, S. K. Conical Intersection Seam and Bound Resonances Embedded in Continuum Observed in the Photodissociation of Thioanisole-d3. *J. Chem. Phys.* **2014,** *140*, 054307.

[8] Wenge, A. M.; Karsili, T. N. V.; Rodriguez, J. D.; Cotterell, M. I.; Marchetti, B.; Dixon, R. N.; Ashfold, M. N. R. Tuning Photochemistry: Substituent Effects on πσ* State Mediated Bond Fission in Thioanisoles. *Phys. Chem. Chem. Phys.* **2015,** *17*, 16246-16256.

[9] Nakamura, H.; Truhlar, D. G. The Direct Calculation of Diabatic States Based on Configurational Uniformity. *J. Chem. Phys.* **2001,** *115*, 10353-10372.

[10] Nakamura, H.; Truhlar, D. G. Direct Diabatization of Electronic States by the Fourfold Way. II. Dynamical Correlation and Rearrangement Processes. *J. Chem. Phys.* **2002,** *117*, 5576-5593.

[11] Nakamura, H.; Truhlar, D. G. Extension of the Fourfold Way For Calculation of Global Diabatic Potential Energy Surfaces of Complex, Multi-Arrangement, Non-Born-Oppenheimer Systems: Application to HNCO (S_0, S_1). *J. Chem. Phys.* **2003,** *118*, 6816-6829.

[12] Yang, K. R.; Xu, X.; Truhlar, D. G. Direct Diabatization of Electronic States by the Fourfold Way: Including Dynamical Correlation by Multi-Configuration Quasidegenerate Perturbation Theory with Complete Active Space Self-Consistent-Field Diabatic Molecular Orbitals. *Chem. Phys. Lett.* **2013,** *573*, 84-89.

[13] Subotnik, J. E.; Yeganeh, S.; Cave, R. J.; Ratner, M. A. Constructing Diabatic States from Adiabatic States: Extending Generalized Mulliken–Hush to Multiple Charge Centers with Boys Localization. *J. Chem. Phys.* **2008,** *129*, 244101.

[14] Zhao, Y.; Truhlar, D. G. The M06 Suite of Density Functionals for Main Group Thermochemistry, Thermochemical Kinetics, Noncovalent Interactions, Excited States, and Transition Elements: Two New Functionals and Systematic Testing of Four M06-Class Functionals and 12 Other Functionals. *Theor. Chem. Acc.* **2008,** *120*, 215-241.

[15] Zhao, Y.; Truhlar, D. G. Density Functionals with Broad Applicability in Chemistry. *Acc. Chem. Res.* **2008,** *41*, 157-167.

[16] Lynch, B. J.; Zhao, Y.; Truhlar, D. G. Effectiveness of Diffuse Basis Functions for Calculating Relative Energies by Density Functional Theory. *J. Phys. Chem. A* **2003,** *107*, 1384-1388.

[17] Li, S. L.; Xu, X.; Truhlar, D. G. Computational Simulation and Interpretation of the Low-Lying Excited Electronic States and Electronic Spectrum of Thioanisole. *Phys. Chem. Chem. Phys.* **2015** *17*, 20093.

[18] Li, S. L.; Truhlar, D. G.; Schmidt, M. W.; Gordon, M. S. Model Space Diabatization for Quantum Photochemistry. *J. Chem. Phys.* **2015,** *142*, 064106.

[19] Krishnan, R.; Binkley, J. S.; Seeger, R.; Pople, J. A. Self-Consistent Molecular Orbital Methods. XX. A Basis Set for Correlated Wave Functions. *J. Chem. Phys.* **1980,** *72*, 650-654.

[20] Clark, T.; Chandrasekhar, J.; Spitznagel, G. W.; Schleyer, P. V. R. Efficient Diffuse Function-Augmented Basis Sets for Anion Calculations. III. The 3-21+G Basis Set for First-Row Elements, Li–F. *J. Comput. Chem.* **1983,** *4*, 294-301.

[21] Werner, H.-J.; Knowles, P. J.; Knizia, G.; Manby, F. R.; Schütz, M. Molpro: A General-Purpose Quantum Chemistry Program Package. *Wiley Interdiscip. Rev. Comput. Mol. Sci.* **2012,** *2*, 242-253.

[22] *MOLPRO,* version 2012.1, a package of ab initio programs, H.-J. Werner, P. J. Knowles, G. Knizia, F. R. Manby, M. Schütz, and others, see http://www.molpro.net

[23] Jasper, A. W.; Truhlar, D. G. Non-Born-Oppenheimer Molecular Dynamics for Conical Intersections, Avoided Crossings, and Weak Interactions. In *Conical Intersections: Theory,*

Computation, and Experiment, Domcke, W.; Yarkony, D. R.; Koppel, H., Eds.; Advanced Series in Physical Chemistry, Vol. 17; World Scientific: Singapore, 2011; pp. 375-414.

[24] Frisch, M. J.; Trucks, G. W.; Schlegel, H. B.; Scuseria, G. E.; Robb, M. A.; Cheeseman, J. R.; Scalmani, G.; Barone, V.; Mennucci, B.; Petersson, G. A.; *et al*. *Gaussian 09*, Revision D.01, Gaussian, Inc., Wallingford CT, 2009.

[25] Schmidt, M. W.; Baldridge, K. K.; Boatz, J. A.; Elbert, S. T.; Gordon, M. S.; Jensen, J. H.; Koseki, S.; Matsunaga, N.; Nguyen, K. A.; Su, S. J.; *et al*. General Atomic and Molecular Electronic-Structure System. *J. Comput. Chem.* **1993,** *14*, 1347-1363.

[26] Gordon, M. S.; Schmidt, M. W. Advances in Electronic Structure Theory: GAMESS a Decade Later. In *Theory and Applications of Computational Chemistry: The First Forty Years*, Dykstra, C. E.; Frenking, G.; Kim, K. S.; Scuseria, G. E., Eds.; Elsevir: Amsterdam, 2005; pp. 1167-1189.

[27] Karlström, G.; Lindh, R.; Malmqvist, P.-Å.; Roos, B. r. O.; Ryde, U.; Veryazov, V.; Widmark, P.-O.; Cossi, M.; Schimmelpfennig, B.; Neogrady, P.; *et al*. MOLCAS: A Program Package for Computational Chemistry. *Comput. Mater. Sci.* **2003,** *28*, 222-239.

[28] Veryazov, V.; Widmark, P.-O.; Serrano-Andrés, L.; Lindh, R.; Roos, B. O. Molcas as a Development Platform for Quantum Chemistry Software. *Int. J. Quantum Chem.* **2004,** *100*, 626-635.

[29] Aquilante, F.; De Vico, L.; Ferré, N.; Ghigo, G.; Malmqvist, P.-å.; Neogrády, P.; Pedersen, T. B.; Pitoňák, M.; Reiher, M.; Roos, B. O.; *et al*. Molcas 7: The Next Generation. *J. Comput. Chem.* **2010,** *31*, 224-247.

[30] Hoyer, C. E.; Xu, X.; Ma, D.; Gagliardi, L.; Truhlar, D. G. Diabatization based on the Dipole and Quadrupole: The DQ Method. *J. Chem. Phys.* **2014,** *141*, 114104.

[31] Lim, J. S.; Lim, I. S.; Lee, K.-S.; Ahn, D.-S.; Lee, Y. S.; Kim, S. K. Intramolecular Orbital Alignment Observed in the Photodissociation of [D1]Thiophenol. *Angew. Chem. Int. Ed.* **2006,** *45*, 6290-6293.

[32] Lim, I. S.; Lim, J. S.; Lee, Y. S.; Kim, S. K. Experimental and Theoretical Study of the Photodissociation Reaction of Thiophenol at 243nm: Intramolecular Orbital Alignment of the Phenylthiyl Radical. *J. Chem. Phys.* **2007,** *126*, 034306.

[33] Atchity, D. J.; Ruedenberg, K. Determination of Diabatic States through Enforcement of Configurational Uniformity. *Theor. Chem. Acc.* **1997**, *97*, 47-58.

[34] Faraji, S.; Gómez-Carrasco, S.; Köppel, H. Multistate vibronic Dynamics and Multiple Conical Intersections. In *Conical Intersections: Theory, Computation, and Experiment*, Domcke, W.; Yarkony, D. R.; Koppel, H., Eds.; Advanced Series in Physical Chemistry, Vol. 17; World Scientific: Singapore, 2011; pp. 249-300.

[35] Domcke, W. General Discussion, *Faraday Discuss.* **2013**, *163*, 126.

[36] Truhlar, D. G.; Duff, J. W.; Blais, N. C.; Tully, J. C.; Garrett, B. C. The Quenching of Na(3 ^2P) by H_2: Interactions and Dynamics. *J. Chem. Phys.* 1982, 77, 764-776.

[37] Jasper, A. W.; Kendrick, B. K.; Mead, C. A.; Truhlar, D. G. Non-Born-Oppenheimer Chemistry: Potential Surfaces, Couplings, and Dynamics. In *Modern Trends in Chemical Reaction Dynamics: Experiment and Theory (Part 1)*, Yang, X.; Liu, K., Eds.; Advanced Series in Physical Chemistry, Vol. 14; World Scientific: Singapore, 2004; pp. 329-391.

[38] Xu, X.; Yang, K. R.; Truhlar, D. G. Diabatic Molecular Orbitals, Potential Energies, and Potential Energy Surface Couplings by the Fourfold Way for Photodissociation of Phenol. *J. Chem. Theory Comput.* **2013,** *9*, 3612-3625.

[39] Fatehi, S.; Alguire, E.; Subotnik, J. E. Derivative Couplings and Analytic Gradients for Diabatic States, with an Implementation for Boys-Localized Configuration-Interaction Singles. *J. Chem. Phys.* **2013,** *139*, 124112.

[40] Xu, X.; Zheng, J.; Yang, K. R.; Truhlar, D. G. Photodissociation Dynamics of Phenol: Multistate Trajectory Simulations Including Tunneling. *J. Am. Chem. Soc.* **2014,** *136*, 16378-16386.

Chapter 8. Photochemistry and Spectroscopy of Thioanisole. III. Full-dimensional ground- and excited-state potential energy surfaces and state couplings

8.1. INTRODUCTION

Nonadiabatic transitions happen most efficiently near conical intersection seams,[1,2,3,4,5] and the characteristics of coupled potential energy surfaces near such seams are critical for understanding many spectroscopic observables and electronically nonadiabatic processes.[6,7,8,9,10,11,12,13,14,15,16,17,18,19,20,21,22,23,24,25,26,27] The photodissociation of thioanisole, as well as that of similar molecules such as phenol, thiophenol, and anisole,[28,29,30,31,32,33,34,35,36] is a prototype of the photo-induced hydrogen/methyl detachment and proton transfer reactions mediated by conical intersections between a bound $^1\pi\pi^*$ state and a repulsive $^1\pi\sigma^*$ or $^1n\sigma^*$ state.[37,38,39,40] For thioanisole, the role that conical intersections play in the mechanism has been studied both theoretically and experimentally.[13,41,42] The proposed mechanism can be understood based on Figure 8.1, a schematic of the relevant adiabatic potential energy surfaces along the S-CH_3 bond stretch coordinate, R. At the equilibrium geometry (with $R \cong 1.8$ Å), the molecule is first excited (by an ultraviolet photon with energy 4.3–4.5 eV) from the closed-shell ground state S_0 to the bound singlet excited state S_1 with $\pi\pi^*$ character. The reactive flux then transfers in the region near the S_1-S_2 conical intersection (labeled CI1) to the repulsive $n\sigma^*$ state and proceeds to the region near the S_0-S_1 conical intersection (labeled CI2) with elongated S-CH_3 bond. Finally the flux bifurcates near CI2, and the molecule dissociates to either the D_0 or D_1 state of thiophenoxyl radical plus methyl radical. In Figure 8.1 and also in the remainder of this chapter, "$\pi\pi$", "$\pi\pi^*$", and "$n\sigma^*$" are used as diabatic labels based on the character of the diabatic states; the diabatic potential energy surfaces (PESs) are the diagonal elements of the diabatic potential energy matrix and are denoted by U_{11}, U_{22}, U_{33}. On the other hand, "S_0", "S_1", and "S_2" are used as adiabatic labels for the

potential energy functions of the adiabatic states, whose PESs are denoted by $V_1 < V_2 < V_3$.

Previous theoretical studies have focused on either the local topography of the PESs at the minimum-energy conical intersection (MECI) geometries or on the global topography of the PESs along only two dimensions, namely the S-CH_3 bond stretch and the C-C-S-C torsion.[13,14] Although these two coordinates are considered to be the most important "reaction coordinates," the PESs can still have important dependence on the other 40 "spectator" degrees of freedom. In particular, the conical intersection seam is multi-dimensional in nature, and the reactive flux can access the seam or a low barrier near the seam at geometries where the 40 "spectator" degrees of freedom are away from their values for the equilibrium geometry or the MECI geometry. Therefore, all degrees of freedom can be important for nonadiabatic dynamical simulations. This is a challenge because a set of full-dimensional analytic potential surfaces and couplings has never previously been presented for a system with this many degrees of freedom. We shall address the challenge by using a diabatic representation. The advantage of a diabatic representation is that PESs and state couplings are smooth scalars in a diabatic representation, whereas in an adiabatic representation the PESs have cuspidal ridges at high-dimensional seams of conical intersection, and the state couplings are vectors become singular at these ridges. Note that we define a diabatic representation as one that reduces the coupling of electronic states due to nuclear momentum and nuclear kinetic energy "to a level comparable to the nonadiabatic coupling that occurs in the BO representation in regions where the Born-Oppenheimer approximation is a good approximation"[43] so they may be neglected, and all the coupling that needs to be retained for a realistic treatment of dynamics comes from the electronic Hamiltonian. Furthermore, we assume that the fourfold way diabatization scheme[44] produces a good approximation to such a diabatic representation.

In the present work we present an analytic fit to the full-dimensional diabatic PESs and diabatic state couplings of the three lowest singlet states of thioanisole. Note that, following the usual conventions, the couplings in the diabatic representation are called

diabatic couplings, whereas the couplings in the adiabatic representation are called nonadiabatic couplings. The diabatic PESs are diagonal elements of the diabatic potential energy matrix, and the diabatic couplings are off-diagonal elements of this matrix; thus – as mentioned in the previous paragraph – the diabatic PESs and diabatic couplings are scalars. The scalar adiabatic PESs and vector nonadiabatic couplings are also available from these fits since they are easily calculated[45] by a diabatic-to-adiabatic diagonalization with a small number of states, in particular three states in the present case.

The present fits cover a wide range of geometries from the Franck-Condon region to the dissociation of the S-CH3 bond. By using the Anchor Points Reactive Potential (APRP) scheme developed by our group,[33,46] we treat two coordinates, which are called reactive coordinates, globally, and we treat other coordinates by system-specific, reaction-coordinate-specific molecular mechanics (MM). In constructing the PESs of thioanisole we have made two improvements of the APRP scheme as compared to its previous employment: (1) we generalized the scheme, which originally was implemented with one reactive coordinate, to include two reactive coordinates (and the same kind of generalization could be used in the future to treat more than two reactive coordinates); (2) we made the fitting of the potential functions along the non-reactive coordinates much more convenient by using a locally modified version[47] of the *QuickFF* package[48] for "automatic" force field generation.

The PESs are full-dimensional in the sense that they are functions of all the 42 internal degrees of freedom of thioanisole. By construction, however, the PESs are most accurate near the anchor points, which are the most important for the photodissociation of the S-CH_3 bond. The PESs are not appropriate for study of other reaction channels of thioanisole.

The rest of this chapter is arranged as follows. Section 8.2 gives the technical details of the construction of the APRP potential energy matrix. Section 8.3 compares the APRP potential energy matrix elements and derived properties, such as equilibrium and saddle point geometries, conical intersections, excitation energies, and vibrational

frequencies, with experiment and with electronic structure calculations. Section 8.4 is a summary.

8.2. METHODS AND COMPUTATIONAL DETAILS

8.2.1. Introduction

The APRP can be applied to a single potential energy surface or to a diabatic potential energy matrix, whose diagonal elements are called diabatic potential energy surfaces, and whose off-diagonal elements are called diabatic couplings. The whole potential energy matrix is referred to as the "potential" in this work. In the present case we fit three diabatic surfaces and their couplings. The APRP scheme involves two steps. In the first step of the present work we fit the diabatic potential energy matrix in the reactive degrees of freedom, which are called the primary and secondary degrees of freedom.

First we review the fitting of a single one of the diabatic potential energy surfaces. The reactive coordinates must be able to describe any bond breaking, bond making, or bond rearrangements and any other coordinates that have wider-amplitude motion than can accurately be described by nonreactive molecular mechanics. The reactive coordinates can be subdivided into two groups; those with a strong coupling to nonreactive degrees of freedom are called primary coordinates, and those, if any, with a negligible coupling to nonreactive degrees of freedom are called secondary coordinates. The method that can be used for fitting the dependence of the surface on the reactive degrees of freedom is completely general and depends on the system under study; for the present application it is described in Section 8.2.3.1. The dependence of the potential for the reactive degrees of freedom is fitted with the remaining coordinates fixed, for example, at their equilibrium values in the reactant or product or at partially optimized values with fixed secondary and tertiary coordinates; these remaining coordinates are called the tertiary coordinates. In the second step we add the dependence of the potential on the tertiary coordinates. This is done by identifying a number of points, called anchor points, specified by their values of the primary and secondary coordinates (the primary

coordinates differ among the anchor points, but the secondary coordinates, if any, do not), and fitting a nonreactive molecular mechanics potential to each surface and coupling in the tertiary coordinates at each anchor point. The regional potentials at the anchor points are then sewn together into a single tertiary potential by functions called tent functions. In this way the potential as a function of the tertiary coordinates also depends on, i.e., is coupled to, the primary coordinates. To make the procedure more robust, the nonreactive molecular mechanics potential is expressed in terms of Simon-Parr-Finlan coordinates[49] for stretches (rather than the usual bare bond extension coordinates) and trigonometric functions[33] for bends (rather than as the usual bare bond angles). Because these coordinates extend the region over which the fits are valid, as compared to using the usual internal coordinates, we label the anchor-point fits as regional potentials rather than local potentials.

In the present case, we use one primary coordinate, one secondary coordinate, and a set of 73 or 67 redundant internal coordinates as tertiary coordinates for diabatic potential energy surfaces. We use two primary coordinates, no secondary coordinates, and a set of 8 tertiary coordinates for diabatic couplings. The diabatic potential energy surfaces in the primary coordinates and all the diabatic couplings are fitted to the corresponding quantities obtained by extended multi-configurational quasi-degenerate perturbation theory (XMC-QDPT)[50,51,52] followed by the fourfold way[44,53,54,55] and model space diabatization[56]. The diabatic potential energy surfaces in the tertiary coordinates are fitted to those computed by Kohn-Sham density functional theory (DFT)[57,58] and linear-response time-dependent DFT (TDDFT).[59] (Details are given in Section 8.2.5.)

Figure 8.2(a) shows our convention for numbering the atoms. We do not distinguish elements for the numbering; for instance, we have “C1” and “H9” rather than “C1” and “H1”. We will refer to the atoms by “element + number” (e.g., S7), by number only (e.g., 7), or by element only (e.g. S), depending on the context.

8.2.2. Primary and secondary coordinates

In the APRP scheme we need to define a set of "reactive" internal coordinates that must be treated globally to describe the reaction; in the present application of the APRP scheme, these are primary and secondary coordinates. Primary coordinates can have arbitrarily large amplitude of motion in the reaction, and they have strong potential energy coupling to other coordinates. Secondary coordinates can have arbitrarily large amplitude of motion in the reaction and are treated globally as well, but they have weaker coupling to coordinates other than the primary ones. For photodissociation of thioanisole, the S-CH_3 bond stretch and C-C-S-C torsion are the conventional internal coordinates that play the most prominent roles. In our previous work[60] we studied the diabatic PESs of thioanisole along these two coordinates, and we showed that they both play significant roles in the adiabatic-to-diabatic transformation. A more detailed examination, though, shows that the diabatization depends most strongly on the orientation of the S-CH_3 bond relative to the phenyl plane. The C-C-S-C torsion is a good representation of this orientation only when C2, C1, C6, and S are coplanar. Therefore, in the present work, in which these four atoms are not constrained to be coplanar, we use an alternative angular coordinate as a primary or secondary coordinate (secondary for fitting the diabatic potential energy surfaces and primary for fitting the diabatic couplings); in particular, we use the angle between the vector C6-C2 and the projection of vector S-C8 on the plane defined by the vector C6-C2 and the normal vector of the C6-C1-C2 plane. Hereafter we label this angular coordinate as ϕ and the S-C8 bond length as R. They are defined explicitly as

$$R = \left|\mathbf{r}_{7\text{-}8}\right| \tag{8.1}$$

$$\cos\phi = \frac{\mathbf{r}_{6\text{-}2} \cdot \mathbf{v}_{\mathrm{p}}}{\left|\mathbf{r}_{6\text{-}2}\right|\left|\mathbf{v}_{\mathrm{p}}\right|}$$

$$\mathbf{v}_{\mathrm{p}} = \mathbf{r}_{7\text{-}8} - \mathbf{v}_{\mathrm{x}} \frac{\mathbf{v}_{\mathrm{x}} \cdot \mathbf{r}_{7\text{-}8}}{\left|\mathbf{v}_{\mathrm{x}}\right|^2} \tag{8.2}$$

$$\mathbf{v}_{\mathrm{x}} = \mathbf{r}_{6\text{-}2} \times \left(\mathbf{r}_{6\text{-}1} \times \mathbf{r}_{1\text{-}2}\right)$$

where $\mathbf{r}_{i\text{-}j}$ is the vector from atom *i* to atom *j*. These two coordinates are illustrated in Figure 8.2(b). For treating the diabatic potential energy surfaces, R is a primary and ϕ is a secondary coordinate, whereas for treating the diabatic couplings, both R and ϕ are primary. The key distinction between the treatments of diabatic potential energy surfaces and diabatic couplings is that the tertiary couplings depend on both R and ϕ, while the tertiary potential energy surfaces depend only on R.

We note that some coordinates involving the S-CH_3 bond such as the C-S-C bond angle can have large amplitude of motion when the S-CH_3 bond stretches and may be treated as secondary coordinates. However, based on the excessive energy of S_1 compared to the dissociation asymptote and our previous work on a similar system, phenol,[32] we expect that the molecule will dissociate quickly once it goes past CI1 into the repulsive region and will not have time to distribute energy to such coordinates as the C-S-C bond angle to have large amplitude of motion. Therefore we treat those coordinates as tertiary coordinates for simplicity. Our sample trajectories show that the molecule dissociates in less than 0.5 ps after entering the repulsive region, which supports our decision.

8.2.3. Anchor points reactive potential (APRP) for constructing the diabatic potential energy matrix

To apply the APRP scheme to thioanisole, the diabatic potential energy matrix elements for diabatic states *i* and *j* are written as

$$U_{ij}(R,\phi,\mathbf{Q}) = U_{ij}^{[1,2]}(R,\phi) + U_{ij}^{[3]}(\mathbf{Q} \mid R,\phi) \tag{8.3}$$

where R and ϕ denote the two reactive coordinates; $\mathbf{Q}$ denotes collectively all the other internal coordinates, which are the tertiary coordinates; and the notation $f(\mathbf{Q} \mid R, \phi)$ means a function f of $\mathbf{Q}$ that depends parametrically on R and ϕ.

The diagonal elements of $\mathbf{U}$ are the diabatic potential energy surfaces and the off-diagonal elements are the diabatic couplings. The two terms on the right-hand side of eq. (8.3) are respectively called reactive-coordinates diabatic potential energy surfaces and tertiary diabatic potential energy surfaces for $i = j$ and are respectively called primary and tertiary diabatic couplings for $i \neq j$. The reactive-coordinates diabatic potential energy surfaces and primary diabatic couplings are fitted globally with general functional forms. The tertiary diabatic potential energy surfaces and diabatic couplings are fitted regionally with MM functional forms. Standard MM fits are local, by which we mean that they are valid only in a quadratic or near-quadratic region around their central point, except for torsions, which are usually fitted with more widely valid trigonometric functions; our tertiary potential goes beyond standard MM in two ways: (i) we use more widely valid internal coordinates than those usually used in MM; (ii) we tie several such MM fits (each centered at an anchor point) together via tent functions of the primary coordinates. Thus the molecular mechanics expressions in the tertiary diabatic potential energy surfaces depend parametrically on the primary coordinates.

1. Reactive-coordinates diabatic potential energy surfaces and primary diabatic couplings. As mentioned in Section 8.2.1, the reactive-coordinates matrix elements are fitted to values calculated by XMC-QDPT followed by fourfold way and model space diabatization. These are single-point calculations at geometries on a two-dimensional grid of R and ϕ values, while the other coordinates are fixed at values of the S_0 equilibrium geometry. These diabatic potential energy surfaces and diabatic couplings are then fitted with general analytic functions.

For diabatic state $\pi\pi$ (corresponding to S_0 in the Franck-Condon region), the surface is fitted with the following function including a Rydberg model potential[61] term:

$$\begin{aligned} U_{11}^{[1,2]}(R,\phi) = {} & A_1 - D_1[1 + b_1(R - R_{11})]e^{-b_1(R-R_{11})} \\ & + B_1 \exp[-\alpha_1(R - R_{12})^2](1 - \cos 2\phi) \end{aligned} \tag{8.4}$$

where A_1, D_1, b_1, R_{11}, B_1, α_1, and R_{12} are parameters.

Diabatic state ππ* (corresponding to S_1 in the Franck-Condon region) is energetically accessible only for small-R geometries, and it is fitted with the following function including a Morse potential[62] term:

$$U_{22}^{[1,2]}(R,\phi) = A_2 + D_2(1-e^{-b_2(R-R_{21})})^2 + B_2 e^{-\alpha_2(R-R_{22})^2}(1-\cos 2\phi) \tag{8.5}$$

where A_2, D_2, b_2, R_{21}, B_2, α_2, and R_{22} are parameters.

For diabatic state nσ* (corresponding to S_2 in the Franck-Condon region), the surface is fitted with the following function:

$$U_{33}^{[1,2]}(R,\phi) = A_3 + D_3 e^{-b_3 R} + \left[B_3 e^{-\alpha_3(R-R_3)^2} + C_3 e^{-4\alpha_3(R-R_3)^2} \right](1-\cos 2\phi) \tag{8.6}$$

where A_3, D_3, b_3, B_3, C_3, α_3, and R_3 are parameters.

The primary diabatic couplings are fitted with

$$U_{12}^{[1]}(R,\phi) = B_0^{(12)} + B_2^{(12)} \exp\left[-\alpha_2^{(12)}(R-R_2^{(12)})^2\right]\sin^2\phi + B_4^{(12)} \exp\left[-\alpha_4^{(12)}(R-R_4^{(12)})^2\right]\sin^4\phi \tag{8.7}$$

$$U_{13}^{[1]}(R,\phi) = B_2^{(13)} \exp\left[-\alpha_2^{(13)}(R-R_2^{(13)})^2\right]\sin 2\phi + (c_0^{(13)} + c_1^{(13)}R)\exp\left[-\alpha_4^{(13)}R\right]\sin 4\phi \tag{8.8}$$

$$U_{23}^{[1]}(R,\phi) = B_4^{(23)} \exp\left[-\alpha_4^{(23)}(R-R_4^{(23)})^2\right]\sin 4\phi + B_6^{(23)} \exp\left[-\alpha_6^{(23)}(R-R_6^{(23)})^2\right]\sin 6\phi \tag{8.9}$$

where $B_k^{(ij)}$, $\alpha_k^{(ij)}$, $R_k^{(ij)}$, and $c_k^{(ij)}$ (i, j = 1, 2, 3*; k* is an integer) are parameters. These functional forms are chosen to have the correct symmetry about $\phi = n\pi/2$ (where n is an integer, including zero), namely U_{12} is even and U_{13} and U_{23} are odd.

2. Tertiary diabatic potential energy surfaces. The tertiary diabatic potential energy surfaces are constructed via interpolation of MM-like potentials modeled at predetermined anchor point geometries, each of which has primary and secondary coordinates fixed at certain values (referred to as "anchor point nodes" for the individual primary and secondary coordinates and as "anchor point locations" for the set of primary and secondary coordinates) and tertiary coordinates relaxed by partial geometry optimization.

The tertiary diabatic potential energy surfaces are given by

$$U_{ii}^{[3]}(\mathbf{Q}\,|\,R) = \sum_{a=1}^{A(ii)} U_{ii}^{[3](a)}(\mathbf{Q}) T^{(a)}\left(R, \left\{R_a^{(ii)}\right\}_{a=1}^{A(ii)}\right) \tag{8.10}$$

where $A(ii)$ is the number of anchor point nodes for fitting $U_{ii}^{[3]}$, where $\left\{R_a^{(ii)}\right\}_{a=1}^{A(ii)}$ is the set of the nodes specifying these anchor points, where $U_{ii}^{[3](a)}$ is tertiary surface *i* at anchor point node *a*, and where T, called a tent function, gives the weight of the anchor point node in the interpolation. The tent functions are given by

$$T^{(1)}\left(q, \left\{q_a\right\}_{a=1}^{A}\right) = \begin{cases} 1, & q < q_1 \\ \dfrac{(q-q_2)^4}{(q-q_2)^4 + (q-q_1)^4}, & q_1 \le q < q_2 \\ 0, & \text{otherwise} \end{cases} \tag{8.11}$$

$$T^{(a)}\left(q, \left\{q_a\right\}_{a=1}^{A}\right) = \begin{cases} \dfrac{(q-q_{a-1})^4}{(q-q_a)^4 + (q-q_{a-1})^4}, & q_{a-1} \le q < q_a \\ & \text{for } a = 2,\ldots,A-1 \\ \dfrac{(q-q_{a+1})^4}{(q-q_{a+1})^4 + (q-q_a)^4}, & q_a \le q < q_{a+1} \\ 0, & \text{otherwise} \end{cases} \tag{8.12}$$

$$T^{(A)}\left(q,\left\{q_a\right\}_{a=1}^{A}\right)=\begin{cases}\dfrac{(q-q_{A-1})^4}{(q-q_A)^4+(q-q_{A-1})^4}, & q_{A-1}\le q<q_A\\ 1, & q>q_A\\ 0, & \text{otherwise}\end{cases} \tag{8.13}$$

where q_a is the value of q at anchor point node a, and the anchor point nodes are arranged in ascending order of q_a.

The tertiary surface $U_{ii}^{[3](a)}$ at an anchor point location is modeled by force field terms whose parameters are optimized to reproduce the Hessian matrix at a partially optimized anchor point geometry calculated by DFT and TDDFT. (The procedure of optimizing the parameters will be discussed later in this section.) In particular, it is written as

$$U_{ii}^{[3](a)}=U_{\mathrm{rel},ii}^{[3](a)}+U_{ii}^{\mathrm{S}(a)}+U_{ii}^{\mathrm{B}(a)}+U_{ii}^{\mathrm{T}(a)}+U_{ii}^{\mathrm{D}(a)} \tag{8.14}$$

where $U_{\mathrm{rel},ii}^{[3](a)}$ is the energy of the partially optimized anchor point geometry relative to the geometry with primary and secondary coordinates fixed at their anchor point values and tertiary coordinates fixed at values corresponding to the S_0 equilibrium geometry. Notice that eq. (8.14) does not contain the optional van der Waals terms or electrostatic terms of the *QuickFF* procedure; they could be included in the general case but were deemed unnecessary for the present problem. The last four terms on the right-hand side of eq. (8.14) are contributions from bond stretches, valence angle bends, torsions, and out-of-plane distances (defined as the distance d from one atom to the plane formed by another three atoms).[48] These terms are given respectively by

$$U_{ii}^{\mathrm{S}(a)}(\{R_\mu\})=\frac{1}{2}\sum_{\mu}k_{\mu,ii}^{\mathrm{S}(a)}\left(\frac{R_\mu-R_{0,\mu ii}^{(a)}}{R_\mu}\right)^2 \tag{8.15}$$

$$U_{ii}^{\mathrm{B}(a)}(\{\theta_\mu\}) = \frac{1}{2}\sum_\mu k_{\mu,ii}^{\mathrm{B}(a)}(\cos\theta_\mu - \cos\theta_{0,\mu ii}^{(a)})^2 \tag{8.16}$$

$$U_{ii}^{\mathrm{T}(a)}(\{\phi_\mu\}) = \frac{1}{2}\sum_\mu k_{\mu,ii}^{\mathrm{T}(a)}\left(1 - \cos\left[n_\mu(\phi_\mu - \phi_{0,\mu ii}^{(a)})\right]\right) \tag{8.17}$$

$$U_{ii}^{\mathrm{D}(a)}(\{d_\mu\}) = \frac{1}{2}\sum_\mu k_{\mu,ii}^{\mathrm{D}(a)}(d_\mu - d_{0,\mu ii}^{(a)})^2 \tag{8.18}$$

where μ runs over the appropriate tertiary coordinates (note that eq. (8.17) is equivalent to eq. 14c of ref. 33); the k quantities are force constants, the variables with a subscript 0 are force field parameters representing position of the minimum of the term, and the n parameters are dihedral multiplicities. The dihedral multiplicities are predetermined based on local or regional symmetry, and the force constants and minimum-position parameters are determined by the fitting procedure described in Section 8.2.3.3 rather than fixed at values for the partially optimized anchor point geometry. The functional forms of the stretches, valence bends, and torsions terms in eqs. (8.15)–(8.18) have better global behavior than simple harmonic terms. Notice that the force field used here has no cross terms that couple different tertiary coordinates; this would be a poor approximation if made in Cartesian coordinates, but it is much safer to neglect cross terms when one uses internal coordinates.[63]

The tertiary coordinates used are all the (redundant) bond stretches, valence bends, torsions, and out-of-plane distances based on the connectivity of the atoms shown in Figure 8.2. They are listed in Table 8.1 along with the dihedral multiplicities.

3. Determination of force field parameters for tertiary diabatic potential energy surfaces. A four-step procedure is used to determine the force field parameters for the tertiary diabatic potential energy surface of each diabatic state. (1) A set of anchor point values of R is chosen. (2) An anchor point geometry is obtained for each anchor point value of R by partial geometry optimization on the corresponding adiabatic state using DFT or TDDFT with the constraint that R is fixed at the chosen node and ϕ fixed at 0°. (In the original *QuickFF* procedure, force fields are constructed around one location,

which is the equilibrium geometry. Here with multiple anchor point locations, partial optimization is needed for each anchor point.) (3) The Cartesian Hessian matrix is obtained for each partially optimized anchor point geometry by DFT or TDDFT. (4) The force field parameters are optimized against the DFT or TDDFT Hessian matrix. This procedure is repeated for each of the three diabatic states.

For step (1), anchor point nodes of R = 1.8, 2.2, 3.2, and 6.0 Å are chosen for $U_{11}^{[3]}$, R = 1.8 and 2.2 Å for $U_{22}^{[3]}$, and R = 1.9, 2.2, 3.2, and 6.0 Å for $U_{33}^{[3]}$. All these anchor point geometries have C_s symmetry, for which we can model the dependence of the diagonal diabatic potentials on the tertiary coordinates as being the same as the dependence of the adiabatic potentials on these coordinates; therefore we use the Hessian matrix of the adiabatic state for modeling the tertiary diabatic potential energy surfaces. The first anchor point value is chosen to be at or near the S_0 equilibrium value of 1.8 Å. (1.9 Å is chosen for $U_{33}^{[3]}$ because at R = 1.8 Å the partial geometry optimization for this state does not converge.) The last anchor point is chosen in the asymptotic region, and the geometry optimizations at this anchor point were carried out separately for the thiophenoxyl and methyl radicals.

Step (4) was carried out by using our own modified version[47] of the *QuickFF* package.[48] For each anchor point, *QuickFF* takes as input the anchor point geometry, the set of internal coordinates and the corresponding force field functions in eqs. (8.15)–(8.18), and the ab initio Cartesian Hessian matrix. The internal coordinates are the tertiary coordinates listed in Table 8.1, plus the S7-C8 bond stretch, the C2-C1-S7-C8 torsion, and the C6-C1-S7-C8 torsion for anchor points with $R \neq$ 6.0 Å. The last three coordinates are closely correlated with primary and secondary coordinates. They are needed for *QuickFF* to construct the force field, but their corresponding potential functions are replaced by the reactive-coordinates surface terms when the reactive-coordinates and tertiary diabatic potential energy surfaces are combined for the full surface. *QuickFF* optimizes the force field parameters by optimizing the Cartesian Hessian derived from the force field against the ab initio Hessian. The details of how

QuickFF derives force field parameters using information in the ab initio Hessian matrix can be found in ref. 48. With our improved force field functional forms, the procedure is essentially the same, except that the simple quadratic functions in eqs. (2.11) and (2.12) of ref. 44 are replaced by our improved functions, with the parameters to be fitted being the ones in eqs. (8.15)–(8.18) of this chapter. For asymptotic anchor points with R = 6.0 Å, we use force constants derived from isolated thiophenoxyl and methyl radicals in order that the diabatic potential energy surfaces will have the correct asymptotic behavior.

4. Born-Mayer potential. To avoid the non-bonded carbons from coming too close during a trajectory, we added additional Born-Mayer potentials between all pairs of *para* carbon atoms (C1-C4, C2-C5, C3-C6) to all diagonal elements of the diabatic potential energy matrix. The Born-Mayer potential is given by

$$V_{\mathrm{BM}} = B \sum_{i\text{-}j=1\text{-}4,2\text{-}5,3\text{-}6} \exp(-\alpha r_{i\text{-}j}) \tag{8.19}$$

where the parameters are set to B = 42000 kcal mol^{-1} and α = 3.58 Å^{-1}.[64]

5. Tertiary diabatic couplings. Similar to tertiary diabatic potential energy surfaces, tertiary diabatic couplings are built by interpolating the couplings modeled at preselected anchor point locations. However, the set of anchor point locations for the tertiary couplings is different from the set used for tertiary diabatic potential energy surfaces, and we will refer to the set for tertiary couplings simply as "anchor point locations for couplings" throughout Section 8.2.3.5. Unlike those for tertiary diabatic potential energy surfaces, the anchor point geometries for couplings differ from the S_0 equilibrium geometry only in the values of R and ϕ; the tertiary coordinates are not optimized for fitting the couplings. The expression for the tertiary couplings is

$$\begin{aligned}
&U_{ij}^{[3]}(\mathbf{Q} \mid R,\phi) = \\
&s_{ij}(\phi)\sum_{a=1}^{2}\sum_{b=1}^{3} U_{ij}^{[3](a,b)}(\mathbf{Q})\left(T^{(a)}\left(R,\left\{R_a^{\mathrm{C}}\right\}_{a=1}^{2}\right)\right)\left(T^{(b)}\left(y(\phi),\left\{y_b^{\mathrm{C}}\right\}_{b=1}^{3}\right)\right), \quad i \neq j \\
&y(\phi) = -\cos 2\phi \\
&y_b^{\mathrm{C}} = -\cos 2\phi_b^{\mathrm{C}}
\end{aligned} \tag{8.20}$$

The argument of the second tent function is chosen to be $y = -\cos 2\phi$ so that it has the correct periodicity along ϕ and so that the argument is monotonically increasing in $\phi \in [0, \pi/2]$. Eq. (8.20) can describe the tertiary diabatic couplings for geometries of any ϕ value by choosing anchor point nodes of ϕ only in [0, π/2]. The additional multiplicative factor s_{ij} is given by

$$\begin{aligned} s_{12}(\phi) &= 1 \\ s_{13}(\phi) &= s_{23}(\phi) = \mathrm{sign}(\sin 2\phi) \end{aligned} \tag{8.21}$$

where the sign function is defined by

$$\mathrm{sign}(x) = \begin{cases} 1, & x > 0 \\ 0, & x = 0 \\ -1, & x < 0 \end{cases} \tag{8.22}$$

The s_{ij} factor is introduced because U_{12} is even and U_{13} and U_{23} are odd about $\phi = n\pi/2$ (where n is an integer, including zero). The double sum over anchor points in eq. (8.20) will be constructed, as described in Section 8.2.3.6, such that it is zero at $\phi = n\pi/2$ (where n is an integer, including zero) and that the s_{ij} factor does not cause discontinuity.

The $U_{ij}^{[3]}$ so defined have periodicity along ϕ because of the definition of y in eq. (8.20) and the s_{ij} factor in eq. (8.21). Such periodicity exists only for a relaxed scan along ϕ, where the molecule has C_s symmetry for $\phi = 0$ or 90 deg. In practice, however, we make an approximation of assuming such periodicity for general geometries in the anchor point interpolation along ϕ.

A set of nonredundant internal coordinates is used to expand the tertiary diabatic couplings. These coordinates are different from those used for the tertiary diabatic potential energy surfaces. We examined the magnitude of diabatic couplings introduced by changing each angular coordinate (valence bends, torsions, and out-of-plane bends), and we chose only eight coordinates that are symmetric and make the most significant contributions to the variations of the couplings; these are listed in Table 8.2.

The diabatic coupling at an anchor point, $U_{ij}^{[3](a,b)}$, is a sum of terms, each term corresponding to one coordinate,

$$U_{ij}^{[3](a,b)}(\mathbf{Q}) = \sum_{\mu} U_{ij,\mu}^{[3](a,b)}(Q_\mu) \tag{8.23}$$

For most coordinates Q_μ, the corresponding term in the sum is a second-degree polynomial damped by a Gaussian function,

$$\begin{aligned} U_{ij,\mu}^{[3](a,b)}(Q_\mu) = &\left[K_{1,\mu ij}^{(a,b)} \left(Q_\mu - Q_{\mathrm{e},\mu} \right) + K_{2,\mu ij}^{(a,b)} \left(Q_\mu - Q_{\mathrm{e},\mu} \right)^2 \right] \\ &\times \exp\left[-\left(Q_\mu - Q_{\mathrm{e},\mu} \right)^2 / \sigma^2 \right] \end{aligned} \tag{8.24}$$

where the K parameters are to be fitted and the parameters with subscript e are fixed at values for the S_0 equilibrium geometry. The Gaussian function is used to damp the diabatic couplings when $(Q_\mu - Q_{\mathrm{e},\mu})$ is large, because the polynomial may have too large values for those unphysical distorted geometries. The parameter σ is set to 100 deg so that it does not compromise the physical region with small $(Q_\mu - Q_{\mathrm{e},\mu})$.

For the C-S-C bending coordinate (coordinate 8 in Table 8.2), however, the term is a second-degree polynomial of the cosine of the coordinate,

$$\begin{aligned} U_{ij,\mu}^{[3](a,b)}(Q_\mu) = &K_{1,\mu ij}^{(a,b)} \left(\cos Q_\mu - \cos Q_{\mathrm{e},\mu} \right) \\ &+ K_{2,\mu ij}^{(a,b)} \left(\cos Q_\mu - \cos Q_{\mathrm{e},\mu} \right)^2, \quad \text{for } Q_\mu = \theta_{\mathrm{CSC}} \end{aligned} \tag{8.25}$$

The reason for this treatment is that $\cos\theta_{CSC}$ has better behavior for large amplitude motion of θ_{CSC}, which can occur as R increases and the S-CH_3 bond weakens.

6. Determination of force field parameters for tertiary diabatic couplings. A three-step procedure, different from the modified *QuickFF* procedure used for the tertiary diabatic potential energy surfaces, is used to numerically fit the polynomial coefficients in eqs. (8.24) and (8.25). (1) A set of anchor point locations are chosen and the corresponding anchor point geometries are built. Every pair of (R_a^C, ϕ_b^C) corresponds to an anchor point location. Every anchor point geometry has primary coordinates specified by the anchor point location, with the other coordinates fixed at values of S_0 equilibrium geometry. (Partial optimization is not used in this fit.) (2) For each anchor point geometry, each coordinate in Table 8.2 is in turn displaced by -30, -20, -10, -5, -4, -3, -2, -1, 1, 2, 3, 4, 5, 10, 20, 30 deg and the tertiary diabatic couplings are computed by XMC-QDPT followed by the fourfold way and model space diabatization. (3) The K parameters in eqs. (8.24) and (8.25) are determined by fitting eq. (8.24) or (8.25) to the difference of the ab initio data from step (2) and the primary diabatic couplings.

For step (1), we choose R_a^C = 1.97 and 3.5 Å and ϕ_b^C = 0, 10, 45, 80, and 90 deg as anchor point nodes. The two anchor point nodes of R are chosen to be near the two conical intersections where the state couplings are most important.

For steps (2) and (3), for each anchor point location with ϕ_b^C = 10, 45, or 80 deg, ab initio calculations were carried out and the K parameters in eqs .(8.24) and (8.25) are determined by fitting eqs. (8.24) or (8.25) to the difference of the ab initio diabatic couplings and the already-determined primary diabatic couplings. For each anchor point location with ϕ_b^C = 0 or 90 deg, the K parameters are set to zero so that $U_{ij,\mu}^{[3](a,b)} = 0$ and that the s_{ij} factor in eq. (8.20) does not cause discontinuity.

8.2.4. Gradients, adiabatic potentials, and nonadiabatic couplings.

The gradients of diabatic matrix elements with respect to Cartesian coordinates are given by the chain rule,

$$\frac{\partial U_{ij}}{\partial x_\alpha} = \sum_\mu \frac{\partial U_{ij}}{\partial q_\mu} \frac{\partial q_\mu}{\partial x_\alpha} \tag{8.26}$$

where x_α and q_μ are Cartesian and internal coordinates and μ runs over all internal coordinates on which U_{ij} depends. The derivatives $\partial q_\mu / \partial x_\alpha$ are given by the Wilson B matrix,[65] which is coded in the FORTRAN PES subroutine.

The adiabatic potentials are obtained by diagonalizing the diabatic potential energy matrix,

$$V_i = \sum_j \sum_k C_{ji} U_{jk} C_{ki} \tag{8.27}$$

where **C** is the orthogonal matrix that diagonalizes **U**.

The gradients of adiabatic potentials and the nonadiabatic couplings are given by[45]

$$\frac{\partial V_i}{\partial x_\alpha} = \sum_j \sum_k C_{ji} \frac{\partial U_{jk}}{\partial x_\alpha} C_{ki} \tag{8.28}$$

$$F_{ij}^\alpha = \left\langle \psi_i \left| \frac{\partial}{\partial x_\alpha} \right| \psi_j \right\rangle = \begin{cases} \dfrac{1}{V_j - V_i} \displaystyle\sum_k \sum_l C_{ki} \frac{\partial U_{kl}}{\partial x_\alpha} C_{lj} & (i \neq j) \\ 0 & (i = j) \end{cases} \tag{8.29}$$

where $|\psi_i\rangle$ is the ith adiabatic state.

8.2.5. Additional computational details

The ab initio data used for constructing the reactive-coordinates diabatic potential energy surfaces and all the diabatic couplings were calculated by extended multiconfigurational quasidegenerate perturbation theory (XMC-QDPT) followed by the fourfold way and model space diabatization, with a mixed, minimally augmented basis set of 6-311+G(d)[66,67] for carbon and hydrogen and MG3S[68] for sulfur, denoted by maTZ

in this chapter (standing for minimally augmented triple zeta). (The same basis set was denoted by MB in refs. 60 and 69.) Details of the calculations such as active orbitals and diabatic prototypes, as well as detail discussion about the diabatization, can be found in refs. 60 and 56. The *GAMESS*[70,71] electronic structure package was used for these calculations.

The partial geometry optimizations and Hessian calculations for constructing the tertiary diabatic potential energy surfaces were performed by Kohn-Sham DFT for the ground state and linear-response TDDFT for the excited states. The M06-2X[72,73] exchange-correlation functional and the jul-cc-pV(D+d)Z[74,75,76,77] basis set were used for DFT. The τ-HCTHhyb[78] functional and the jul-cc-pV(D+d)Z basis set were used for TDDFT. The *Gaussian 09* [79] electronic structure package was used for these calculations.

The minimum energy conical intersections (MECIs) between adiabatic states *i* and *j* are obtained by minimizing the following function using an in-house BFGS optimizer,[80]

$$\frac{V_i + V_j}{2} + \alpha(V_i - V_j)^2 \tag{8.30}$$

where V_i is the adiabatic energy of state *i* and the parameter α is set to $10^5\ E_h^{-2}$.

The geometry optimization, vibrational analysis, and minimum energy path calculations with the fitted APRP potential matrices were done with POLYRATE.[81] We have run thousands of sample trajectories with the APRP potential matrices interfaced to ANT[82] to ensure they conserve energy and do not visit unphysical geometries.

8.3. RESULTS AND DISCUSSION

8.3.1. Excitation energies in the Franck-Condon region.

Tables 8.3 and 8.4 compare the vertical, adiabatic, and 0–0 excitation energies given by APRP to various electronic structure methods and to experiment. Here vertical excitation energy is defined as the difference of potential energies at the S_0 equilibrium geometry; adiabatic energy is defined as the difference of potential energies of S_1 and S_0 at their respective equilibrium geometry (S_2 is not considered since it does not have a

minimum); 0–0 excitation energy is defined as the adiabatic excitation energy plus the difference of zero-point vibrational energy of S_1 and S_0 at their respective equilibrium geometry. (The zero point energies are computed in the harmonic approximation).

Table 8.3 shows that APRP compares well with the best estimates of vertical excitation energy, which are the ones given by completely-renormalized equation-of-motion coupled cluster theory with singles, doubles, and noniterative connected triples (CR-EOM-CCSD(T))[83,84] with the aug-cc-pV(T+d)Z basis set[74,75,76,77] and by SA(3)-MC-QDPT(12,11)/aug-cc-pV(T+d)Z. Table 8.4 shows that the adiabatic excitation energy given by APRP also compares well with XMC-QDPT, while the 0–0 excitation energy is underestimated by 0.2 eV compared to experiment. This deviation is presumably due to the difficulty of modeling the topography and thus the vibrational frequencies of S_1, as will be discussed in Section 8.3.2.

8.3.2. Equilibrium geometries and vibrational frequencies

Whether the equilibrium geometry of S_0 has the methyl carbon in the phenyl plane (with C_s symmetry) or out of the plane is a question that has been under debate for years. The older literature concluded that it is out of the plane,[85] but more recent experimental and theoretical studies consistently agree on the opposite.[86,87,88,89] Our geometry optimization by M06-2X/MG3S leads to a C_s geometry, which is consistent with the recent experimental and theoretical studies.

Geometry optimization with our fitted APRP PES of S_0 also leads to a C_s geometry. Table 8.5 lists the bond lengths and bond angles of the equilibrium geometry of S_0 given by APRP, by M06-2X, and by experiments. APRP compares quite well with experiment, with errors less than 0.01 Å and 0.5 deg for most bond lengths and bond angles. Larger deviations from the experiment values from ref. 89 occur for the S7-C8 (0.014 Å) and C-H (0.028 Å) bond lengths and the C1-S7-C8 (1.6 deg) bond angle. The deviations of the C-H bond length and the C1-S7-C8 bond angle are due to the deviation of the ab initio values to which APRP is fitted. The deviation of the S7-C8 bond length is due to the fact

that its ab initio value is not used explicitly in the fitting. Nevertheless, all the deviations are small.

The equilibrium geometry of S_1 ($\pi\pi^*$ in the Franck-Condon region) is a more complicated issue. Experimentally the electronic spectrum exhibits resolved $S_1 \leftarrow S_0$ origin band structure[14] and the origin band further shows resolved rotational structure.[87] The observed rotational constants in S_1 are similar to those in S_0, which implies that S_1 is a bound state with an equilibrium geometry not too different from the S_0 one. Our CASSCF/maTZ geometry optimization also resulted in an S_1 equilibrium geometry with C_s symmetry similar to that of S_0. However, geometry optimization by TDDFT with various functionals (M06-2X, τ-HCTHhyb, B3LYP) and basis sets (6-31+G(d), jun-cc-pV(D+d)Z, maTZ) was not successful. Optimizations with a C_s symmetry constraint all resulted in one imaginary frequency for the C-C-S-C out-of-plane torsional mode. Optimizations without symmetry constraint went through a S_1-S_2 conical intersection and were unable to locate a minimum for the $\pi\pi^*$ state. This disagrees with the experimental findings. The reason is likely to be that the barrier separating the S_1 minimum from the S_1-S_2 conical intersection is very small and thus hard to calculate accurately. This barrier is likely to be located along the C-C-S-C torsional path, because our CASSCF/maTZ calculation gives the frequency of the corresponding torsional mode to be as low as 22 cm^{-1}. Failure of TDDFT for calculating this shallow potential well leads to the negative frequency along the torsional mode. Nevertheless, we fitted the tertiary APRP potential to the geometry optimized with the C_s constraint and the Cartesian Hessian matrix computed by TD-τ-HCTHhyb. The resulting tertiary surface does not have the correct terms for the C-C-S-C torsional motion. However, these terms essentially correspond to the secondary coordinate ϕ, and they are therefore replaced by the reactive-coordinates surface terms in the full surface.

Table 8.6 compares the bond lengths and bond angles of the S_1 equilibrium geometry optimized with APRP to those obtained with TDDFT. APRP matches well with TDDFT, to which the tertiary diabatic potential energy surfaces are fitted, with most deviations within 0.01 Å for bond lengths and 0.5 deg for bond angles. This accuracy is

also achieved for the D_0 and D_1 states of the thiophenoxyl radical (not shown here). These results are very encouraging for the ability of APRP to fit complex-molecule potential energy surfaces.

Figure 8.3 compares APRP and DFT for the vibrational frequencies of the thioanisole S_0 state. Although the parameters of the tertiary APRP surface are fitted to the M06-2X frequencies, they do not perfectly match because of the restricted form of the tertiary surface (especially the lack of cross terms between internal coordinates). Nonetheless, the median signed and absolute percentage deviations in the 42 frequencies are -4% and 5% respectively, and 38 of the 42 frequencies are well reproduced with a deviation of less than 10%. APRP gives the frequency of the C-C-S-C torsional mode of the S_1 equilibrium geometry to be 38 cm^{-1}, a small value consistent with the preceding discussion.

8.3.3. S_1 saddle point geometry separating equilibrium and repulsive regions

Previous work[13,14] has indicated the important role of the S_1-S_2 conical intersection at $R \sim 2$ Å in the dynamics; it was proposed that the photodissociation starts with reactive flux from the bound $\pi\pi^*$ state to the repulsive $n\pi^*$ state through the conical intersection. However, we emphasize that the reactive flux need not go through the conical intersection. In fact, when moving away from the conical intersection in the branching space, the energy of the lower state often decreases as the degeneracy is lifted, and such a decrease is found in the present case. Thus there is often a saddle point on the shoulder of a conical intersection,[90,91,92] and such a saddle point is found here. Therefore the barrier on the S_1 PES separating the equilibrium and repulsive regions is likely to occur at a geometry near, but not at, the conical intersection seam.

The optimization of saddle points on an excited state PES is a very difficult task for electronic structure methods because it requires calculation of the excited state Hessian. With the analytic APRP PESs, however, we are able to do it with little computational cost. The energies and geometric parameters of the S_1 saddle point and the S_1-S_2 MECI

optimized with the APRP PES are listed in Table 8.7. The saddle point is 0.20 eV lower than the MECI, with a similar S-CH_3 distance *R*. Previous work has indicated the possibility that such a saddle point may be located with a large value of the C-C-S-C torsion.[14] This is indeed the case in our calculation. Moreover, the C_6H_5S moiety is significantly distorted from planar. For instance, the C1-C2-C3-C4 torsion is 7.9 deg, and there is an angle of 11.0 deg between the C1-S7 bond and the C6-C1-C2 plane.

In terms of energies relative to the S_0 equilibrium geometry, the saddle point is 4.33 eV while the S_1 equilibrium geometry is 4.35 eV. The reason that the saddle point is lower in energy than the equilibrium geometry of S_1 is that there is another saddle point (4.36 eV) and another local minimum (4.33 eV) near the equilibrium, located on a path corresponding to the torsional motion of C-C-S-C. The aforementioned "true" saddle point leading to dissociation is between the 4.33 eV local minimum and the repulsive region. Recalling the preceding discussion of the difficulty of modeling the S_1 PES around its equilibrium geometry, the existence of the 4.36 eV saddle point and the 4.33 eV local minimum is likely due to the minor unsmoothness of the S_1 PES. Nevertheless, the difference of 0.02 eV should not have significant effect on the dynamics.

To ensure the profile of the APRP PES of S_1 in the Franck-Condon region is reasonable, we selected a set of plots at which we compare V_2 (which is the adiabatic potential energy of S_1) as computed by APRP with its value computed by several high-level ab initio methods. The geometries are specified in Table 8.8, and the comparison is in Table 8.9, which shows that V_2 of APRP, which is fitted to data from XMC-QDPT and TD-τ-HCTHhyb, but not at these geometries, deviates from these two methods by only ~0.1 eV or less.

8.3.4. Conical intersections.

The MECIs are important qualitative features of the PESs. We optimized the S_1-S_2 MECI (MECI1, belonging to the CI1 seam in Figure 8.1) and S_0-S_1 MECI (MECI2, belonging to the CI2 seam in Figure 8.1) with the fitted APRP PESs. Both MECIs have C_s symmetry, with *R* equal to 1.96 Å at MECI1 and 3.22 Å at MECI2.

In addition to the MECIs, with the fitted full-dimensional PESs, we can also map cuts of the conical intersection seams along some paths. As illustrations, here we map one-dimensional cuts of the S_1-S_2 CI1 seam and the S_0-S_1 CI2 seam along two paths. The first path is determined by minimizing eq. (8.30) with R fixed at certain values and other coordinates relaxed. The second path is determined by minimizing eq. (8.30) with the bond lengths $r_{2\text{-}1}$ and $r_{1\text{-}7}$ and the bond angle $\theta_{2\text{-}1\text{-}7}$ fixed at the equilibrium values for S_0, with the torsion $\varphi_{2\text{-}1\text{-}7\text{-}8}$ fixed at certain values, and with the other coordinates relaxed. The two paths are computed for each of the two conical intersection seams, which yield four one-dimensional conical intersection cuts.

The adiabatic energies and some geometric parameters along these four cuts are given in Tables 8.10–8.13. The geometric parameters include the coordinates R and ϕ, the C-S-C bend $\theta_{2\text{-}1\text{-}7}$, and three torsional coordinates of the ring that measure its distortion from planar. It can be clearly seen that away from the MECI of states i and j, the adiabatic energies of the two states increase, and the C_6 ring becomes more distorted.

Table 8.14 compares the adiabatic energies of S_0 and S_1 given by the APRP model and by XMC-QDPT for the geometries in Table 8.10. The mean unsinged deviation of the APRP energies from the XMC-QDPT ones is 0.10 eV, and the deviation is less than 0.30 eV even for the significantly distorted geometry with R = 3.0 Å. Note that the location of conical intersections is sensitive to potential energies, so it is not surprising that conical intersections within the APRP model are not precisely degenerate in XMC-QDPT; the seams are slightly shifted.

8.3.5. Cuts of adiabatic and diabatic potential energy surfaces and diabatic couplings

To evaluate the quality of our fitting, Figures 8.4–8.6 compares the diabatic potential energy curves, diabatic couplings, and adiabatic potential energy curves given by APRP and XMC-QDPT along R with four ϕ values and with the other coordinates fixed at their values for the S_0 equilibrium geometry. The fit is very good for ϕ = 0 deg. For $\phi \neq 0$, the error is larger where the XMC-QDPT data are less smooth. The U_{13} for R <

1.7 Å and ϕ = 30 deg in Figure 8.5(a) has noticeable error, but the two diabatic potential energies U_{11} and U_{33} at those points are widely separated so that the error in the diabatic couplings does not affect the adiabatic energies much, as can be seen in Figure 8.6(b). The small bump in U_{12}^2 and U_{23}^2 between R = 2.5 and 3.0 Å in Figure 8.5(b) is an artifact due to a crossing of the second diabatic state ($\pi\pi^*$) with a higher state that is not computed, and thus the bump is intentionally not fitted. Overall itthese plots show that the fit is a satisfactory. Figure 8.7 shows the overall topography of the diabatic and adiabatic PESs along R and ϕ.

Next we test our fit outside the set of training data. Figure 8.8 shows diabatic potential energy curves along R with the C-S-C bond angle ($\theta_{\text{C-S-C}}$) not equal to its value for the S_0 equilibrium geometry (103 deg) and with the other coordinates fixed at their values for the S_0 equilibrium geometry. For $\theta_{\text{C-S-C}}$ = 120 deg the fit remains good agreement with XMC-QDPT. For $\theta_{\text{C-S-C}}$ = 90 deg the error is larger but still in an acceptable range (~0.2 eV). As an additional test, we compared adiabatic energies by APRP and XMC-QDPT for two distorted geometries arbitrarily selected from a trajectory. The geometric parameters and the energies are listed in Table 8.15. The mean unsigned difference between APRP and XMC-QDPT is 0.21 eV for these geometries not in the training set, which is consistent with the accuracy of the APRP fit observed in the other tests.

8.4. SUMMARY

In this work, we constructed analytic full-dimensional diabatic potential energy surfaces and state couplings of the three lowest singlet electronic states of thioanisole by using an improved APRP scheme. The diabatic potential energy surfaces and diabatic couplings form a 3×3 matrix of scalar functions of the internal coordinates and were fitted for geometries extending from the Franck-Condon region to the asymptote for breaking the S-CH_3 bond; they are thus suitable for the study of the dissociation of the bond following photo-excitation. Various tests confirm that the APRP PESs are usefully accurate compared to ab initio calculations and experimental data. The analytic

representations allowed us to optimize upper surface saddle points and trace out the potential energy surfaces along seams of conical intersection. The PESs can be interfaced with software packages such as ANT for dynamical simulations in either the diabatic or adiabatic representation.[32]

Table 8.1. Tertiary coordinates used for modeling tertiary diabatic potential energy surfaces.[a]

Coordinate type	Tertiary coordinates for anchor points with $R \neq 6.0$ Å [b]	Tertiary coordinates for anchor points with $R = 6.0$ Å [c]
Bond stretches	C-C (6), C-H (8), C1-S7	C-C (6), C-H (8), C1-S7
Valence bends	C-C-C (6), C-C-H (10), C-C-S (2), C-S-C, S-C-H (3), H-C-H (3)	C-C-C (6), C-C-H (10), C-C-S (2), H-C-H (3)
Torsions [d]	C-C-C-C (6,2), C-C-C-H (10,2), C-C-C-S (2,2), H-C-C-H (4,2), H-C-C-S (2,2), C-S-C-H (3,3)	C-C-C-C (6,2), C-C-C-H (10,2), C-C-C-S (2,2), H-C-C-H (4,2), H-C-C-S (2,2)
Out-of-plane distance [e]	H9-C1-C3-C2, H10-C2-C4-C3, H11-C3-C5-C4, H12-C4-C6-C5, H13-C1-C5-C6, S7-C2-C6-C1	H9-C1-C3-C2, H10-C2-C4-C3, H11-C3-C5-C4, H12-C4-C6-C5, H13-C1-C5-C6, S7-C2-C6-C1, H14-H15-H16-C8

[a] For bond stretches and valence bends, the number in parentheses, if given, is the number of coordinates of the given type; for example, C-C (6) means six C-C bond stretches are used. If no number is given there is just one.

[b] Internal coordinates are chosen based on the connectivity in Figure 8.2.

[c] Internal coordinates are chosen based on the connectivity in Figure 8.2 except that C7 and C8 are disconnected due to R being large.

[d] The first number in parentheses is the number of coordinates of the given type, and the second number in parentheses is the dihedral multiplicity.

[e] Notation for out-of-plane distances: *a-b-c-d* denotes the distance from atom *d* to the *a-b-c* plane.

Table 8.2. Coordinates along which tertiary diabatic couplings are modeled.[a]

	coordinate type	description	symmetry ($\phi = 0$)[b]	symmetry ($\phi = 90$ deg)[c]
1	out-of-plane bend	$\vartheta_{7\text{-}1\text{-}6\text{-}2}$ [d]	a″	a′
2	ring puckering	$\varphi_{1\text{-}2\text{-}3\text{-}4} - \varphi_{2\text{-}3\text{-}4\text{-}5} + \varphi_{3\text{-}4\text{-}5\text{-}6}$ $-\varphi_{4\text{-}5\text{-}6\text{-}1} + \varphi_{5\text{-}6\text{-}1\text{-}2} - \varphi_{6\text{-}1\text{-}2\text{-}3}$	a″	a″
3	ring asymmetric torsion	$-\varphi_{1\text{-}2\text{-}3\text{-}4} - \varphi_{2\text{-}3\text{-}4\text{-}5} + 2\varphi_{3\text{-}4\text{-}5\text{-}6}$ $-\varphi_{4\text{-}5\text{-}6\text{-}1} - \varphi_{5\text{-}6\text{-}1\text{-}2} + 2\varphi_{6\text{-}1\text{-}2\text{-}3}$	a″	NS
4	ring asymmetric bend	$-\theta_{1\text{-}2\text{-}3} + 2\theta_{2\text{-}3\text{-}4} - \theta_{3\text{-}4\text{-}5}$ $-\theta_{4\text{-}5\text{-}6} + 2\theta_{5\text{-}6\text{-}1} - \theta_{6\text{-}1\text{-}2}$	a′	NS
5	ring asymmetric bend	$-\theta_{1\text{-}2\text{-}3} + \theta_{3\text{-}4\text{-}5}$ $-\theta_{4\text{-}5\text{-}6} + \theta_{6\text{-}1\text{-}2}$	a′	NS
6	asymmetric bend	$\theta_{2\text{-}1\text{-}12} - \theta_{6\text{-}1\text{-}12}$	a′	a″
7	ring asymmetric torsion	$-\varphi_{1\text{-}2\text{-}3\text{-}4} + \varphi_{2\text{-}3\text{-}4\text{-}5}$ $-\varphi_{4\text{-}5\text{-}6\text{-}1} + \varphi_{5\text{-}6\text{-}1\text{-}2}$	a″	NS
8	bend	$\theta_{1\text{-}7\text{-}8}$	a′	a′

[a] In the table, φ denotes torsion, θ denotes bond angle, NS stands for "not symmetric", and symmetries are for the C_s point group.

[b] C_s point group for geometries where $\phi = 0$ deg and the symmetry plane is the coplanar C_6H_5SC.

[c] C_s point group for geometries where $\phi = 90$ deg and the C-S-C symmetry plane is perpendicular to the coplanar C_6H_5S.

[d] Out-of-plane angle between vector C1-S7 and plane C1-C6-C2. The sign is determined by the sign of $(\mathbf{v}_{6\text{-}1} \times \mathbf{v}_{1\text{-}2}) \cdot \mathbf{v}_{1\text{-}7}$ where $\mathbf{v}_{i\text{-}j}$ is the vector pointing from atom i to atom j.

Table 8.3. Vertical excitation energies (in eV) of thioanisole. [a]

Method	S_0–S_1 (2 A′)	S_0–S_2 (1 A″)	Reference
APRP[b]	4.56	5.02	This work
EOM-CCSD/aug-cc-pV(T+d)Z	4.84	5.21	69
TD–M06-2X/MG3S	4.94	5.05	69
TD–B3LYP/maTZ	4.60	4.82	69
TDA–τ-HCTHhyb/6-31+G*	4.65	4.97	69
SA(3)-MC-QDPT(12,11)/maTZ	4.64	5.13	69
SA(3)-XMC-QDPT(12,11)/maTZ	4.64	5.13	69
SA(3)-MC-QDPT(12,11)/aug-cc-pV(T+d)Z	4.52	5.02	69
CR-EOM-CCSD(T)/aug-cc-pV(T+d)Z	4.53	5.03	69

[a] All data are calculated at the equilibrium geometry optimized by M06-2X/MG3S, unless specified otherwise. The references for methods and basis sets not described in this chapter can be found in ref. 69.

[b] Calculated at the equilibrium geometry optimized by APRP.

Table 8.4. S_0–S_1 adiabatic and 0–0 excitation energies (in eV) of thioanisole.[a]

	Adiabatic	0–0
APRP	4.35	4.08
SA(3)-XMC-QDPT/maTZ//CASSCF/maTZ	4.36	4.22
exp.[b]	-	4.28

[a] See text for definition of adiabatic and 0–0 excitation energies.

[b] Ref. 13

Table 8.5. Geometric parameters of the S_0 equilibrium geometry of thioanisole

	APRP	M06-2X[a]	Electron diffraction[b]	Electron diffraction[c]
Bond lengths (Å)				
C1-C2	1.407	1.392	1.402[d]	1.391
C2-C3	1.405	1.390	1.399[d]	1.391
C3-C4	1.400	1.385	1.395[d]	1.391
C4-C5	1.405	1.391	1.399[d]	1.391
C5-C6	1.398	1.383	1.393[d]	1.391
C6-C1	1.412	1.397	1.406[d]	1.391
C1-S7	1.765	1.761	1.775	1.749
S7-C8	1.827	1.797	1.813	1.803
C-H (average)	1.092	1.084	1.120	1.096
Bond angles (deg)				
C1-C2-C3	119.9	120.0	120.2	120.0
C2-C3-C4	120.7	120.8	120.8	120.0
C3-C4-C5	119.3	119.2	119.3	120.0
C4-C5-C6	120.5	120.4	120.6	120.0
C5-C6-C1	120.3	120.4	119.8	120.0
C6-C1-C2	119.3	119.1	119.3	120.0
C1-S7-C8	102.9	102.9	104.5	105.6

[a] Basis set: MG3S.

[b] Ref. 89

[c] Ref. 85

[d] This experiment did not distinguish the different C-C bonds in the phenyl; these values were refined using B3LYP.

Table 8.6. Geometric parameters of the S_1 equilibrium geometry of thioanisole

	APRP	TD-τ-HCTHhyb[a]
Bond lengths (Å)		
C1-C2	1.408	1.400
C2-C3	1.455	1.446
C3-C4	1.426	1.418
C4-C5	1.407	1.400
C5-C6	1.457	1.448
C6-C1	1.432	1.421
C1-S7	1.758	1.758
S7-C8	1.809	1.800
C-H (average)	1.094	1.094
Bond angles (deg)		
C1-C2-C3	117.7	117.4
C2-C3-C4	118.6	118.4
C3-C4-C5	122.9	123.3
C4-C5-C6	119.4	119.3
C5-C6-C1	116.8	116.4
C6-C1-C2	124.6	125.2
C1-S7-C8	107.0	107.0

[a] Basis set: jul-cc-pV(D+d)Z. Imaginary frequency of 53*i* cm^{-1} is present for the C-C-S-C torsional mode.

Table 8.7. Energies and geometric parameters of S_1 saddle point and S_1-S_2 MECI.

Coordinate	S_1 saddle point	S_1-S_2 MECI
V_2[a] (eV)	4.33	4.53
R[b] (Å)	1.909	1.959
ϕ[c] (deg)	23.1	0.0
$\varphi_{2\text{-}1\text{-}7\text{-}8}$[d] (deg)	32.9	0.0
$\varphi_{1\text{-}2\text{-}3\text{-}4}$[d] (deg)	7.9	0.0
$\vartheta_{7\text{-}1\text{-}6\text{-}2}$[e] (deg)	11.0	0.0

[a] Adiabatic potential energy of S_1 relative to the S_0 energy at the S_0 equilibrium geometry.

[b] S7-C8 bond length.

[c] See Section 8.2.2 for definition.

[d] Torsions.

[e] Coordinate 1 in Table 8.2.

Table 8.8. Values of primary and secondary coordinates at some key geometries.

Geometry	Description[a]	R (Å)	ϕ (deg)
1	Planar minimum	1.809	0.0
2	Saddle point 1	1.811	6.1
3	Nonplanar minimum	1.867	22.0
4	Saddle point 2	1.909	23.1
5	Point along MEP[b] at 0.529 Å from geometry 4	2.023	24.1
6	Point along MEP[b] at 1.038 Å from geometry 4	2.087	25.4

[a] Minimum geometries, saddle point geometries, and MEP[b] optimized with the APRP PES.

[b] Minimum energy path scaled to a reduced mass of one amu.

Table 8.9. V_2 (eV) at some important geometries as given by APRP and by electronic structure methods.[a]

Geometry[b]	APRP	XMC-QDPT /maTZ	TD-τ-HCTHhyb /jul-cc-pV(D+d)Z
1	4.1370	4.1227	3.9972
2	4.1376	4.1239	3.9974
3	4.1142	3.9802	4.0489
4	4.1152	4.0002	4.0931
5	4.0795	4.0739	4.1875
6	4.0380	4.0171	4.0705

[a] Energies are relative to V_1 at geometry 1 given by the respective methods.

[b] See Table 8.8 for description of the geometries.

Table 8.10. Adiabatic energies and geometric parameters of S_0-S_1 conical intersections along a path with selected R values.[a]

R (Å)	V_1 (eV)	V_2 (eV)	V_3 (eV)	ϕ (deg)	$\theta_{2\text{-}1\text{-}7}$ (deg)	coord. 2[b] (deg)	coord. 3[c] (deg)	coord. 7[d] (deg)
3.0	3.14	3.14	7.03	0.0	114.1	9.3	-41.4	-21.6
3.1	2.95	2.95	6.91	0.0	111.9	0.5	-3.7	-4.8
3.2	2.89	2.89	6.81	0.0	106.3	0.6	-0.8	-2.0
3.3	2.90	2.90	6.79	0.0	104.6	-0.4	0.2	-1.4
3.4	2.97	2.97	6.83	0.0	103.4	-0.7	-0.8	-3.6
3.5	3.06	3.06	6.90	0.0	102.6	-2.2	-1.6	-3.3

[a] See text for details of the path. Adiabatic energies are relative to V_1 at the S_0 equilibrium geometry.

[b] Coordinate 2 in Table 8.2 (ring puckering).

[c] Coordinate 3 in Table 8.2 (ring asymmetric torsion).

[d] Coordinate 7 in Table 8.2 (ring asymmetric torsion).

Table 8.11. Adiabatic energies and geometric parameters of S_0-S_1 conical intersections along a path with selected $\varphi_{2\text{-}1\text{-}7\text{-}8}$ values. [a]

$\varphi_{2\text{-}1\text{-}7\text{-}8}$ (deg)	V_1 (eV)	V_2 (eV)	V_3 (eV)	R (Å)	ϕ (deg)	$\theta_{2\text{-}1\text{-}7}$ (deg)	coord. 2[b] (deg)	coord. 3[c] (deg)	coord. 7[d] (deg)
0	2.88	2.88	6.81	3.217	0.0	108.9	0.0	0.0	0.0
5	2.90	2.90	6.79	3.220	0.0	109.3	-12.2	19.3	-6.2
10	2.94	2.94	6.82	3.221	0.0	110.4	-17.7	23.4	-15.1
15	3.03	3.03	6.85	3.294	8.2	104.6	-5.4	8.3	-46.1
20	3.07	3.07	6.88	3.271	8.4	107.0	-11.0	15.0	-49.7

[a] See text for details of the path. Adiabatic energies are relative to V_1 at the S_0 equilibrium geometry.

[b] Coordinate 2 in Table 8.2 (ring puckering).

[c] Coordinate 3 in Table 8.2 (ring asymmetric torsion).

[d] Coordinate 7 in Table 8.2 (ring asymmetric torsion).

Table 8.12. Adiabatic energies and geometric parameters of S_1- S_2 conical intersections along a path with selected R values. [a]

R (Å)	V_1 (eV)	V_2 (eV)	V_3 (eV)	ϕ (deg)	$\theta_{2\text{-}1\text{-}7}$ (deg)	coord. 2[b] (deg)	coord. 3[c] (deg)	coord. 7[d] (deg)
1.8	1.79	5.53	5.53	0.0	98.0	-53.5	-60.0	55.8
1.9	0.48	4.78	4.78	0.0	99.1	-0.6	1.0	-3.5
2.0	0.54	4.62	4.62	0.0	107.0	2.4	-2.2	3.8
2.1	0.87	4.83	4.83	0.0	105.7	0.0	0.0	0.0
2.2	1.58	5.21	5.21	0.0	106.5	5.5	-8.2	1.1

[a] See text for details of the path. Adiabatic energies are relative to V_1 at the S_0 equilibrium geometry.

[b] Coordinate 2 in Table 8.2 (ring puckering).

[c] Coordinate 3 in Table 8.2 (ring asymmetric torsion).

[d] Coordinate 7 in Table 8.2 (ring asymmetric torsion).

Table 8.13. Adiabatic energies and geometric parameters of S_1-S_2 conical intersections along a path with selected $\varphi_{2\text{-}1\text{-}7\text{-}8}$ values. [a]

$\varphi_{2\text{-}1\text{-}7\text{-}8}$ (deg)	V_1 (eV)	V_2 (eV)	V_3 (eV)	R (Å)	ϕ (deg)	$\theta_{2\text{-}1\text{-}7}$ (deg)	coord. 2[b] (deg)	coord. 3[c] (deg)	coord. 7[d] (deg)
0	0.31	4.53	4.53	1.959	0.0	105.2	0.0	0.0	0.0
5	0.33	4.53	4.53	1.960	0.0	105.8	-9.0	10.4	-0.1
10	0.35	4.55	4.55	1.954	8.7	105.5	-26.7	26.4	14.0
15	0.38	4.57	4.57	1.952	12.4	105.9	-39.4	41.1	5.7
20	0.42	4.60	4.60	1.943	20.3	105.9	-47.3	49.3	19.0

[a] See text for details of the path. Adiabatic energies are relative to V_1 at the S_0 equilibrium geometry.

[b] Coordinate 2 in Table 8.2 (ring puckering).

[c] Coordinate 3 in Table 8.2 (ring asymmetric torsion).

[d] Coordinate 7 in Table 8.2 (ring asymmetric torsion).

Table 8.14. Adiabatic energies [a] given by APRP and XMC-QDPT of the S_0-S_1 conical intersections along a path with selected R values.[b]

	APRP		XMC-QDPT/maTZ	
R (Å)	V_1	V_2	V_1	V_2
3.0	3.14	3.14	3.08	3.43
3.1	2.95	2.95	2.94	3.15
3.2	2.89	2.89	2.88	3.04
3.3	2.90	2.90	2.88	2.99

[a] Energies in eV relative to those for the S_0 equilibrium geometry.

[b] Geometries are the same as the first four in Table 8.10.

Table 8.15. Adiabatic energies and geometric parameters of S_1-S_2 conical intersections along a path with selected R values. [a]

R (Å)	ϕ (deg)	$\theta_{2\text{-}1\text{-}7}$ (deg)	coord. 2[b] (deg)	coord. 3[c] (deg)	coord. 7[c] (deg)	APRP (eV)			XMC-QDPT/maTZ (eV)		
						V_1	V_2	V_3	V_1	V_2	V_3
1.831	-1.3	110.0	0.8	-2.3	-1.0	0.62	4.66	5.28	0.37	4.47	5.52
1.781	-2.2	104.9	-0.9	0.8	-3.3	0.41	4.67	5.30	0.18	4.49	5.45

[a] Adiabatic energies are relative to V_1 at the S_0 equilibrium geometry.

[b] Coordinate 2 in Table 8.2 (ring puckering).

[c] Coordinate 3 in Table 8.2 (ring asymmetric torsion)

[d] Coordinate 7 in Table 8.2 (ring asymmetric torsion)

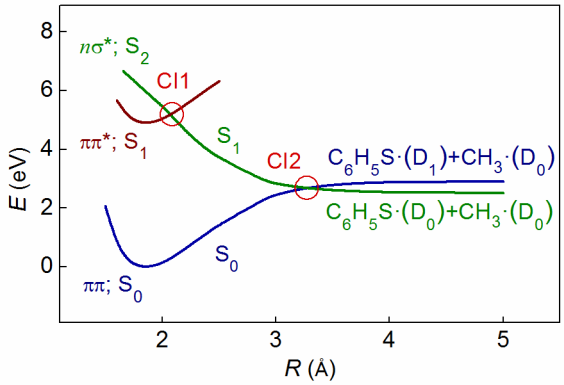

Figure 8.1. Schematic cut of the adiabatic potential energy surfaces of thioanisole along the S–C bond stretch coordinate, *R*.

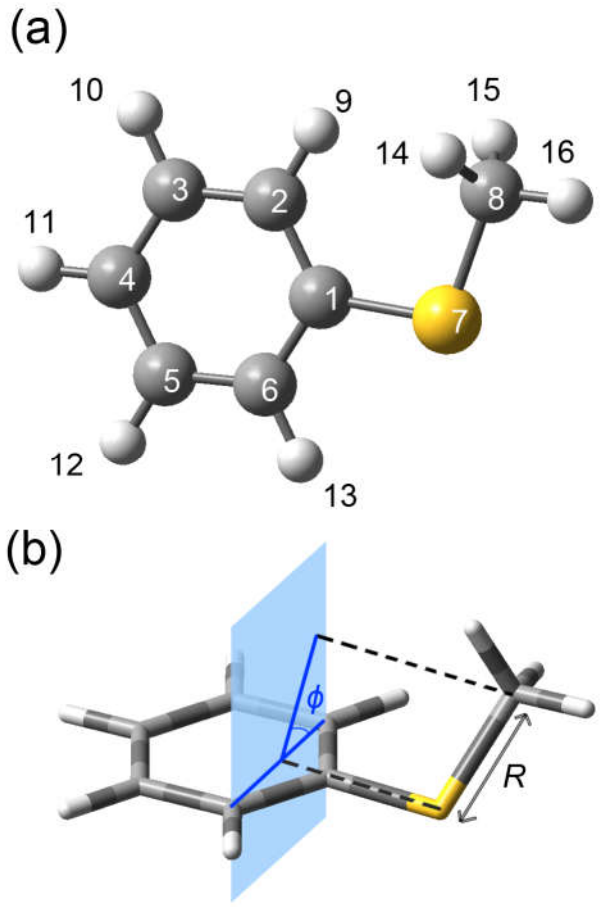

Figure 8.2. (a) Numbering of atoms. (b) Definition of coordinates R and ϕ; the blue plane contains C2 and C6 and is normal to the C6-C1-C2 plane.

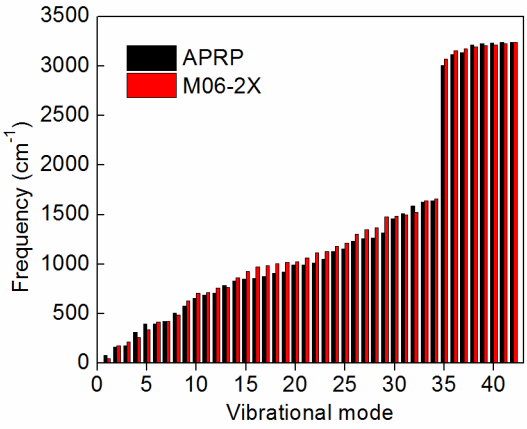

Figure 8.3. Frequencies of S_0 equilibrium geometry of thioanisole computed by APRP and by DFT with M06-2X.

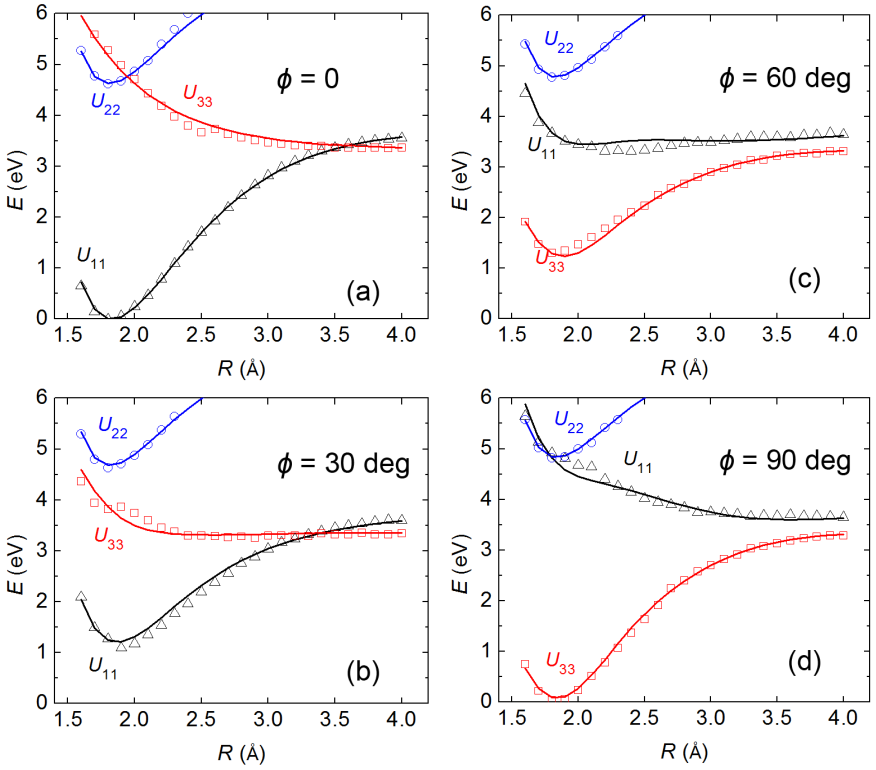

Figure 8.4. Diabatic potential energy curves given by APRP (solid lines) and XMC-QDPT/maTZ (open symbols) along R for different values of ϕ. (Other internal coordinates are fixed at values for the S_0 equilibrium geometry.)

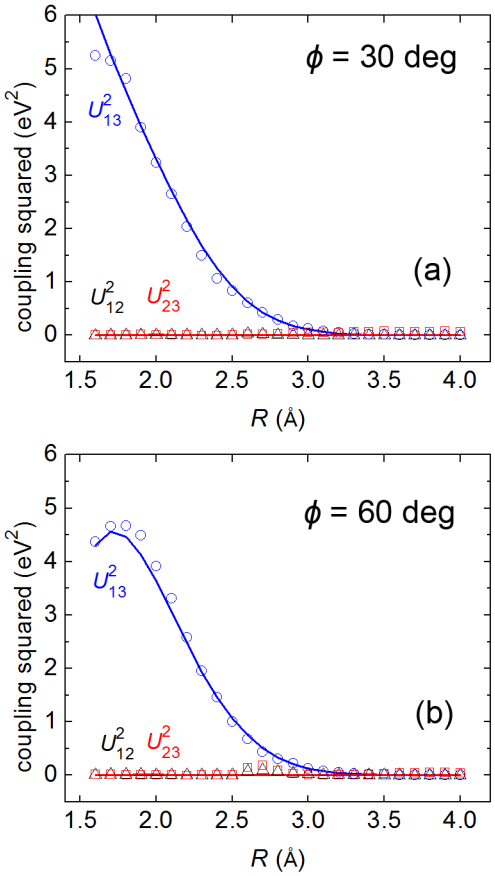

Figure 8.5. Diabatic couplings given by APRP (solid lines) and XMC-QDPT/maTZ (open symbols) along R for different values of ϕ. (Other internal coordinates are fixed at values for the S_0 equilibrium geometry. Those for ϕ = 0 and 90 deg are not shown since the couplings are negligible in those cases.)

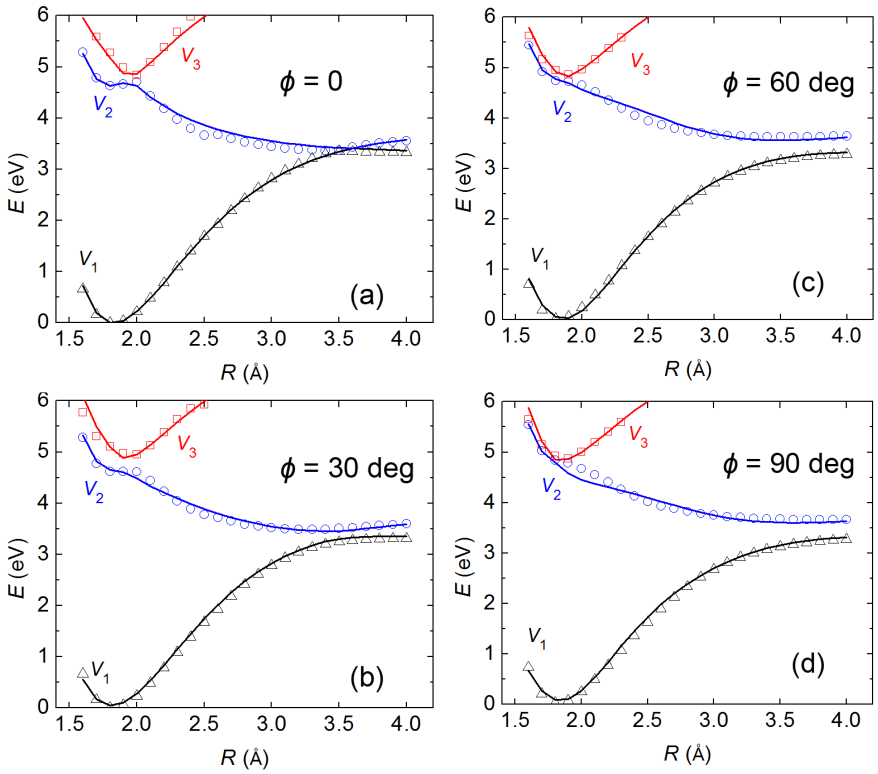

Figure 8.6. Adiabatic potential energy curves given by APRP (solid lines) and XMC-QDPT/maTZ (open symbols) along R for different values of ϕ. (Other internal coordinates are fixed at values for the S_0 equilibrium geometry.)

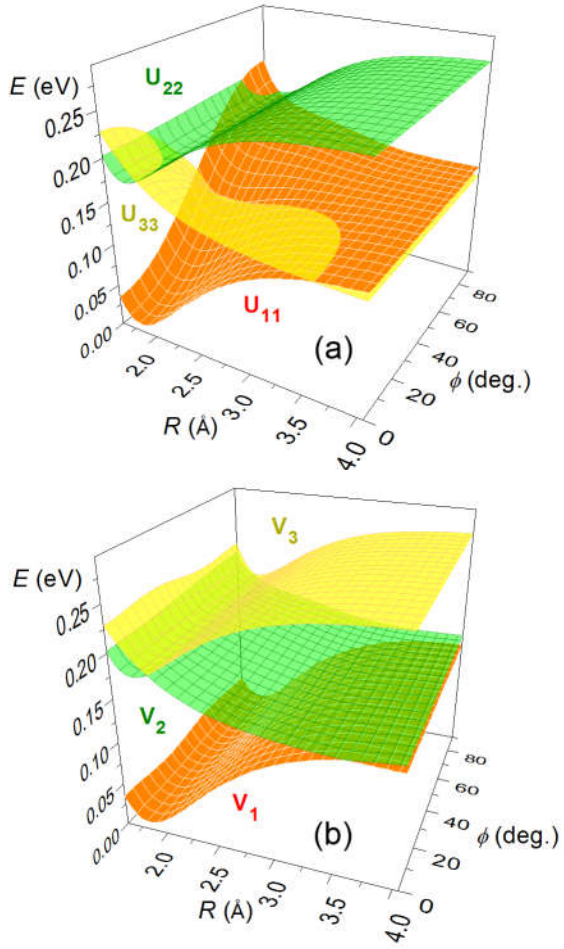

Figure 8.7. APRP diabatic (a) and adiabatic (b) PESs along R and ϕ. (Other internal coordinates are fixed at values for the S_0 equilibrium geometry.)

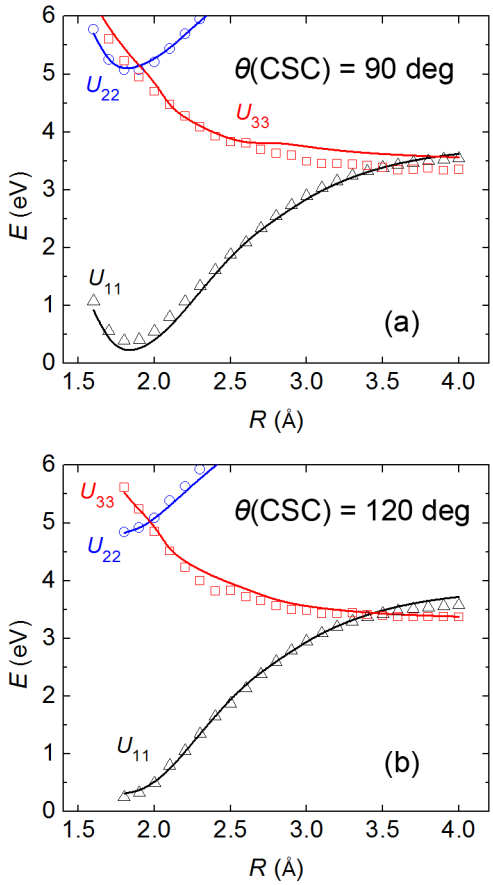

Figure 8.8. Diabatic potential energy curves given by APRP (solid lines) and XMC-QDPT/maTZ (open symbols) along R for two values of the C-S-C bond angle not equal to its value for the S_0 equilibrium geometry. (Other internal coordinates are fixed at values for the S_0 equilibrium geometry.)

REFERENCES FOR CHAPTER 8

[1] E. Teller, J. Phys. Chem. 41, 109 (1937).

[2] *Conical Intersections: Theory, Computation, and Experiment*, edited by W. Domcke, D. R. Yarkony, and H. Köppel (World Scientific, Hackensack, NJ, 2011).

[3] S. Matsika and P. Krause, Annu. Rev. Phys. Chem. 62, 621 (2011).

[4] W. Domcke and D. R. Yarkony, Annu. Rev. Phys. Chem. 63, 325 (2012).

[5] L. Blancafort, ChemPhysChem **15**, 3166 (2014).

[6] C. E. Caplan and M. S. Child, Mol. Phys. **23**, 249 (1972).

[7] C. Sannen, G. Raşeev, C. Galloy, G. Fauville, J.-C. Lorquet, J. Chem. Phys. **74**, 2402 (1981).

[8] H. Köppel, L. S. Cederbaum, and W. Domcke, J. Chem. Phys. **77**, 2014 (1982).

[9] V. Bonačić-Koutecký and J. Michl, Theor. Chim. Acta **68**, 45 (1985).

[10] N. C. Blais, D. G. Truhlar, and C. A. Mead, J. Chem. Phys. 89, 6204 (1988).

[11] S. Yabushita and K. Morokuma, Chem. Phys. Lett. **153**, 517 (1988).

[12] G. Hirsch, R. J. Buenker, and C. Petrongolo, Mol. Phys. **73**, 1085 (1991).

[13] M. Braunstein, P. J. Hay, R. L. Martin, and R. T Pack, J. Chem. Phys. **95**, 8239 (1991).

[14] M. R. Manaa and D. R. Yarkony, J. Chem. Phys. **97**, 715 (1992).

[15] D. W. Schwenke, S. L. Mielke, G. J. Tawa, R. S. Friedman, P. Halvick, and D. G. Truhlar, Chem. Phys. Lett. **203**, 565-572 (1993).

[16] S. L. Mielke, G. J. Tawa, D. G. Truhlar, and D. W. Schwenke, J. Amer. Chem. Soc. **115**, 6436 (1993).

[17] S. L. Mielke, G. J. Tawa, D. G. Truhlar, and D. W. Schwenke, Int. J. Quantum Chem. Symp. **27**, 621 (1993).

[18] W. Domcke, A. L. Sobolewski, and C. Woywod, Chem. Phys. Lett. **203**, 220 (1993).

[19] M. Olivucci, I. N. Ragazos, F. Bernardi, and M. A. Robb, J. Am. Chem. Soc. **115**, 3710 (1993).

[20] H. Köppel, Faraday Discuss. **127**, 35 (2004).

[21] A. Toniolo, S. Olsen, I. Manohar, and T. J. Martinez, Faraday Discuss. **127**, 149 (2004).

[22] A. Migani, A. Sinocropi, N. Ferré, A. Cembran, M. Garavelli, and M. Olivucci, Faraday Discuss. **127**, 179 (2004).

[23] D. G. Truhlar, Faraday Discuss. **127**, 242 (2004).

[24] J. Wei, J. Riedel, A. Kuczmann, F. Renth, and F. Temps, Faraday Discuss. **127**, 267 (2004).

[25] D. R. Yarkony, Faraday Discuss. **127**, 325 (2004).

[26] I. Burghardt, L. S. Cederbaum, and J. T. Hynes, Faraday Discuss. **127**, 395 (2004).

[27] V. Kokoouline and C. H. Greene, Faraday Discuss. **127**, 413 (2004).

[28] Z. Lan, W. Domcke, V. Vallet, A. L. Sobolewski, and S. Mahapatra, J. Chem. Phys. 122, 224315 (2005).

[29] M. G. D. Nix, A. L. Devine, B. Cronin, R. N. Dixon, and M. N. R. Ashfold, J. Chem. Phys. 125, 133318 (2006).

[30] O. P. J. Vieuxmaire, Z. Lan, A. L. Sobolewski, and W. Domcke, J. Chem. Phys. 129, 224307 (2008).

[31] X. Xu, K. R. Yang, and D. G. Truhlar, J. Chem. Theory Comput. 9, 3612 (2013).

[32] X. Xu, J. Zheng, K. R. Yang, and D. G. Truhlar, J. Am. Chem. Soc. 136, 16378 (2014).

[33] K. R. Yang, X. Xu, J. Zheng, and D. G. Truhlar, Chem. Sci. 5, 4661 (2014).

[34] I. S. Lim, J. S. Lim, Y. S. Lee, and S. K. Kim, J. Chem. Phys. 126, 034306 (2007).

[35] R. Omidyan and H. Rezaei, Phys. Chem. Chem. Phys. 16, 11679 (2014).

[36] J. S. Lim and S. K. Kim, Nat. Chem. 2, 627 (2010).

[37] A. L. Sobolewski and W. Domcke, Chem. Phys. Lett. 315, 293 (1999).

[38] A. L. Sobolewski and W. Domcke, Chem. Phys. 259, 181 (2000).

[39] A. L. Sobolewski and W. Domcke, J. Phys. Chem. A 105, 9275 (2001).

[40] A. L. Sobolewski, W. Domcke, C. Dedonder-Lardeux, and C. Jouvet, Phys. Chem. Chem. Phys. 4, 1093 (2002).

[41] G. M. Roberts, D. J. Hadden, L. T. Bergendahl, A. M. Wenge, S. J. Harris, T. N. V. Karsili, M. N. R. Ashfold, M. J. Paterson, and V. G. Stavros, Chem. Sci. 4, 993 (2013).

[42] A. M. Wenge, T. N. V. Karsili, J. D. Rodriguez, M. I. Cotterell, B. Marchetti, R. N. Dixon, and M. N. R. Ashfold, Phys. Chem. Chem. Phys. 17, 16246 (2015).

[43] B. K. Kendrick, C. A. Mead, and D. G. Truhlar, Chem. Phys. **277**, 31 (2002).

[44] H. Nakamura and D. G. Truhlar, J. Chem. Phys. 115, 10353 (2001).

[45] A. W. Jasper and D. G. Truhlar, in Conical Intersections: Theory, Computation, and Experiment, edited by W. Domcke, D. R. Yarkony, and H. Koppel (World Scientific, Singapore, 2011), p. 375.

[46] K. R. Yang, X. Xu, and D. G. Truhlar, J. Chem. Theory Comput. 10, 924 (2014).

[47] S. L. Li and D. G. Truhlar, *QuickFFmn 2016* (http://comp.chem.umn.edu/abcrate/) based on *QuickFF* – version 1.0.1 (http://molmod.github.io/QuickFF) as described in ref. 48.

[48] L. Vanduyfhuys, S. Vandenbrande, T. Verstraelen, R. Schmid, M. Waroquier, and V. Van Speybroeck, J. Comput. Chem. 36, 1015 (2015).

[49] G. Simons, R. G. Parr, and J. M. Finlan, J. Chem. Phys. **59**, 3229 (1973).

[50] H. Nakano, J. Chem. Phys. 99, 7983 (1993).

[51] H. Nakano, Chem. Phys. Lett. 207, 372 (1993).

[52] A. A. Granovsky, J. Chem. Phys. 134, 214113 (2011).

[53] H. Nakamura and D. G. Truhlar, J. Chem. Phys. 117, 5576 (2002).

[54] H. Nakamura and D. G. Truhlar, J. Chem. Phys. 118, 6816 (2003).

[55] K. R. Yang, X. Xu, and D. G. Truhlar, Chem. Phys. Lett. 573, 84 (2013).

[56] S. L. Li, D. G. Truhlar, M. W. Schmidt, and M. S. Gordon, J. Chem. Phys. 142, 064106 (2015).

[57] P. Hohenberg, and W. Kohn, Phys. Rev. B **136**, B864 (1964).

[58] W. Kohn, and L. J. Sham, Phys. Rev. **140**, A1133 (1965).

[59] M. E. Casida, in *Recent Advances in Density Functional Methods, Part I*, edited by D. P. Chong (World Scientific: Singapore, 1995), pp. 155.

[60] S. L. Li, X. Xu, C. E. Hoyer, and D. G. Truhlar, J. Phys. Chem. Lett. 6, 3352 (2015).

[61] Y. P. Varshni, Rev. Mod. Phys. 29, 664 (1957).

[62] P. M. Morse, Phys. Rev. 34, 57 (1929).

[63] D. G. Truhlar, R. W. Olson, A. C. Jeannotte II, and J. Overend, J. Am. Chem. Soc. **98**, 2373-2379 (1976).

[64] S. Gupta, K. Dharamvir, and V. K. Jindal, Int. J. Mod. Phys. B **18**, 1021 (2004).

[65] E. B. Wilson, J. Decius, and P. Cross, *Molecular Vibrations* (McGraw-Hill, New York, 1955).

[66] R. Krishnan, J. S. Binkley, R. Seeger, and J. A. Pople, J. Chem. Phys. 72, 650 (1980).

[67] T. Clark, J. Chandrasekhar, G. W. Spitznagel, and P. V. R. Schleyer, J. Comput. Chem. 4, 294 (1983).

[68] B. J. Lynch, Y. Zhao, and D. G. Truhlar, J. Phys. Chem. A 107, 1384 (2003).

[69] S. L. Li, X. Xu, and D. G. Truhlar, Phys. Chem. Chem. Phys. 17, 20093 (2015).

[70] M. W. Schmidt, K. K. Baldridge, J. A. Boatz, S. T. Elbert, M. S. Gordon, J. H. Jensen, S. Koseki, N. Matsunaga, K. A. Nguyen, S. J. Su, T. L. Windus, M. Dupuis, and J. A. Montgomery, J. Comput. Chem. 14, 1347 (1993).

[71] M. S. Gordon and M. W. Schmidt, in *Theory and Applications of Computational Chemistry: The First Forty Years*, edited by C. E. Dykstra, G. Frenking, K. S. Kim, and G. E. Scuseria (Elsevier, Amsterdam, 2005), p. 1167.

[72] Y. Zhao and D. G. Truhlar, Theor. Chem. Acc. 120, 215 (2008).

[73] Y. Zhao and D. G. Truhlar, Acc. Chem. Res. 41, 157 (2008).

[74] T. H. Dunning, J. Chem. Phys. 90, 1007 (1989).

[75] D. E. Woon and T. H. Dunning, J. Chem. Phys. 98, 1358 (1993).

[76] T. H. Dunning, K. A. Peterson, and A. K. Wilson, J. Chem. Phys. 114, 9244 (2001).

[77] E. Papajak, J. Zheng, X. Xu, H. R. Leverentz, and D. G. Truhlar, J. Chem. Theory Comput. 7, 3027 (2011).

[78] A. D. Boese and N. C. Handy, J. Chem. Phys. 116, 9559 (2002).

[79] M. J. Frisch, G. W. Trucks, H. B. Schlegel, G. E. Scuseria, M. A. Robb, J. R. Cheeseman, G. Scalmani, V. Barone, B. Mennucci, G. A. Petersson, H. Nakatsuji, M. Caricato, X. Li, H. P. Hratchian, A. F. Izmaylov, J. Bloino, G. Zheng, J. L. Sonnenberg, M. Hada, M. Ehara, K. Toyota, R. Fukuda, J. Hasegawa, M. Ishida, T. Nakajima, Y. Honda, O. Kitao, H. Nakai, T. Vreven, J. A. Montgomery, Jr., J. E. Peralta, F. Ogliaro, M. Bearpark, J. J. Heyd, E. Brothers, K. N. Kudin, V. N. Staroverov, R. Kobayashi, J. Normand, K. Raghavachari, A. Rendell, J. C. Burant, S. S. Iyengar, J. Tomasi, M. Cossi, N. Rega, J. M. Millam, M. Klene, J. E. Knox, J. B. Cross, V. Bakken, C. Adamo, J. Jaramillo, R. Gomperts, R. E. Stratmann, O. Yazyev, A. J. Austin, R. Cammi, C. Pomelli, J. W. Ochterski, R. L. Martin, K. Morokuma, V. G. Zakrzewski, G. A. Voth, P. Salvador, J. J. Dannenberg, S. Dapprich, A. D. Daniels, Ö. Farkas, J. B. Foresman, J. V. Ortiz, J. Cioslowski, and D. J. Fox, *Gaussian 09*, Revision D.01, Gaussian, Inc., Wallingford CT, 2009.

[80] W. H. Press, S. A. Teukolsky, W. T. Vetterling, and B. P. Flannery, *Numerical Recipes in Fortran 77,* 2nd ed. (Cambridge University Press, 1992).

[81] J. Zheng, S. Zhang, B. J. Lynch, J. C. Corchado, Y.-Y. Chuang, P. L. Fast, W.-P. Hu, Y.-P. Liu, G. C. Lynch, K. A. Nguyen, C. F. Jackels, A. Fernandez Ramos, B. A. Ellingson, V. S. Melissas, J. Villà, I. Rossi, E. L. Coitino, J. Pu, T. V. Albu, R. Steckler, B. C. Garrett, A. D. Isaacson, and D. G. Truhlar, *POLYRATE*–version 2010-A, University of Minnesota, Minneapolis, 2010. http://comp.chem.umn.edu/polyrate (accessed June 14, 2016)

[82] J. Zheng, Z.-H. Li, A. W. Jasper, D. A. Bonhommeau, R. Valero, R. Meana-Paneda, and D. G. Truhlar, *ANT*, version 2014-2, University of Minnesota, Minneapolis, 2015. http://comp.chem.umn.edu/ant (accessed June 14, 2016)

[83] K. Kowalski, and P. Piecuch, J. Chem. Phys. **120**, 1715 (2004).

[84] K. Kowalski, J. Chem. Phys. **130**, 194110 (2009).

[85] N. M. Zaripov, Russ. J. Struct. Chem. (Engl.) 17, 640 (1976).

[86] M. Nagasaka-Hoshino, T. Isozaki, T. Suzuki, T. Ichimura, and S. Kawauchi, Chem. Phys. Lett. 457, 58 (2008).

[87] M. Hoshino-Nagasaka, T. Suzuki, T. Ichimura, S. Kasahara, M. Baba, and S. Kawauchi, Phys. Chem. Chem. Phys. 12, 13243 (2010).

[88] M. Bossa, S. Morpurgo, and S. Stranges, J. Mol. Struct. THEOCHEM 618, 155 (2002).

[89] I. F. Shishkov, L. V. Khristenko, N. M. Karasev, L. V. Vilkov, and H. Oberhammer, J. Mol. Struct. 873, 137 (2008).

[90] T. C. Allison, G. C. Lynch, D. G. Truhlar, and M. S. Gordon, J. Phys. Chem. **100**, 13575 (1996).

[91] D. G. Truhlar and C. A. Mead, Phys. Rev. A **68**, 032501 (2003).

[92] O. Tishchenko, D. G. Truhlar, A. Ceulemans, and M. T. Nguyen, J. Am. Chem. Soc. **130**, 7000 (2008).

Bibliography

1 Adamo, C.; Barone, V. *J. Chem. Phys.* **1999**, *110*, 6158.

2 ADF2014, SCM, Theoretical Chemistry, Vrije Universiteit, Amsterdam, The Netherlands, http://www.scm.com (accessed March 14, 2017).

3 Aidas, K.; Kongsted, J.; Osted, A.; Mikkelsen, K. V.; Christiansen, O. *J. Phys. Chem. A* **2005**, *109*, 8001.

4 Allison, T. C.; Lynch, G. C.; Truhlar, D. G.; Gordon, M. S. *J. Phys. Chem.* **1996**, *100*, 13575.

5 Angeli, C.; Borini, S.; Cestari, M.; Cimiraglia, R. *J. Chem. Phys.* **2004**, *121*, 4043.

6 Aquilante, F.; De Vico, L.; Ferré, N.; Ghigo, G.; Malmqvist, P.-å.; Neogrády, P.; Pedersen, T. B.; Pitoňák, M.; Reiher, M.; Roos, B. O.; Serrano-Andrés, L.; Urban, M.; Veryazov, V.; Lindh, R. *J. Comput. Chem.* **2010**, *31*, 224.

7 Atchity, G. J.; Ruedenberg, K. *Theor. Chem. Acc.* **1997**, *97*, 47.

8 Becke, A. D. *J. Chem. Phys.* **1993**, *98*, 5648.

9 Becke, A. D. *Phys. Rev. A* **1988**, *38*, 3098.

10 Ben-Nun, M.; Quenneville, J.; Martinez, T. J. *J. Phys. Chem. A* **2000**, *104*, 5161.

11 Blais, N. C.; Truhlar, D. G.; Mead, C. A. *J. Chem. Phys.* **1988**, *89*, 6204.

12 Blancafort, L. *Chemphyschem* **2014**, *15*, 3166.

13 Boese, A. D.; Handy, N. C. *J. Chem. Phys.* **2002**, *116*, 9559.

14 Bonačić-Koutecký, V.; Michl, J. *Theor. Chim. Acta* **1985**, *68*, 45.

15 Bossa, M.; Morpurgo, S.; Stranges, S. *J. Mol. Struct. THEOCHEM* **2002**, *618*, 155.

16 Braunstein, M.; Hay, P.; Martin, R.; T Pack, R. *J. Chem. Phys.* **1991**, *95*, 8239.

17 Brunschwig, B. S.; Creutz, C.; Sutin, N. *Chem. Soc. Rev.* **2002**, *31*, 168.

18 Burghardt, I.; Cederbaum, L. S.; Hynes, J. T. *Faraday Discuss.* **2004**, *127*, 395.

19 Caplan, C.; Child, M. *Mol. Phys.* **1972**, *23*, 249.

20 Caricato, M.; Trucks, G. W.; Frisch, M. J.; Wiberg, K. B. *J. Chem. Theory Comput.* **2010**, *6*, 370.

21 Casida, M. E. In *Recent Advances in Density Functional Methods, Part I*; Chong, D. P., Ed.; World Scientific: Singapore: 1995, p 155.

22 Casida, M. E.; Huix-Rotllant, M. *Annu. Rev. Phys. Chem.* **2012**, *63*, 287.

23 Casida, M. E.; Jamorski, C.; Casida, K. C.; Salahub, D. R. *J. Chem. Phys.* **1998**, *108*, 4439.

24 Cederbaum, L. S. In *Conical Intersections: Electronic Structure, Dynamics and Spectroscopy*; Domcke, W., Yarkony, D. R., Köppel, H., Eds.; World Scientific Publishing Co. Pte. Ltd.: 2004.

25 Cembran, A.; Song, L.; Mo, Y.; Gao, J. *J. Chem. Theory Comput.* **2009**, *5*, 2702.

26 Charaf-Eddin, A.; Cauchy, T.; Felpin, F.-X.; Jacquemin, D. *RSC Advances* **2014**, *4*, 55466.

27 Charaf-Eddin, A.; Planchat, A. l.; Mennucci, B.; Adamo, C.; Jacquemin, D. *J. Chem. Theory Comput.* **2013**, *9*, 2749.

28 Cimiraglia, R. In *Time-Dependent Quantum Molecular Dynamics*; Broeckhoeve, J., Lathouwers, L., Eds.; Plenum: New York, 1992, p 11.

29 Clark, T.; Chandrasekhar, J.; Spitznagel, G. W.; Schleyer, P. V. R. *J. Comput. Chem.* **1983**, *4*, 294.

30 Cohen, A. J.; Mori-Sánchez, P.; Yang, W. *Science* **2008**, *321*, 792.

31 *Conical Intersections: Theory, Computation, and Experiment*; Domcke, W., Yarkony, D. R., Koppel, H., Eds.; World Scientific: Singapore, 2011, p 249.

32 Cordova, F.; Doriol, L. J.; Ipatov, A.; Casida, M. E.; Filippi, C.; Vela, A. *J. Chem. Phys.* **2007**, *127*, 164111.

33 Crespo-Otero, R.; Barbatti, M. *Theor. Chem. Acc.* **2012**, *131*, 1.

34 Dancoff, S. M. *Phys. Rev.* **1950**, *78*, 382.

35 Delos, J. B. *Rev. Mod. Phys.* **1981**, *53*, 287.

36 Dierksen, M.; Grimme, S. *J. Phys. Chem. A* **2004**, *108*, 10225.

37 Dirac, P. A. M. *Proc. Cambridge Philos. Soc.* **1930**, *26*, 376.

38 Domcke, W. *Faraday Discuss.* **2013**, *163*, 126.

39 Domcke, W.; Sobolewski, A.; Woywod, C. *Chem. Phys. Lett.* **1993**, *203*, 220.

40 Domcke, W.; Woywod, C. *Chem. Phys. Lett.* **1993**, *216*, 362.

41 Domcke, W.; Yarkony, D. R. In *Annual Review of Physical Chemistry, Vol 63*; Johnson, M. A., Martinez, T. J., Eds. 2012; Vol. 63, p 325.

42 Dreuw, A.; Head-Gordon, M. *Chem. Rev.* **2005**, *105*, 4009.

43 Dreuw, A.; Weisman, J. L.; Head-Gordon, M. *J. Chem. Phys.* **2003**, *119*, 2943.

44 Dunning, T. H. *J. Chem. Phys.* **1989**, *90*, 1007.

45 Dunning, T. H.; McKoy, V. *J. Chem. Phys.* **1967**, *47*, 1735.

46 Dunning, T. H.; Peterson, K. A.; Wilson, A. K. *J. Chem. Phys.* **2001**, *114*, 9244.

47 Duschinsky, F. *Acta Physicochim. URSS* **1937**, *7*, 551.

48 Ebisuzaki, R.; Watanabe, Y.; Kawashima, Y.; Nakano, H. *J. Chem. Theory Comput.* **2011**, *7*, 998.

49 Ebisuzaki, R.; Watanabe, Y.; Nakano, H. *Chem. Phys. Lett.* **2007**, *442*, 164.

50 Eisfeld, W.; Vieuxmaire, O.; Viel, A. *J. Chem. Phys.* **2014**, *140*, 224109.

51 Engel, E.; Chevary, J. A.; Macdonald, L. D.; Vosko, S. H. *Zeitschrift für Physik D Atoms, Molecules and Clusters* **1992**, *23*, 7.

52 Engel, E.; Dreizler, R. M. *Density Functional Theory: An Advanced Course*; Springer-Verlag Berlin Heidelberg, 2011.

53 Faraji, S.; Gómez-Carrasco, S.; Köppel, H. In *Conical Intersections: Theory, Computation, and Experiment*; Domcke, W., Yarkony, D. R., Koppel, H., Eds.; World Scientific: Singapore, 2011, p 249.

54 Farrer, N. J.; Woods, J. A.; Salassa, L.; Zhao, Y.; Robinson, K. S.; Clarkson, G.; Mackay, F. S.; Sadler, P. J. *Angew. Chem. Int. Ed.* **2010**, *49*, 8905.

55 Fatehi, S.; Alguire, E.; Subotnik, J. E. *J. Chem. Phys.* **2013**, *139*, 124112.

56 Ferguson, J.; Reeves, L.; Schneider, W. *Can. J. Chem.* **1957**, *35*, 1117.

57 Fernández-Hernández, J. M.; Yang, C.-H.; Beltrán, J. I.; Lemaur, V.; Polo, F.; Fröhlich, R.; Cornil, J.; De Cola, L. *J. Am. Chem. Soc.* **2011**, *133*, 10543.

58 Ferrer, F. J. A.; Santoro, F. *Phys. Chem. Chem. Phys.* **2012**, *14*, 13549.

59 Finley, J.; Malmqvist, P.-Å.; Roos, B. O.; Serrano-Andrés, L. *Chem. Phys. Lett.* **1998**, *288*, 299.

60 Francl, M. M.; Pietro, W. J.; Hehre, W. J.; Binkley, J. S.; Gordon, M. S.; DeFrees, D. J.; Pople, J. A. *J. Chem. Phys.* **1982**, *77*, 3654.

61 Frisch, M. J.; Trucks, G. W.; Schlegel, H. B.; Scuseria, G. E.; Robb, M. A.; Cheeseman, J. R.; Scalmani, G.; Barone, V.; Mennucci, B.; Petersson, G. A.; Nakatsuji, H.; Caricato, M.; X. Li; Hratchian, H. P.; Izmaylov, A. F.; Bloino, J.; Zheng, G.; Sonnenberg, J. L.; Hada, M.; Ehara, M.; Toyota, K.; Fukuda, R.; Hasegawa, J.; Ishida, M.; Nakajima, T.; Honda, Y.; Kitao, O.; Nakai, H.; Vreven, T.; Montgomery, J. A., Jr.; Peralta, J. E.;

Ogliaro, F.; Bearpark, M.; Heyd, J. J.; Brothers, E.; Kudin, K. N.; Staroverov, V. N.; Keith, T.; Kobayashi, R.; Normand, J.; Raghavachari, K.; Rendell, A.; Burant, J. C.; Iyengar, S. S.; Tomasi, J.; Cossi, M.; Rega, N.; Millam, J. M.; Klene, M.; Knox, J. E.; Cross, J. B.; Bakken, V.; Adamo, C.; Jaramillo, J.; Gomperts, R.; Stratmann, R. E.; Yazyev, O.; Austin, A. J.; Cammi, R.; Pomelli, C.; Ochterski, J. W.; Martin, R. L.; Morokuma, K.; Zakrzewski, V. G.; Voth, G. A.; Salvador, P.; Dannenberg, J. J.; Dapprich, S.; Daniels, A. D.; Farkas, O.; Foresman, J. B.; Ortiz, J. V.; Cioslowski, J.; Fox, D. J.; *Gaussian 09*, C.01 ed.; Gaussian, Inc., Wallingford CT: 2010.

62 Fülscher, M. P.; Serrano-Andrés, L. *Mol. Phys.* **2002**, *100*, 903.

63 Gaiduk, A. P.; Firaha, D. S.; Staroverov, V. N. *Phys. Rev. Lett.* **2012**, *108*, 253005.

64 Gaiduk, A. P.; Mizzi, D.; Staroverov, V. N. *Phys. Rev. A* **2012**, *86*, 052518.

65 Gaiduk, A. P.; Staroverov, V. N. *J. Chem. Phys.* **2009**, *131*, 044107.

66 Garrett, B. C.; Truhlar, D. G. In *Theoretical Chemistry: Theory of Scattering: Papers in Honor of Henry Eyring*; Henderson, D., Ed.; Academic: New York, 1981, p 215.

67 Gáspár, R. *Acta Phys. Acad. Scientiarum Hungaricae* **1954**, *3*, 263.

68 Godsi, O.; Evenhuis, C. R.; Collins, M. A. *J. Chem. Phys.* **2006**, *125*, 104105.

69 Gonzalez, L.; Escudero, D.; Serrano-Andres, L. *ChemPhysChem* **2012**, *13*, 28.

70 Gordon, M. S.; Schmidt, M. W. In *Theory and Applications of Computational Chemistry: The First Forty Years*; Dykstra, C. E., Frenking, G., Kim, K. S., Scuseria, G. E., Eds. 2005, p 1167.

71 Gozem, S.; Huntress, M.; Schapiro, I.; Lindh, R.; Granovsky, A. A.; Angeli, C.; Olivucci, M. *J. Chem. Theory Comput.* **2012**, *8*, 4069.

72 Granovsky, A. A. *J. Chem. Phys.* **2011**, *134*, 214113.

73 Gritsenko, O. V.; Schipper, P. R. T.; Baerends, E. J. *Chem. Phys. Lett.* **1999**, *302*, 199.

74 Guerra, C. F.; Snijders, J.; Te Velde, G.; Baerends, E. *Theor. Chem. Acc.* **1998**, *99*, 391.

75 Gupta, S.; Dharamvir, K.; Jindal, V. K. *Int. J. Mod Phys B* **2004**, *18*, 1021.

76 Han, S.; Lim, J. S.; Yoon, J.-H.; Lee, J.; Kim, S.-Y.; Kim, S. K. *J. Chem. Phys.* **2014**, *140*, 054307.

77 Hanrath, M. *Mol. Phys.* **2008**, *106*, 1949.

78 Hariharan, P. C.; Pople, J. A. *Theor. Chim. Acta* **1973**, *28*, 213.

79 Hashimoto, T.; Nakano, H.; Hirao, K. *J. Chem. Phys.* **1996**, *104*, 6244.

80 Hazra, A.; Nooijen, M. *Int. J. Quantum Chem.* **2003**, *95*, 643.

81 Hehre, W. J.; Ditchfield, R.; Pople, J. A. *J. Chem. Phys.* **1972**, *56*, 2257.

82 Helgaker, T.; Jorgensen, P.; Olsen, J. *Molecular Electronic-Structure Theory*; John Wiley & Sons Ltd West Sussex, 2000.

83 Heller, E. J. *J. Chem. Phys.* **1978**, *68*, 2066.

84 Herzenberg, A.; Sherrington, D.; Süveges, M. *Proc. Phys. Soc.* (London) **1964**, *84*, 465.

85 Hirao, K. *Chem. Phys. Lett.* **1992**, *190*, 374.

86 Hirao, K. *Chem. Phys. Lett.* **1992**, *196*, 397.

87 Hirao, K. *Int. J. Quantum Chem.* **1992**, *44*, 517.

88 Hirata, S.; Head-Gordon, M. *Chem. Phys. Lett.* **1999**, *314*, 291.

89 Hirata, S.; Zhan, C.-G.; Aprà, E.; Windus, T. L.; Dixon, D. A. *J. Phys. Chem. A* **2003**, *107*, 10154.

90 Hirsch, G.; Buenker, R. J.; Petrongolo, C. *Mol. Phys.* **1991**, *73*, 1085.

91 Hohenberg, P.; Kohn, W. *Phys. Rev.* **1964**, *136*, B864.

92 Holt, S. L.; Ballhausen, C. J. *Theor. Chim. Acta* **1967**, *7*, 313.

93 Hoshino-Nagasaka, M.; Suzuki, T.; Ichimura, T.; Kasahara, S.; Baba, M.; Kawauchi, S. *Phys. Chem. Chem. Phys.* **2010**, *12*, 13243.

94 Hoyer, C. E.; Xu, X.; Ma, D.; Gagliardi, L.; Truhlar, D. G. *J. Chem. Phys.* **2014**, *141*, 114104.

95 http://cccbdb.nist.gov/expbondlengths2.asp?descript=rLiH&all=0 (accessed 3 October 2014.)

96 http://comp.chem.umn.edu/db/dbs/mgae109.html (accessed April 12, 2015.)

97 https://bse.pnl.gov/bse/portal (accessed Mar. 24, 2014).

98 Huix-Rotlland, M. Ph.D. thesis, Joseph Fourier University (Grenoble I), Mar. 17, 2012, http://tel.archives-ouvertes.fr/tel-00680039 (accessed Dec. 19, 2013)

99 Huix-Rotllant, M.; Ipatov, A.; Rubio, A.; Casida, M. E. *Chem. Phys.* **2011**, *391*, 120.

100 Huix-Rotllant, M.; Natarajan, B.; Ipatov, A.; Wawire, C. M.; Deutsch, T.; Casida, M. E. *Phys. Chem. Chem. Phys.* **2010**, *12*, 12811.

101 Ianconescu, R.; Pollak, E. *J. Phys. Chem. A* **2004**, *108*, 7778.

102 Iikura, H.; Tsuneda, T.; Yanai, T.; Hirao, K. *J. Chem. Phys.* **2001**, *115*, 3540.

103 Isegawa, M.; Peverati, R.; Truhlar, D. G. *J. Chem. Phys.* **2012**, *137*, 244104.

104 Isegawa, M.; Truhlar, D. G. *J. Chem. Phys.* **2013**, *138*, 134111.

105 Ivanic, J. *J. Chem. Phys.* **2003**, *119*, 9364.

106 Jacquemin, D.; Planchat, A.; Adamo, C.; Mennucci, B. *J. Chem. Theory Comput.* **2012**, *8*, 2359.

107 Jasper, A. W.; Kendrick, B. K.; Mead, C. A.; Truhlar, D. G. In *Modern Trends in Chemical Reaction Dynamics: Experiment and Theory (Part 1)*; Yang, X., Liu, K., Eds.; World Scientific: Singapore, 2004, p 329.

108 Jasper, A. W.; Truhlar, D. G. In *Conical Intersections: Theory, Computation, and Experiment*; Domcke, W., Yarkony, D. R., Koppel, H., Eds.; World Scientific, Singapore: 2011.

109 Jiang, X.; Karlsson, K. M.; Gabrielsson, E.; Johansson, E. M.; Quintana, M.; Karlsson, M.; Sun, L.; Boschloo, G.; Hagfeldt, A. *Adv. Funct. Mater.* **2011**, *21*, 2944.

110 Kaduk, B.; Van Voorhis, T. *J. Chem. Phys.* **2010**, *133*, 061102.

111 Karasulu, B.; Götze, J. P.; Thiel, W. *J. Chem. Theory Comput.* **2014**, *10*, 5549.

112 Karlström, G.; Lindh, R.; Malmqvist, P.-Å.; Roos, B. r. O.; Ryde, U.; Veryazov, V.; Widmark, P.-O.; Cossi, M.; Schimmelpfennig, B.; Neogrady, P.; Seijo, L. *Comput. Mater. Sci.* **2003**, *28*, 222.

113 Karplus, M.; Kolker, H. *J. Chem. Phys.* **1963**, *39*, 2997.

114 Kendall, R. A.; Dunning, J. T. H.; Harrison, R. J. *J. Chem. Phys.* **1992**, *96*, 6796.

115 Kendrick, B. K.; Mead, C. A.; Truhlar, D. G. *Chem. Phys.* **2002**, *277*, 31.

116 Koch, H.; Jørgensen, P. *J. Chem. Phys.* **1990**, *93*, 3333.

117 Kohn, W.; Sham, L. J. *Phys. Rev.* **1965**, *140*, A1133.

118 Kokoouline, V.; Greene, C. H. *Faraday Discuss.* **2004**, *127*, 413.

119 Köppel, H. *Faraday Discuss.* **2004**, *127*, 35.

120 Köppel, H. In *Conical Intersections: Electronic Structure, Dynamics and Spectroscopy*; Domcke, W., Yarkony, D. R., Köppel, H., Eds.; World Scientific Publishing Co. Pte. Ltd.: 2004.

121 Köppel, H.; Cederbaum, L.; Domcke, W. *J. Chem. Phys.* **1982**, *77*, 2014.

122 Kowalski, K. *J. Chem. Phys.* **2009**, *130*, 194110.

123 Kowalski, K.; Piecuch, P. *J. Chem. Phys.* **2004**, *120*, 1715.

124 Krishnan, R.; Binkley, J. S.; Seeger, R.; Pople, J. A. *J. Chem. Phys.* **1980**, *72*, 650.

125 Kryachko, E. S.; Yarkony, D. R. *Int. J. Quantum Chem.* **2000**, *76*, 235.

126 Kulander, K. C.; Heller, E. J. *J. Chem. Phys.* **1978**, *69*, 2439.

127 Kümmel, S.; Kronik, L. *Rev. Mod. Phys.* **2008**, *80*, 3.

128 Kupka, H. J. *Transitions in molecular systems*; WILEY-VCH Verlag GmbH & Co. KGaA: Weinheim, 2010.

129 Lan, Z.; Domcke, W.; Vallet, V.; Sobolewski, A. L.; Mahapatra, S. *J. Chem. Phys.* **2005**, *122*, 224315.

130 Lasorne, B.; Jornet-Somoza, J.; Meyer, H. D.; Lauvergnat, D.; Robb, M. A.; Gatti, F. *Spectroc. Acta Pt. A* **2014**, *119*, 52.

131 Laurent, A. D.; Jacquemin, D. *Int. J. Quantum Chem.* **2013**, *113*, 2019.

132 Lee, C. T.; Yang, W. T.; Parr, R. G. *Phys. Rev. B* **1988**, *37*, 785.

133 Lee, S. Y.; Heller, E. J. *J. Chem. Phys.* **1979**, *71*, 4777.

134 Levine, B. G.; Ko, C.; Quenneville, J.; MartÍnez, T. J. *Mol. Phys.* **2006**, *104*, 1039.

135 Levy, M. *Proc. Natl. Acad. Sci. U.S.A.* **1979**, *76*, 6062.

136 Li, S. L. and D. G. Truhlar, FCBand 2017; available for free download at http://comp.chem.umn.edu/fcband/ (accessed March 26, 2017).

137 Li, S. L.; D. G. Truhlar, *QuickFFmn 2016* (http://comp.chem.umn.edu/abcrate/) based on *QuickFF* version 1.0.1 (http://molmod.github.io/QuickFF)

138 Li, S. L.; Marenich, A. V.; Xu, X.; Truhlar, D. G. *J. Phys. Chem. Lett.* **2013**, *5*, 322.

139 Li, S. L.; Truhlar, D. G. *J. Chem. Phys.* **2014**, *141*, 104106.

140 Li, S. L.; Truhlar, D. G. *J. Chem. Phys.* **2017**, *146*, 064301.

141 Li, S. L.; Truhlar, D. G. *J. Chem. Theory Comput.* **2015**, *11*, 3123.

142 Li, S. L.; Truhlar, D. G.; Schmidt, M. W.; Gordon, M. S. *J. Chem. Phys.* **2015**, *142*, 064106.

143 Li, S. L.; Xu, X.; Hoyer, C. E.; Truhlar, D. G. *J. Phys. Chem. Lett.* **2015**, *6*, 3352.

144 Li, S. L.; Xu, X.; Truhlar, D. G. *Phys. Chem. Chem. Phys.* **2015**, *17*, 20093.

145 Li, Z. H.; Valero, R.; Truhlar, D. *Theor. Chem. Acc.* **2007**, *118*, 9.

146 Lichten, W. *Phys. Rev.* **1963**, *131*, 229.

147 Lim, I. S.; Lim, J. S.; Lee, Y. S.; Kim, S. K. *J. Chem. Phys.* **2007**, *126*, 034306.

148 Lim, J. S.; Kim, S. K. *Nat. Chem.* **2010**, *2*, 627.

149 Lim, J. S.; Lim, I. S.; Lee, K.-S.; Ahn, D.-S.; Lee, Y. S.; Kim, S. K. *Angew. Chem. Int. Ed.* **2006**, *45*, 6290.

150 Liu, M.-X.; Xie, B.-B.; Li, M.-J.; Zhao, Y.-Y.; Pei, K.-M.; Wang, H.-G.; Zheng, X. *Journal of Raman Spectroscopy* **2013**, *44*, 440.

151 Longuet-Higgins, H. C. *Proc. R. Soc. London, Ser. A* **1975**, *344*, 147.

152 Lu, T.; Chen, F. *J. Comput. Chem.* **2012**, *33*, 580.

153 Lynch, B. J.; Zhao, Y.; Truhlar, D. G. *J. Phys. Chem. A* **2003**, *107*, 1384.

154 Ma, D.; Li Manni, G.; Gagliardi, L. *J. Chem. Phys.* **2011**, *135*, 044128.

155 Macak, P.; Luo, Y.; Ågren, H. *Chem. Phys. Lett.* **2000**, *330*, 447.

156 Macias, A.; Riera, A. *J. Phys. B* **1978**, *11*, L489.

157 Maitra, N. T.; Zhang, F.; Cave, R. J.; Burke, K. *J. Chem. Phys.* **2004**, *120*, 5932.

158 Manaa, M. R.; Yarkony, D. R. *J. Chem. Phys.* **1992**, *97*, 715.

159 Marenich, A. V.; Cramer, C. J.; Truhlar, D. G. *J. Phys. Chem. B* **2014**, *119*, 958.

160 Marques, M. A. L.; Gross, E. K. U. *Annu. Rev. Phys. Chem.* **2004**, *55*, 427.

161 Matsika, S.; Krause, P. In *Annual Review of Physical Chemistry, Vol 62*; Leone, S. R., Cremer, P. S., Groves, J. T., Johnson, M. A., Eds. 2011; Vol. 62, p 621.

162 McLachlan, A.; Ball, M. *Rev. Mod. Phys.* **1964**, *36*, 844.

163 Mead, C. A. *J. Chem. Phys.* **1979**, *70*, 2276.

164 Mead, C. A.; Truhlar, D. G. *J. Chem. Phys.* **1979**, *70*, 2284.

165 Mead, C. A.; Truhlar, D. G. *J. Chem. Phys.* **1982**, *77*, 6090.

166 Meyer, H. D.; Miller, W. H. *J. Chem. Phys.* **1979**, *70*, 3214.

167 Miehlich, B.; Savin, A.; Stoll, H.; Preuss, H. *Chem. Phys. Lett.* **1989**, *157*, 200.

168 Mielke, S. L.; Tawa, G. J.; Truhlar, D. G.; Schwenke, D. W. *J. Am. Chem. Soc.* **1993**, *115*, 6436.

169 Migani, A.; Sinicropi, A.; Ferré, N.; Cembran, A.; Garavelli, M.; Olivucci, M. *Faraday Discuss.* **2004**, *127*, 179.

170 Minezawa, N.; Gordon, M. S. *J. Phys. Chem. A* **2009**, *113*, 12749.

171 Miyajima, M.; Watanabe, Y.; Nakano, H. *J. Chem. Phys.* **2006**, *124*, 044101.

172 Morse, P. M. *Phys. Rev.* **1929**, *34*, 57.

173 Mota, V. C.; Varandas, A. J. **2008**.

174 Mulliken, R. S. *Phys. Rev.* **1936**, *50*, 1028.

175 Nagasaka-Hoshino, M.; Isozaki, T.; Suzuki, T.; Ichimura, T.; Kawauchi, S. *Chem. Phys. Lett.* **2008**, *457*, 58.

176 Nakamura, H.; Truhlar, D. G. *J. Chem. Phys.* **2001**, *115*, 10353.

177 Nakamura, H.; Truhlar, D. G. *J. Chem. Phys.* **2002**, *117*, 5576.

178 Nakamura, H.; Truhlar, D. G. *J. Chem. Phys.* **2003**, *118*, 6816.

179 Nakano, H. *Chem. Phys. Lett.* **1993**, *207*, 372.

180 Nakano, H. *J. Chem. Phys.* **1993**, *99*, 7983.

181 Nakano, H.; Hirao, K. *Chem. Phys. Lett.* **2000**, *317*, 90.

182 Nakano, H.; Uchiyama, R.; Hirao, K. *J. Comput. Chem.* **2002**, *23*, 1166.

183 Nangia, S.; Truhlar, D. G. *J. Chem. Phys.* **2006**, *124*, 124309.

184 Neese, F. *WIREs Comput. Mol. Sci.* **2012**, *2*, 73.

185 Neugebauer, J.; Baerends, E. J.; Nooijen, M. *J. Phys. Chem. A* **2005**, *109*, 1168.

186 Nguyen, K. A.; Day, P. N.; Pachter, R. *J. Chem. Phys.* **2011**, *135*, 074109.

187 Nix, M. G. D.; Devine, A. L.; Cronin, B.; Dixon, R. N.; Ashfold, M. N. R. *J. Chem. Phys.* **2006**, *125*, 133318.

188 Olsen, J.; Roos, B. O.; Jo/rgensen, P.; Jensen, H. J. r. A. *J. Chem. Phys.* **1988**, *89*, 2185.

189 Omidyan, R.; Rezaei, H. *Phys. Chem. Chem. Phys.* **2014**, *16*, 11679.

190 Pacher, T.; Cederbaum, L. S.; Köppel, H. *Adv. Chem. Phys.* **1993**, *84*, 293.

191 Papajak, E.; Zheng, J.; Xu, X.; Leverentz, H. R.; Truhlar, D. G. *J. Chem. Theory Comput.* **2011**, *7*, 3027.

192 Parr, R. G.; Yang, W. *Density-Functional Theory of Atoms and Molecules*; Oxford University Press: New York, 1989.

193 Peng, Q.; Niu, Y.; Deng, C.; Shuai, Z. *Chem. Phys.* **2010**, *370*, 215.

194 Per, S.; Anders, H.; Björn, R.; Bernard, L. *Phys. Scr.* **1980**, *21*, 323.

195 Perdew, J. P.; Burke, K.; Ernzerhof, M. *Phys. Rev. Lett.* **1996**, *77*, 3865.

196 Perdew, J. P.; Parr, R. G.; Levy, M.; Balduz, J. L. *Phys. Rev. Lett.* **1982**, *49*, 1691.

197 Perdew, J. P.; Yue, W. *Phys. Rev. B* **1986**, *33*, 8800.

198 Petrenko, T.; Neese, F. *J. Chem. Phys.* **2007**, *127*, 164319.

199 Peverati, R.; Truhlar, D. G. *J. Chem. Phys.* **2011**, *135*, 191102.

200 Press, W. H.; Teukolsky, S. A.; Vetterling, W. T.; Flannery, B. P. *Numerical Recipes in Fortran 77*; 2nd ed.; Cambridge University Press, 1992.

201 Roberts, G. M.; Hadden, D. J.; Bergendahl, L. T.; Wenge, A. M.; Harris, S. J.; Karsili, T. N. V.; Ashfold, M. N. R.; Paterson, M. J.; Stavros, V. G. *Chem. Sci.* **2013**, *4*, 993.

202 Salassa, L.; Garino, C.; Salassa, G.; Gobetto, R.; Nervi, C. *J. Am. Chem. Soc.* **2008**, *130*, 9590.

203 Sannen, C.; Raşeev, G.; Galloy, C.; Fauville, G.; Lorquet, J. *J. Chem. Phys.* **1981**, *74*, 2402.

204 Santoro, F.; Improta, R.; Lami, A.; Bloino, J.; Barone, V. *J. Chem. Phys.* **2007**, *126*, 084509.

205 Santoro, F.; Jacquemin, D. *WIREs Comput. Mol. Sci.* **2016**, *6*, 460.

206 Santoro, F.; Lami, A.; Improta, R.; Barone, V. *J. Chem. Phys.* **2007**, *126*, 184102.

207 Santoro, F.; Lami, A.; Improta, R.; Bloino, J.; Barone, V. *J. Chem. Phys.* **2008**, *128*, 224311.

208 Schäfer, A.; Horn, H.; Ahlrichs, R. *J. Chem. Phys.* **1992**, *97*, 2571.

209 Schäfer, A.; Huber, C.; Ahlrichs, R. *J. Chem. Phys.* **1994**, *100*, 5829.

210 Schipper, P. R. T.; Gritsenko, O. V.; van Gisbergen, S. J. A.; Baerends, E. J. *J. Chem. Phys.* **2000**, *112*, 1344.

211 Schmidt, M. W.; Baldridge, K. K.; Boatz, J. A.; Elbert, S. T.; Gordon, M. S.; Jensen, J. H.; Koseki, S.; Matsunaga, N.; Nguyen, K. A.; Su, S. J.; Windus, T. L.; Dupuis, M.; Montgomery, J. A. *J. Comput. Chem.* **1993**, *14*, 1347.

212 Schmidt, M. W.; Gordon, M. S. *Annu. Rev. Phys. Chem.* **1998**, *49*, 233.

213 Schreiber, M.; Silva-Junior, M. R.; Sauer, S. P. A.; Thiel, W. *J. Chem. Phys.* **2008**, *128*, 134110.

214 Schwenke, D. W.; Mielke, S. L.; Tawa, G. J.; Friedman, R. S.; Halvick, P.; Truhlar, D. G. *Chem. Phys. Lett.* **1993**, *203*, 565.

215 Shao, Y.; Head-Gordon, M.; Krylov, A. I. *J. Chem. Phys.* **2003**, *118*, 4807.

216 Shavitt, I.; Bartlett, R. J. *Many-Body Methods in Chemistry and Physics*; Cambridge University Press, 2009.

217 Shiozaki, T.; Győrffy, W.; Celani, P.; Werner, H.-J. *J. Chem. Phys.* **2011**, *135*, 081106.

218 Shishkov, I. F.; Khristenko, L. V.; Karasev, N. M.; Vilkov, L. V.; Oberhammer, H. *J. Mol. Struct.* **2008**, *873*, 137.

219 Sidis, V. *Adv. Chem. Phys* **1992**, *82*, 73.

220 Simah, D.; Hartke, B.; Werner, H.-J. *J. Chem. Phys.* **1999**, *111*, 4523.

221 Simons, G.; Parr, R. G.; Finlan, J. M. *J. Chem. Phys.* **1973**, *59*, 3229.

222 Sobolewski, A. L.; Domcke, W. *Chem. Phys.* **2000**, *259*, 181.

223 Sobolewski, A. L.; Domcke, W. *Chem. Phys. Lett.* **1999**, *315*, 293.

224 Sobolewski, A. L.; Domcke, W. *J. Phys. Chem. A* **2001**, *105*, 9275.

225 Sobolewski, A. L.; Domcke, W.; Dedonder-Lardeux, C.; Jouvet, C. *Phys. Chem. Chem. Phys.* **2002**, *4*, 1093.

226 Song, J.-W.; Hirosawa, T.; Tsuneda, T.; Hirao, K. *J. Chem. Phys.* **2007**, *126*, 154105.

227 Spiegelmann, F.; Malrieu, J. *J. Phys. B* **1984**, *17*, 1259.

228 Stanton, J. F.; Bartlett, R. J. *J. Chem. Phys.* **1993**, *98*, 7029.

229 Stephens, P. J.; Devlin, F. J.; Chabalowski, C. F.; Frisch, M. J. *J. Phys. Chem.* **1994**, *98*, 11623.

230 Stewart, J. J. P. *J. Comput. Chem.* **1989**, *10*, 209.

231 Stewart, J. J. P. *J. Comput. Chem.* **1989**, *10*, 221.

232 Stewart, J. J. P., L. Fiedler, P. Zhang, J. Zheng, I. Rossi, W.-P. Hu, G. C. Lynch, Y.-P. Liu, Y.-Y. Chuang, J. Pu, J. Li, C. J. Cramer, P. L. Fast, J. Gao, and D. G. Truhlar, MOPAC–version 5.021mn (2013), University of Minnesota, Minneapolis, MN 55455.

233 Stwalley, W. C.; Zemke, W. T. *J. Phys. Chem. Ref. Data* **1993**, *22*, 87.

234 Subotnik, J. E.; Yeganeh, S.; Cave, R. J.; Ratner, M. A. *J. Chem. Phys.* **2008**, *129*, 244101.

235 Szabo, A.; Ostlund, N. S. *Modern Quantum Chemistry: Introduction to Advanced Electronic Structure Theory*; McGraw-Hill, Inc., 1989.

236 Tamm, I. *J. Phys. (Moscow)* **1945**, *9*, 449.

237 Tang, J.; Lee, M. T.; Lin, S. H. *J. Chem. Phys.* **2003**, *119*, 7188.

238 Tannor, D. J.; Heller, E. J. *J. Chem. Phys.* **1982**, *77*, 202.

239 Tapavicza, E.; Tavernelli, I.; Rothlisberger, U.; Filippi, C.; Casida, M. E. *J. Chem. Phys.* **2008**, *129*, 124108.

240 Te Velde, G. t.; Bickelhaupt, F. M.; Baerends, E. J.; Fonseca Guerra, C.; van Gisbergen, S. J.; Snijders, J. G.; Ziegler, T. *J. Comput. Chem.* **2001**, *22*, 931.

241 Teller, E. *J. Phys. Chem.* **1937**, *41*, 109.

242 Tishchenko, O.; Truhlar, D. G.; Ceulemans, A.; Nguyen, M. T. *J. Am. Chem. Soc.* **2008**,

130, 7000.

243 Toniolo, A.; Olsen, S.; Manohar, L.; Martinez, T. *Faraday Discuss.* **2004**, *127*, 149.

244 Tozer, D. J.; Handy, N. C. *J. Chem. Phys.* **1998**, *108*, 2545.

245 Tozer, D. J.; Handy, N. C. *Phys. Chem. Chem. Phys.* **2000**, *2*, 2117.

246 Truhlar, D. G. *Int. J. Quantum Chem.* **1973**, *7*, 807.

247 Truhlar, D. G.; Duff, J. W.; Blais, N. C.; Tully, J. C.; Garrett, B. C. *J. Chem. Phys.* **1982**, *77*, 764.

248 Truhlar, D. G.; Mead, C. A. *Phys. Rev. A* **2003**, *68*, 032501.

249 Truhlar, D. G.; Olson, R. W.; Jeannotte, A. C.; Overend, J. *J. Am. Chem. Soc.* **1976**, *98*, 2373.

250 Tsuneda, T.; Suzumura, T.; Hirao, K. *J. Chem. Phys.* **1999**, *110*, 10664.

251 Tully, J. C. *J. Chem. Phys.* **1990**, *93*, 1061.

252 Valero, R.; Song, L.; Gao, J.; Truhlar, D. G. *J. Chem. Theory Comput.* **2009**, *5*, 1.

253 Valero, R.; Truhlar, D. G. *J. Chem. Phys.* **2006**, *125*, 194305.

254 Valero, R.; Truhlar, D. G. *J. Chem. Phys.* **2012**, *137*, 22A539.

255 Valero, R.; Truhlar, D. G. *J. Phys. Chem. A* **2007**, *111*, 8536.

256 Valero, R.; Truhlar, D. G.; Jasper, A. W. *J. Phys. Chem. A* **2008**, *112*, 5756.

257 Valiev, M.; Bylaska, E. J.; Govind, N.; Kowalski, K.; Straatsma, T. P.; Van Dam, H. J. J.; Wang, D.; Nieplocha, J.; Apra, E.; Windus, T. L.; de Jong, W. *Comput. Phys. Commun.* **2010**, *181*, 1477.

258 van Leeuwen, R.; Baerends, E. J. *Phys. Rev. A* **1994**, *49*, 2421.

259 Van Lenthe, E.; Baerends, E. J. *J. Comput. Chem.* **2003**, *24*, 1142.

260 van Meer, R.; Gritsenko, O. V.; Baerends, E. J. *J. Chem. Theory Comput.* **2014**, *10*, 4432.

261 Van Voorhis, T.; Kowalczyk, T.; Kaduk, B.; Wang, L.-P.; Cheng, C.-L.; Wu, Q. *Annu. Rev. Phys. Chem.* **2010**, *61*, 149.

262 Vanduyfhuys, L.; Vandenbrande, S.; Verstraelen, T.; Schmid, R.; Waroquier, M.; Van Speybroeck, V. *J. Comput. Chem.* **2015**, *36*, 1015.

263 Varandas, A. J. C. *J. Chem. Phys.* **2009**, *131*, 124128.

264 Varshni, Y. P. *Rev. Mod. Phys.* **1957**, *29*, 664.

265 Veryazov, V.; Widmark, P.-O.; Serrano-Andrés, L.; Lindh, R.; Roos, B. O. *Int. J.*

Quantum Chem. **2004**, *100*, 626.

266 Vieuxmaire, O. P. J.; Lan, Z.; Sobolewski, A. L.; Domcke, W. *J. Chem. Phys.* **2008**, *129*, 224307.

267 Wang, F.; Ziegler, T. *Int. J. Quantum Chem.* **2006**, *106*, 2545.

268 Wang, F.; Ziegler, T. *J. Chem. Phys.* **2004**, *121*, 12191.

269 Wang, F.; Ziegler, T. *J. Chem. Phys.* **2005**, *122*, 074109.

270 Wei, J.; Riedel, y.; Kuczmann, A.; Renth, F.; Temps, F. *Faraday Discuss.* **2004**, *127*, 267.

271 Wenge, A. M.; Karsili, T. N. V.; Rodriguez, J. D.; Cotterell, M. I.; Marchetti, B.; Dixon, R. N.; Ashfold, M. N. R. *Phys. Chem. Chem. Phys.* **2015**, *17*, 16246.

272 Werner, H. J.; Meyer, W. *J. Chem. Phys.* **1981**, *74*, 5794.

273 Werner, H.-J.; Knowles, P. J.; Knizia, G.; Manby, F. R.; Schütz, M. *WIREs Comput. Mol. Sci.* **2012**, *2*, 242.

274 Werner, H.-J.; P. J. Knowles, G. Knizia, F. R. Manby, M. Schütz, and others, MOLPRO, version 2012.1, a package of ab initio programs, see http://www.molpro.net

275 Wiberg, K. B.; de Oliveira, A. E.; Trucks, G. *J. Phys. Chem. A* **2002**, *106*, 4192.

276 Wilson, E. B.; Decius, J.; Cross, P. *Molecular Vibrations*; McGraw-Hill: New York, 1955.

277 Witek, H. A.; Choe, Y.-K.; Finley, J. P.; Hirao, K. *J. Comput. Chem.* **2002**, *23*, 957.

278 Woon, D. E.; Dunning, T. H. *J. Chem. Phys.* **1993**, *98*, 1358.

279 Worth, G. A.; Cederbaum, L. S. *Annu. Rev. Phys. Chem.* **2004**, *55*, 127.

280 Woywod, C.; Stengle, M.; Domcke, W.; Flöthmann, H.; Schinke, R. *J. Chem. Phys.* **1997**, *107*, 7282.

281 Xu, X.; Gozem, S.; Olivucci, M.; Truhlar, D. G. *J. Phys. Chem. Lett.* **2012**, *4*, 253.

282 Xu, X.; Yang, K. R.; Truhlar, D. G. *J. Chem. Theory Comput.* **2013**, *9*, 3612.

283 Xu, X.; Yang, K. R.; Truhlar, D. G. *J. Chem. Theory Comput.* **2014**, *10*, 2070.

284 Xu, X.; Zheng, J.; Yang, K. R.; Truhlar, D. G. *J. Am. Chem. Soc.* **2014**, *136*, 16378.

285 Yabushita, S.; Morokuma, K. *Chem. Phys. Lett.* **1988**, *153*, 517.

286 Yanai, T.; Tew, D. P.; Handy, N. C. *Chem. Phys. Lett.* **2004**, *393*, 51.

287 Yang, C.-H.; Beltran, J.; Lemaur, V.; Cornil, J.; Hartmann, D.; Sarfert, W.; Fröhlich, R.; Bizzarri, C.; De Cola, L. *Inorg. Chem.* **2010**, *49*, 9891.

288 Yang, K. R.; Xu, X.; Truhlar, D. G. *Chem. Phys. Lett.* **2013**, *573*, 84.

289 Yang, K. R.; Xu, X.; Truhlar, D. G. *J. Chem. Theory Comput.* **2014**, *10*, 924.

290 Yang, K. R.; Xu, X.; Zheng, J.; Truhlar, D. G. *Chem. Sci.* **2014**, *5*, 4661.

291 Yarkony, D. R. *Faraday Discuss.* **2004**, *127*, 325.

292 Yarkony, D. R. *Rev. Mod. Phys.* **1996**, *68*, 985.

293 Yu, H. S.; Li, S. L.; Truhlar, D. G. *J. Chem. Phys.* **2016**, *145*, 130901.

294 Zaripov, N. M. *Russ. J. Struct. Chem. (Engl.)* **1976**, *17*, 640.

295 Zhang, A.-J.; Zhang, P.-Y.; Chu, T.-S.; Han, K.-L.; He, G.-Z. *J. Chem. Phys.* **2012**, *137*, 194305.

296 Zhao, Y.; Schultz, N. E.; Truhlar, D. G. *J. Chem. Theory Comput.* **2006**, *2*, 364.

297 Zhao, Y.; Truhlar, D. G. *Acc. Chem. Res.* **2008**, *41*, 157.

298 Zhao, Y.; Truhlar, D. G. *Theor. Chem. Acc.* **2008**, *120*, 215.

299 Zheng, J., Z.-H. Li, A. W. Jasper, D. A. Bonhommeau, R. Valero, R. Meana-Pañeda, and D. G. Truhlar, ANT, version 2014-2, University of Minnesota, Minneapolis, 2015. http://comp.chem.umn.edu/ant

300 Zheng, J.; S. Zhang, B. J. Lynch, J. C. Corchado, Y.-Y. Chuang, P. L. Fast, W.-P. Hu, Y.-P. Liu, G. C. Lynch, K. A. Nguyen, C. F. Jackels, A. Fernandez Ramos, B. A. Ellingson, V. S. Melissas, J. Villà, I. Rossi, E. L. Coitino, J. Pu, T. V. Albu, R. Steckler, B. C. Garrett, A. D. Isaacson, and D. G. Truhlar, *POLYRATE*–version 2010-A, University of Minnesota, Minneapolis, 2010. http://comp.chem.umn.edu/polyrate (accessed June 14, 2016)

301 Zheng, J.; Z.-H. Li, A. W. Jasper, D. A. Bonhommeau, R. Valero, R. Meana-Paneda, and D. G. Truhlar, *ANT*, version 2014-2, University of Minnesota, Minneapolis, 2015. http://comp.chem.umn.edu/ant (accessed June 14, 2016)

302 Zhu, C. Y.; Nangia, S.; Jasper, A. W.; Truhlar, D. G. *J. Chem. Phys.* **2004**, *121*, 7658.

303 Ziegler, T. In *Molecular Electronic Structures of Transition Metal Complexes II*; Mingos, D. M. P., Day, P., Dahl, J. P., Eds.; Springer-Verlag: Berlin Heidelberg, 2012, p 1.

Appendices

A1. HOW THE PHASES OF WAVE FUNCTIONS AFFECT THE MSD STRATEGRY

A1.1. The relation between the phases of wave functions and the signs of rows and columns of a transformation matrix

To be concrete, let us consider the transformation matrix $\mathbf{B}^{\mathrm{CM}}$ converting CASSCF states to (X)MC-QDPT model states for a two-state problem (with two-dimensional model space) as an example. Suppose a valid relation is

$$\begin{pmatrix}\mathbf{c}_1 & \mathbf{c}_2\end{pmatrix}\begin{pmatrix}B_{11}^{\mathrm{CM}} & B_{12}^{\mathrm{CM}} \\ B_{21}^{\mathrm{CM}} & B_{22}^{\mathrm{CM}}\end{pmatrix}=\begin{pmatrix}\mathbf{m}_1 & \mathbf{m}_2\end{pmatrix} \tag{A1.1}$$

where bold-faced letters denote CAS-CI vectors, in particular $\mathbf{c}_1$ and $\mathbf{c}_2$ are CASSCF states, and $\mathbf{m}_1$ and $\mathbf{m}_2$ are model states. If $\mathbf{c}_i$ changes its sign, the i-th row of $\mathbf{B}^{\mathrm{CM}}$ has to change sign accordingly; e.g. for $i = 2$,

$$\begin{pmatrix}\mathbf{c}_1 & -\mathbf{c}_2\end{pmatrix}\begin{pmatrix}B_{11}^{\mathrm{CM}} & B_{12}^{\mathrm{CM}} \\ -B_{21}^{\mathrm{CM}} & -B_{22}^{\mathrm{CM}}\end{pmatrix}=\begin{pmatrix}\mathbf{m}_1 & \mathbf{m}_2\end{pmatrix} \tag{A1.2}$$

On the other hand, if $\mathbf{m}_i$ changes sign, the i-th column of $\mathbf{B}^{\mathrm{CM}}$ has to change sign accordingly; e.g. for $i = 2$,

$$\begin{pmatrix}\mathbf{c}_1 & \mathbf{c}_2\end{pmatrix}\begin{pmatrix}B_{11}^{\mathrm{CM}} & -B_{12}^{\mathrm{CM}} \\ B_{21}^{\mathrm{CM}} & -B_{22}^{\mathrm{CM}}\end{pmatrix}=\begin{pmatrix}\mathbf{m}_1 & -\mathbf{m}_2\end{pmatrix} \tag{A1.3}$$

Apparently this applies to any N by N transformation. We conclude that the signs of the rows of a transformation are related to the phases of the states *to be transformed*, while the signs of the columns are related to the phases of the *transformed* states.

A1.2 The effect of the phases of the transformation matrices on the calculation of the diabatic potential energy matrix

To see how the signs of the elements of the transformation matrices affect the calculation of the diabatic potential energy matrix **U**, we note first that changing the signs of some rows of a matrix **B** is equivalent to left-multiplying it by a diagonal matrix whose diagonal element is -1 if the corresponding row is to change sign or 1 if otherwise, e.g.

$$\begin{pmatrix} B_{11} & B_{12} \\ -B_{21} & -B_{22} \end{pmatrix} = \begin{pmatrix} 1 & 0 \\ 0 & -1 \end{pmatrix} \begin{pmatrix} B_{11} & B_{12} \\ B_{21} & B_{22} \end{pmatrix} \tag{A1.4}$$

Changing the signs of some columns of a matrix **B** is equivalent to right-multiplying it by a diagonal matrix whose diagonal element is -1 if the corresponding column is to change sign or 1 if otherwise, e.g.

$$\begin{pmatrix} B_{11} & -B_{12} \\ B_{21} & -B_{22} \end{pmatrix} = \begin{pmatrix} B_{11} & B_{12} \\ B_{21} & B_{22} \end{pmatrix} \begin{pmatrix} 1 & 0 \\ 0 & -1 \end{pmatrix} \tag{A1.5}$$

Therefore we can account for the sign changes of the rows and columns of a matrix by left- and right-multiplying it by such matrices which we will denote as **J**:

$$J_{ij} = (-1)^{\alpha_i} \delta_{ij} \tag{A1.6}$$

where $\alpha_i = 0$ or 1, δ_{ij} is the Kronecker delta function. Different **J** matrices commute. Each **J** matrix satisfies the following equality:

$$\mathbf{J}^{\mathrm{T}} = \mathbf{J}^{-1} = \mathbf{J} \tag{A1.7}$$

where superscripts "T" and "–1" denote transpose and inverse respectively.

Now let us assume that a $\mathbf{B}^{\mathrm{MC}}$ and a $\mathbf{B}^{\mathrm{CD}}$ corresponding to consistent choices of phase for the wave functions have been found, and the following relation is valid (equivalent to eq. (4.15)):

$$\mathbf{U} = \left(\mathbf{B}^{\mathrm{CD}}\right)^{\mathrm{T}} \left(\mathbf{B}^{\mathrm{MC}}\right)^{\mathrm{T}} \mathbf{V}\mathbf{B}^{\mathrm{MC}}\mathbf{B}^{\mathrm{CD}} \tag{A1.8}$$

However, the matrices printed by electronic structure calculations, denoted as $\tilde{\mathbf{B}}^{\mathrm{MC}}$ and $\tilde{\mathbf{B}}^{\mathrm{CD}}$, may differ from the ones above by the signs of rows and columns. Using the **J** matrices, we can write in general

$$\tilde{\mathbf{B}}^{\mathrm{MC}} = \mathbf{J}_{\mathrm{r}}^{\mathrm{MC}}\mathbf{B}^{\mathrm{MC}}\mathbf{J}_{\mathrm{c}}^{\mathrm{MC}}, \quad \tilde{\mathbf{B}}^{\mathrm{CD}} = \mathbf{J}_{\mathrm{r}}^{\mathrm{CD}}\mathbf{B}^{\mathrm{CD}}\mathbf{J}_{\mathrm{c}}^{\mathrm{CD}} \tag{A1.9}$$

where the subscripts "r" and "c" of the **J** matrices signify that they are responsible for the sign change of rows and columns respectively. Using these matrices, the calculated diabatic potential energy matrix is

$$\begin{aligned} \tilde{\mathbf{U}} &= \left(\tilde{\mathbf{B}}^{\mathrm{CD}}\right)^{\mathrm{T}} \left(\tilde{\mathbf{B}}^{\mathrm{MC}}\right)^{\mathrm{T}} \mathbf{V}\tilde{\mathbf{B}}^{\mathrm{MC}}\tilde{\mathbf{B}}^{\mathrm{CD}} \\ &= \mathbf{J}_{\mathrm{c}}^{\mathrm{CD}} \left(\mathbf{B}^{\mathrm{CD}}\right)^{\mathrm{T}} \mathbf{J}_{\mathrm{r}}^{\mathrm{CD}}\mathbf{J}_{\mathrm{c}}^{\mathrm{MC}} \left(\mathbf{B}^{\mathrm{MC}}\right)^{\mathrm{T}} \mathbf{J}_{\mathrm{r}}^{\mathrm{MC}}\mathbf{V}\mathbf{J}_{\mathrm{r}}^{\mathrm{MC}}\mathbf{B}^{\mathrm{MC}}\mathbf{J}_{\mathrm{c}}^{\mathrm{MC}}\mathbf{J}_{\mathrm{r}}^{\mathrm{CD}}\mathbf{B}^{\mathrm{CD}}\mathbf{J}_{\mathrm{c}}^{\mathrm{CD}} \end{aligned} \tag{A1.10}$$

Our aim is to analyze the effect of the **J** matrices on the calculated $\tilde{\mathbf{U}}$, compared to the **U** in eq. (A1.8) that is correct by assumption.

The first observation is that $\mathbf{J}_{\mathrm{r}}^{\mathrm{MC}}\mathbf{V}\mathbf{J}_{\mathrm{r}}^{\mathrm{MC}} = \mathbf{V}$. It means the signs of the rows of $\tilde{\mathbf{B}}^{\mathrm{MC}}$, corresponding to the phases of the (X)MC-QDPT model states, have no consequence. Secondly, if we rewrite eq. (A1.10) as

$$\mathbf{J}_{\mathrm{c}}^{\mathrm{CD}}\tilde{\mathbf{U}}\mathbf{J}_{\mathrm{c}}^{\mathrm{CD}} = \left(\mathbf{B}^{\mathrm{CD}}\right)^{\mathrm{T}} \mathbf{J}_{\mathrm{r}}^{\mathrm{CD}}\mathbf{J}_{\mathrm{c}}^{\mathrm{MC}} \left(\mathbf{B}^{\mathrm{MC}}\right)^{\mathrm{T}} \mathbf{J}_{\mathrm{r}}^{\mathrm{MC}}\mathbf{V}\mathbf{J}_{\mathrm{r}}^{\mathrm{MC}}\mathbf{B}^{\mathrm{MC}}\mathbf{J}_{\mathrm{c}}^{\mathrm{MC}}\mathbf{J}_{\mathrm{r}}^{\mathrm{CD}}\mathbf{B}^{\mathrm{CD}} \tag{A1.11}$$

we see that $\mathbf{J}_{\mathrm{c}}^{\mathrm{CD}}$, responsible for the signs of columns of $\tilde{\mathbf{B}}^{\mathrm{CD}}$ and the phases of the diabatic states, only affects the signs of the off-diagonal elements of the diabatic potential energy matrix without changing its nature. The only significant part is the product of $\mathbf{J}_{\mathrm{c}}^{\mathrm{MC}}$ and $\mathbf{J}_{\mathrm{r}}^{\mathrm{CD}}$. The calculated $\tilde{\mathbf{U}}$ will be correct (differing from **U** only by the signs of

off-diagonal elements) if and only if $\mathbf{J}_{\mathrm{c}}^{\mathrm{MC}}\mathbf{J}_{\mathrm{r}}^{\mathrm{CD}} = \pm\mathbf{I}$ where $\mathbf{I}$ is the identity matrix. This corresponds to the consistency of the phases of CASSCF wave functions used in the construction of the two matrices. One may keep $\mathbf{J}_{\mathrm{c}}^{\mathrm{MC}}$ intact and adjust $\mathbf{J}_{\mathrm{r}}^{\mathrm{CD}}$, equivalent to changing the signs of rows of $\tilde{\mathbf{B}}^{\mathrm{CD}}$, to satisfy the condition, which is what we adopted in Chapter 4.